Dissertation

submitted to the

Combined Faculty of Natural Sciences and Mathematics

of the Ruperto Carola University Heidelberg, Germany

for the degree of

Doctor of Natural Sciences

Presented by:

M. Sc. Molecular Biosciences	Janine Kristin Reinert
Born in	Pforzheim, Germany
Oral examination	30.07.2019

Odour discrimination in mice with perturbed granule cells, assayed by automated behavioural testing

Referees: Prof. Dr. Thomas Kuner

Prof. Dr. Stefan Frings

Summary

Olfaction, the sense of smell, is one of the most important sensory stimuli for any organism, from unicellular bacteria to highly complex metazoans like humans. Volatile chemicals constituting olfactory cues can carry a vast range of information, enabling animals to detect and locate food, mates or shelter. The structure of the olfactory system has remained remarkably conserved, indicating that the precise anatomy is integral to the detection and discrimination of odours. Previous studies have shown that the connectivity of olfactory bulb mitral and granule cells plays a crucial role in odour discrimination in mice, yet several aspects of granule cell function remain unclear.

To investigate the impact of modified granule cell function on odour discrimination in mice, we first established a novel automated operant conditioning setup. This setup allowed us to train large (>20 animals) groups of mice on a go/no-go odour discrimination task with minimal experimenter interference. It was used for detailed analysis olfactory behaviour by assessing parameters such as the discrimination time, the speed at which animals were able to discriminate and odour and initiate a corresponding behavioural response.

As neurobiological function follows form, we focussed on the specialized dendrodendritic connection between the principal output neurons of the mammalian olfactory bulb, the mitral cells, and the most abundant inhibitory interneurons of the olfactory bulb, the granule cells. As inhibition of mitral cells from granule cell has been shown to directly affect the discrimination of odour mixtures, we sought to modulate the strength of this inhibition using two different approaches. The first strategy was based on increasing the inhibitory output through the overall increase of granule cells. Towards this end, a novel transgenic mouse line was used, in which the pool of neuronal stem cells can be temporarily increased resulting in an olfactory bulb specific increase of physiologically normal and functionally integrated granule cells. Utilizing the automated behaviour setup, we were able to show that discrimination accuracy, but not the discrimination time of highly similar mixtures of two enantiomers is increased in mice harbouring an increased number of granule cells.

The second approach was based on reducing the inhibitory output of granule cells by reducing the global activation of granule cells following local dendritic activation, a feature which is thought to be gated by T-type calcium channels. Therefore, we established a simultaneous triple knock-down of all three T-type subunits using adeno-associated virus-based shRNA expression in granule cells. We found that mice with reduced T-type expression did not show the typical increase in discrimination times when comparing simple with complex odours, suggesting that a lack of global activation affects discrimination of simple odours.

In summary, these findings highlight the importance of granule cell-derived inhibitory input onto mitral cells for the discrimination of highly similar odour stimuli. Taking into account the subtle nature of the molecular modifications and the flexibility of the novel approach to behavioural phenotyping, these results clearly outline the path to a large-scale, systematic investigation into the limits of olfaction.

Zusammenfassung

Olfaktion, die Wahrnehmung von Duftstoffen, ist einer der wichtigsten Sinneseindrücke für jeden Organismus, von einzelligen Bakterien bis hin zu hoch komplexen Mehrzellern wie dem Menschen. Flüchtige Moleküle, aus denen sich Gerüche zusammensetzen, können eine Fülle von Informationen beinhalten, die es einem Tier ermöglichen, Nahrung, Sexualpartner oder einen Unterschlupf zu finden. Im Gegensatz dazu ist der Aufbau des Riechsystems erstaunlich konserviert, was darauf hindeutet, dass der genaue anatomische Aufbau ein wichtiger Bestandteil für die Wahrnehmung und Unterscheidung von Duftstoffen ist. Frühere Veröffentlichungen haben gezeigt, dass die Verbindung zwischen Mitralzellen und Körnerzellen des *Bulbus Olfactorius* in Mäusen eine entscheidende Rolle bei der Duftstoffunterscheidung spielt. Trotzdem sind einige Gesichtspunkte der Funktion von Körnerzellen weiterhin unklar.

Um den Einfluss veränderter Körnerzellfunktionalität auf die Duftstoffunterscheidung in Mäusen untersuchen zu können, wurde zunächst ein neuartiges automatisiertes Setup zur operanten Konditionierung etabliert. Mittels dieses Setups konnten große (>20 Tiere) Gruppen von Mäusen mit minimalen Eingriffen des Experimentators in einem „go/no-go"-Paradigma zur Unterscheidung von Duftstoffen trainiert werden. Dieses Setup wurde zur detaillierten Untersuchung des Riechvermögens eingesetzt indem zum Beispiel mittels der Diskriminationszeit bestimmt wurde, mit welcher Geschwindigkeit die Tiere einen Duftstoff identifizieren und die zugehörige Verhaltensreaktion ausführen konnten.

Da die neurobiologische Funktion durch die Form bedingt wird, wurden die Experimente auf die dendro-dendritische Verbindung zwischen den wichtigsten efferenten Zellen des *Bulbus Olfaktorius*, den Mitralzellen, und den häufigsten inhibitorischen Interneuronen, den Körnerzellen, fokussiert. Da bereits gezeigt werden konnte, dass Inhibierung der Mitralzellen durch die Körnerzellen einen direkten Einfluss auf Unterscheidung komplexer Duftstoffgemische hat, sollte die Stärke dieser Inhibition auf zwei verschiedene Wege modifiziert werden. Der erste Ansatz beruhte auf der Steigerung der Inhibition durch eine Erhöhung der Körnerzellanzahl. Hierfür wurde eine neuartige transgene Mauslinie eingesetzt, in der der Pool an neuronalen Stammzellen temporär vergrößert werden konnte, was einem Anstieg an physiologisch normalen und funktionsfähigen Körnerzellen spezifisch im *Bulbus Olfaktorius* zur Folge hat. Mit Hilfe des automatisierten Verhaltenssetups konnte gezeigt werden, dass die Treffsicherheit bei der Unterscheidung einer extrem schwierigen Mischung zweier Enantiomere in transgenen Tieren mit erhöhter Anzahl an Körnerzellen gesteigert war.

Der zweite Ansatz beruhte auf der Verminderung der Inhibition von Mitralzellen, indem die globale Aktivierung der gesamten Körnerzelle nach einer lokalen dendritischen Aktivierung unterbunden werden sollte. Es wird angenommen, dass diese globale Aktivierung der Körnerzellen wird von so genannten T-Typ Kalziumkanälen vermittelt wird, weshalb eine zeitgleiche Unterdrückung der Expression aller drei T-Typ Untereinheiten mit Hilfe von shRNA etabliert wurde. Hierbei konnte gezeigt werden, dass Tiere mit verminderter T-Typ Expression nicht den typischen Anstieg der Diskriminationszeiten bei komplexen

Duftstoffen verglichen mit reinen Düften aufwiesen. Dies deutet darauf hin, dass die fehlende globale Aktivierung der Körnerzellen bereits die Unterscheidung einfacher Duftstoffe beeinflusst.

Zusammenfassend unterstreichen diese Befunde die Bedeutung des inhibitorischen Inputs auf Mitralzellen bei der Unterscheidung von sehr ähnlichen Duftstoffmischungen. Wenn man dabei die Geringgradigkeit der Modifikationen auf molekularer Ebene und die Flexibilität des neuartigen Ansatzes zur Verhaltensphänotypisierung berücksichtigt, so zeigen diese Ergebnisse deutlich einen Weg für eine umfangreiche systematische Untersuchung der Grenzen des olfaktorischen Systems auf

Declaration

I, Janine Kristin Reinert, hereby declare that the work in this thesis represents my original research results. The thesis has been written by myself using the references and resources indicated. Any work of other has been appropriately marked.
The work has been conducted under the supervision of Prof. Dr. Thomas Kuner at the Institute of Anatomy and Cell Biology, Department of Functional Neuroanatomy, Medical Faculty, Heidelberg University, Germany.

This thesis is being submitted for the degree of Doctor of Natural Sciences at Heidelberg University, Germany, and has not been presented to any other university as part of an examination or degree.

Heidelberg, May 23rd

.....
Janine Kristin Reinert

Table of content

Summary i

Zusammenfassung ii

Declaration iv

Table of content v

Introduction 1

The olfactory system 1

Functional anatomy of the murine olfactory system 1

Transmission of olfactory stimuli throughout the olfactory bulb 6

Intra-glomerular circuits 7

Inter-glomerular circuits 8

Modulating olfactory bulb output through manipulation of granule cells 9

Molecular perturbation of granule cells 9

Modulating overall granule cell number 10

Tools for high-throughput olfactory phenotyping 11

Aims of this study 12

Materials and methods 13

Animals 13

C57Bl/6N mice 13

GluA2$^{\Delta GCL}$ mice 13

4D mice 13

Plasmid design and cloning 14

Design of shRNA sequences 15

Production of adeno-associated viruses 15

Affinity-chromatography purification 16

Fast protein liquid chromatography based purification 16

Stereotaxic injections 17

Implantation of RFID chips 17

Preparation of fixed tissue slices 18

Primary cell cultures 18

Quantification of shRNA-mediated knockdown efficiencies 18

RNA isolation from primary cell cultures 18

RNA isolation from acute tissue slices 19

Reverse transcription PCR and PCR cDNA amplification 19

Quantitative real-time PCR 19

Immunohistochemistry and immunocytochemistry 20

Fixed tissue samples 20
Cell culture samples 21
Antibodies 21
Microscopy 22
3D Reconstruction 22
Olfactory behaviour testing 22
Automated behaviour setup 22
Behaviour setup control and analysis software 31
Behaviour training paradigm 33
Odours used 34
Analysis parameters 35
Data analysis and presentation 37
Contributions 38
Peer-reviewed publications 38

Results 39
Part 1: Establishing an automated behaviour setup for odour discrimination 39
Technical validation of a novel automated behaviour setup 39
Effect of non-olfactory cues in automated behaviour training 40
Operant conditioning of small cohorts 41
Operant conditioning of large cohorts 43
Effects of group size on olfactory conditioning 46
Part 2: Influence of increased neurogenesis on odour discrimination 52
Biomolecular characterization of 4D expression in the olfactory system 52
Behavioural effects of increased neurogenesis in the olfactory system 56
Part 3: Influence of T-type calcium channels in olfactory bulb granule cells on odour discrimination 63
In vitro screening of putative shRNA sequences 63
In vitro validation of pre-screened shRNA sequences 67
In vivo analysis of shRNA sequences 68
Effect of the T-type calcium channels knock-down on odour discrimination 70
Post-hoc verification of the knock-down of T-type calcium channel expression 74

Discussion 77
Part 1: Establishing an automated behaviour setup for odour discrimination 77
Technical validation 77
Behavioural validation 78
Effects of varying group size on olfactory conditioning 79
Advantages and limitations of automated olfactory conditioning 80
Part 2: Influence of increased neurogenesis on odour discrimination 82
Part 3: Influence of T-type calcium channels in olfactory bulb granule cells on odour discrimination 84

Establishing a T-type calcium channel knock-down using shRNA 84
Effect of the T-type calcium channel knock-down on odour discrimination 85

Acknowledgements 87

Abbreviations 88

References 91

Appendix 100
List of supplementary figures 100
Assembly of the automated behaviour setup 100
Assembly of the setup frame 101
Construction of the housing cage 104
Construction of the bedding stopper 104
Construction of the housing cage lid 105
Construction of the tunnel leading towards the odour port 105
Placement of the tunnel on the housing cage lid 106
Construction of the olfactometer 106
Detailed overview of the input connections into the olfactometer 107
Assembly of the odour port 107
Detailed overview of the water delivery system 108
Preparation of the odour reservoir caps 109
Detailed overview of the placement of the air filters 109
Detailed overview of the pneumatics back plane 110
Connection of the pneumatics tubing 111
Detailed analysis of 4D transgenes 112
Electrophysiological properties of supernumerary olfactory bulb granule cells 113
Detailed analysis of the effect of the 4D transgene on odour discrimination 117
Detailed analysis T-type calcium channel knock-downs 119

Introduction

The olfactory system

For virtually all animals, olfaction, the sense of smell, constitutes one of the most important sensory modalities. Indeed, the ability to sense and discriminate volatile chemical compounds is present in macrosmic animals like dogs or honeybees, but it is likewise present in rather primitive organisms like the nematode *C. elegans*[1–3]. Even humans, which are typically classified as microsmic and rely heavily on the visual system, can discriminate mixtures composed of dozens of individual odours and even successfully track a scent trail across a field[4–6]. Yet, unlike auditory or visual stimuli, olfactory stimuli do not originate from a finite continuous spectrum like sound or light waves but rather from a potentially infinite number of molecules. Further, these stimuli can encode highly critical information, ranging from the distinction between prey and predator to the location and identity of food sources or even the degree of kinship with potential mates. The discovery of the olfactory receptor gene family has shed some light on how the olfactory system copes with the high diversity of potential stimuli[7]. The high dimensionality of the chemical space is reflected in the evolution of specific G-protein coupled receptors, encoded by hundreds or even thousands of genes constituting up to 5% of the total genome of some animals[7–9]. But nearly three decades later, despite the clear importance of olfaction on all facets of life, the precise mechanisms underlying identification and discrimination of odours remain far from solved.

Functional anatomy of the murine olfactory system

Both the anatomy as well as the functional principles governing olfaction are remarkably conserved between different species[10]. In mammals, odour molecules are detected by primary sensory neurons located in the vomeronasal organ (VNO) (in case of water-soluble pheromones and labile molecules) as well as in the in the olfactory epithelium (OE) (in case of volatile odours; Figure 1)[11,12].

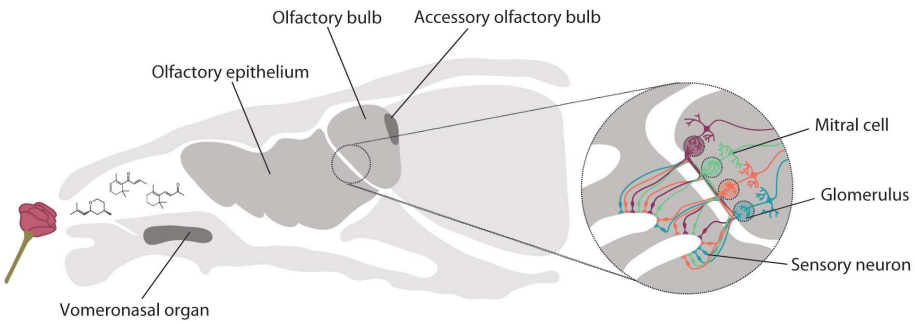

Figure 1 Schematic overview of the murine olfactory system. Left: Mixtures of odour molecules originating from a source (rose) enter the nasal cavity. They are detected by sensory neurons located in the olfactory epithelium (OE; light grey) or the vomeronasal organ (VNO; dark grey). Information from the OE is processed in the olfactory bulb (OB) while information from the VNO is processed in the accessory olfactory bulb (AOB) **Right:** Sensory neurons in the OE express one type of odour receptor (denoted by differing colours). Upon entering the OB, their axons coalesce and transmit their information onto so called mitral cells (MCs) at specialized neuropil structures termed glomeruli. Modified from[13] with permission from the publisher.

Apart from few exceptions, each olfactory sensory neuron (OSN) expresses only one odour receptor, which in turn is usually not tuned to a single odour molecule but can rather be activated by a large number of different but often chemically similar odour molecules[14–19]. Stimuli detected by the VNO are mostly pheromones and are largely transmitted to the amygdala or the hypothalamus via the accessory olfactory bulb (AOB)[18]. Conversely, stimuli detected by neurons located in the OE are transmitted to higher brain areas like the piriform cortex (PirCtx) or the hippocampus by way of the olfactory bulb (OB)[18].

The OB is a highly structured brain region, comprising (from outermost to innermost) the glomerular layer (GL), the external plexiform layer (EPL), the mitral cell layer (MCL), the internal plexiform layer (IPL) as well as the granule cell layer (GCL; Figure 2)[18,20].

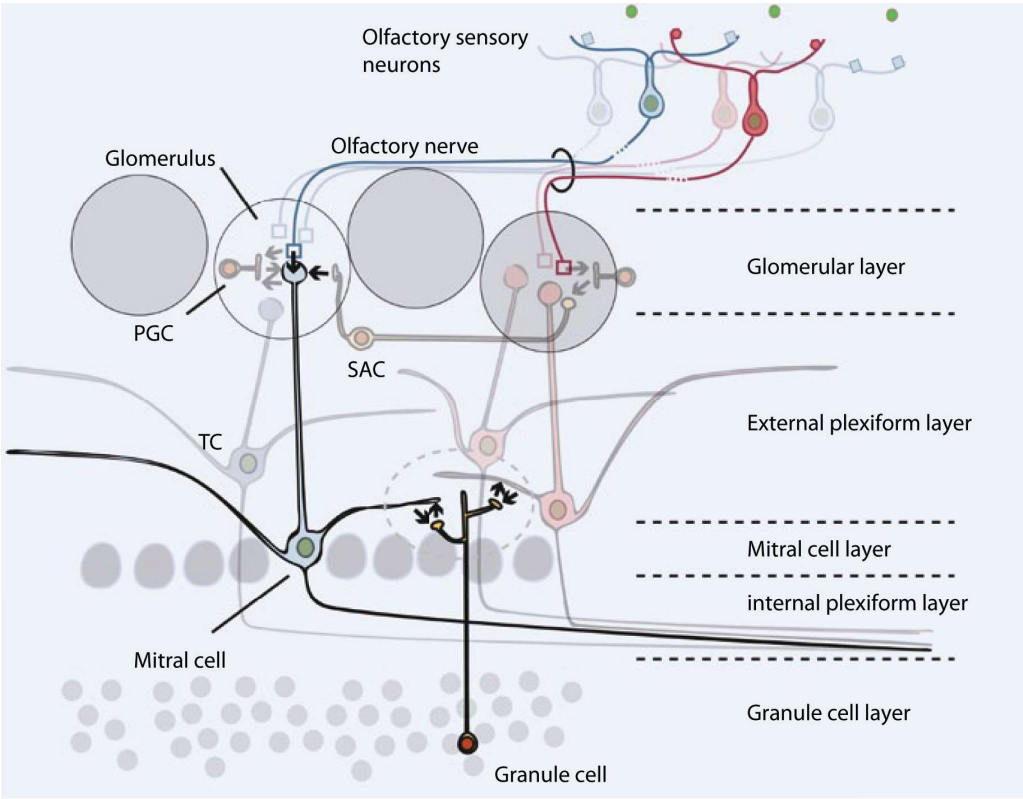

Figure 2 Anatomy of the olfactory bulb. Odour molecules (green) bind to odour receptors expressed by olfactory sensory neurons (OSNs). The axons of all primary sensory neurons expressing the same receptor coalesce at neuropil structures termed glomeruli, which also encompass the apical dendrites of mitral cells (MC) and tufted cells (TC) as well as inhibitory interneurons like periglomerular cells (PGC) and short-axon cells (SAC). The cell bodies of MCs are located in the mitral cell layer (MCL) while their lateral dendrites extend through the external plexiform layer and their axons transmit odour information onto higher brain regions. Inhibitory granule cells (GC), whose somata are located in the granule cell layer (GCL) send their apical dendrites into the EPL, forming reciprocal dendrodendritic synapses with MCs from different glomeruli. Modified from[21] with permission from the publisher.

The sensory input detected by the OSNs is relayed to the principal output neurons of the OB, the mitral and tufted cells (MC and TCs), at spherical neuropil structures termed glomeruli located in the glomerular

layer[22–25]. In each glomerulus, the axons from thousands of olfactory sensory neurons (OSNs) expressing the same odour receptor coalesce and form excitatory glutamatergic synapses with the apical dendrites of the roughly 60 MCs and TCs associated with this glomerulus[20,26]. Additionally, each glomerulus may include excitatory external tufted cells (ETCs), inhibitory interneurons, like periglomerular cells (PGCs) as well as misleadingly named short-axon cells (SACs) which can connect multiple glomeruli and can have axons of up to 1mm length[27–29]. The somata of MCs are located in the mitral cell layer (MCL) and can be classified, depending on the location of their lateral dendrites within the EPL, as either type-I (lateral dendrites in deep EPL areas) or type-II (lateral dendrites in superficial EPL areas)[30,31]. Both types of MCs, however, form extensive synaptic connections throughout the EPL, both with themselves, with other MCs or TCs, or with granule cells and their axons target virtually all regions of the piriform cortex[32–36].

On the other hand, TCs are typically divided into three different types based on the location of their soma within the EPL. The somata of both internal as well as middle TCs are located in the deep EPL, the middle EPL or even close to the MCL[23]. On the other hand, the somata of ETCs are located in the periglomerular region[23]. Similar to MCs, internal and middle TCs extend their apical dendrite into the glomerular layer and form connections there albeit within a slightly smaller area of a given glomerulus compared to MCs. Their lateral dendrites also extend through the superficial EPL, forming similar synaptic connections with MCs and TCs and GCs. Their axons, too, target the piriform cortex but have been shown to preferentially innervate the anterior and rostral piriform cortex[35,36].

In contrast, ETCs form extensive connections typically only within a single glomerulus through their primary dendrite and may or may not possess secondary dendrites[37–39]. Even if a secondary dendrite is present, ETCs rarely appear to (if at all) form connections with GCs but rather synapse onto MCs and TCs, other ETCs or inhibitory interneurons in the periglomerular region, hence they are typically considered to be juxtaglomerular cells and not principal cells[40,41].

Olfactory bulb interneurons

Granule cells

Granule cells are the most numerous cell type in the OB and constitute the major source of inhibition onto MCs and TCs[26,42–45]. Their somata are mostly located in the GCL and their dendrites extend through the GCL, IPL as well as the EPL. Depending on the precise location of the somata and the termination of the dendrites, GCs can be subdivided into six different subgroups, all of which are axon less, mostly GABAergic and form reciprocal dendrodendritic synapses with MCs and TCs (Figure 3)[33,46,47]. Interestingly, all but one subtype of GCs (type-S cells) are replenished throughout life and several studies have suggested, that integration of these adult-born GCs is location specific[48–52]. For instance, it has been shown that adult-born GCs preferentially integrate into the deeper layers of the GCL, resulting in changing innervation patterns in the EPL due to neurogenesis[48,52]. Further, adult-born GCs have been implicated in contributing to odour

discrimination, odour memory and maintaining high odour detection flexibility throughout an animal's life[53–55].

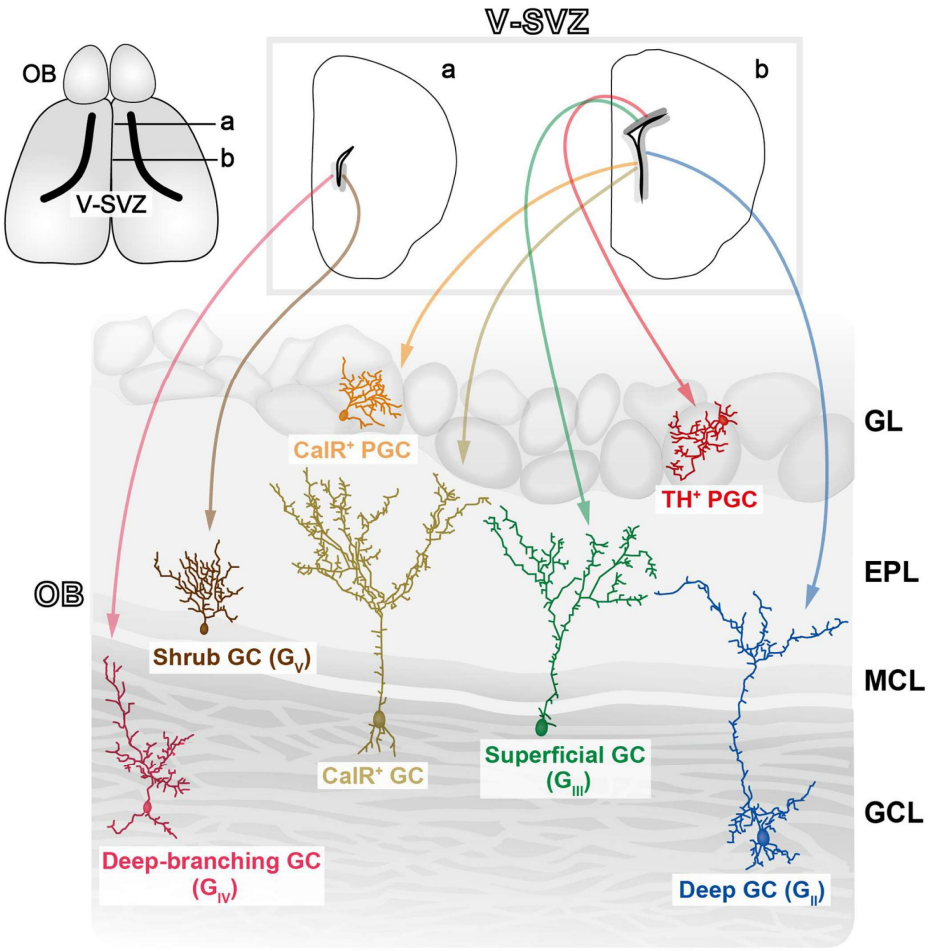

Figure 3 Schematic representation of the integration of adult-born interneurons in the olfactory bulb. Neuronal stem cells (NSCs) from different regions of the ventricular-subventricular zone (V-SVZ) give rise to distinct types of interneurons. NSCs from the anterior part of the SVZ **(a)** preferentially give rise to shrub (type-V) and deep-branching GCs (type-IV). NSCs from the dorsal medial SVZ **(b)** give rise to calretinin-expressing (type-I) GCs as well as periglomerular cells (PGCs), which express either calretinin (CalR), calbindin (CalB; not shown) or tyrosine hydroxylase (TH). NSCs from the ventral medial SVZ typicaly integrate as superficial (type-III) or deep (type-II) GCs. Note: Type-S GCs are not shown as these are not generated in adult animals. OB: olfactory bulb. GL: glomerular layer. EPL: external plexiform layer. MCL: mitral cell layer. GCL: granule cell layer. Modified from[56] with permission from the publisher.

Morphologically, GC spines are distinct from other OB interneuron synapses, as they possess elongated necks which have been suggested to act as individual compartments independent from other spines or even the remaining cell[57–60]. Apart from ionotropic glutamate receptors like AMPA and NMDA receptors, the GC spine also contains a multitude of ion channels like voltage-gated sodium channels, N/P/Q/T-type calcium channels, transient receptor potential (TRP) channels, A-type potassium channels or GABA receptors[61–65]. Hence, release of glutamate from MCs and TCs activates AMPA and NMDA receptors (AMPAR and NAMDAR respectively) located at the dendritic spines of GCs[21,64]. This activation triggers a local depolarization of the

GC spine which eventually leads to the release of GABA from these spines, causing the so-called recurrent (self-) inhibition of the MCs and TCs[21,64]. Further, as GCs are connected to many MCs and TCs, often from multiple glomeruli, they can also cause so-called lateral inhibition which results in a centre-surround inhibition of MCs and TCs from neighbouring glomeruli[27,33,64,66,67].

Periglomerular cells

Analogous to GCs, PGCs constitute the most abundant cell type in the GL and are also mostly GABAergic with some PGCs being dopaminergic[45,68,69]. As their name suggests, their somata are located in the GL and their axons typically only extend into one or very few glomeruli (Figure 4). According to the region of the glomerulus innervated by the PGCs, they can be classified as type-I cells, which innervate the entire glomerulus area, or type-II cells, which innervate the glomerulus area not targeted by the axons of OSNs (Figure 4)[70].

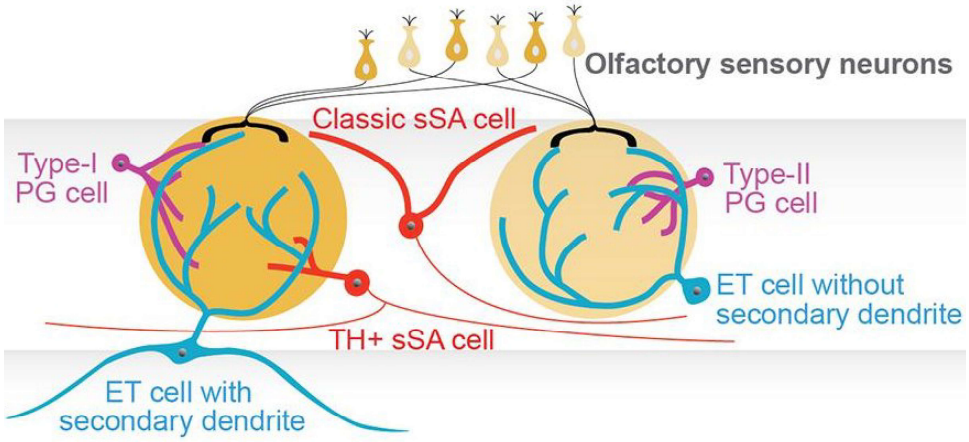

Figure 4 Subtypes of interneurons in the olfactory bulb. Schematic representation of different juxtaglomerular cells including periglomerular (PG; purple), external tufted (ET; blue) and short-axon (SA; red) cells. Depending on the innervation pattern of the glomerulus as well as their inputs, PG cells are divided into type-I or type-II cells. The somata of ET cells without secondary dendrites are located near a glomerulus while the somata of ETs with secondary dendrites are located closer to the superficial external plexiform layer. Classical superficial short-axon (sSA) cells have dendrites not entering the glomerulus in contrast to tyrosine hydroxylase (TH) expressing sSAs whose dendrites enter the glomerulus and can connect multiple distant glomeruli. Modified from[30] with permission from the publisher.

Similar to GCs, PGCs are replenished throughout adulthood and adult-born PGCs can be segregated into mutually exclusive groups according to the expression of three molecular markers, namely calbindin (CalB), calretinin (CalR) and tyrosine hydroxylase (TH) (Figure 3 and Figure 4)[50]. Analogous to GCs, both the number and the origin within the SVZ of the three molecularly defined PGC-types have been shown to differ[50,71,72]. Interestingly, in mice, type-I PGCs were found to be exclusively TH-expressing, while type-II PGCs expressed CalB or CalR, suggesting differential physiological roles of these cells[70,73]. Whereas CalB and CalR expressing cells are GABAergic and form inhibitory synapses with the axons of OSNs, TH-expressing cells are

dopaminergic and act on D2 receptors present in OSN terminals, causing inhibition of the OSNs[67,74–78]. In addition, PGCs can form dendrodendritic synapses with ETCs as well as MCs and TCs, providing an additional source of inhibition onto these cells[22,79,80].

Lastly, PGCs have also been shown to differ quite substantially both in their spontaneous as well as stimulus induced activity. However the differing responses did not align directly with the innervation pattern or the molecular identity of the PGCs but were distributed among all three PGC types, suggesting a more complex role in shaping olfactory information than previously thought[29,77].

Transmission of olfactory stimuli throughout the olfactory bulb

Although OSNs expressing different receptors are interspersed in the olfactory epithelium, axons of OSNs expressing the same odour receptor coalesce upon reaching the OB thus separating information from different odour receptors into different glomeruli and, in turn, different MCs and TCs. This separation as well as the high convergence ratio of approximately 11000:1 means that odour information can be decoded through the specific activation patterns of the involved glomerular microcircuits[20,81–88]. Nevertheless, olfactory stimuli consist of multiple molecules that typically bind to several olfactory receptors and glomeruli sensitive to structurally similar molecules are often located in similar OB regions, resulting in highly similar spatial activation patterns when presented with multiple similar odours or even physiological odour plumes[86,87,89]. Additionally, olfactory receptors usually bind different odour molecules with different affinities, resulting in differential activation of glomeruli depending on the concentrations of the individual odour molecules[16,19,82,84,90]. Further, olfaction is not a passive sense, as odour sampling involves active inhalations which can cause odour molecules to bind to odour receptors in discrete interspersed intervals. Last but not least, OB activity has been shown to change already within the time course of a single inhalation period suggesting the possibility of stimulus information encoding relative to the breathing rhythm, adding another layer of complexity to any odour stimulus[91,92]. In spite of these multiple dimensions encoding any given olfactory cue, odour discrimination in rodents is remarkably fast an can generate a corresponding behavioural response within a single “sniff”, i.e. in less than 200ms[26,81,93,94].

Understanding of the multiple interwoven intra- as well as inter-glomerular microcircuits may explain how the olfactory system processes odours at this speed despite the multidimensional nature of the stimuli.

Intra-glomerular circuits

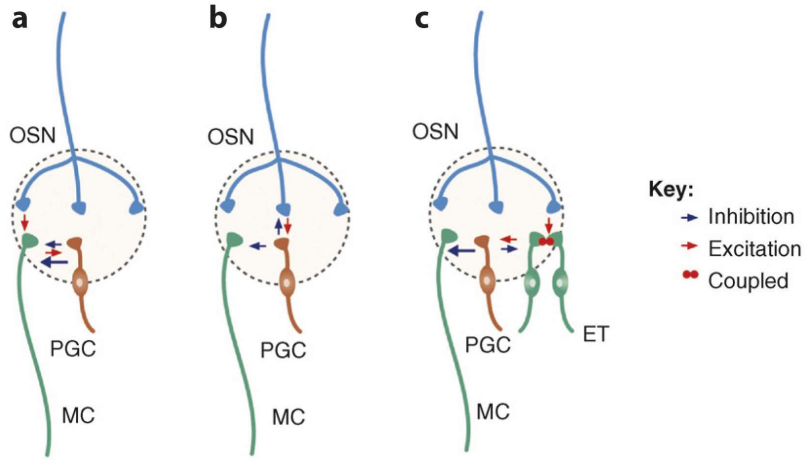

Figure 5 Schematic representation of glomerular microcircuits. (a) Activation of an olfactory sensory neuron (OSN; blue) leads to activation of the apical dendrite of a mitral cell (MC; green) within the glomerulus. This MC excitation can in turn activate periglomerular cells (PGC; orange) within the same glomerulus, which reciprocally inhibit the MC dendrite. **(b)** OSNs share a direct reciprocal connection with PGs, resulting in recurrent inhibition upon OSN activation. Subsequently, PGC activation causes feed-forward inhibition of MCs. **(c)** External tufted cells (ET; green) receive direct OSN input which leads to activation of electrically coupled ETs as well as synaptically connected PGCs. This PGC activation can cause both feed-forward inhibition of connected MCs as well as recurrent inhibition of ETs. Modified from[95] with permission from the publisher.

Canonically, binding of an odorant to an olfactory receptor causes activation of the respective OSNs, which in turn activate MCs, the principal output neurons of the OB (Figure 5a)[23,96]. Since OSNs have a high but fast depressing release probability, this results in a slightly delayed excitatory response in MCs, consistent with a monosynaptic input[97,98]. As MCs form synaptic connections with apical as well as lateral dendrites of "sister" MCs associated with the same glomerulus, the initial OSN-evoked activation is further distributed among the principal cells targeting the same glomerulus[79,99–101]. Additionally, glutamate spill-over can lead to recurrent self-excitation which has been shown to further amplify and synchronise the activation[32,102,103]. In turn, activated MCs can excite connected PGCs which provide recurrent inhibitory feedback[104]. In electrophysiological recordings it was shown that MCs exhibit an initial hyperpolarisation observed in MCs after OSN stimulation which can be further enhanced through the recurrent inhibition from PGCs[104].

Furthermore, OSNs have been shown to form direct reciprocal connections with roughly 20% of PGCs, resulting in recurrent feedback inhibition of the OSN terminals as well as invariant, short latency post-synaptic potentials in the PGCs due to OSN-derived activation (Figure 5b)[40,67,77,98,105–107]. In addition to recurrent feedback inhibition, this pathway can provide feed-forward inhibition into MCs, which has been shown to drastically attenuate overly high OSN input[22,108,109]. Further, PGCs can inhibit other PGCs through lateral inhibition and are susceptible to self-inhibition as they express $GABA_A$ receptors[110–112].

However, more recent studies have shown that ETCs receive direct input OSNs, which causes ETCs to fire repetitive bursts of action potentials, that are highly correlated in "sister" ETCs associated with the same

glomerulus (Figure 5c)[79,113,114]. As studies have shown that ETCs alone can drive MCs, it has been suggested that this ETC-derived activation is a major contributor to MCs depolarisation after stimulation of OSNs[40,115]. On the other hand, ETs can activate PGCs resulting in rhythmic bursts of both excitatory post-synaptic currents and potentials in PGCs[114]. This rhythmic activity has been shown to attenuate MC excitability as well as shape the hyperpolarizing response after OSN stimulation, suggesting ETC-activity may play a crucial role during integration of sensory inputs MCs[77,79,80,114,116].

Inter-glomerular circuits

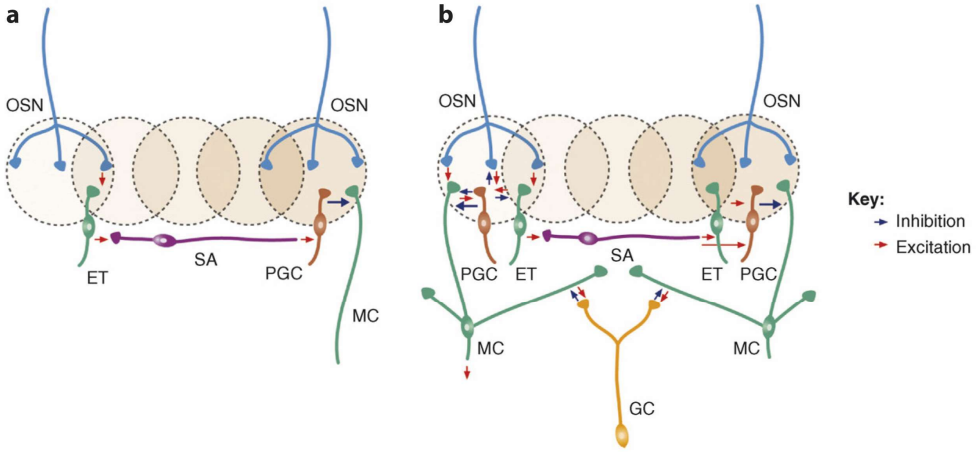

Figure 6 Schematic representation of inter-glomerular circuits in the olfactory bulb. (a) Activation of an olfactory sensory neuron (OSN; blue) causes activation of external tufted (ET; green) cells associated with the same glomerulus. In turn, this causes activation of short-axon (SA; purple) cells, whose lateral dendrites can extend up to 1mm and excite periglomerular cells (PGCs; orange) several glomeruli away. Subsequently, the activation of PGCs can inhibit apical dendrites of mitral cells (MC; green) associated with this distant glomerulus. **(b)** MCs from different glomeruli can additionally be connected through inhibitory granule cells (GC; yellow). The MC-GC synapses are dendrodendritic, reciprocal synapses where activation of a GC results in recurrent inhibition of the initial MC as well as lateral inhibition of MCs associated with different glomeruli. Ultimately, these local circuits modulate the excitatory output of MCs which transmit the olfactory information to their downstream targets. Modified from[95] with permission from the publisher.

In the glomerular layer, short axon (SA) cells extend their dendrites across multiple glomeruli which can be considerably distant (Figure 6a)[27,29,117]. Hence they are an ideal candidate for the integration of sensory information across glomeruli. SA cells receive direct monosynaptic excitatory input from ETCs and potentially also directly from OSNs[27,41,114,117]. In turn, SA cells can provide excitatory input to both PGCs as well as ETCs, which ultimately causes inhibition of the MC and TCs receiving input from these ETs and PGCs[27]. Interestingly, this inhibition can be sufficiently high to eliminate excitation in MCs after OSN stimulation[27]. Thus, SA cells can provide a first level of inter-glomerular inhibition which can contribute to a centre-surround inhibition between multiple differentially activated glomeruli, providing contrast enhancement. Moreover, this mechanism can regulate excitability of MCs and TCs or supress their activation[41].

Similarly, in the GCL, GCs integrate information from various glomeruli as they form reciprocal dendrodendritic connections with lateral dendrites of MCs from multiple glomeruli (Figure 6b)[27,67]. At these synapses, activation of GCs through glutamate release from MCs causes recurrent inhibition back onto the activating MC through release of GABA[21,64,118]. Due to the peculiar morphology of the GC spine, this direct recurrent inhibition acts mostly locally on the originating MC and can reduce excitability and firing directly after activation, effectively causing temporary silencing of the output of this MC[64,119]. However, given strong enough activation, GCs have been shown to release GABA from multiple local spines, causing the so-called local lateral inhibition which typically affects MCs in close proximity to one another[47,120,121]. Indeed, many studies have found that this lateral inhibition creates a centre-surround inhibition amongst neighbouring glomeruli[122–125]. As odour mixtures activate many glomeruli, this local lateral inhibition can separate individual glomeruli given large scale OB activation. Recently, Economo and colleagues have shown, that strongly activated glomeruli can completely silence neighbouring glomeruli, highlighting the efficiency of centre-surround inhibition in separating glomerular units from one another[125]. Last but not least, very high activation of GCs, i.e. through strong input at multiple spines, can result in the so-called global lateral inhibition during which action potentials are evoked in the GC and GABA is released from all synaptic contacts causing inhibition of all connected MCs[120,126,127]. However, the firing threshold of GCs is relatively high while the resulting firing frequency of GCs is low and quickly subsiding[128,129]. In light of this, several studies have raised the possibility of eliciting global lateral inhibition independently of action potential firing, yet this has not been verified *in vivo*[120,130,131].

Modulating olfactory bulb output through manipulation of granule cells

Molecular perturbation of granule cells

Given the abundance of GCs in the OB and their direct impact on MC activity, multiple studies have focussed on modifying GCs to attenuate MC output. Many efforts have been directed towards molecular perturbation of GCs to regulate their influence on MCs. For example, GC specific knock-outs of AMPA receptor subunits have been shown to directly increase the influx of calcium into the GC spine, resulting in increased recurrent inhibition of connected MCs[132]. Conversely, knock-outs of NMDA receptor subunits have been shown to decrease calcium influx into the GC spine, resulting in reduced recurrent inhibition of MCs[132]. Importantly, both modifications were sufficient to decrease or increase the discrimination time of complex odour mixtures, directly linking GC activity to a behavioural response[132,133]. Similarly, knock-down of GC sodium channels resulted in reduced GC activation leading to reduced MC inhibition and increased discrimination times[60,62]. Further, knock-out of the $GABA_A$ receptor subunit responsible for GC inactivation increased recurrent inhibition onto MCs, leading to reduced discrimination times[61]. Interestingly, none of these modifications impacted the learning speed of the behavioural task. Conversely, optogenetic activation of the GCL has been shown to enhance decorrelation of overlapping glomerular activation patterns and increased the learning speed for discrimination of odour mixtures[134]. This suggests, that local

or even global lateral inhibition may have a larger impact on odour discrimination than recurrent inhibition. However, while GC spiking does occur upon odour stimulation *in vivo*, is was shown to be rare[126–129,135]. Notably, calcium transients measured *in vitro* in GGs are highly dependent on the membrane potential, increasing with hyperpolarization and decreasing with depolarization[120,130]. These transients were shown to depend on T-type calcium channels, which are named for their transient and "tiny" calcium currents[120,130]. Their relevant pore-forming α1 subunits are encoded by three genes, designated $Ca_V3.1$, $Ca_V3.2$ and $Ca_V3.3$[136–138]. All three subunits show high sequence similarity, are highly conserved among species and all mediate low-threshold calcium spikes, albeit with some variation in their physiological properties like the time-course of activation and deactivation, the time required to recover from deactivation or the sensitivity to blockers like nickel or mibefradil[136]. While all subunits are differentially expressed throughout the brain, the GCL of the OB is one of the few brain regions showing high expression of all three subunits[139–141]. Astonishingly, T-type mediated calcium transients in GCs were shown to contribute at least half of the global lateral inhibition of MCs *in vitro*, yet so far *in vivo* investigations have been lacking[130].

Modulating overall granule cell number

The most straight forward approach to modifying GC activity on a large scale is to adjust the overall number of GCs. In mice roughly 10000 newly generated neurons enter the OB through the rostral migratory stream every day and replace apoptotic interneurons[142–144]. As the overwhelming majority (approximately 94%) of these adult-born cells integrate as GCs, modifying the balance between neurogenesis and apoptosis is an attractive way to regulate overall GC numbers[145,146]. For instance, short term ablation of neurogenesis has been shown to reduce the amount of inhibition of MCs as well as increase the detection threshold of odours but did not affect discrimination of simple odours, odour memory or the overall number of GCs[53]. On the other hand, irradiation of the subventricular zone resulted in greatly reduced numbers of granule cells and impaired odour memory but did not impair discrimination of odours or odour learning[147]. Reducing migration or retention of new-born neurons impaired odour memory but not odour discrimination in one study, while others detected no changes in odour discrimination[148–150]. Conversely, increased neurogenesis natively occurs during pregnancy but studies trying to increase the number of neuronal stem cells by grafting cells resulted in physiologically abnormal cells[151,152].

While these confounding results may partially be explained by the differing approaches in modulating neurogenesis, the vast majority of these studies have focussed on ablating neurogenesis. Indeed, studies specifically increasing the number of neuronal stem cells to increase the numbers of new-born neurons are virtually non-existent. Further, all of these studies use different behavioural tasks (if any) to investigate the impact on odour discrimination, greatly hampering comparability.

Tools for high-throughput olfactory phenotyping

Assessment of odour discrimination fundamentally requires quantitative *in vivo* testing. Like most behavioural paradigms, olfactory testing is typically done in a semi-automated setting in which mice are individually placed into the test apparatus. For instance, in the most commonly used "Knosys" system as pioneered by Slotnick and colleagues in 1999, animals are manually placed into a dedicated test chamber connected to a single eight-channel olfactometer[153,154]. For practical reasons, this requires animals to be i) individually housed to prevent switching of animals, ii) water-deprived for most of the day to ensure high motivation, iii) at least minimally habituated to the experimenter and iv) forced to perform trials only during their allotted test sessions. Apart from being prone to experimenter-induced variability, testing of large numbers of animals using these semi-automated setups can only be done by increasing the number of setups, increasing the number of experimenters performing the experiments or by a combination of both. This makes high-throughput analysis highly labour and cost intensive, on top of creating further potential sources of variation to the experimental design.

Recently, many non-commercial as well as commercial automated behavioural setups have been developed, all intended to increase standardization of testing and increase data quality and quantity. However, most of the commercial setups have been focussed on general behavioural parameters (i.e. IntelliCage (TSE Systems), PhenoTyper (Noldus Information Technology), ColonyRack (PhenoSys GmbH), "Self head-restraining platform" (O'Hara & Co)) and are difficult to adjust to individual experimental designs due to their commercial nature. Additionally, these setups either still require individual testing of animals in separate test chambers or limit access to a shared testing area to certain time points, potentially biasing the results despite automating the testing itself[155–157]. In terms of non-commercial setups, a number of groups have developed automated behaviour setups, some even explicitly aimed at sensory phenotyping like the "Educage" by Maor et al. (2018) or the functional imaging setup developed by Murphy et al. (2016)[158,159]. Still, despite the claimed "high throughput" of these systems, testing was limited to 5-11 animals per cohort, a group size that is far smaller than the typically 16-20 animals used odour discrimination in a go/no-go task[81,132,160].

In contrast to these existing systems, an ideal setup for large-scale olfactory phenotyping should allow for the group-housing of roughly 20 (preferably exclusively male) mice. These animals should have free access to a testing chamber or testing area and be allowed to initiate trials at a time point of their choice. Over the course of the training, animals should be automatically trained on a go/no-go task allowing for calculation of the odour discrimination time as established by Abraham et al. (2004), ideally using a range of different odour pairs. Lastly, high-resolution data at millisecond precision should be automatically recorded for all relevant behavioural parameters including sampling behaviour or the go/no-go response, as well as the sensors controlling application of the odour stimulus.

Aims of this study

The central aim of this study is the investigation of the influence of GC activity on odour discrimination *in vivo*. While previous studies aimed at perturbing the dendrodendritic synaptic connections between GCs and MCs have elegantly demonstrated the impact of modified MC activity on odour discrimination, these perturbations have mainly acted on the local recurrent inhibition[61,62,132,161]. On the other hand, studies modulating GC activity directly through changing the number of GCs have mainly done so by ablating neurogenesis to reduce GC number. Apart from being a relatively crude approach which only indirectly serves to elucidate the impact of GCs on odour discrimination, these studies have so far yielded highly contradictory results[53,162–165]. Additionally, the variety of tests used to investigate olfaction make it very difficult to compare the effects of either of these modulations on odour discrimination *in vivo*. In fact, even studies measuring reaction times to different odours have reached opposing conclusions due to variations in task design[81,166].

Hence, this study aims to address three major points:

1) Establish a novel automated behaviour setup dedicated to operant conditioning of mice to achieve standardized high-throughput *in vivo* testing of odour discrimination. Once validated, this setup will be used for all subsequent behavioural studies providing a comparable framework for *in vivo* studies.
2) Analyse the impact of increased GC numbers on odour discrimination through increased adult neurogenesis resulting in higher numbers of physiologically normal granule cells. Toward this aim, a transgenic mouse line ("4D") will be used to achieve a spatially and temporally defined increase of the number of interneurons in the OB[167,168].
3) Investigate the proposed gating of global activation of GCs via T-type calcium channels *in vivo* through a shRNA mediated knock-down. Based on *in vitro* findings by Egger and colleagues (2003 and 2005), a lack of T-type calcium channels should reduce global activation of GCs upon local stimulation, ultimately resulting in reduced global lateral inhibition of connected MCs[120,130]. Due to the expression of all three known subunits of T-type calcium channels throughout the OB, this requires establishing a simultaneous triple knock-down which will be spatially limited to the GCL through AAV-mediated expression of shRNA sequences.

Materials and methods

Animals

All experiments described in this thesis were conducted in accordance with the German animal welfare guidelines and approved by the responsible authority (Regierungspräsidium Karlsruhe, Germany; experimental licence 35-9185.81/G-61/15 and Landesverwaltungsamt Sachsen, Germany; experimental licence DD24-9168.11-1/2011-11, TVV13/2016). Mice aged at least three weeks were housed in a non-inverted day-night cycle (12h/12h) with ad libitum access to food and water. During behavioural experiments, water was only available as a reward for correctly identified S+ trials (see Table 25) while the remaining parameters remained unchanged. For behaviour experiments, only male mice were used.

C57Bl/6N mice

For the initial verification of the behaviour apparatus, wild-type C57Bl/6N mice were obtained from Charles River (Sulzfeld, Germany). To investigate the effect of T-type calcium channels on the processing of olfactory information, wild-type C57Bl/6 mice were also obtained from Charles River (Sulzfeld, Germany) and used for shRNA-mediated knockdown studies.

GluA2$^{\Delta GCL}$ mice

For the proof of concept validation of the behaviour apparatus, mice in which exon 11 of the GRIA2 gene encoding the ionotropic glutamate receptor subunit 2 was flanked by loxP-sites were used (a kind gift from Prof. Dr. Peter Seeburg and Dr. Rolf Sprengel, Max Planck Institute for Medical Research, Germany). Expression of the Cre-recombinase in these mice leads to the deletion of the pore-forming loop helix M2 which renders the ion channel constitutively calcium permeable. Studies, in which Cre-recombinase was selectively expressed in the granule cell layer (GCL) of the olfactory bulb of mice have shown that these mice have faster discrimination times for the discrimination of complex odour mixtures compared to wild-type mice[132,160]. Cre-recombinase was not expressed in any of the mice used in this study and the mice were used exclusively as initial test cohorts during establishing of the automated behaviour setup.

4D mice

To analyse the effect of newly integrated granule cells into the olfactory bulb circuitry, nestin$^{CreERT2+/-}$/ROSA26$^{loxP(rtTA)\text{-}flox\ +/+}$/tet-bi$^{4D\text{-}RFP+/-}$ transgenic mice were used (kindly provided by Prof. Dr. Federico Calegari, CRTD Dresden, Germany). Activity of the Cre-ER^{T2}-recombinase was induced by oral administration of tamoxifen (Sigma, #T5648) at 250 mg/kg body weight (dissolved 1:10 in corn oil) once per day for three consecutive days. Through the recombinase activity, the reverse tetracycline-controlled transactivator (rtTA) is expressed in these cells. Subsequently, overexpression of the cell-cycle regulators Cdk4/cyclin D1 (“4D”) was achieved through subcutaneous injection of 9-tert-butyl doxycycline (Echelon Biosciences,

#B0801) at 50mg/kg body weight (dissolved 1:10:1 in DMSO, corn oil and water) twice daily for four days. This induction protocol ultimately causes a temporary overexpression of the Cdk4/cyclinD1 complex which inhibits the differentiation of neural stem and progenitor cells causing an overall increase of these cells[167]. After the overexpression of the 4D-complex, the cell cycle reverts to its normal state with the increased number of precursor cells resuming differentiation which leads to an overall increase in new-born neurons. Use of these specific induction conditions in post-natal animals not only limits the effects to nestin-positive cells but further to new-born interneurons in the olfactory system (see[169]).

For morphological analysis as well as electrophysiology, the original triple-transgenic lines were further crossed with a $RCE^{GFP\text{-}flox+/+}$ mouse line[170]. In these mice, the fluorophore EGFP is expressed under the control of the CAG promoter but preceded by a STOP-cassette flanked by loxP sites. In cells expressing the Cre-recombinase, the STOP-cassette is removed resulting in expression of the fluorophore. Thus, the resulting quadruple transgenic mice may carry the EGFP or the rtTA transactivator as either or both of the two alleles of the ROSA26 locus. Hence, GFP^+/RFP^- cells were classified as $4D^-$ cells while GFP^+/RFP^+ cells were classified as $4D^+$ cells for the purpose of the morphological and electrophysiological analyses.

Plasmid design and cloning

Plasmids used for generation of chimeric AAVs with a serotype mixture of serotype 1 and serotype 2 can be found in Table 1. These plasmids carry the genes necessary for replication of the AAVs (termed *rep* genes) as well as the genes encoding the protein capsids forming the hull of the virus (termed *cap* genes). Additionally, they express a fluorescent marker protein (RFP) for easy verification of transfection efficiencies.

For packaging a certain transgene into AAVs, the gene of interest was subcloned into an expression-vector (termed pAM-Vector; a kind gift from Matthias Klugmann[171]). In this vector, expression was aided by the inclusion of the woodchuck post-transcriptional regulatory element (WPRE) as well as the bovine growth hormone poly-A (PA) sequences. Lastly, the gene of interest and the regulatory sequences are flanked by the inverted-tandem-repeats (ITRs) of serotype 2. The expression-vector as well as the plasmids used for subcloning of genes of interest can be found in Table 2.

Table 1 Plasmids used for AAV production

Plasmid Name	Insert	Origin
pDP1rs	*rep* genes from serotype 2 and *cap* genes for serotype 1	Plasmidfactory, #PF401
pDP2rs	*rep* and *cap* genes for AAV serotype 2	Plasmidfactory, #PF402

Table 2 Plasmids used for AAV-mediated gene expression

Plasmid Name	Insert	Vector	Origin
pAM-Vector	-	-	Matthias Klugmann, University of New South Wales, Australia
pAM-eGFP	eGFP-Fluorophore	pAM-Vector	Matthias Klugmann, University of New South Wales, Australia
pAM-Cre	Cre-Recombinase	pAM-Vector	Matthias Klugmann, University of New South Wales, Australia
pCNDA3-mOrange2	mOrange2-Fluorphore	-	Roger Tsien, University of California, USA
pCDNA3-mGFP	membrane-bound GFP-Fluorophore	-	Pico Caroni, FMI Basel, Switzerland

All shRNA sequences were subcloned into the pAM-vector and expressed under control of the U6 promoter[172]. In case of the final virus construct containing three different shRNAs, shRNA expression was controlled by the U6 or the H1 promoter[172,173]. Additionally, the fluorophore mOrange was expressed under control of the chicken-beta-actin (CBA) promoter[174].

Design of shRNA sequences

As a control, a commercially available non-targeting sequence (see [175]) was used as the high sequence homology of the T-type subunits precluded use of scrambled or even mismatch control sequences. The shRNA sequence targeting the $Ca_V3.1$ subunit was obtained from published literature[176]. The putative shRNA sequences targeting the $Ca_V3.2$ and $Ca_V3.3$ subunits can be found in Table 3 and were designed by Michaela Kaiser using the freely available web-based tool "BLOCK-iT RNAi Designer" (Invitrogen, https://rnaidesigner.ThermoFisher.com/rnaiexpress).

Table 3 shRNA sequences used for knockdown of T-type ion channel expression

Target Gene	ID	Sequence (5'-3')
Non-targeting control	Control	See
CAGNA1G	$Ca_V3.1$ Variant 1	GAAGATCGTAGATAGCAAA
CACNA1H	$Ca_V3.2$ Variant 1	GCTGAAGAGCTGCCCATATTG
CACNA1H	$Ca_V3.2$ Variant 2	GCAGCCATCCTCGTCAATACT
CACNA1H	$Ca_V3.2$ Variant 3	GGGTGAGGCGCAAATACAACT
CACNA1I	$Ca_V3.3$ Variant 1	GCATATCTTTGGCTGCAAATT
CACNA1I	$Ca_V3.3$ Variant 2	GCAATGGCAGAATGCCCAACA
CACNA1I	$Ca_V3.3$ Variant 3	GCTGGGTGCATCACAAATACA

Production of adeno-associated viruses

Adeno-associated viruses (AAVs) were produced by transfection of HEK293 (Agilent Technologies, #240073) cells with the rAAV vector plasmids (Table 2) and the helper plasmids (Table 1). All viruses were produced as chimeras of serotype 1 and 2.

Transfection was carried out using either a calcium phosphate based transfection or a polyethilenimine (PEI, Sigma, #408727) based transfection method. In brief, $4x10^6$ HEK cells were seeded in 14cm cell culture dishes (Corning, #353025) and grown in DMEM (Gibco, #41966-029; supplemented with 10% FCS, 0.2mM non-essential amino acids, 2mM Na-pyruvate and 1% penicillin/streptomycin) for 24hours. For calcium-phosphate transfection, 2ml of the transfection mixture (125mM $CaCl_2$ and 37.5µg DNA in HBS (140nM NaCl, 25mM HEPES, 0.7mM Na_2HPO_4, pH 7.05)) was applied drop wise to each culture dish and incubated for 24hours. For PEI-based transfection, 2,5ml of the transfection mixture (1mg/ml PEI in OptiMEM (Invitrogen, #31985062) and 37.5µg DNA) was applied drop wise to each culture dish. Transfection was subsequently stopped by medium exchange and virus purification was performed three days post-transfection. Cells were removed from the culture dishes, pelleted (200g, 10min, 4°C), resuspended in 1ml lysis buffer (150mM NaCl, 50mM Tris-HCl, pH 8.5) per culture dish and lysed using three consecutive freeze/thaw cycles. Genomic DNA was removed using a Benzonase digest (50U/culture dish, Sigma, #E1014) at 37°C for 2hours. Remaining cell debris was pelleted (3600g, 15min, 4°C) and the supernatant was filtered using 0.45µm pore-size membrane filters (Millex, #SLHV013SL).

Affinity-chromatography purification

For affinity-chromatography purification of AAVs, chromatography columns (Biorad, #7321010) were washed in 10ml equilibration buffer (1mM $MgCl_2$, 2mM KCl in PBS, pH 7.2) and filled with 5ml heparin agarose beads (Sigma, #H6508) and 10ml equilibration buffer. After settling of the beads, the equilibration buffer was drained and the filtered supernatant applied to the columns and incubated for 2hours at 4°C under gentle agitation. Subsequently, the columns were drained, washed with 20ml equilibration buffer and the virus eluted in 15ml elution buffer (500mM NaCl, 50mM Tris-HCl, pH 7.2). The elution was concentrated in filter tubes (Amicon, #UFC910024) at 3645g at 4°C until less than 1ml of the original volume remained. The concentrate was washed twice in 15ml PBS and subsequently concentrated to a final volume of 200µl. The concentrated virus was filtered using 0.22µm pore-size filters (Millex, #SLGV004SL) and stored at 4°C in aliquots of 50µl until use.

Fast protein liquid chromatography based purification

For fast protein liquid chromatography (FPLC) purification to generate high-purity and high-titer AAVs, a commercially available chromatography system (GE, #ÄKTAprime plus) was used. AVB-sepharose columns (GE, #28411211) were equilibrated in 10ml PBS applied at 0.5ml/min. The cell lysate and supernatant were additionally filtered using 0.22µm pore-size filters (Millex, #SLGV004SL) and applied to the columns at 0.5ml/min. Subsequently, the column was washed with 10ml PBS at 0.5ml/min and the viral particles eluted in glycine-HCl (50mM glycine, pH 2.7) at 0.5ml/min. The elution was fractioned in 1ml fractions and directly collected and equilibrated in 0.1ml Tris-HCl (1M Tris, pH 8.0). The protein absorption measurement of the FPLC system was used to identify the three fractions containing the highest amount of protein. These

fractions were collected in filter tubes (Amicon, #UFC910024) and concentrated as described for the affinity-chromatography purification.

Stereotaxic injections

Mice were anesthetized via intraperitoneal injection of the anaesthesia mixture (0.715mg/kg body weight Medetomidine (Alvetra, #401295.00.00); 9.3mg/kg body weight Midazolam (Hameln Pharma Plus, #47046.02.00); 0.24mg/kg body weight Fentanyl (Janssen, #6762282.01.00)). Analgesia was provided by subcutaneous injection of Carprofen (Norbrook, #401182.00.00) at 10mg/kg body weight. Anaesthesia depth was confirmed by the absence of retraction reflexes upon toe pinching and body temperature was maintained using a feedback-regulated temperature control system (Stoelting, #50300) set at 33°C-35°C. Mice were head-fixed in a stereotaxic alignment system (Kopf Instruments, #1900), eyes were moisturised using eye ointment (Bepanthen, #"Eye and nose ointment"), the surgical field was shaved and disinfected using 70% ethanol. The skin above the olfactory bulb was opened and the skull was levelled along the anterio-posterior axis by bringing the tip of the olfactory bulb to the same dorso-ventral position as the medio-lateral centre of the rhinal fissure. Medio-lateral levelling was performed by bringing the centres of both olfactory bulbs to the same dorso-ventral position. Bilateral craniotomies were performed at the injection coordinates using a dental drill (Osada, #EXL-40). Injection capillaries were produced by heating micro capillaries (Brand, #708707) in a horizontal puller (Sutter Instruments, #P97). Approximately 300nl of the virus solution was injected at the injection coordinates (AP/ML/DV [mm]: 0.1/0/1.4+2; 0.3/0/1.3; 0.5/0/1.0) using the surface of the dura at the centre of each olfactory bulb as a reference point. After the injections, the skin was sutured using surgical sutures (Braun, #0936022) and the anaesthesia antagonised via intraperitoneal injection or the antidote mixture (1.898mg/kg body weight Atipamezol (Prodivet, #401860.00.00); 0.506mg/kg body weight Flumazenil (Fresenius Kabi, #63156.00.00); 0.304mg/kg body weight Naloxon (Inresa, #32029.00.00)). Post-surgery, animals were kept in their home cage on a heating plate set to 37°C over-night before being returned to the ventilated cage rack. At least during the initial week post-surgery, animals were given Carprofen (Norbrook, #401182.00.00) at 5mg/kg body weight to alleviate any pain.

Implantation of RFID chips

RFID chips were implanted as described previously[177]. Briefly, anaesthesia, analgesia and antagonisation of anaesthesia were performed as described for Stereotaxic injections. Anaesthesia depth was confirmed by the absence of retraction reflexes upon toe pinching and body temperature was maintained using a feedback-regulated temperature control system (Stoelting, #50300) set at 33°C-35°C. Eyes were moisturised using eye ointment (Bepanthen, #"Eye and nose ointment") and as small patch of skin on the lower back (approximately 1cm x 1cm) was shaved. The surgical field disinfected using 70% ethanol and the skin opened through a small incision. The RFID injector (EURO ID, #IID100) was loaded with a sterile injection

needle containing a single RFID chip (EURO ID, #ID100). The injection needle was inserted into the incision and pushed parallel to the spinal cord towards the neck of the animal. The RFID was released at the fold of the neck using the plunger of the injector and the injection needle was subsequently removed. The skin was sutured using surgical sutures (Braun, #0936022) which were additionally secured using skin glue (Braun, #1050052).

Preparation of fixed tissue slices

Animals were sacrificed using an intraperitoneal injection of pentobarbital (Janssen, #"Narcoren"/#6088986.00.00) at 500mg/kg body weight and were transcardially perfused with approximately 40ml PBS followed by approximately 25ml paraformaldehyde (PFA; 4% in PBS). The mice were decapitated and the brain tissue removed and post-fixed in PFA (4% in PBS) at 4°C.

Prior to slicing, the tissue samples were washed in PBS for 10min at room-temperature and embedded in agarose (2% in PBS). Coronal slices of 50µm thickness were prepared using a vibratome (Leica, #VT100S) and stored in PBS at 4°C until further use.

Primary cell cultures

Primary cultures of mice hippocampal and cortical neurons were prepared from embryonic day 19 (E19) rat embryos as previously described by Dresbach et al.[178]. For virus testing, cells were grown on glass coverslips (Marienfeld, #0111520) coated with poly-L-lysine (Sigma, #P4832) in 24-well culture plates (Corning, #3527) and infected with virus (0.5-1µl per well) at the earliest 7 days after plating. For quantification of shRNA mediated knockdowns, approximately 100000 cells were grown in lysine-coated 12-well culture plates (Corning, #35225), infected with virus (0.5-1.5µl per well in triplicates) 7 days after plating and harvested 14-18 days after infection.

Quantification of shRNA-mediated knockdown efficiencies

RNA isolation from primary cell cultures

Cells were briefly washed with PBS at 37°C (1ml per well) and incubated in TRIzol (Ambion, #15596018; 1ml/well) for 5min at room-temperature. Per 1ml TRIzol, 0.2ml chloroform was added, vigorously mixed and incubated for 3min at room temperature. Phases were separated by centrifugation at 14000g for 15min to 30min at 4°C. Subsequently, 500µl of the aqueous RNA-containing phase were removed and incubated in 500µl isopropanol for 1-7 days at -20°C. RNA was pelleted via centrifugation at 14000g for 30min at 4°C and washed twice in ice-cold 75% ethanol. After each wash step, the samples were again pelleted at 14000g for 30min at 4°C. After the last wash step, the supernatant was removed and the pellet air-dried for 10min at room-temperature. Lastly, the pellet was dissolved in 20µl RNase-free water, incubated at 55°C for 10min

and the RNA concentration determined via absorption (Thermo Fisher Scientific, Nanodrop 2000c). RNA samples were frozen in liquid nitrogen and stored at -80°C until further processing.

RNA isolation from acute tissue slices

Mice were sacrificed by decapitation and the brains were dissected in ice cold slicing solution (125mM NaCl, 25mM $NaHCO_3$, 2.5mM KCl, 1.25mM NaH_2PO_4, 3mM myoinositol, 2mM Na-pyruvate, 0.4mM ascorbic acid, 0.1mM $CaCl_2$, 3mM $MgCl_2$, 25mM glucose, aerated with carbogen, pH 7.3). Horizontal slices of 350-450µm thickness were prepared using a vibratome (Leica, #VT1200S) and stored in artificial cerebro-spinal fluid (ACSF; 125mM NaCl, 25mM $NaHCO_3$, 2.5mM KCl, 1.25mM NaH_2PO_4, 2mM $CaCl_2$, 1mM $MgCl_2$, 25mM glucose, aerated with carbogen, pH 7.3) at room temperature during further processing. The granule cell layer of each slice was manually dissected and subsequently incubated in TRIzol (Ambion, #15596018; 1ml/animal). Further sample processing was identical to the method used for cultured cells, the only deviation being the addition of the co-precipitant glycogen (Thermo Fisher Scientific, #AM9515) at 0.075-0.15mg per 500µl isopropanol during incubation of the aqueous phase in isopropanol to facilitate RNA precipitation.

Reverse transcription PCR and PCR cDNA amplification

For each sample, 1.5µg (for cell culture samples) or 2µg (for tissue samples) of the isolated RNA was transcribed to cDNA using a ready-made reaction mix (Thermo Fisher Scientific, #11755050) according to the manufacturer's specifications. Resulting samples were directly diluted 10-fold in water, frozen in liquid nitrogen and stored at -80°C until further use.

Presence of selected genes of interest (see Table 4) was verified by PCR amplification using a ready-made polymerase mix (Bioline, #BIO-25043) according to the manufacturer's specifications. Primers were custom ordered (Sigma) with the sequences listed in Table 4. Amplicon presence was verified via gel electrophoresis (2% agarose gel in TAE (40mM Tris, 20mM acetic acid, 1mM EDTA) run at 120V) and only samples positive for all genes of interest were used for subsequent quantitative real-time PCR (qPCR).

Table 4 Primer sequences used for PCR

Target Gene	Forward Primer	Reverse Primer
YWHAZ	GGGTCTGGCCCTCAACTT	CGCTTCTGCTTCGTCTCC
CAGNA1G	TCTGAGCAAAGGGGAACG	TGTGGGGGTCAATTTTGG
CAGNA1H	GCATCATGCGTGTGCTTC	CCTCGCAGGGGTTATCCT
CACNA1I	GCCCAACATAGCCAAGGA	TTCTCGGGGGAGAAGAGG

Quantitative real-time PCR

Quantification of the knockdown efficiency was performed using TaqMan-Assays (coupled to the FAM-dye) and a quantitative real-time PCR System (Applied Biosystems, #4351104). For each sample, 3µl cDNA (1:10 diluted in water) was mixed with 12.5µl ready-made TaqMan PCR Mix (Applied Biosystems, #4440040) and

1.25µl of the respective TaqMan probes (see Table 5). Final volume was adjusted to 25µl using water and all samples were run in triplicates.

Table 5 Probes used for quantitative real-time PCR

Target Gene	Species	Catalogue number	Lot Number
YWHAZ	rat	Rn00755072_m1	1586273
CAGNA1G	rat	Rn01299126_m1	1499385
CAGNA1H	rat	Rn01460348_m1	1557414
CACNA1I	rat	Rn01505208_m1	1499385
YWHAZ	mouse	Mm03950126_s1	1264481
GAPDH	mouse	Mm99999915_g1	872515
CAGNA1G	mouse	Mm00486572_m1	1446483
CAGNA1H	mouse	Mm00445382_m1	1689802
CACNA1I	mouse	Mm01299033_m1	1358517

Amplification was performed via an initial heating step (2min at 50°C) followed by heat-activation of the polymerase (10min at 95°C) and 55 cycles of DNA denaturing (15s at 95°C) and primer annealing and extension (1min at 60°C).

The cycle threshold (C_t) values for each gene were determined as the cycles, at which fluorescence of the amplification curve exceeded a background-corrected fluorescence of 0.2 and the knockdown efficiency was calculated using the $\Delta\Delta C_t$ method and the following formulas:

$$\Delta C_t = C_t(\text{target gene}) - C_t(\text{reference gene})$$

$$\Delta\Delta C_t = \Delta C_t(\text{virus treated sample}) - \Delta C_t(\text{untreated sample})$$

$$Fold\ expression\ change = 2^{-(\Delta\Delta C_t)}$$

$$Knock-down\ efficiency\ [\%] = \left(1 - 2^{-(\Delta\Delta C_t)}\right) * 100\%$$

For cell culture samples, only YWHAZ was used as a reference gene, while both YWHAZ and GAPDH were used as reference genes for tissue samples to provide more accurate results.

Immunohistochemistry and immunocytochemistry

All antibody stainings were performed using gentle agitation on a horizontal shaker (Neolab, #E-1113).

Fixed tissue samples

For the 4D project, slices were incubated in blocking buffer A (10% donkey serum, 0.3% Triton in PBS, pH 7.4) for 60min at room-temperature while primary and secondary antibody stainings were performed in antibody buffer A (3% donkey serum, 0.3% Triton in PBS, pH 7.4) at 4°C over-night.

For the T-type projects, fixed slices were incubated in the blocking buffer B (1% BSA, 10% NGS, 0.3% Triton, 0.1% fish gelatine in PBS, pH 7.4) for 30-45min and washed once for 10min in antibody buffer B (1% BSA, 10% NGS, 0.3% Triton in PBS, pH 7.4) at room-temperature. Samples were incubated in antibody buffer B containing the primary antibody over-night at 4°C and subsequently washed twice for 10min each in

antibody buffer at room-temperature. Secondary antibody staining was performed by incubating the slices in antibody buffer B containing the appropriate secondary antibodies and DAPI (Sigma, #D9542-10MG; 0.05-0.1mg/ml) for 90-120min at room-temperature. All slices were washed three times in PBS for 10min each at room-temperature, mounted on glass slides in "SlowFade" mounting medium (Thermo Fisher Scientific, #S36936) and stored at 4°C until imaging.

Cell culture samples

Cells were washed in PBS (10min at 37°C) and fixed using PFA (4% in PBS; 10min at 37°C). Samples were incubated in blocking buffer (1% BSA, 10% NGS, 0.3% Triton, 0.1% fish gelatine in PBS, pH 7.4) for 10min at room temperature and subsequently washed three times in antibody buffer (1% BSA, 10% NGS, 0.3% Triton in PBS, pH 7.4) at room-temperature for 10min each. Cells were incubated in antibody buffer (1% BSA, 10% NGS, 0.3% Triton in PBS, pH 7.4) containing the primary antibodies for 30min at room-temperature and washed thrice in antibody buffer (1% BSA, 10% NGS, 0.3% Triton in PBS, pH 7.4) for 10min each at room-temperature. Lastly, cells were incubated in antibody buffer (1% BSA, 10% NGS, 0.3% Triton in PBS, pH 7.4) containing the secondary antibodies and DAPI (Sigma, #D9542-10MG; 0.05-0.1mg/ml) for 30min at room-temperature, washed twice in antibody buffer (1% BSA, 10% NGS, 0.3% Triton in PBS, pH 7.4) for 10min each at room temperature and mounted on glass slides in "SlowFade" mounting medium (Thermo Fisher Scientific, #S36936). Slides were stored at 4°C until imaging.

Antibodies

Table 6 Primary Antibodies

Target Antigen	Host species	Dilution	Company	Catalogue #
BrdU	rat	1:250	Abcam	ab6326
CalB	mouse	1:250	Swant	300
CalR	rabbit	1:250	Swant	CR7697
DCX	goat	1:100	Santa Cruz Biotechnology	Sc-8066
Mash1	mouse	1:100	BD Biosciences	556604
NeuN	mouse	1:250	Millipore	MAB377
RFP	mouse	1:2000	Rockland	200-301-379
TH	mouse	1:250	Millipore	MAB5280

Table 7 Secondary Antibodies

Name	Target Antigen	Host Species	Dilution	Company	Catalogue #
Alexa Fluor 488	mouse	goat	1:1000	Thermo Fisher Scientific	A11017
Alexa Fluor 647	goat	donkey	1:1000	Thermo Fisher Scientific	A21447
Alexa Fluor 647	rabbit	goat	1:1000	Thermo Fisher Scientific	A21245
Alexa Fluor 647	rat	goat	1:1000	Thermo Fisher Scientific	A21247
F(ab')2 GAR Ultra Small	mouse	goat	1:30	Aurion	800-166

Microscopy

Confocal images for the T-type project were acquired using a Leica SP8 microscope equipped with 10X/0.4NA (Leica Microsystems, #11506293), 20X/0.75NA (Leica Microsystems, #11506343) and 63X/1.40NA (Leica Microsystems, #11506350) objectives. Image resolution was kept constant at 1024x1024 pixels while scan speed was set to 200Hz with solely unidirectional scanning. All fluorophores were imaged sequentially to prevent bleed-through. Image processing was performed using Fiji[179].

For the 4D project, images were acquired using an automated Zeiss Apotome or a Zeiss LSM780 and images were quantifies using the Zeiss Axiovision software, Photoshop CS5 (Adobe) and Fiji[179].

3D Reconstruction

Reconstruction of fluorescently labelled cells was performed using Amira 6.2 (Thermo Fisher Scientific, USA) as described previously[61,180]. In brief, the signal for all individual staining channels was binarized (with 0 indicating no signal and 1 indicating signal presence) and multiplied with the equally treated RFP channel. This procedure yielded the staining signal contained only within RFP^+ cells.

Olfactory behaviour testing

Automated behaviour setup

A novel automated behaviour setup was custom build based on a concept by Dr. Andreas Schaefer (University College London, United Kingdom). The actual behaviour testing areas (cage lid and tunnel leading towards the odour port) as well as the bedding removal system were completely redesigned and built by Gero Hofmann (mechanical workshop, Heidelberg University, Germany) according to the author's specifications to better suit the differing experimental approach and circumvent certain built-in limitations of the original concept. The odour port and certain vital smaller parts (see Table 10) were designed and manufactured by the author using the 3D printing technique. The following paragraph will focus on the main components of the setup and the overall design rationale. All CAD drawings can be found in the accompanying online repository (https://github.com/AutomatedOlfactoryBehaviour/Beast) while detailed assembly instructions can be found in the appendix.

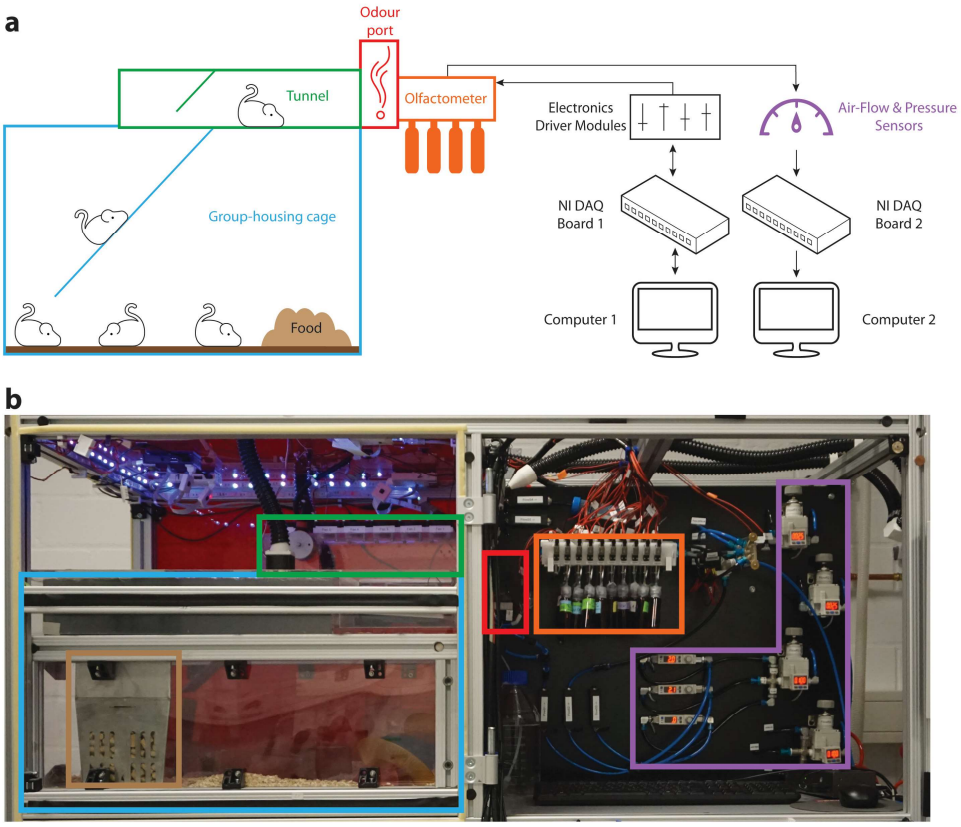

Figure 7 Schematic representation and overview of the behaviour setup. (a) Mice are collectively housed in the group housing cage (blue) and can access the tunnel leading towards the odour port (green) through a ramp. Food (brown) is available ad libitum while water has to be earned through initiation of trials at the odour port (red). Odours are presented from a dual channel olfactometer (orange) which is supplied with clean air through multiple air flow meters and pressure sensors (purple). Directionality of the input and output of the main electronics components (black) is indicated by black arrows. **(b)** Photograph of the upper half of the setup with the main components highlighted as in **(a)**. Note that two of the three doors covering the housing area have been removed to provide an unobstructed view while the electronics and computer components are not depicted.

Hardware components

Olfactometer

For reliable and precise delivery of odour stimuli, a dual channel olfactometer was developed (Figure 8a). In this setup, each odour reservoir is connected to the central manifold and one of the two outer olfactometer channels (Figure 8b) and gated by two micro solenoid valves. When no odour is applied, these valves remain closed causing a constant stream of clean air to flow through all parts of the olfactometer and the odour port (Figure 8a, black pathway). To odourise the air flowing through the olfactometer, air is diverted trough one (or multiple) valves located on the outer channels and routed through the odour reservoir towards the central manifold (Figure 8a, orange pathway). This generates one uniform stream of odourised air which is additionally mixed in a dedicated glass mixing bowl before being diverted to the animal by the final valve. At the same time, fine control over the air pressure and speed of odour delivery

is achieved through the so called pre-pulse valves gating the input to the two outer olfactometer channels as well as the two individually regulated air supplies serving those channels.

Validation of the odour presentation at the odour port was performed using a miniPID photo-ionization detector (Aurora Scientific, #200B). For all odour measurements, the odorant 2-Butanone (Sigma, #34861) was used due to its optimal detectability by the miniPID detector.

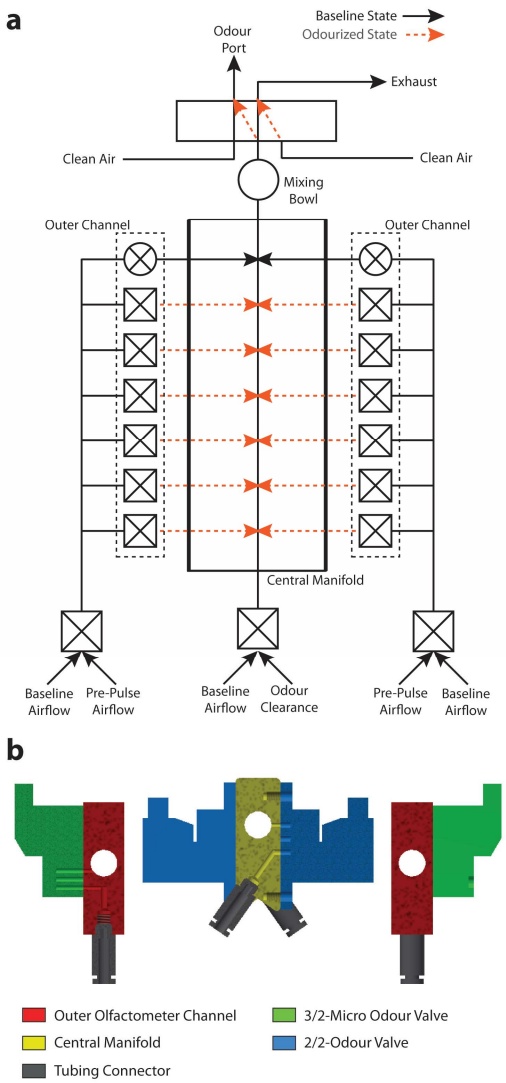

Figure 8 Schematics of the dual channel olfactometer. (a) Schematic representation of the olfactometer. The baseline air flow is shown in black while the air flow during odour presentation is shown in orange. **(b)** Cross section of a CAD drawing of the olfactometer as shown in **(a)**. The odour valves (green and blue) are directly fixed to the central manifold (yellow) and the two outer channels (red) while the odour reservoirs (not shown) are connected to the olfactometer channels through the respective tubing connectors (grey).

Custom made components

The parts listed in Table 8 were custom made by the mechanical workshop (Heidelberg University, Germany) according to the author's specification. If no colour is specified, any colour or transparency grade can be used but parts covering the housing cage should be made from clear or transparent-red materials to allow experimenters to visually observe the animals inside the housing cage. Parts not in direct contact with animals can be made from clear materials and covered with transparent-red self-adhesive foil to substitute transparent-red PVC.

Table 8 Custom made metal and plastic components of the setup.

#	Part Name in CAD Plan	Material	Colour Specifications*	Dimensions (width x height x thickness)	Amount
1	HousingCage_Sidepanel_long	Macrolon	clear or transparent-red	200mm x 650mm x 3mm	2
2	HousingCage_Sidepanel_short	Macrolon	clear or transparent-red	200mm x 529.8mm x 3mm	2
3	PVC_Floorplate	PVC		644mm x 660mm x 8 mm	4
4	Pneumatics_Backplane	PVC		589mm x 730mm x 10mm	1
5	Mousehotel_Backplane	PVC	clear or transparent-red	587mm x 620mm x 5mm	1
6	Mousehotel_Frontcover	PVC	clear or transparent-red	621mm x 701mm x 3mm	1
7	Mousehotel_Sidecover	PVC	clear or transparent-red	661mm x 734mm x 3mm	2
8	Mousehotel_Lid	PVC		696mm x 734mm x 3mm	1
9	BeddingStoper	Stainless Steel	plain sheet metal	607.8mm x 778mm x 2mm	1
10	BeddingShute	Stainless Steel	plain sheet metal	800mm x 1302mm x 2mm	1
11	Tunnel_FloorPlate	Stainless Steel	plain sheet metal	66.8mm x 193.4mm x 2mm	1
12	Tunel_GridPlate	Stainless Steel	perforated sheet metal	80mm x 300mm x 2mm	1
13	HousingCage_FloorGrid	Stainless Steel	perforated sheet metal	603mm x 700mm x 2mm	1
14	Exhaust Tubing (not in CAD Plans)	PVC	reinforced with PVC spiral	Outer diameter: 32mm; Inner diammeter: 30mm	5-10m

The parts listed in Table 9 were custom made by the electronics workshop (Heidelberg University, Germany) according to the author's specifications.

Table 9 Custom made electronics components.

#	Part Name	Amount
1	Rotary Magnet Controller	1
2	Gear Pump Controller	1
3	Valve Controller	1

The parts listed in Table 10 were designed and manufactured by the author using an Ultimaker 2+ 3D printer (Conrad, #1417150-62) and PLA filament (Conrad, #1398205-62) at 0.1mm to 0.2mm printing resolution.

Table 10 Custom designed 3D printed parts.

#	Part Name	Details	Amount
1	Odour Port	Painted black using spray paint (Conrad, #886427-62)	1
2	Odour Port Back Plane	Painted black using spray paint (Conrad, #886427-62)	1
3	Gear Pump Holder		1
4	Tunnel Holder		1

5	Fan Adapters	4
6	Tubing Adapters	1

Commercially available components

The following commercially available components were obtained from the respective companies as indicated.

Table 11 Hardware parts available from Asco Numatics, Germany.

#	Art. Number	Part Name	Details	Amount
1	SC S067A028	Asco Valves, 2/2 NC, 24VDC	2/2-Odour Valve; normally closed	12
2	SC S067A108	Asco Valves, 3/2 Uni, 24VDC	Air diversion valve	2
3	18801088	Asco Micro Valves, NC, 24VDC	3/2-Micro Odour Valve; normally closed	12
4	36100040	Thread UNF	Mounting block for SC S067A108	2
5	88118806	Connectors	Length 0.5m	30
6	SC S067A068	Asco Ventile, 2/2 NO, 24VDC	2/2-Odour Valve; normally open	2
7	18801098	Asco Micro10, NO, 24VDC	3/2-Micro Odour Valve; normally closed	2

Table 12 Hardware parts available from EURO I.D., Germany

#	Art. Number	Name	Amount
1	LID-665-Multi	RFID Reader Control Board; running ASCII-protocol	1
2	LID-665BP	Control Board Base Plate	1
3	CLK-665/650	Control Board Clock Module	1
4	EUR-7005	Control Board Enclosure	1
5	EUR-3120-3m	Microchip Antenna; Diameter: 55mm	1
6	EUR-5015	Interface Cable	1
7	EUR-12V/850	RFID Reader Power Supply	1
8	ID 100	RFID Chips; Size: 2,22mm x 12mm	30
9	IID 100	Microchip Injector	1
10	LID 560	Microchip Handheld Reader	1

Table 13 Hardware parts available from Festo, Germany.

#	Art. Number	Part Name	Details	Amount
1	PUN-6x1-SW	Plastic Tubing PUN	Outer diameter: 6mm; Inner diameter: 4mm; Colour: Black	1
2	PUN-6x1-BL	Plastic Tubing PUN	Outer diameter: 6mm; Inner diameter: 4mm; Colour: Blue	1
3	PUN-4X0,75-BL	Plastic Tubing PUN	Outer diameter: 4mm; Inner diameter: 2,6mm; Colour: Blue	1
4	PUN-8x1,25-SW	Plastic Tubing PUN	Outer diameter: 8mm; Inner diameter: 5,7mm; Colour: Black	1
5	NPFC-X-R14-3G14-MFFF	Kreuzstück	Messing, vernickelt; Außengewinde 1/4; 10 per package	1
6	CK-1/8-PK-4	Threaded Fitting	Outer thread: 1/8; Tubing size: 4mm	1
7	CK-1/4-PK-4	Threaded Fitting	Outer thread: 1/4; Tubing size: 4mm	1

8	LCKN-1/8-PK-4	Threaded L-fitting	Outer thread: 1/8; Tubing size: 4mm	2
9	LCKN-1/4-PK-4	Threaded L-fitting	Outer thread: 1/4; Tubing size: 4mm	1
10	NPFC-Y-3G14-F	Threaded Y-fitting	Inner thread: 1/4	2
11	QS-8-6	Push-In Fitting	Tube to Tube Connectors; Outer diameter tube 1: 8mm; Outer diameter Tube 2: 6mm	1
12	QS-6-4	Push-In Fitting	Tube to Tube Connectors; Outer diameter tube 1: 6mm; Outer diameter Tube 2: 4mm	1
13	QSY-4	Push-In Fitting	For all tubes with outer diameter 4mm	1

Table 14 Hardware parts available from First Sensor, Germany.

#	Art. Number	Part Name	Details	Amount
1	WTAL005DUP	Flow Sensor	5V@5slpm	2
2	WTAL010DUP	Flow Sensor	5V@10slpm	1
3	WBAM200DuHo	Mass Flow Sensors	5V@200sccm	2

Table 15 Hardware parts available from HNP Mikrosysteme, Germany.

#	Art. Number	Part Name	Details	Amount
1	11010103	Micro Annular Gear Pump	Type MRZ-2521	1
2	66020101	Gear Pump Control Board	Type S-ND	1
3	41030100	Check Valve RSV-UP-210	PEEK; Inlet: 1/4''-28 UNF; Outlet: 1/4''-28 UNF	1
4	54020101	Filter	Type: F-UP2; AD 1/8"; Pore Size: 10µm; Material: EFTE	1
5	51010202	Pipe Fitting	PEEK; Size: 1/4"-28 UNF	1
6	52020302	Fluid Adapter	PEEK; Connector 1: 1/4"-28 UNF; Connector 2: Luer-Lock male	1
7	58010906	Dosing Nozzle	Inner diameter: 0.16mm	1
8	92000935	Extension Cable	Length: 1.5m	1
9	55020200	Tubing	Length: 1m; Outer diameter: 1/8''; Inner diameter: 1/6''	1

Table 16 Hardware parts available from Mesa Bammental, Germany.

#	Art. Number	Part Name	Details	Amount
1	1.11.040040.43S-AA4AA4/1360	Profile 40, 4E, S, 1360mm	Width bars (4x Edges & 4 supports for middle and upper compartment)	8
2	1.11.040040.43S-AA4AA4/1627	Profile 40, 4E, S, 1627mm	Vertical Bars (4x edges)	4
3	1.11.040040.43S-AA4AA4/200	Profile 40, 4E, S, 200mm	4x Mousehotel (height bars)	4
4	1.11.040040.43S-AA4AA4/330	Profile 40, 4E, S, 330mm	Vertical bars (4x middle compartment)	4
5	1.11.040040.43S-AA4AA4/529,8	Profile 40, 4E, S, 529,8mm	2x drawer depth bars & 4x mousehotel depth bar	6
6	1.11.040040.43S-AA4AA4/550	Profile 40, 4E, S, 550mm	2x vertical bars (bottom compartment)	2
7	1.11.040040.43S-AA4AA4/620	Profile 40, 4E, S, 620mm	Depth bars (4x corners & 6x support for middle and upper compartment & 2x in middle of floor & lid)	11

8	1.11.040040.43S-AA4AA4/587	Profile 40, 4E, S, 587mm	Vertical bars (upper compartment)	2
9	1.11.040040.43S-AA4AA4/660	Profile 40, 4E, S, 660mm	2x mousehotel (width support bars) & 2x width bars for drawer (support for drawer wheels)	4
10	1.11.040040.43S-AA4AA4/700	Profile 40, 4E, S, 700mm	4x mousehotel (width bars; 2x bottom + 2x top)	4
11	1.11.040040.43S-AA4AA4/950	Profile 40, 4E, S, 950mm	2x drawer (width bars)	2
12	1.45.80200.073	Locking castors	Wheels underneath setup	4
13	1.67.42E3M8	slot roller E3; M8	Slot rollers for drawer	12
14	1.32.4EM8	T-nut for insertion into E-profile with spring; M8	For fixing the slot rollers into the profiles	12
15	1.32.4EM6	T-nut for insertion into E-profile with spring; M6	For fixing PVC/macrolon plates or additional profiles into the profiles	≈150
16	1.47.225160.2	Floor mounting plate	Corner Pieces to stabilize floor plates	5
17	1.21.4E0E	Ground connector / Universal connector	Connection of hardware to aluminium profiles	≈100
18	1.64.153030.2.99	Mounting block GD-Zn	Universal fasteners (i.e. for PVC plates)	≈80
19	1.65.2101	Magnetic lock	Closing mechanism for doors	5
20	1.62.842032085	Alu hinges	Holds door covers in place	6
21	1.19.19040-A00A00/329	19”-Profile, cut to 329mm	Holds power supply in place	2
22	1.72.2010.10	Mounting set for 19”-Profiles	Attachments for 19’’ profiles	1
23	0.63.D00912.06016	Cap-screw, DIN 912 – M6x16	Screws corresponding to M6 T-nuts	≈100
24	1.42.20404.2	Cover Cap 40x40, black	Cover for blunt bar ends	8
25	1.42.504.2	Cover plugs 40, black	Covers for universal connectors	100
26	1.41.E346.2	Combination Profiles E 4,5-6; black	Cover of open profiles & to fix PVC plates	5

Table 17 Hardware parts available from National Instruments, Germany.

#	Art. Number	Part Name	Details	Amount
1	NI BNC-2090A	779556-01	Data Acquisition and BNC Connector Block	2
2	NI PCI-6229	779068-01	PCI I/O Device	2
3	NI SHC68-68-EMP	192061-02	Connector cable for PCI-6229	3

Table 18 Hardware parts available from Sigmann Elektronik, Germany.

#	Art. Number	Part Name	Details	Amount
1	3000750	NIM-Bin with Power	Main Power Supply	1

2	3000701	Main Gas Flow Regulator		1
3	3000794	Gas Flow Regulators		2
4	3001048	Darlington Sensor	Lick Sensor	1
5	3001049	Darlington Power Supply	Power Supply for Lick Sensor	1
6	3001046	IR Beam Detector		1
7	3001047	IR Beam LEDs with cable connectors		2

Table 19 Hardware parts available from SMC, Germany.

#	Art. Number	Part Name	Amount
1	AMH250C-F02D	Micro Mist Separator	1
2	AMH250C-F02B	Micro Mist Separator	1
3	AME250C-F02B	Supermicrofilter	1
4	Y300T-A	interface with bracket for air filters	2
5	PFM710S-F01-E	Air Flowmeter	2
6	IR2000-F02	Precision Pressure Regulator 1/8; Supply & out port 1/4	4
7	P36202028	Bracket for IR2000-F02	4
8	ISE30A-01-B-ML	Digital Pressure Gauge	4
9	TIUB01C-20	Odour Tubing; inner diameter: 3.18mm	≈20m
10	KQ2S23-M5N	Push-Fitting for odour tubing; Tubing diameter: 3.2mm; Thread size: M5	4
11	KQ2S04-M5N	Push-Fitting for tubing; Tubing diameter: 4mm; Thread size: M5	1
12	VK3120-5D-M5	Final Valve with DIN-type connector; Thread sizes: M5	1

Electrical connections

Table 20 Connections of the BNC connectors on BNC1.

BNC Label	Connection 1	Connection 2
AI 0	BNC 1 on IR Detector Module	AI 0 BNC Connector on BNC 2
AI 1	BNC 2 on IR Detector Module	AI 1 BNC Connector on BNC 2
AI 2	Output from Darlington Lick Sensor	AI 2 BNC Connector on BNC 2
AO 0	Analog-IN on Water Pump Module	

Table 21 Connections of the spring block terminal on BNC1.

Terminal Label	Connection 1	Connection 2	Connection 3	Connection 4
DGND	First DGDN on BNC 2 Spring Block Terminal	AI 7 BNC Connector on BNC 2	AI 15 BNC Connector on BNC 2	PFI 0 BNC Connector on BNC 2
P0 0	PFI 0 BNC Connector on BNC 2			
P0 1	AI 7 BNC Connector on BNC 2			
P0 4	P0 4 on BNC 2 Spring Block Terminal			
P0 5	PFI 2 on BNC 2 Spring Block Terminal			
P0 6	P0 6 on BNC 2 Spring Block Terminal			
P0 7	P0 7 on BNC 2 Spring Block Terminal			

DGND	Trig. In Signal on Air Regulator Module	Second DGDN on BNC 2 Spring Block Terminal
PFI 6	Trig. In Signal on Air Regulator Module	

Table 22 Connections of the BNC connectors on BNC2.

BNC Label	Connection 1	Connection 2
AI 0	AI 0 BNC Connector on BNC 1	
AI 1	AI 1 BNC Connector on BNC 1	
AI 2	AI 2 BNC Connector on BNC 1	
AI 3	Mass Flow Sensor 7 (Flow S7)	
AI 4	Mass Flow Sensor 6 (Flow S6)	
AI 5	Gas Flow Regulator 1 (GFR 1)	
AI 6	Gas Flow Regulator 2 (GFR 2)	
AI 7	P0 1 on BNC 1 Spring Block Terminal	First DGND on BNC 1 Spring Block Terminal
AI 8	Mass Flow Sensor 1 (FlowS1)	
AI 9	Mass Flow Sensor 2 (FlowS2)	
AI 10	Mass Flow Sensor 3 (FlowS3)	
AI 11	BNC 3 on IR Detector Module	
AI 12	Air Flow Switch 1 (FlowM1)	
AI 13	Air Flow Switch 2 (FlowM2)	
AI 14	Air Flow Switch 3 (FlowM3)	
AI 15	PFI 0 BNC Connector on BNC 2	
PFI 0	AI 15 BNC Connector on BNC 2	

Table 23 Connections of the spring block terminal on BNC1.

Terminal Label	Connection 1
DGND	First DGDN on BNC 1 Spring Block Terminal
P0 0	PFI 0 BNC Connector on BNC 1
P0 1	AI 7 BNC Connector on BNC 1
P0 4	P0 4 on BNC 1 Spring Block Terminal
P0 6	P0 6 on BNC 1 Spring Block Terminal
P0 7	P0 7 on BNC 1 Spring Block Terminal
DGND	Second DGDN on BNC 1 Spring Block Terminal
PFI 2	P0 5 on BNC 1 Spring Block Terminal

Table 24 Connections of the valve driver connector.

Pin	Olfactometer channel	Valve number on Channel	Connector 2
1	1 (Back Block)	1	P0 8
2	1 (Back Block)	2	P0 9
3	1 (Back Block)	4	P0 10
4	1 (Back Block)	8	P0 11
5	1 (Back Block)	16	P0 12

6	1 (Back Block)	32	P0 13
7	1 (Back Block)	64	P0 14
8	1 (Back Block)	128	P0 15
9	1 (Back Block)	256	P0 16
10	2 (Front Block)	1	P0 17
11	2 (Front Block)	2	P0 18
12	2 (Front Block)	4	P0 19
13	2 (Front Block)	8	P0 20
14	2 (Front Block)	16	P0 21
15	2 (Front Block)	32	P0 22
16	2 (Front Block)	64	P0 23
17	2 (Front Block)	128	P0 24
18	2 (Front Block)	256	P0 25
19			P0 26
20	1 (Back Block)	Odour Pre-Pulse	P0 27
21	2 (Front Block)	Odour Pre-Pulse	P0 28
22	1 (Back Block)	Relief Valve	P0 29
23	2 (Front Block)	Relief Valve	P0 30
24		Final Valve	P0 31
25			24V DC

Construction of the behaviour setup

To construct the complete automated behaviour setup, the main components of the setup (i.e. housing cage, the bedding stopper and the cage lid assembly) were first assembled individually and placed into the setup frame (Supplementary Figure 4-Supplementary Figure 12). Subsequently, the olfactometer and pneumatics parts were fixed to the pneumatics back plane (Supplementary Figure 9-**Fehler! Verweisquelle konnte nicht gefunden werden.**). The individual electronics driver modules were attached to the NIM Bin power supply unit (Sigmann Elektronik, #3000750) and fixed in the setup frame. Lastly, all pneumatic parts were connected using dedicated pressurized air pneumatic tubing (Supplementary Figure 16) while the electronic components were connected according to the specifications found in Table 20 to Table 24. The odour reservoirs were filled with the respective training odours (see Table 26), sealed with custom made bottle caps (Supplementary Figure 13) and attached to the olfactometer. Lastly, the housing cage was supplied with bedding (Abedd, #LTE-E-001 or #LTE-E-002), food (LasVendi, #Rod16), nesting material (Abedd, #NBG-E-012) and the water reservoir was filled with water (Danone Waters Germany, “Volvic Natural Mineral Water”).

Behaviour setup control and analysis software

The overall code structure and core algorithms used to control the hardware components were written by Prof. Dr. Andreas Schaefer (University College London, United Kingdom) using Igor 4 (Wavemetrics, USA). However, the entire code was ported to Igor 6 (Wavemetrics, USA) and the majority of the setup control

software was modified by the author to account for the changed hardware and the differing experimental approach. The entire recording software for acquisition of the sensor data as well as the entire analysis code was custom written by the author using Igor 6 (Wavemetrics, USA). The source code is available from the online repository (https://github.com/AutomatedOlfactoryBehaviour/Beast).

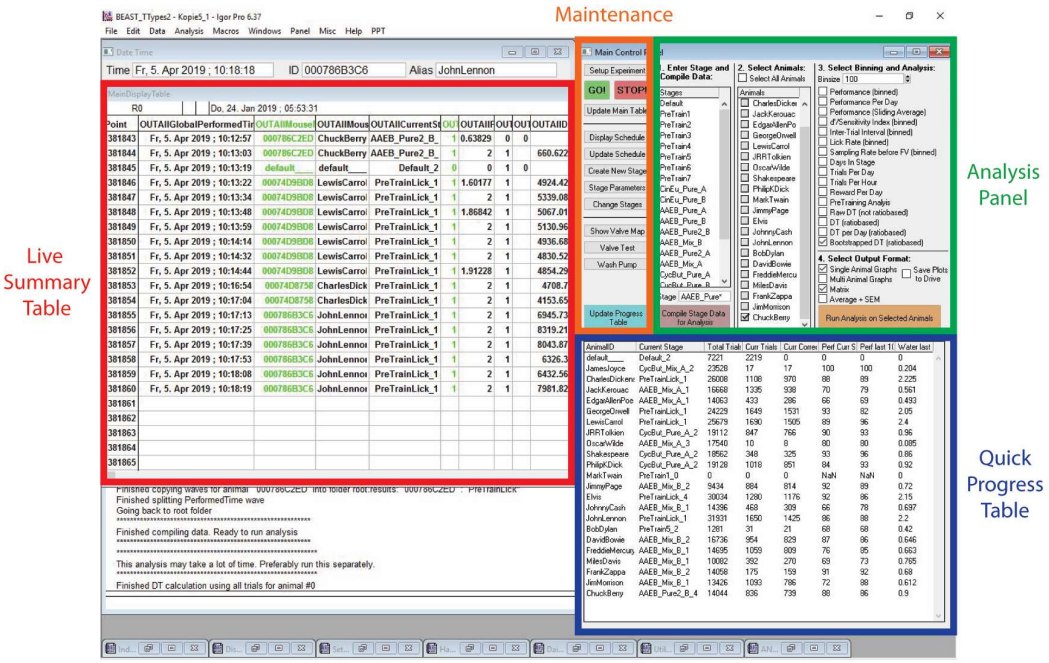

Figure 9 Overview of the interface of the main behaviour control software. The most important parameters of each trial are continuously logged in the Live Summary Table (left; red) while the current training progress of each animal is logged in the Quick Progress Table (blue). The in-depth analysis functions as well as the graphical output options are available from the Analysis Panel (green) while routine maintenance options can be executed through the buttons in the Maintenance area (orange).

Briefly, the control software contains the training sequences for each animal while simultaneously monitoring the most important parameters of each trial (Figure 9). For ease of use, these parameters are continuously logged in a summary table that is updated live (Figure 9, red). Additionally, the current training progress of each animal is shown, including the performance within the last 100 trials and the water reward obtained in those trials. All routine maintenance procedures (i.e. stopping and restarting the software, testing the valves and water pump) can be executed from the maintenance area (Figure 9, orange). Lastly, in-depth analysis with various output formats is available from the dedicated Analysis Panel (Figure 9, green). It is worth to note, that the training sequences can be adjusted individually for each animal, allowing faster animals to progress to subsequent tasks (i.e. the next odour pair) without being slowed down by other animals. Further, any parameter within any given training stage (i.e. water reward per trial or pre-sampling threshold) can be freely adjusted for each animal allowing the user to optimize the training for each animal without interfering with the cohort as a whole.

Behaviour training paradigm

Mice were trained on a go/no-go operant conditioning paradigm as described previously[61,81,153]. Access to the odour port was blocked by closing the door of the tunnel leading to the odour port and mice were placed in the group housing cage. The animals were allowed to acclimatize to the setup for at least one hour during which the access to the odour port remained closed. After grantig access to the tunnel leading towards the odour port, the training was started and mice were free to explore and find the odour port. Initially, a so-called pre-training protocol is initiated which gradually introduced new conditions for receiving a water reward (see Table 25). Mice could only progress from one training stage to the next upon completing a certain minimal number of trials and performing with at least 80% accuracy within the last 20 trials. If the performance criterion was not met, the mice remain in the stage for more trials. The last phase of the pre-training is identical to the trial structure during odour discrimination (Figure 10), the only exception being that mice are presented not with odourised air but clean air only.

Table 25 Parameters used during pre-training in automated behaviour setup

Pre-Training Phase	Dwell Threshold [Minimal dwell rate before FV opening]	Lick criterion [Number of 500ms blocks until water reward is given]	Delay until water reward [ms]	Minimal Trial Number	Water reward [µl]	Inter-Trial Interval [s]
1	0	0	0	50	20	0-0.5
2	0	0	0	50	20-10.5	0.5-3.9
3	12.5%	0	21-500	100	10	1
4	25%	0	500-1980	100	10	1
5	50%	1	2000	100	10	1
6	75%	2	2000	100	10	1
7	87.5%	3	2000	100	15	1

After completing at least 100 trials and reaching a performance of at least 80% in the last pre-training phase, animals automatically progress to the actual odour discrimination task.

During odour discrimination, animals are presented with either of two odours with one being rewarded (S+ odour) and the other one not (S- odour). Animals will gradually cease licking for the unrewarded odour and retracted their head while they would leave their head in the odour port and continue licking for the rewarded odour to receive the water reward.

The sequence of trials was pseudo-randomized in blocks of 1000 trials with i) no more than three consecutive rewarded or unrewarded trials, ii) approximately 50 rewarded and unrewarded trials within each 100 trial bin. Every sequence of 1000 trials could only be repeated after completion of the full sequence of 1000 trials. Additionally, designation of the odours as rewarded and unrewarded was counterbalanced within each treatment group to ensure that no intrinsic preferences for any odour could confound the results. Neither we nor previous studies found any differences between counterbalanced odours in any experiment, hence all data is shown as pooled data for each odour pair[61,62,81,132,181].

The amount of water reward delivered during odour discrimination was adjusted based on the overall consumption of the animal to ensure each animal received minimally 1ml of water per day. The range across all experiments was 10µl to 30µl per correctly identified rewarded trial.

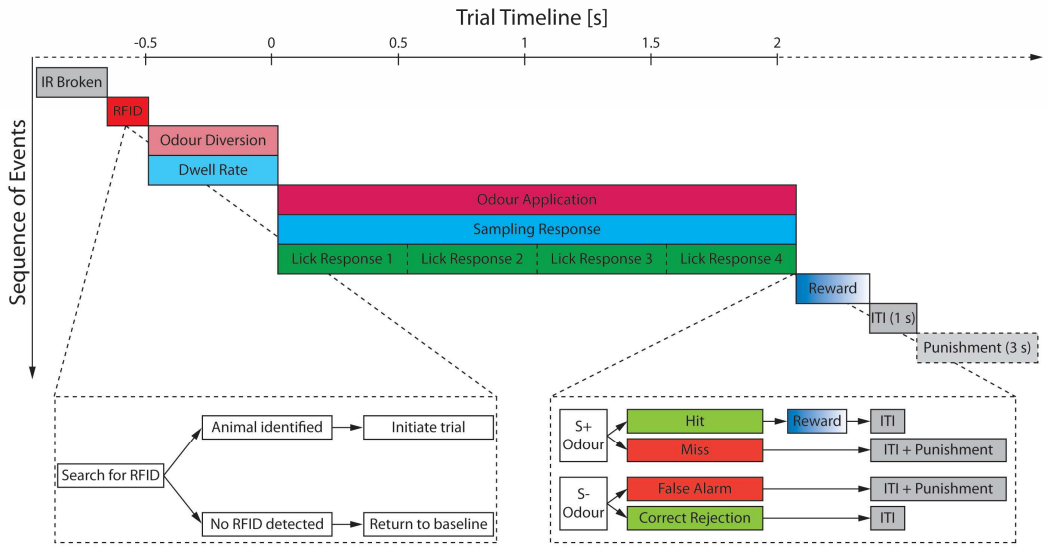

Figure 10 Schematic representation of the trial structure. Once a break of the IR Beam (grey) has been detected by the behaviour control software, the search for an RFID signal is initiated (red). If a RFID sequence corresponding to an animal has been identified, a trial is initiated starting with 500ms of odour diversion from the reservoirs to the central manifold ("Odour Diversion"; light magenta). During this time, the sampling behaviour of the animal at the odour port is recorded ("Dwell Rate"; light blue). If the dwell rate exceeds the defined threshold, the odour is presented to the animal for a maximal duration of 2s (magenta). During this time, the sampling behaviour (blue) as well as the lick response (green) are recorded. Delivery of the water reward (blue) occurs only if the animal correctly identified the S+ odour ("Hit"). Incorrect responses ("Miss" or "False Alarm") cause an extension of the inter-trial interval (ITI) by a time punishment of 3s during which no trial can be initiated.

Odours used

All odours (see Table 26) used during the behavioural experiments and during validation of the olfactometer were diluted in mineral oil (Sigma, #69794) to a final concentration of 1% (v/v). All odours were presented at a speed of 2 l/min.

Table 26 Odours used for behavioural training

Odour	Company	Catalog #
Cineol	Sigma	27395
Eugenol	Fluka	46100
Amylacetate	Sigma	109584
Ethylbutyrate	Sigma	E15701
2-Butanone	Sigma	34861
(+)-Octanol	Fluka	74863
(-)-Octanol	Fluka	74865

Analysis parameters

For the analysis of the behaviour data, any samples below the threshold dwell rate prior to opening of the final valve were discarded. The remaining trials were used for the binned analyses with the performance being defined as the fraction of correct choices (Hits or Correct Rejections) within a respective bin. Similarly, the sensitivity index (d-prime) was calculated using the inverse of the standard normal cumulative distribution function (z) according to the following formula:

$$d - Prime = z(Hit\ Rate) - z(False\ Alarm\ Rate)$$

In the case of perfect Hit or False Alarm rates (i.e. 100% Hits or False Alarms respectively), the Hit or False Alarm rates needed to be lowered by 0.5%, as the standard normal cumulative distribution for perfect scores cannot be calculated. For the same reason, a substitute Hit or False Alarm rate of 0.5% was used in the case of 0% Hits or False Alarms.

An individual trial was scored as "licked" if the animal licked in at least three out of the four 500ms bins after opening of the final valve (see Figure 10 for details). An individual bin was scored as "licked", if the animal licked at the lick spout for at least 50% of the bin. The lick frequency was defined as the fraction of trials within the bin, in which the animal licked, regardless of the original type (rewarded or unrewarded) of the trial. The inter-trial interval (ITI) was calculated as the time difference between the initiations of successive trials of an animal. Any ITIs exceeding one minute were discarded. The dwell rate prior to the opening of the final valve was defined as the fraction of the pre-final valve odour diversion time (500ms) during which the head of the animal was inside the odour port (as measured by the two IR beams at the odour port).

For the analysis of post-criterion baseline-data (i.e. supra-threshold performance, lick frequency, ITI and dwell rate), the respective values were only included for bins in which the binned performance was ≥95%.

Calculation of the discrimination time

To determine the discrimination time (DT), i.e. the minimal time necessary to discriminate two odours), only correct trials after the initial reaching of the performance threshold were used and performance-thresholded using a sliding window of 100 trials. From the resulting pool of thresholded rewarded and unrewarded trials, 500 trials per trial type were randomly selected by bootstrapping (with replacement) and used to determine the discrimination time as established previously[61,62,81,132]. The bootstrapping was repeated 1000 times and the final DT was determined by averaging the individual DTs calculated during the individual bootstrapping iterations. As manual inspection of the individual bootstrapping results was not feasible, a more stringent threshold p-value of 0.001 (instead of 0.05) was used to circumvent problems described in the previous publications due to atypical sampling behaviour of the mice. Typically, the more stringent threshold p-value yields higher DTs compared to the less stringent value (Figure 11a). Due to the large number of available trials, however, the sampling rates for rewarded and unrewarded trials may diverge substantially already shortly after the opening of the final valve (Figure 11b). In these instances, a

higher threshold p-value will fail completely to yield a DT, while a more stringent value can still accurately determine the point at which the sampling behaviour differs substantially. Further, some animals show an atypical sampling behaviours as they may retract their head directly after opening of the final valve but resume sampling afterwards (Figure 11c). Again, a less stringent threshold will lead to incorrect DTs and potentially require discarding all data obtained for this animal.

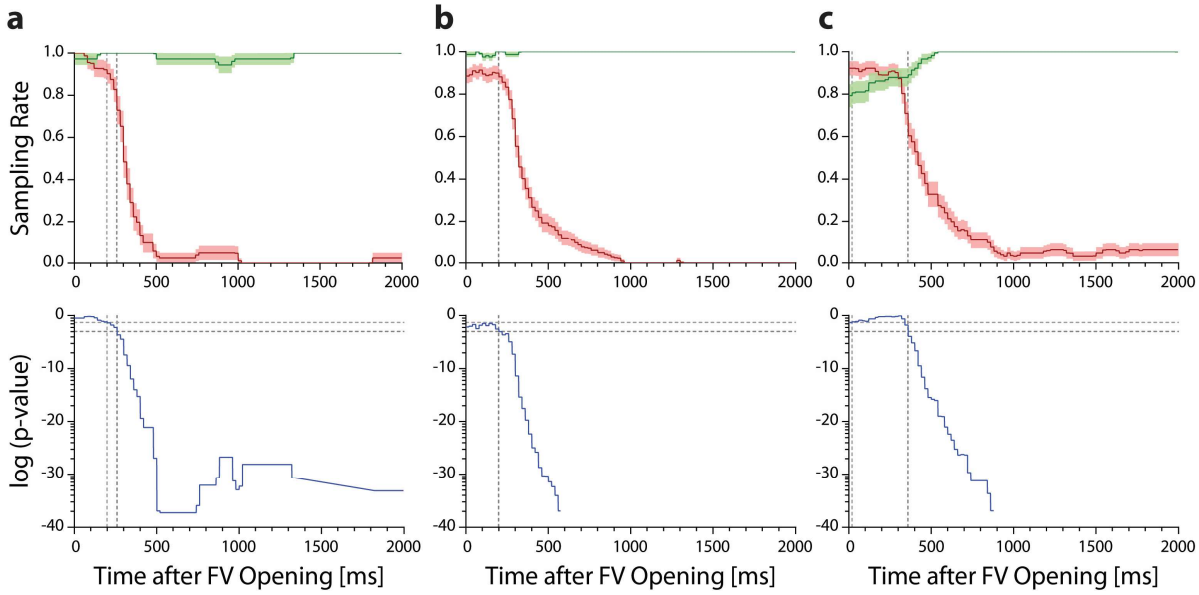

Figure 11 Effect of the p-value threshold on the resulting discrimination time. Representative sampling rates during odour presentation for rewarded (green) and unrewarded (red) trials as well as the p-value determined by pointwise comparisons of sampling rates for unrewarded and rewarded trials. **(a)** Animal displaying typical sampling behaviour resulting in similar DTs despite different thresholds used. **(b)** Animal displaying reduced sampling behaviour for unrewarded trials resulting in a failure to obtain a DT with the less stringent threshold. **(c)** Animal displaying atypical sampling behaviour for rewarded and unrewarded trials resulting in an obviously incorrect DT when using the less stringent threshold p-value. Vertical and horizontal grey lines denote differing p-value thresholds (light grey: 0.05; dark grey: 0.001). **Sampling Rates**: Lines denote average of 500 trials (± SEM) for one representative animal each.

This bootstrapping approach was validated by re-analysing a previously published data set[61]. Towards this end, the data was analysed using bootstrapping algorithm and both threshold p-values (Figure 12a). When using the established p-value of 0.05, our approach yielded virtually identical DTs while the more stringent p-value resulted in the expected higher DTs. As animals in the automated behaviour setup will typically perform many more trials than in the previously used manual setups, we investigated the effect of overtraining on the discrimination time (Figure 12b). Here, we found a significant decrease in DTs with increasing number of performed trials. Hence, we limited training of the animals to maximally 1000 high-performance trials to avoid artificially changed DTs due to overtraining. In behavioural runs where not all animals reached 1000 high-performance trials, the analysis was limited to the initial 500 high-performance trials after reaching the performance criterion. Lastly, we sought to reproduce the established effect of odour complexity on the DT and hence compared DTs for the discrimination of “simple” odour pairs with

DTs required for the discrimination of their more complex binary mixtures (Figure 12c). Not only could we successfully reproduced the significant increase in DTs for complex stimuli using the automated setup and our novel algorithm but we also found a difference of 80.20ms which is very close to the previously reported value of 88.6ms as shown by Abraham et al. in 2010[132].

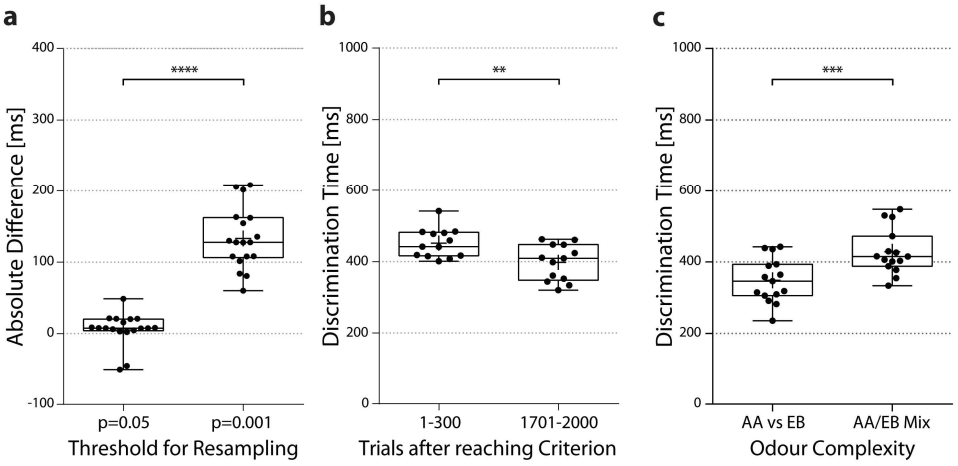

Figure 12 Factors influencing the discrimination time. (a) Comparison of discrimination times (DTs) from a published dataset (see [61]) with the DTs obtained using the bootstrap algorithm with different threshold p-values (mean difference: 126.7ms ± 11.21; paired t-test, p<0.0001; n=18). **(b)** Comparison of DTs calculated using the first and last 300 trials after reaching the performance criterion (mean difference: 53.65ms ± 14.34; paired t-test, p=0.0028; n=13). **(c)** Comparison of DTs obtained using the bootstrap algorithm and a threshold p-value of 0.001 (mean difference: 80.20ms ± 17.06; paired t-test, p=0.0004; n=15). Whiskers show 1.5 interquartile range, line denotes median while cross denotes mean and dots show individual animals.

Data analysis and presentation

CAD models of the behaviour setup were generated using Autodesk Inventor Professional 2016 (Autodesk, USA) as well as using Autodesk Inventor Professional 2018 (Autodesk, USA) and processed using Adobe Illustrator CS4 (Adobe Systems, USA).

Behavioural data was acquired and analysed using custom written algorithms based on Igor 6 (Wavemetrics, USA) utilizing the Igor XOP Toolkit and the NIDAQ Tools MX package. Statistical analysis was performed using Igor 6 (Wavemetrics, USA) and Prism 6.0 (Graphpad, USA) (* = p <0.05; ** = p <0.001; *** = p <0.001). Potential outliers in the 4D electrophysiological and biomolecular analyses were identified using Tuckey's test while potential outliers in any other analysis were identified using the ROUT method as detailed here[182] and as implemented in Prism 6.0 (Graphpad, USA).

Graphical representations were generated using Prism 6.0 (Graphpad, USA) and Adobe Illustrator CS4 (Adobe Systems, USA). Unless otherwise noted data is shown as mean ± SEM.

Contributions

The design of the shRNA, subcloning and purification of plasmids was performed by Michaela Kaiser (Institute for Anatomy and Cell Biology, Heidelberg University, Germany). Routine cell culture for the production of AAV viruses was performed by Claudia Kocksch (Institute for Anatomy and Cell Biology, Heidelberg University, Germany) and Annette Herold (Max-Planck Research Group, Institute for Anatomy and Cell Biology, Heidelberg University, Germany). Preparation of primary hippocampal and cortical cell cultures was performed by Gabriele Krämer and Marion Schmitt (Institute for Anatomy and Cell Biology, Heidelberg University, Germany). The original concept of the behaviour setup was conceived by Dr. Andreas Schaefer (University College London, United Kingdom) and the lid and tunnel of the behaviour setup were designed and built by Gero Hofmann (mechanical workshop, Heidelberg University, Germany) according to the author's specifications. Lastly, biomolecular characterisation of the 4D mouse line, induction of the 4D transgenic mice via oral administration of tamoxifen and post-hoc analysis of the mice used during the behavioural experiments was performed by Dr. Sara Bragado Alonso (CRTD Dresden, Germany). Electrophysiological recordings from superficial olfactory bulb granule cells was performed by Dr. Nicolas Marichal (Institute of Physiological Chemistry, University Mainz, Germany).

Peer-reviewed publications

Parts of this thesis were published in a peer-reviewed publication:

Bragado Alonso S, Reinert JK, Marichal N, Massalini S, Berninger B, Kuner T, Calegari F, 2019. An increase in neural stem cells and olfactory bulb adult neurogenesis improves discrimination of highly similar odorants. *The EMBO Journal*, 38(6), p.e98791.

Results

Part 1: Establishing an automated behaviour setup for odour discrimination

Technical validation of a novel automated behaviour setup

Figure 13a shows that odour onset at the sampling port is both fast as well as precise after opening of the final valve. No air ionization is detectable for pure mineral oil alone, which is especially important, as this ensures that there is no cross-contamination between odour reservoirs and that unused valves are in fact tightly closed with no leakage into the olfactometer.

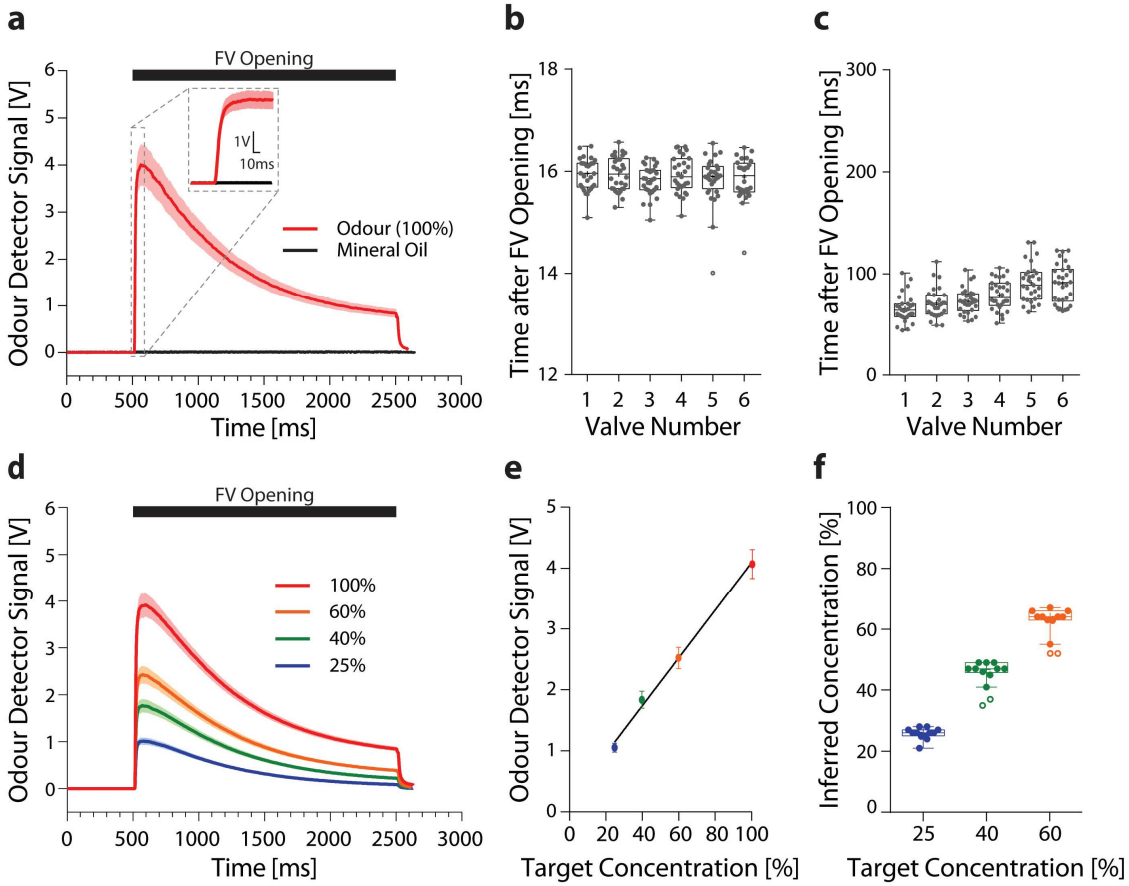

Figure 13 Temporal analysis of odour presentation at the odour port. (a) Representative measurement obtained using an ionization detector during presentation of an odour (red trace, n=12) or mineral oil (black trace, n=10). Insert shows 20ms prior and 100ms after opening of the final valve in more detail. **(b)** Onset of the odour after opening of the final valve. **(d)** Representative odour pulse measurements for different odour dilutions generated directly within the olfactometer (n=12 per dilution). **(e)** Correlation between the detected ionisation intensity and the target odour dilution (n=12 per dilution). **(f)** Relationship of the intended target odour concentration and the inferred odour concentrations, extrapolated from the measured odour detector signal (n=12 per dilution). **(a)/(b)**: Line graphs show mean ± SEM. **(b)/(c)/(f)**: Whiskers show 1.5 interquartile range, line denotes median while cross denotes mean. Dots represent individual measurements while circles represent potential outliers as identified by ROUT test.

To analyse the odour presentation in more detail, the odour onset (defined as the time point at which 10% of the maximum odour concentration was reached) as well as the time point of the peak odour concentration were determined. Odour onset was detected 16ms (15.91ms ± 0.02) post opening of the final

valve regardless of distance to the final valve (Figure 13b; one-way ANOVA, $F(5, 167)=0.6601$; $p=0.654$). On the other hand, the peak odour concentration was reached on average 80ms (78.30ms ± 3.98) post opening of the final valve, yet there was a significant increase with increasing distance to the final valve (Figure 13c; one-way ANOVA, $F(5, 172)=13.33$; $p<0.0001$). Despite this correlation, the maximal difference between the valves was less than 30ms (valve 1: 65.38ms ± 2.55; valve 5: 91.38ms ± 3.48). As any given odour is always presented from multiple randomly assigned odour valves, it is unlikely that this marginal difference could influence the behaviour of the animals.

To validate the option of directly generating odour dilutions using the olfactometer instead of premixing dilutions, four different concentrations were generated within the olfactometer. Here we found that the shape and variability of the odour pulses was similar across all dilutions (Figure 13d). Analysis of the measured ionization and the intended odour concentration revealed a strong correlation between the two (Figure 13e; Pearson correlation $r=1.00$; $R^2=1.00$; $n=12$ per dilution). Conversion of the signals measured by the sensor into odour concentrations showed a close match between intended concentration and the actual measured concentration (Figure 13f; 60%: 63.60% ± 1.05; 40%: 46.70% ± 0.76; 25%: 25.75% ± 0.55; $n=12$ per dilution).

Taken together, these values clearly show, that the novel olfactometer allows for fast and precise delivery of odour pulses with minimal variation between odour valves. Further, odour dilutions can be directly generated within the setup, allowing not only for the generation of arbitrary dilutions from stock reservoirs, but ultimately also for the generation of mixtures of different odours. As these mixtures would not need to be pre-mixed, this greatly increases the flexibility of this system and makes novel training paradigms involving complex mixtures possible.

Effect of non-olfactory cues in automated behaviour training

To rule out potential non-olfactory cues (i.e. differences in valve noises, air flow variations, minimal delays in odour peaks, etc.), three wild-type mice were tasked to distinguish rewarded from unrewarded trials without any odorants being added to the mineral oil in the odour reservoirs (Figure 14). Even over thousands of trials the performance (Figure 14a) remained at chance level while d-prime scores (Figure 14b) remains at zero, clearly reflecting the lack of cues, olfactory or otherwise.

In-depth analysis of the fraction of trials in which the animals responded with licking (lick frequency; Figure 14c) showed an overly large response rate of 100% indicating that the animals reverted to licking at all trials, a strategy which maximises chance of obtaining a water rewarded. This behaviour remained stable throughout the entire training duration.

The 500ms time window prior to opening if the final valve was analysed to determine during which fraction of this time period the animal had its head in the odour port (dwell rate; Figure 14d). This dwell rate, a marker for the animals' motivation to perform trials, remained stably high over the first thousand trials but showed a decrease thereafter, indicating a decrease in motivation with prolonged training. The inter-trial

interval (ITI; Figure 14d), an additional indicator of motivation, revealed some fluctuation over time but remained well within the range of 10-30ms previously described for manual behaviour setups[61,81].

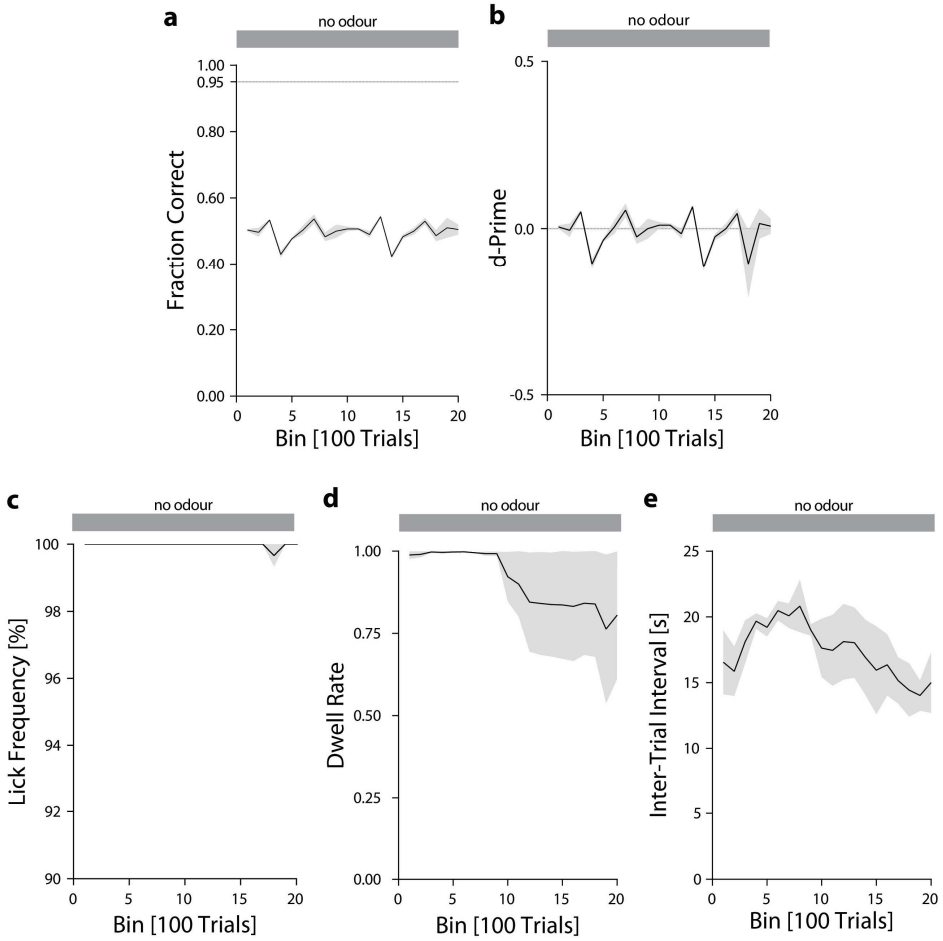

Figure 14 Performance of mice in an automated behaviour setup without odour cues. (a) Performance and **(b)** d-prime over two-thousand trials without presentation of odour cues. **(c)** Lick frequency, the raction of all trials (rewarded as well as unrewarded ones) at which the animals licked, **(d)** dwell rate prior to final valve opening and **(e)** the inter-trial interval (ITI). Line plots show mean ± SEM (n=3).

Operant conditioning of small cohorts

As animals failed to solve the go/no-go task in the absence of odour cues, we next sought to determine whether they could solve the task when olfactory cues were present. Indeed, animals were able to reach ≥95% performance within less than a thousand trials for the first odour pair (cineole vs eugenol; Figure 15a and b). The ability to distinguish the two signals is also reflected in the d-prime scores which surpass the criterion of ≥1 within 300 trials for this initial odour pair. Since the acquisition of the initial odour pair also involved learning of the odour discrimination task itself (i.e. that one odour signals a rewarded trial while another odour signals an unrewarded one), animals were far quicker to acquire the subsequent odour pair (amyl acetate vs ethyl butyrate; Figure 15a and b) which did not involve learning of the discrimination paradigm. This is evident from the lower number or trials needed to reach both the performance criterion (300 trials) as well as the d-prime criterion (200 trials).

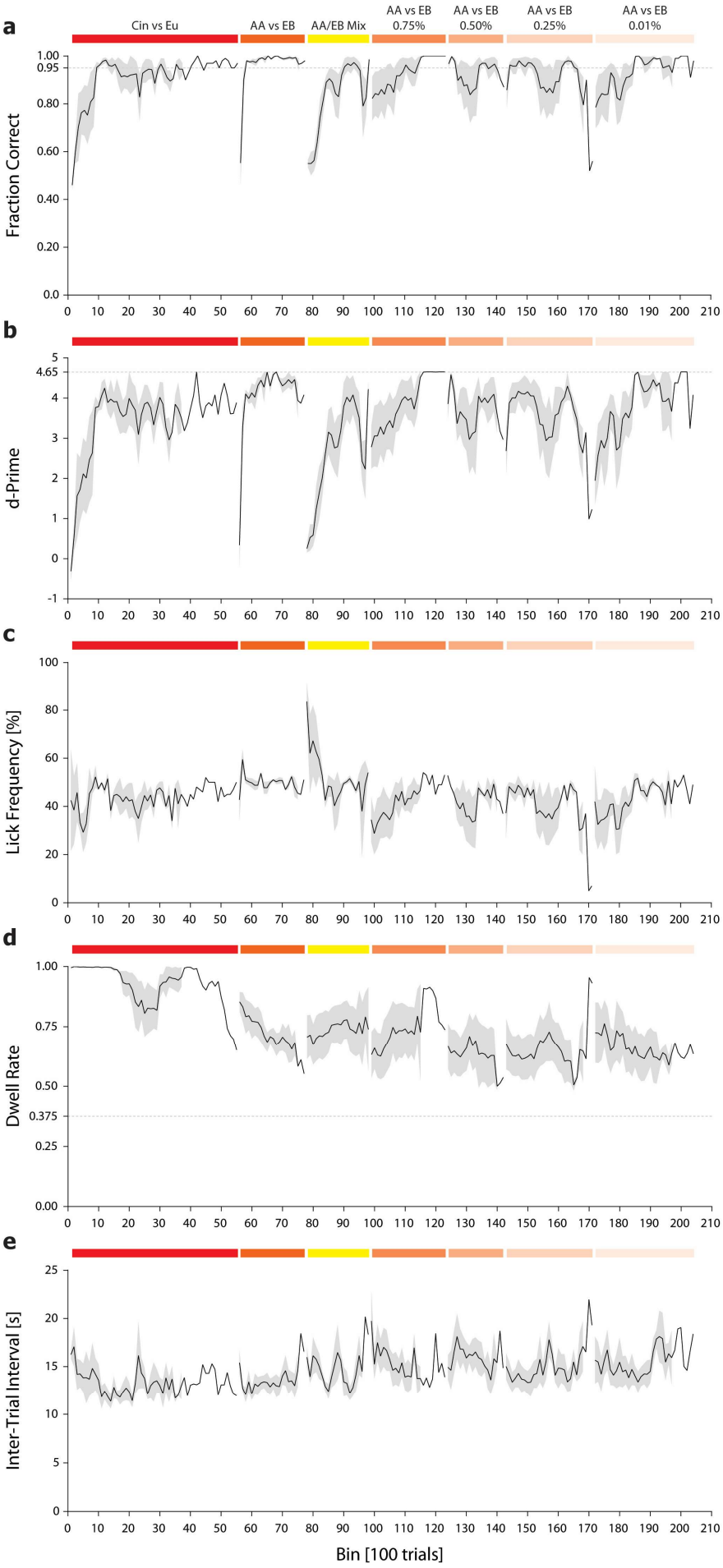
a
Cin vs Eu
AA vs EB
AA/EB Mix
AA vs EB 0.75%
AA vs EB 0.50%
AA vs EB 0.25%
AA vs EB 0.01%
Fraction Correct
b
d-Prime
c
Lick Frequency [%]
d
Dwell Rate
e
Inter-Trial Interval [s]
Bin [100 trials]

Figure 15 Performance with odour cues at varying concentrations. Detailed breakdown of discrimination performance showing **(a)** fraction of correct trials, **(b)** d-prime, **(c)** fraction of trials at which the animals licked (lick frequency), **(d)** dwell rate prior to final valve opening and the **(e)** inter-trial interval (ITI) over more than twenty-thousand trials with presentation of odour cues in different combinations and at different concentrations. Animals were presented with cineole or eugenol (Cin vs Eu, red bar), amyl acetate or ethyl butyrate (AA vs EB, orange bar), a mixture of amyl acetate and ethyl butyrate (AA/EB Mix, yellow bar) and amyl acetate or ethyl butyrate at varying concentrations (AA vs EB 0,75%-0,01%, opaque orange bars). Line plots show mean ± SEM (n=4).

Similarly, acquisition of a 60%/40% binary mixture of a learned odour pair (amyl acetate/ethyl butyrate mixture; Figure 15a and b) again required more trials to stably reach high performance (performance: 1300 trials; d-prime: 400 trials), reflecting the higher degree of difficulty for this task.

Lastly, when tasked with again distinguishing a previously learned odour pair but at lower reservoir concentrations (0.75% to 0.01% in mineral oil compared to the initial presentation at 1% in mineral oil), animals readily distinguished the two odours reflected by performances continuously exceeding 80% and d-prime scores well above two (Figure 15a and b).

As the lick frequency (Figure 15c) is intrinsically linked to the performance, these values remained around the expected value of 50% (overall mean 44.89% ± 1.54) and deviated only during initial exposures to odour pairs (i.e. binary mixture of amyl acetate and ethyl butyrate) or after prolonged training durations with the same odour pair (i.e. towards the end of 0.25% amyl acetate and ethyl butyrate).

To measure motivation of the animals, the dwell rate prior to opening of the final valve as well as the inter-trial interval (ITI) were recorded. Despite initial dwell rates (Figure 15d) of 100%, the animals drastically decreased their sampling to roughly 65% over the course of the training. The most striking example of this was observed with the second odour pair (amyl acetate vs ethyl butyrate) where the dwell rate dropped from 85% at the beginning of the task nearly linearly to only 55% at the end of the task, an effect not previously seen using manual behaviour setups. Conversely, the ITI did not show a clear in- or decrease but remained well within the range of 10-30ms as determined previously with manual setups.

Operant conditioning of large cohorts

Since this initial testing was only conducted with a small number of animals resulting in considerable variance, we sought to analyse the effect of prolonged training and group size in more detail. Toward this aim, a larger group of wild-type animals (n=18) was trained on a more limited set of odour pairs. Similar to the pilot study, animals were able to reach ≥95% performance for the initial odour pair (cineole vs eugenol) within roughly 400 trials (trials to criterion: 392.1 trials ± 67.02) and a d-prime score ≥ 1 in less than 100 trials (Figure 16a and b). The subsequent odour pair (amyl acetate vs ethyl butyrate) was again acquired faster with the performance threshold being reached within 200 trials (trials to criterion: 202.9 trials ± 35.88) and the d-prime threshold being reached within the first 100 trials (Figure 16a and b). Analogous to the previous results, the performance thresholds for the more challenging mixture of the two odours (amyl

acetate/ethyl butyrate mixture; Figure 16a and b) were only reached after over 400 trials (trials to criterion: 433.5 trials ± 75.38) or 200 trials (d-prime) respectively. While we did not observe any differences in the supra-threshold performance (Cin vs Eu: 97.56% ± 0.20; AA vs EB: 98.08% ± 0.17; AA/EB Mix: 98.30% ± 0.16; paired t-test, p=0.05 and p=0.26 respectively; Figure 16a1), we did find a significant increase in the d-prime scores between the first and the second odour pair (Cin vs Eu: 3.25 ± 0.13; AA vs EB: 3.82 ± 0.08; AA/EB Mix: 3.98 ± 0.06; paired t-test, p=0.003 and p=0.13 respectively; Figure 16b1) indicating increased discriminability of the two odours constituting this second odour pair.

The lick frequency (Figure 16c) showed an overall fluctuation around 50% (overall mean: 50.88% ± 0.50), as seen previously, with a transient increase upon initial exposure to the binary mixture of amyl acetate and ethyl butyrate. This change may reflect a change in the strategy the animals employ to solve the task: an increased lick frequency means the animals also lick at unrewarded trials and incur a time penalty for these false alarms, yet this behaviour increases the chance of receiving a water reward if the identity of the trial is uncertain to the animal. This may also explain, why the animals only show this behaviour when initially faced with a more difficult task and cease to lick at more trials than necessary once they have learned to solve the task (reflected by increased performance and d-prime scores). Consistently, the supra-threshold lick frequency for all odour pairs was virtually 50% (Cin vs Eu: 49.56% ± 0.62; AA vs EB: 48.63% ± 0.32; AA/EB Mix: 50.68% ± 0.89; paired t-test, p=0.24 and p<0.0001 respectively; Figure 16c1).

In contrast to the initial pilot experiments, the lick frequency did not decrease with prolonged training, indicating constant high motivation of the animals. This is also reflected in the dwell rate (Figure 16d) which remained close to 1 (equivalent to 100%) throughout the training, even after reaching the performance criterion (Cin vs Eu: 0.999 ± 0.0002; AA vs EB: 0.998 ± 0.0003; AA/EB Mix: 0.999 ± 0.0002; paired t-test, p=0.047 and p=0.01 respectively; Figure 16d1). One should note that the threshold for the dwell rate prior to opening of the final valve was intentionally increased to 87.5% to prevent drops in dwell rate seen in the previous cohort which could result in drops in performance. The lasting high motivation is also reflected in the ITI (Figure 16d), which showed very little change over time or between odour pairs (overall mean: 16.55s ± 0.17; Cin vs Eu: 17.3s ± 0.33; AA vs EB: 16.64s ± 0.31; AA/EB Mix: 16.01 ± 0.24; paired t-test, p=0.08 and p=0.09 respectively; Figure 16e1).

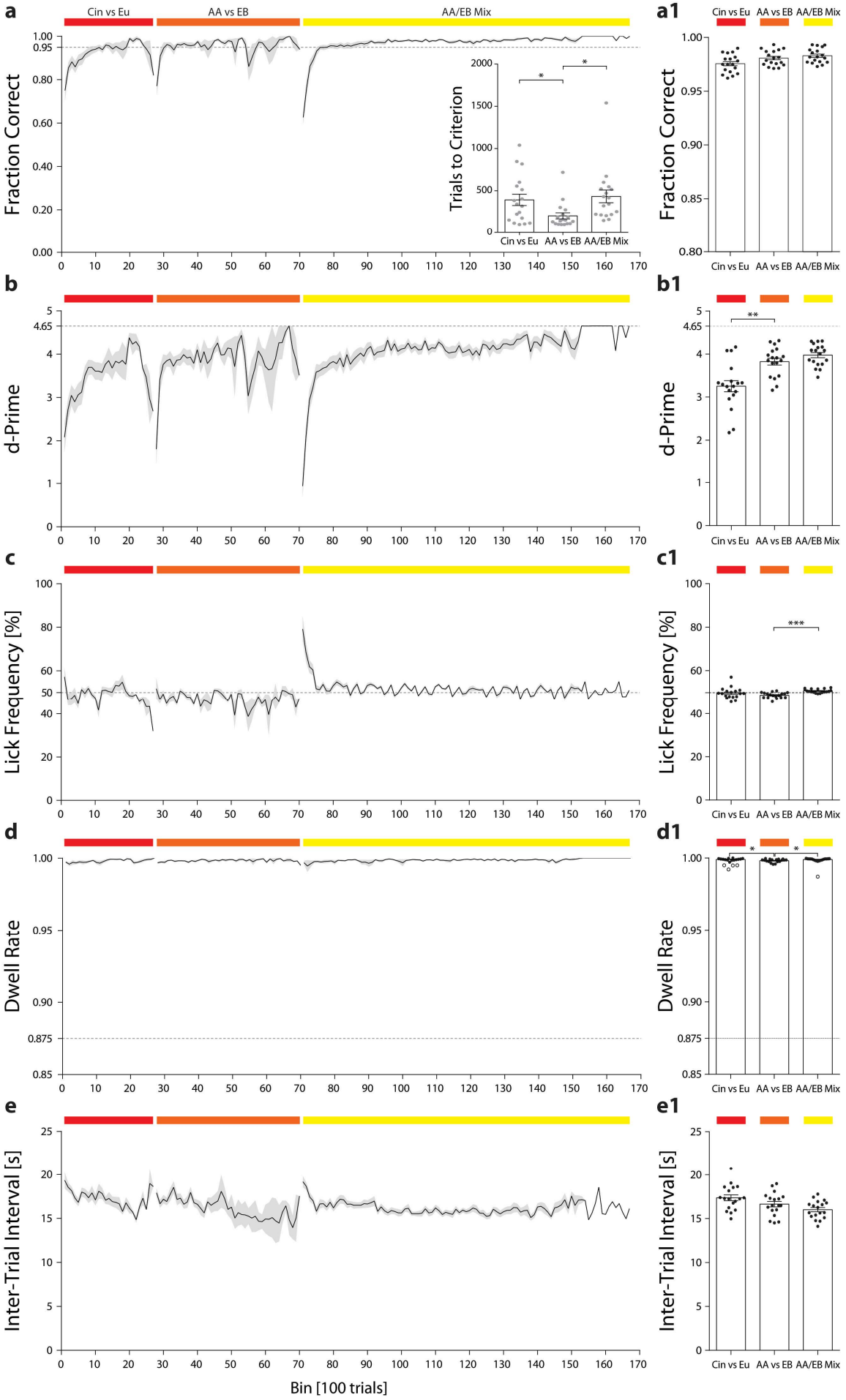
a
Cin vs Eu
AA vs EB
AA/EB Mix
Fraction Correct
Trials to Criterion
a1
b
d-Prime
b1
c
Lick Frequency [%]
c1
d
Dwell Rate
d1
e
Inter-Trial Interval [s]
e1
Bin [100 trials]

Figure 16 Performance with odour cues for a larger cohort of animals. Detailed breakdown of discrimination performance showing **(a)** fraction of correct trials with inset showing trials to criterion, **(b)** d-prime, **(c)** fraction of trials at which the animals licked (lick frequency), **(d)** dwell rate prior to final valve opening and the **(e)** inter-trial interval (ITI) over seventeen-thousand trials with presentation of odour cues in different combinations and at different concentrations. Animals were presented with cineole or eugenol (Cin vs Eu, red bar), amyl acetate or ethyl butyrate (AA vs EB, orange bar), a mixture of amyl acetate and ethyl butyrate (AA/EB Mix, yellow bar). Line plots show mean ± SEM. **(a)** Inset shows trials to criterion (mean ± SEM) while grey dots show values of individual animals (n=18). Dashed line in **(a)** shows the performance threshold while the dashed line in **(b)** shows the maximal possible d-prime score. **(a1)/(b1)/(c1)/(d1)/(e1)**: Bars show mean ± SEM of all supra-threshold bins per odour pair while dots show averages for individual animals. Circles shows potential outliers as identified by ROUT test.

Furthermore, we sought to determine, if this new setup could also be used to accurately determine the discrimination time (DT) of the animals, i.e. the time required to distinguish to different odours and elicit a behavioural response based upon this odour discrimination. As established by Abraham et al. in 2004, the DT is determined by comparing the sampling behaviour for rewarded and unrewarded trials using a point-wise t-test[81]. The DT is defined as the time point, at which the p-value of the t-test reaches the threshold of 0.001, indicating that the sampling behaviour for rewarded and unrewarded trials became significantly different at this time. Using this metric, we found an increased DT for differentiation of complex binary odour mixtures compared to the easier task of discriminating pure odours (AA vs EB: 408.4ms ± 14.85; AA/EB Mix: 448.5ms ± 10.39; paired t-test, p=0.01; Figure 17).

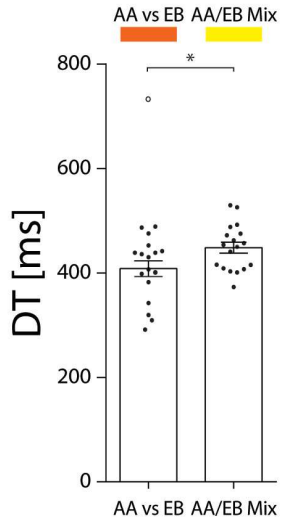

Figure 17 Determination of the discrimination times (DT) for simple and complex odour discrimination tasks. Animals showed a significant increase in the DT for the discrmination of the mixture of amyl acetate and ethyl butyrate compared to the time necessary to discriminate the pure unmixed odours (AA vs EB: 408.4ms ± 14.85; AA/EB Mix: 448.5ms ± 10.39; paired t-test, p=0.01). Bar graphs show mean SEM while dots denote values for individual animals (n=18). Circle shows potential outlier as identified by ROUT test.

Effects of group size on olfactory conditioning

Effect of group size on accuracy and daily activity

To test the effect of different group sizes on the accuracy of odour discrimination, animals were randomly removed from the group after a stable performance baseline for the discrimination of a binary mixture of amyl acetate and ethyl butyrate had been reached. Since analysing the accuracy as a function of training

duration does not account for the number of trials performed, the values will differ from the binned analysis of the same data.

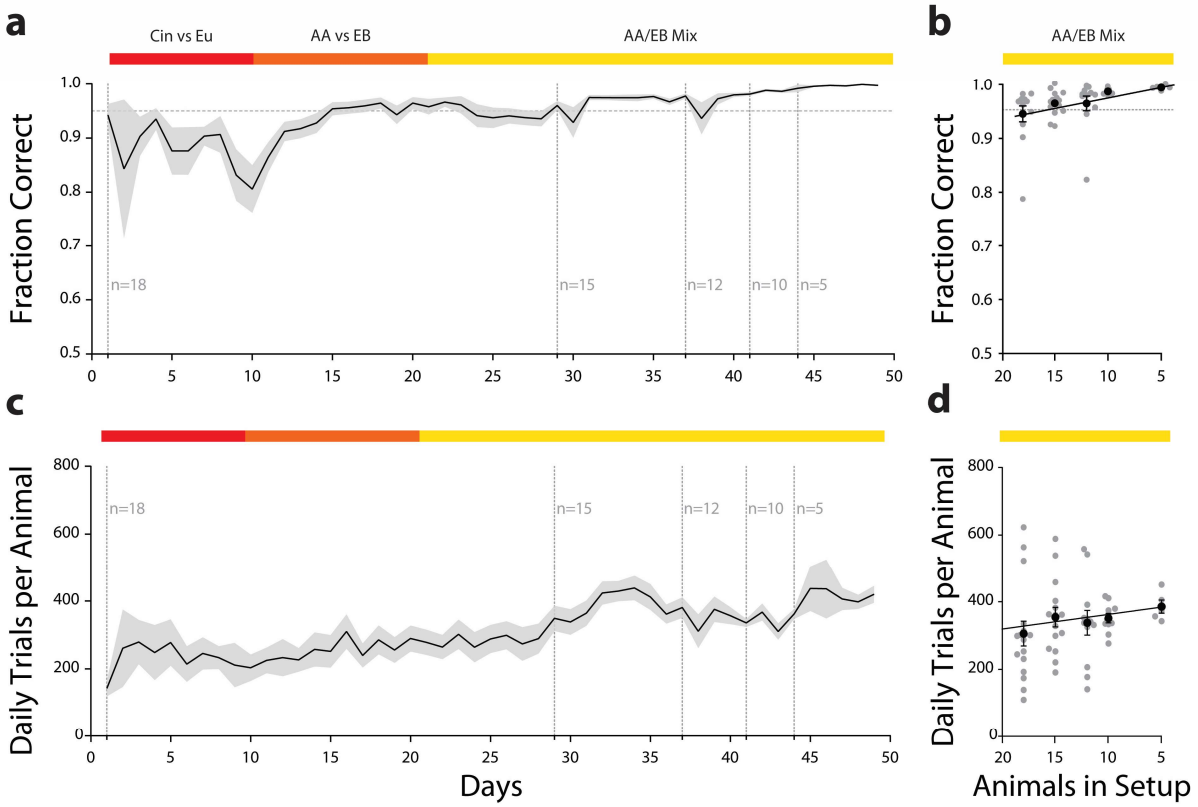

Figure 18 Effect of varying group size on accuracy and trial numbers. (a) Daily discrimination accuracy over time with reduction of group size. **(b)** Discrimination accuracy as a function of the animals in the setup. **(c)** Number of daily trials over time with successive reduction of group size. **(d)** Number of trials per animal as a function of animals in the setup. Animals were presented with cineole or eugenol (Cin vs Eu, red bar), amyl acetate or ethyl butyrate (AA vs EB, orange bar), a mixture of amyl acetate and ethyl butyrate (AA/EB Mix, yellow bar). (n=18 to 5 as indicated). **(a)/(c)**: Mean ± SEM. **(b)/(d)**: Black dots show group mean ± SEM, grey dots show mean for individual animals and black line shows best fit for the individual values.

For the initial odour pair (cineole vs eugenol) the daily accuracy remained below the threshold of 95% (overall mean: 82.67% ± 3.30) with large inter-animal and inter-day variability (Figure 18a; minimal performance: 33.33%; maximal performance: 100%). For the second odour pair (amyl acetate vs ethyl butyrate), the performance gradually increased and subsequently remained around the threshold of 95% (average performance after reaching criterion: 95.68% ± 0.30). Lastly, for the binary mixture of amyl acetate and ethyl butyrate, the daily performance started at the criterion and remained well above it for the remainder of the training (overall average performance: 96.91% ± 0.40).

Concerning the daily activity (Figure 18c), we also observed both a large inter-animal as well as a large inter-day variability for the initial odour pair (overall mean: 210.30 trials ± 29.11; minimal number of trials: 2; maximal number of trials: 709). Interestingly, the number of daily trials for the subsequent odours prior to the removal of animals showed a similar fluctuation as well as a steady increase of daily trials (AA vs EB: overall mean: 247.42 trials ± 33.18; minimal number of trials: 9; maximal number of trials: 960; AA/EB Mix:

overall mean 280.80 trials ± 34.22; minimal number of trials: 16; maximal number of trials: 762). The steady increase in trials over time may be explained by the increased accuracy which reduces the additional time punishment for incorrect trials allowing the animals to initiate more trials in the same time span.

Random removal of animals from the original test cohort showed a strong positive correlation of the average daily performance with reduced group size (Figure 18b; Pearson correlation coefficient r=-0.93; p=0.022; slope -0.49), yet the overall performance increase was found to be negligibly small (fraction correct n=5: 0.99; Fraction correct n=18: 0.93). Similarly, we observed a strong positive correlation between the mean daily trial number and the reduced group size (Figure 18d; average daily trials n=5: 385.76 trials ± 19.38; n=18: 305.71 trials ± 36.75; Pearson correlation coefficient r=-0.88; p=0.049: slope=-5.124).

Most importantly, the reduced group size lead to a significantly reduced inter-animal variance both in the performance (coefficient of variation (CV); n=5: 0.45%; n=18: 6.35%; F(4,14)=179.3, p=0.0001) as well as in the daily trial number (CV n=5: 11.23%; CV n=18: 49.74%; F(4,14)=12.33, p=0.0262).

Effect of daily activity on learning speed

To determine if the daily activity had any effect on the acquisition of the discrimination task, we analysed the performance separately for animals with low (<250 trials per day) or high (>250 trials per day) daily activity. While there was some variability between the learning curves for the two initial odours, the acquisition of the third odour pair (binary mixture of amyl acetate and ethyl butyrate) was virtually identical between the two groups (two-way ANOVA; Cin vs Eu: F(1, 16)=1.36, p=0.26; AA vs EB: F(1, 16)=0.19, p=0.67; AA/EB Mix: F(1, 16)=0.09, p=0.77; Figure 19a). This is also reflected in the trials required to reach the criterion performance, which showed no difference between the groups for any odour pair (Figure 19b; Cin vs Eu: low: 418.8 trials ± 89.55; high: 365.4 trials ± 104.4; AA vs EB: low: 165.8 trials ± 18.93; high: 129.6 trials ± 16.2; AA/EB Mix: low: 405.8 trials ± 57.6; high: 326.4 trials ± 56.20). Within both groups we found an appreciable difference in trials requires to reach the performance criterion for the discrimination of the binary mixture of amyl acetate and ethyl butyrate compared to the pure odours (paired t-test; low: p=0.005; high: p=0.017; Figure 19b), consistent with the increasing difficulty of discriminating complex mixtures. Interestingly, there was no difference in the variance between the groups (Cin vs Eu: low: 64.15%; high: 85.68%; F-test: F(8, 8)=1.36, p=0.68; AA vs EB: low: 32.31%; high: 33.08%; F-test: F(7, 6)=1.56, p=0.60; AA/EB Mix: low: 42.59%; high: 48.70%; F-test: F(7, 7)=1.85, p=0.44), indicating that the daily activity had no influence on the initial acquisition of the odours. Regarding the supra-threshold performance after initially reaching the performance criterion, we found no difference between the groups across all odour pairs (Figure 19c; Cin vs Eu: low: mean: 97.26% ± 0.267; CV: 0.82%; high: mean: 97.65% ± 0.29; CV: 0.88%; AA vs EB: low: mean: 97.51% ± 0.12; CV: 0.38%; high: mean: 98.15% ± 0.22; CV: 0.67%; AA/EB Mix: low: mean: 98.20% ± 0.26; CV: 0.81%; high: mean 98.39% ± 0.19; CV: 0.58%). Intra-group analysis showed an appreciable change in performance only for the low-activity group between the binary mixture of amyl acetate and ethyl butyrate compared to the pure odours (paired t-test, low: p=0.011; high: p=0.369; Figure

19c), indicating a possible effect of low daily activity on high-performance odour discrimination of complex mixtures.

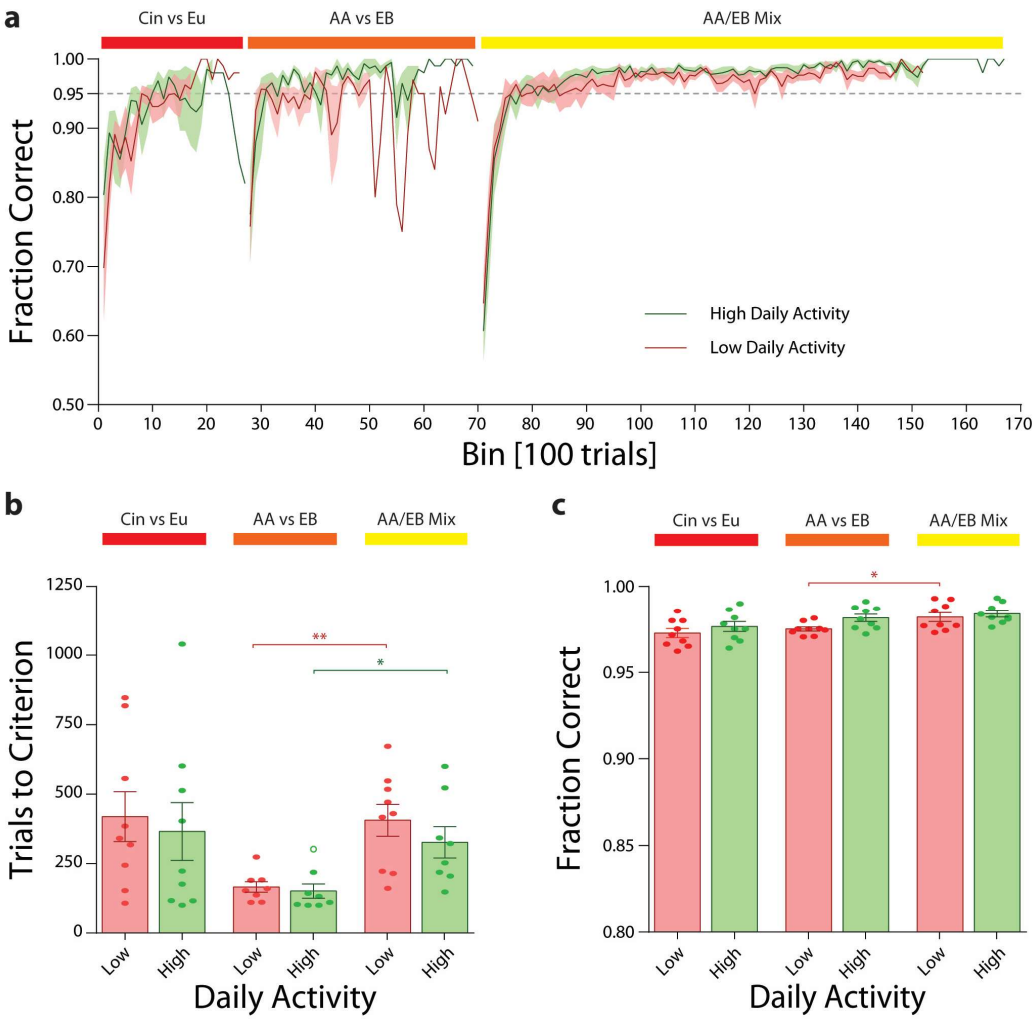

Figure 19 Effect of daily activity on acquisition of odour discrimination. (a) Binned discrimination accuracy for animals with low (red; <250 trials per day; n=9) or high (green; >250 trials per day; n=9) daily activity. **(b)** Trials to criterion of 95% accuracy and **(c)** average supra-threshold performance. Animals were presented with cineole or eugenol (Cin vs Eu, red bar), amyl acetate or ethyl butyrate (AA vs EB, orange bar), a mixture of amyl acetate and ethyl butyrate (AA/EB Mix, yellow bar) **(a)**: Lines show mean ± SEM and dashed line denotes performance threshold. Note: due to the variation in overall trial numbers, some bins were only completed by as little as one animal, hence no error could be determined if less than two animals reached a given bin. **(b)/(c)**: Bar graphs show group mean ± SEM, dots show mean for individual animals (n_{low}=9; n_{high}=9) while circles denote potential outliers as identified by ROUT test.

Effect of group size on distribution of trials

As crepuscular animals, mice are prone to higher night-time activity which is why manual olfactometry is typically conducted only during the dark phase of the day/night cycle. As the automated setup allows

animals to freely choose the time point of trial initiation, we sought to analyse if the activity phase or the performance were impacted by this experimental strategy.

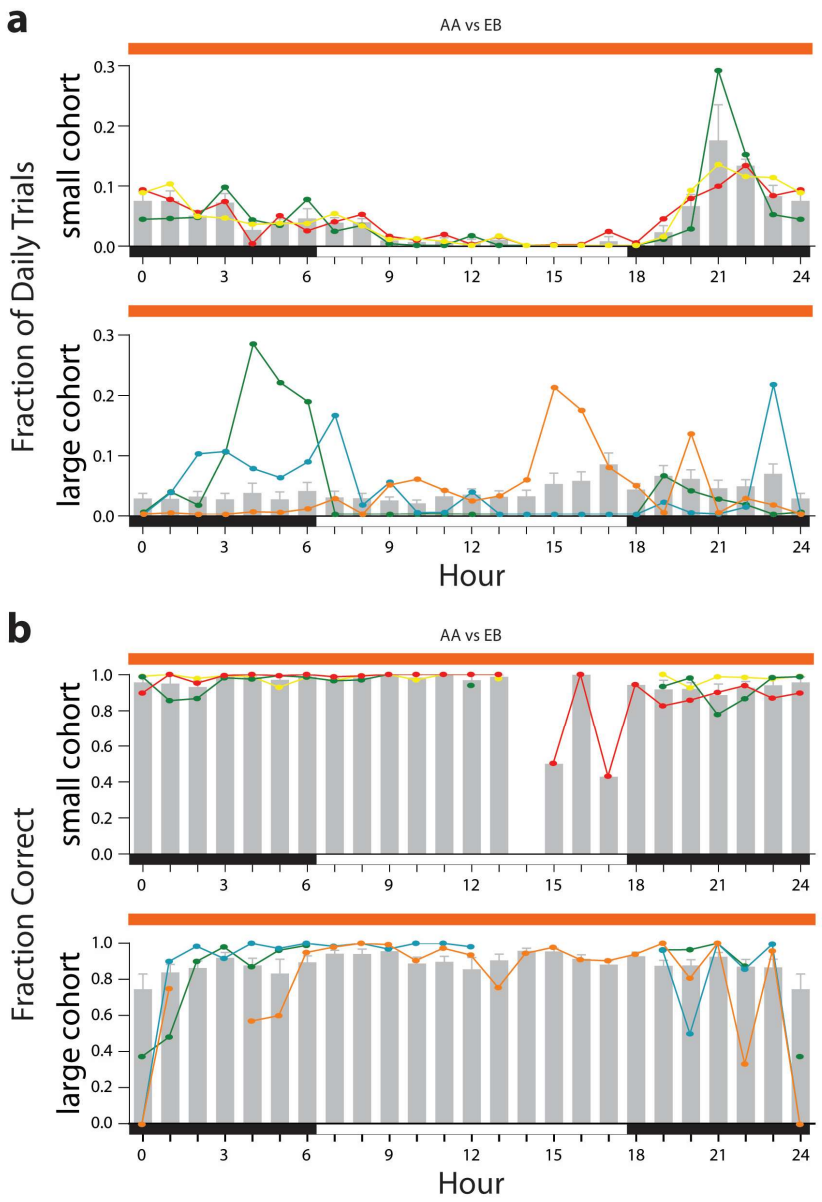

Figure 20 Effect of group size on distribution of daily trials. (a) Average fraction of daily trials for a small cohort (top; n=3) compared to a large cohort (bottom; n=18). Exemplary traces showing the fractions of daily trials of three individual animals per cohort with distinct activity peaks for each animal (top: green, yellow and red; bottom: blue, orange and purple). **(b)** Average performance per hour across all animals in a small cohort (top; n=3; same as in **(a)**) compared to a large cohort (bottom; n=18; same as in **(a)**). Black and white bars denote the dark and light phases of the day-night cycle (6PM till 6AM). Grey bars denote group averages ± SEM. Note that hour 0 and hour 24 are identical and duplicated for display purposes only.

In a small cohort (Figure 20a, top; n=3), mice did indeed show their highest activity during the dark phase with the activity peaking in the fourth hour of the night phase (maximal fraction of trials: 17.6% ± 5.9). This is also reflected in the activity patterns for the individual animals, which all showed their peak activity in

the fourth or fifth hour of the night phase and had a clearly reduced activity during the day phase. Some hours even showed no trial initiation for any of the animals (i.e. hour 14). In a large cohort (Figure 20a, bottom; n=18), however, the activity was distributed more evenly throughout the day, peaking in the 17th hour of the day phase, just prior to the start of the night cycle (maximal fraction of trials: 8.57% ± 1.91). In contrast to the small group, trials were performed throughout the entire day, yet individual animals showed clear preferences for certain hours. This could be due to the animals competing for the single available odour port, hence some animals may shift their activity from the dark phase to a time at which other animals do not frequent the odour port, resulting in distinct activity phases for each animal.

Considering the hourly performance, the only substantial changes for the smaller group occurred during times at which few or no trials were performed (i.e. hour 13 through 16; Figure 20b, top). These drops in performance hence are most likely not true time-dependent deviations but rather caused by the lack of trials. Data outside of these time points, revealed a consistently high performance across all animals with only minor deviations (mean hourly performance: 96.13% ± 0.66). Similarly, the large group (Figure 20b, bottom) showed no gross overall changes (mean hourly performance: 88.61% ± 1.09) with animals performing above threshold across the entire day. As with the smaller group, ostensible drops in performance occurred at time points at which the animals performed very few trials resulting in artificially lower hourly performances due to the lack of trials. It is important to note, that due to the differing activity peaks of the individual animals, any given hour may show multiple animals with drops in performance due to lack of trials, which in sum results in a lowered average performance. Removing the time points where an animal performed less than 5% of its daily trials already raised the average performance per hour while noticeably decreasing the variance (mean hourly performance: 92.47% ± 0.84; data not shown).

In summary, we established an automated behaviour setup, capable of training even large cohorts of animals in an automated fashion. Despite some observed differences dependant on the group size, we were able to replicate the increase in discrimination times reported for the discrimination of complex odour mixtures compared to the discrimination of pure odours[61,81,132]. Hence, this setup was used for all subsequent behavioural tests.

Part 2: Influence of increased neurogenesis on odour discrimination

To investigate the influence of increased inhibition in the olfactory bulb network on odour discrimination, the so-called 4D transgenic mouse line was chosen. In these mice, the expression of the cell cycle regulatory proteins Cdk4 and cyclin D1 (4D) can be increased in a precisely controlled manner (Figure 21).

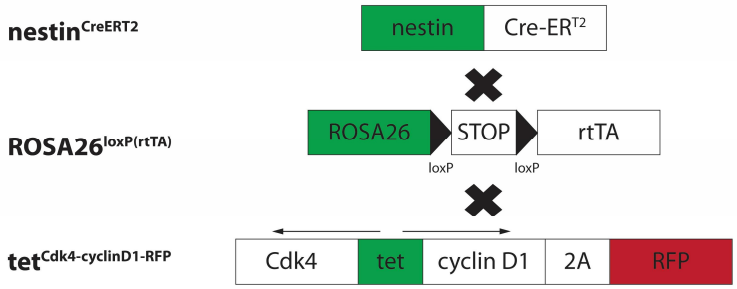

Figure 21 Schematic representation of the 4D transgenic mouse model. The 4D mouse line was generated by crossing three mouse lines (respective promoters highlighted in green). Application of tamoxifen allows for the translocation of Cre-recombinase (Cre-ER^{T2}) into the nucleus causing expression of the reverse tetracycline-controlled transactivator (rtTA) through removal of the stop-codon. Subsequent doxycycline application results in the bicistronic expression of the cell cycle regulators Cdk4 and cyclin D1 as well as the RFP fluorophore (red). Modified from[169] with permission from the publisher.

This is achieved through combination of three different mouse lines: First, in the nestin^{CreERT2} mouse line, the tamoxifen-inducible Cre-ER^{T2} recombinase is expressed under the control of the nestin promoter. Secondly, crossing of the nestin^{CreERT2} line with the ROSA26$^{loxP(rtTA)}$ line leads to the expression of the reverse tetracycline-controlled transactivator (rtTA) under the control of the ROSA26 promoter upon application of tamoxifen. Lastly, crossbreeding with the tet$^{Cdk4\text{-}cyclinD1\text{-}RFP}$ mouse line and application of doxycycline allows for the efficient binding of the rtTA resulting in the expression of the cell cycle regulatory proteins and a red fluorophore (RFP). Notably, the regulatory proteins are expressed from the tet-promoter in a bicistronic fashion while the fluorophore is originally fused to cyclin D1 and separated by virtue of the 2A self-cleaving peptide.

Biomolecular characterization of 4D expression in the olfactory system

As chronic 4D overexpression during embryonic development has previously been shown to enhance neurogenesis and can lead to a 42% increase in brain volume (see[168]), we sought to use this system exclusively in the adult context to selectively increase neurogenesis in the olfactory system. Towards this aim, 4D mice were administered tamoxifen for three consecutive days followed by four days of rest for full removal of the drug (Figure 22a). Subsequently, mice were given doxycycline for 4 days to trigger the expression of the regulatory proteins, which could be directly visualized through the co-expression of the fluorophore. Despite this short induction time, fluorescently labelled cells could be detected in the subventricular zone (SVZ) as well as along rostral migratory stream (RMS) but had not yet reached the OB (Figure 22a and b; Supplementary Figure 17). Importantly, no RFP signal was observed in the dentate gyrus

(DG) or the olfactory epithelium, two regions known for the presence of nestin-positive cells as well as the occurrence of adult neurogenesis. This indicates, that the modified induction protocol successfully limited the expression of the transgenes to the areas giving rise to olfactory bulb interneurons.

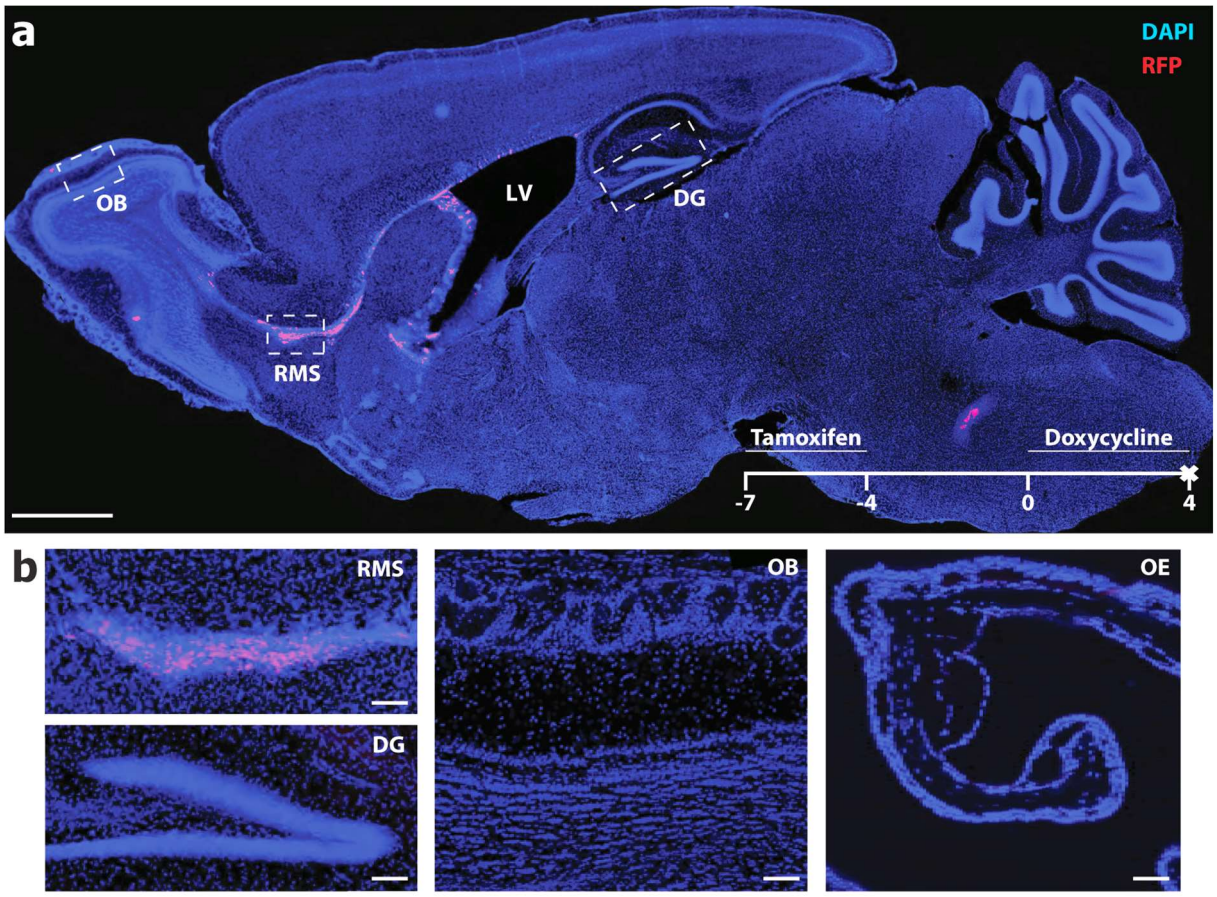

Figure 22 Characterization of the 4D transgenic model. **(a)** Representative sagittal section of a 4D animal showing the RFP signal (red) and the DAPI (blue) counterstaining. Note the confinement of the RFP signal to the rostral migratory stream (RMS) and the subventricular zone (SVZ). OB: olfactory bulb. RMS: rostral migratory stream. LV: lateral ventricle. DG: dentate gyrus. Scale: 500µm. **(b)** Higher magnification images of the areas highlighted in **(a)**. OE: olfactory epithelium. Scale: 100µm. Modified from[169] with permission from the publisher.

Previous studies have shown that adult-born cells integrating into the OB are mostly NeuN-positive GABAergic GC that migrate into the GCL[163,183]. Additionally, a smaller number of cells have been shown to migrate into the GL and can be divided into three mutually exclusive groups expressing either calbindin (CalB), calretinin (CalR) or tyrosine hydroxylase (TH)[45]. To assess the fate of the 4D-derived adult-born cells on a behaviourally and physiologically relevant timescale, the common paradigm was used consisting of simultaneous administration of doxycycline and BrdU for four days followed by sacrificing of the animals either after one or two months (Figure 23a and c). Adult-born cells were identified by the incorporation of BrdU, a synthetic analogue of the nucleoside thymidine, into newly synthesised DNA strands. These cells were subsequently further classified according to the expressed cellular markers (Figure 23b and d).

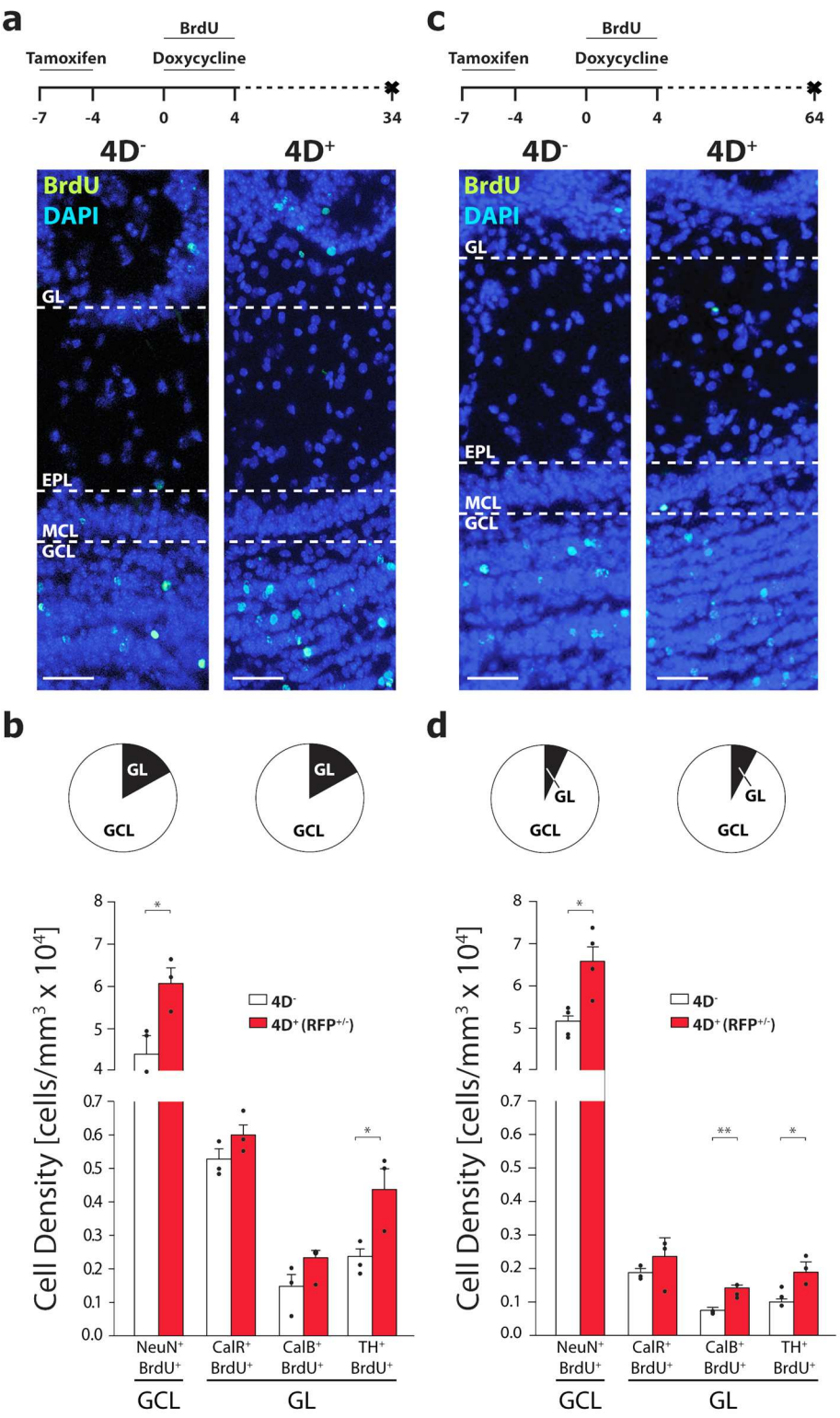

Figure 23 Long-term effect of 4D overexpression on OB neurogenesis. **(a)** Experimental timeline and representative images of olfactory bulb sections stained against BrdU (green) and DAPI (blue) one month post induction. **(b)** Proportion (pie charts) and density (bar graphs) of marker positive cells in $4D^-$ (white) and $4D^+$ (red) animals one month post induction. Note that the cells in the $4D^+$ animals include both RFP positive and negative cells due to use of BrdU as a marker. N_{Mice} = 3, n_{Cells} > 285 per quantification. **(c)** Analogous to **(a)** with animals two months post induction. **(d)** Analogous to **(b)** with animals two months post induction. N_{Mice} = 3, n_{Cells} > 210 per quantification. **(a)**/**(c)** Scale: 50µm. **(b)**/**(d)**: Bar graphs show mean ± SEM, dots show mean for individual animals. Modified from[169] with permission from the publisher.

Using this paradigm, we observed widespread distribution of RFP-positive cells in $4D^+$ animals (data not shown; see[169]) as well as integration of BrdU-positive cells in both the GCL and the GL for both genotypes. Interestingly, the proportional distribution of cells between GCL and GL did not differ between the $4D^+$ and $4D^-$ animals neither one month ($4D^-$: 82.2% ± 2.2 vs 17.2% ± 2.2; $4D^+$: 82.6% ± 1.3 vs 17.4% ± 1.3; Fisher's exact test, p=1.0) nor two months ($4D^-$: 93.1% ± 0.4 vs 6.9%; $4D^+$: 92.2% ± 0.5 vs 7.8%; Fisher's exact test, p=1.0) post induction. We further sought to identify the identity of these BrdU-labelled cells based on the presence or absence of well-established markers. We used NeuN to identify mature granule cells and found a significant increase of these cells in the GCL one month after induction (Figure 23b; $4D^-$: 4.42×10^4 cells/mm^3 ± 0.46; $4D^+$: 6.05×10^4 cells/mm^3 ± 0.36; unpaired t-test, $p<0.05$) which persisted even two months after induction (Figure 23d; unpaired t-test, $p<0.001$). Concerning PGCs integrating into the GL, we assessed the populations of calretinin (CalR), calbindin (CalB) and tyrosine hydroxylase (TH) expressing cells. One month after induction, we found a significant increase of TH-positive cells ($4D^-$: 0.23×10^4 cells/mm^3 ± 0.03; $4D^+$: 0.44×10^4 cells/mm^3 ± 0.07; unpaired t-test, $p<0.05$) as well as smaller but appreciable increases in CalR-positive ($4D^-$: 0.52×10^4 cells/mm^3 ± 0.21; $4D^+$: 0.60×10^4 cells/mm^3 ± 0.35; unpaired t-test, $p>0.05$) and CalB-positive cells ($4D^-$: 0.15×10^4 cells/mm^3 ± 0.42; $4D^+$: 0.23×10^4 cells/mm^3 ± 0.26; unpaired t-test, $p>0.05$). Likewise, we found a significant increase in both TH-positive cells ($4D^-$: 0.11×10^4 cells/mm^3 ± 0.16; $4D^+$: 0.20×10^4 cells/mm^3 ± 0.20; unpaired t-test, $p<0.05$) as well as CalB-positive cells ($4D^-$: 0.77×10^4 cells/mm^3 ± 0.03; $4D^+$: 0.13×10^4 cells/mm^3 ± 0.09; unpaired t-test, $p<0.05$) two months post induction. Similarly to the one-month induction, we found a small but not significant increase in CalR-positive cells ($4D^-$: 0.19×10^4 cells/mm^3 ± 0.16; $4D^+$: 0.23×10^4 cells/mm^3 ± 0.51; unpaired t-test, $p>0.05$).

It is important to note, that while the overwhelming majority of RFP expressing cells in the SVZ of $4D^+$ were BrdU-positive (Supplementary Figure 17b), only about half of the stem and progenitor cell population was found to exhibit RFP expression (data not shown; see[169]), hence the full effect of the 4D overexpression may even be greater than assessed. Yet, these initial results clearly indicate the successful limitation of increased 4D expression to the olfactory system as well as the successful increase of neurogenesis in the olfactory bulb. Moreover, these supernumerary neurons were still detectable even two months post induction of 4D overexpression, making this induction paradigm feasible for long-term behavioural studies. Lastly, electrophysiological recordings of 4D-derived cells and age-matched natively generated granule cells revealed that 4D-expressing GCs were functionally integrated into the olfactory bulb circuitry and were indistinguishable from their native counterparts (Supplementary Figure 18; see[169]). Furthermore, all of the tested values were well within the ranges reported for murine GCs, indicating not only no appreciable difference between 4D-derived cells and their natively generated counterparts but also the absence of (adverse) effects of the genetic background of the (multiple transgenic) mice[184].

Behavioural effects of increased neurogenesis in the olfactory system

As the supernumerary neurons appeared to be both functionally integrated as well as physiologically indistinguishable from natively generated adult-born granule cells, we sought to determine the effect of increased neurogenesis on odour discrimination. Therefore, two independent cohorts of $4D^+$ and littermate $4D^-$ animals were trained on a go/no-go odour discrimination task.

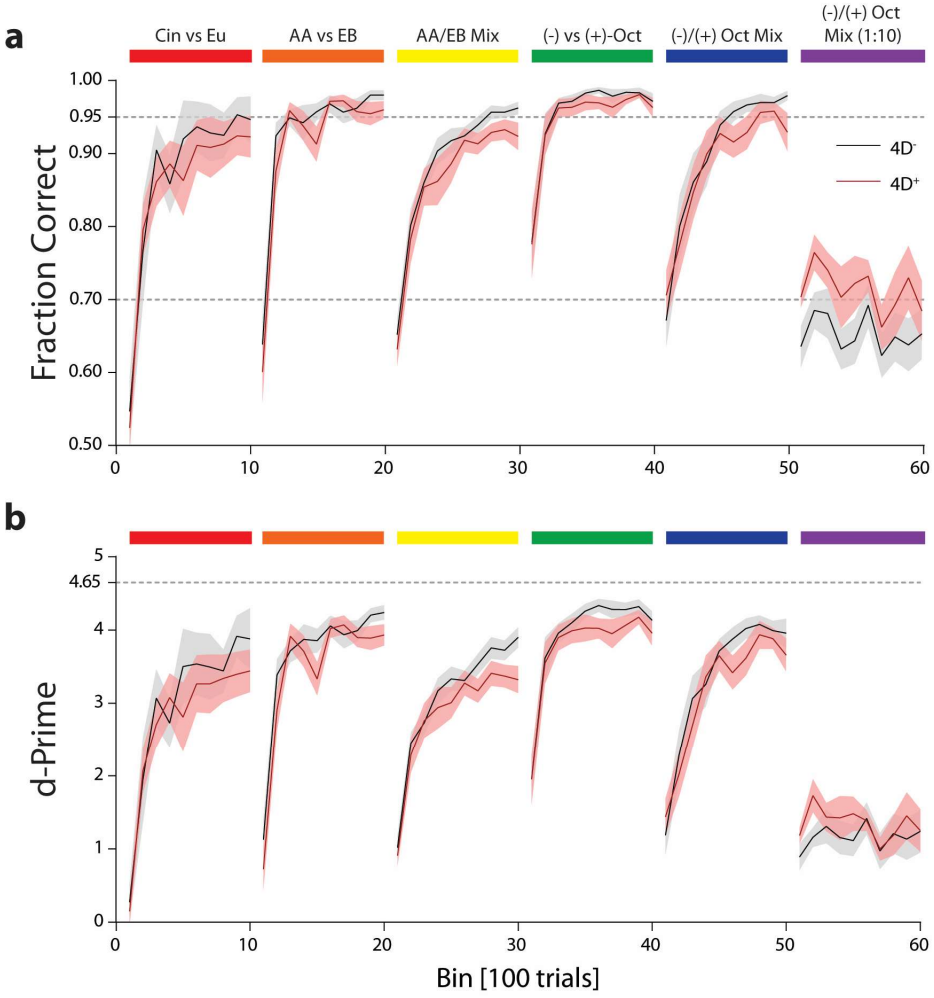

Figure 24 Effect of the 4D transgene on odour discrimination. (a) Discrimination accuracy and **(b)** d-prime scores of $4D^-$ (black) and 4D+ (red) animals for the initial 1000 trials initiated for each odour pair. Animals were presented with cineole or eugenol (Cin vs Eu, red bar), amyl acetate or ethyl butyrate (AA vs EB, orange bar), a mixture of amyl acetate and ethyl butyrate (AA/EB Mix, yellow bar), (-)-octanol or (+)-octanol ((-) vs (+)-Oct, green bar), a mixture of (-)-octanol and (+)-octanol ((-)/(+) Oct Mix, blue bar) and a 1:10 dilution of the mixture of the two enantiomers ((-)/(+) Oct Mix (1:10), purple bar). Group sizes: Cin vs Eu: $4D^-$: n=6; $4D^+$: n=7; (-)/(+) Oct Mix (1:10): $4D^-$: n=15; $4D^+$: n=10; remaining odours: $4D^-$: n=21; $4D^+$: n=17. Lines show mean ± SEM. Dashed lines in **(a)** show the threshold performance for the initial 5 odours (95%) and the dilution of the enantiomer mix (70%). Dashed line in **(b)** shows the maximal possible d-prime score. Modified from[169] with permission from the publisher.

Mice of both genotypes were able to acquire the discrimination task and distinguish all odours except for a dilution of a binary enantiomer mixture at high accuracy with no evident difference between the groups (two-way ANOVA,: Cin vs Eu: $F(1, 11)=0.228$, $p=0.64$; AA vs EB: $F(1 ,36)=0.88$, $p=0.35$; AA/EB Mix: F(1,

36)=1.95, p=0.17; (-) vs (+) Oct: F(1, 35)=0.45, p=0.51; (-)/(+) Oct Mix: F(1, 34)=0.20, p=0.66; (-)/(+) Oct Mix (1:10): F(1, 21)=3.07, p=0.09; Figure 24a).

This is also reflected in the d-prime scores, which consistently reached levels of ≥3 for all odour pairs with the exception of the diluted enantiomer mixture with no differences being apparent between the genotypes (two-way ANOVA,: Cin vs Eu: F(1, 11)=0.43, p=0.53; AA vs EB: F(1 ,36)=1.45, p=0.24; AA/EB Mix: F(1, 36)=2.77, p=0.10; (-) vs (+) Oct: F(1, 35)=1.15, p=0.29; (-)/(+) Oct Mix: F(1, 34)=0.36, p=0.55; (-)/(+) Oct Mix (1:10): F(1, 21)=0.41, p=0.57; Figure 24b).

As all animals failed to reach our established performance criterion of 95% or d-prime scores ≥2 for the diluted enantiomer mixture, we limited the in-depth analysis on the remaining odour pairs. Here we again found that the second odour pair (AA vs EB; Figure 25a) was acquired faster than the initial odour pair (Figure 25a; trials to criterion Cin vs Eu: $4D^-$: 513.3 trials ± 101.2; $4D^+$: 783.7 trials ± 256.3; AA vs EB: $4D^-$: 257.3 trials ± 54.7; $4D^+$: 231.5 trials ± 26.36). Similarly, complex binary mixtures typically required additional trials to reach the performance threshold compared with the easier task of discriminating the pure unmixed odour pairs (AA/EB Mix: $4D^-$: 427.0 trials ± 41.04; $4D^+$: 463.7 trials ± 61.16; (-) vs (+)-Oct: $4D^-$: 243.2 trials ± 74.87; $4D^+$: 219.4 trials ± 38.47; (-)/(+) Oct Mix: $4D^-$: 322.6 trials ± 46.13; $4D^+$: 373.3 trials ± 58.22). We found no differences in task learning between the genotypes for any of the tested odour pairs. After this initial reaching of the criterion performance, the supra-threshold performance was consistently high (≥97%) for all genotypes and odour pairs (Figure 25b). Consistently with this, we found high overall d-prime scores ≥2.5 (Figure 25c) as well as a lick frequency of close to 50% (Figure 25d) for all odours and both genotypes. Lastly, we found a dwell rate prior to the opening of the final valve of nearly 100% (Figure 25e) indicating high motivation of the mice as well as inter-trial intervals of 14-20ms (Figure 25f).

It is noteworthy, that we did observe statistically significant differences for some of these parameters both between the genotypes as well as during comparison of different odour pairs within a genotype (full statistical analyses can be found in Supplementary Table 1 and Supplementary Table 2). Yet, apart from the differences in trials required to reach the performance threshold for the different odours, these changes were subtle at best (i.e. dwell rate AA vs EB: $4D^-$: 0.9994 ± 0.00001; $4D^+$: 0.9996 ± 0.0002). Further, these differences were detected inconsistently and even contradictory in some instances. For example, for the discrimination of the mixture of amyl acetate and ethyl butyrate, we detected a significant difference between the genotypes in the accuracy ($4D^-$: 0.98 ± 0.002; $4D^+$: 0.97 ± 0.002; unpaired t-test, p=0.026) but not in the d-prime score ($4D^-$: 3.09 ± 0.09; $4D^+$: 2.85 ± 0.13; unpaired t-test, p=0.105) nor in the lick frequency ($4D^-$: 51.69% ± 0.46; $4D^+$: 51.33 ± 0.71; unpaired t-test: p=0.657). Similarly, we detected a significant intra-genotype difference for the $4D^+$ animals between the inter-trial interval of the AA/EB Mix compared to the pure enantiomers (AA/EB Mix: 17.43s ± 0.72; (-) vs (+) Oct: 15.71s ± 0.42; paired t-test, p=0.008) while the dwell rate was identical (AA/EB Mix: 0.9997 ± 0.0001; (-) vs (+) Oct: 0.9997 ± 0.0001; paired t-test, p>0.999). Therefore we concluded, that these minor differences are unlikely to reflect true phenotypically relevant differences of the genotypes.

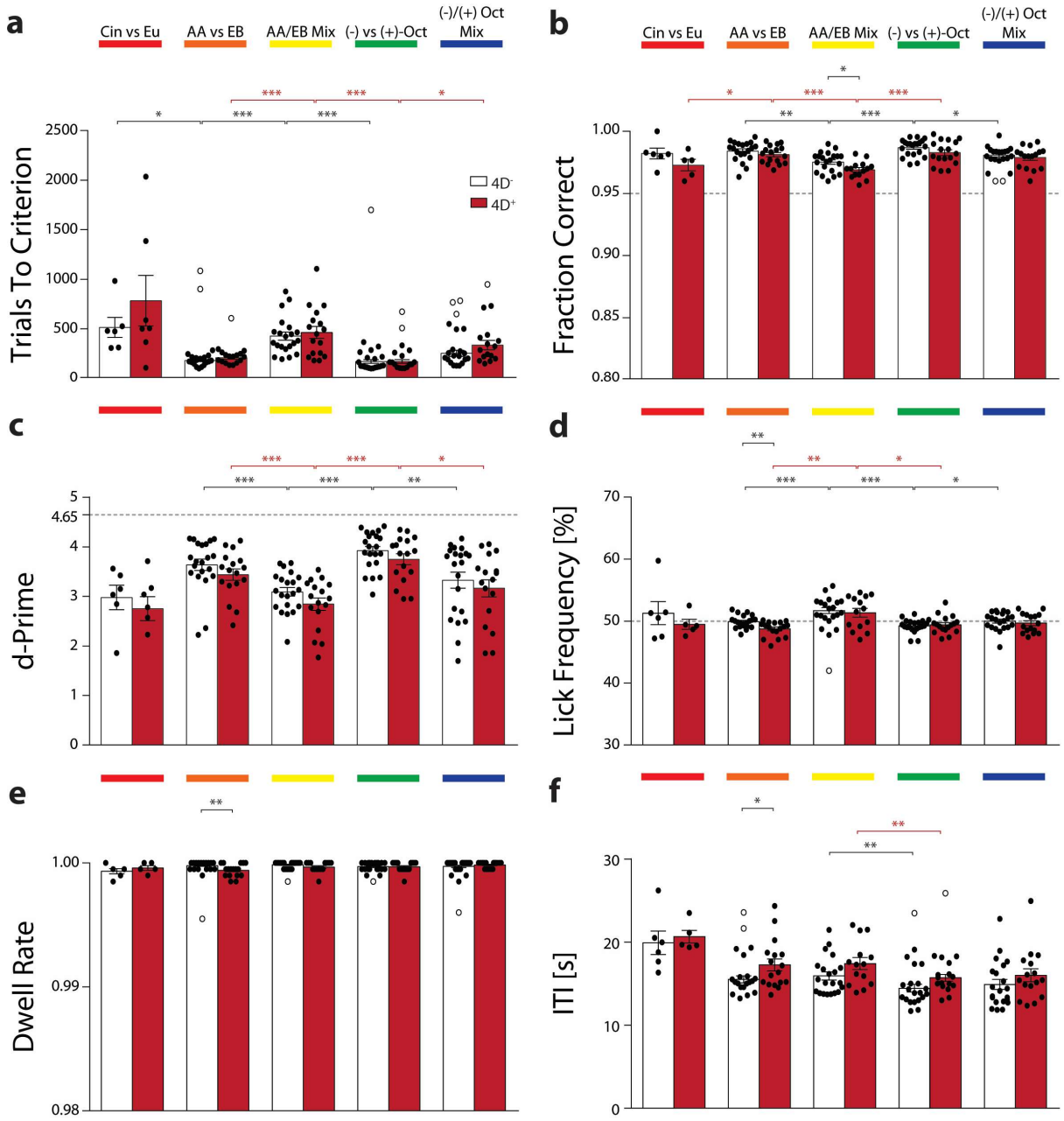

Figure 25 Detailed analysis of the behavioural effect of the 4D transgene on discrimination of different odour pairs. **(a)** Trials to criterion (performance ≥ 95%) for $4D^+$ (red) and $4D^-$ (white) animals. Average **(b)** supra-threshold performance after reaching the criterion, **(c)** d-prime across all trials **(d)** lick frequency, **(e)** dwell rate prior to the opening of the final valve **(f)** inter-trial interval all showed some intra-genotype differences as well as one inter-genotype difference. For complete statistical analysis refer to Supplementary Table 1 and Supplementary Table 2. Bar graphs show mean ± SEM, dots show mean for individual animals while circles show potential outliers as identified by ROUT test. Dashed line in **(b)** shows performance threshold. Dashed line in **(c)** shows the maximal possible d-prime score. Group sizes: Cin vs Eu: $4D^-$: n=6; $4D^+$: n=7; remaining odours: $4D^-$: n=21; $4D^+$: n=17. Modified from[169] with permission from the publisher.

Next we analysed the discrimination time, i.e. the time required to discriminate two different odours from one another, to directly correlate the effect of supernumerary neurons with the speed at which the animals can make their decision (Figure 26). Analogous to the trials needed to reach the performance criterion,

animals required more time to distinguish complex mixtures compared to the respective simple pure odours (AA vs EB: $4D^-$: 448.4ms ± 14.66; $4D^+$: 423.0ms ± 12.71; AA/EB Mix: $4D^-$: 501.9ms ± 16.93; $4D^+$: 530.9ms ± 14.89; (-) vs (+) Oct: $4D^-$: 450.1ms ± 16.51; $4D^+$: 460.9ms ± 21.59; (-)/(+) Oct Mix: $4D^-$: 526.6ms ± 19.24; $4D^+$: 514.0ms ± 16.26) reflecting the increased difficulty of the task. Still, we observed no differences between the genotypes for any of the tested odour pairs, suggesting that the effect of the 4D overexpression may be more subtle than expected.

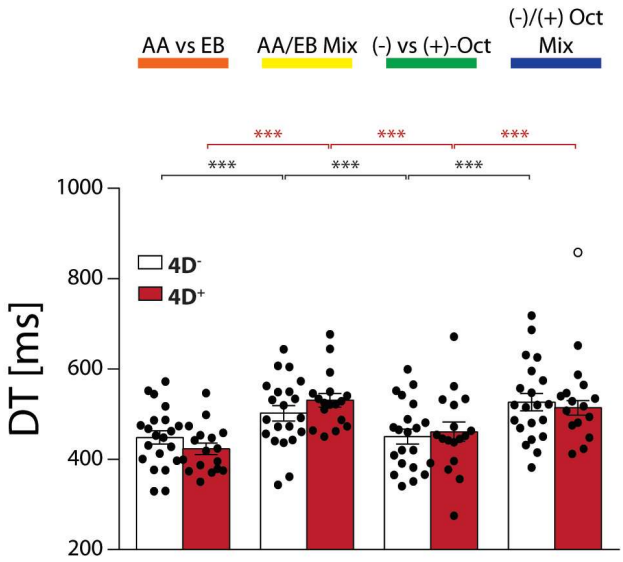

Figure 26 Analysis of the discrimination time. Discrimination times (DTs) of $4D^+$ (red) and $4D^-$ (white) animals measured for pure and mixed odours. Bar graphs show mean ± SEM, dots show mean for individual animals while circles show potential outliers as identified by ROUT test. Group sizes: $4D^-$: n=21; $4D^+$: n=17. Modified from[169] with permission from the publisher.

To tease out any so far undetected minute effects of the 4D-derived neurons, we used the extremely difficult discrimination of the diluted enantiomer mixture to drive the olfactory system of the animals towards its limit. It is crucial to point out, that the animals were on principle still capable of solving the task as evident from the performance of nearly 70% (fraction correct: $4D^-$: 0.69 ± 0.19; $4D^+$: 0.68 ± 0.24; unpaired t-test, p=0.83) and d-prime scores of ≥1 ($4D^-$: 1.53 ± 0.15; $4D^+$: 1.27 ± 0.14; unpaired t-test, p=0.26). Thus we analysed the initial 200 trials of this highly demanding task as a probe, to elucidate the animals' strategy for solving this task. In this probe, $4D^+$ animals showed an increased accuracy compared to the control cohort (fraction correct: $4D^-$: 0.66 ± 0.22; $4D^+$: 0.73 ± 0.19; unpaired t-test, p=0.03; Figure 27a). Closer inspection revealed, that while performance for rewarded trials was similar (fraction correct: $4D^-$: 0.82 ± 0.28; $4D^+$: 0.73 ± 0.52; unpaired t-test, p=0.089; Figure 27b), $4D^-$ animals had a significantly reduced accuracy for unrewarded trials (fraction correct: $4D^-$: 0.50 ± 0.49; $4D^+$: 0.73 ± 0.46; unpaired t-test, p=0.004; Figure 27c). Consistently, the lick rate was elevated in $4D^-$ animals while in $4D^+$ animals it was very close to the 50% lick frequency ($4D^-$: 65.25% ± 3.34; $4D^+$: 49.00% ± 4.76; unpaired t-test, p=0.009) inherent to equal performance for both rewarded and unrewarded trials (Figure 27d). Lastly, we determined the DT using a lowered 70% performance threshold as mice failed to reach the typically used 95%. While we found no difference in the DT between the groups ($4D^-$: 466.2ms ± 20.64; $4D^+$: 469.5ms ± 27.67; unpaired t-test, p=0.923; Figure 27e), the times were considerably faster than the times measured for the undiluted enantiomer mixture and very close to the values determined for the discrimination of the pure enantiomers. As a lower threshold was used to calculate the DT, these values are not directly comparable

to the values determined at ≥95% performance. However, a decreased reaction time is expected for such a difficult task, as animals will inevitably try to maximise their chances of obtaining a reward by reacting faster if performing the task at high accuracy is not feasible[185–187].

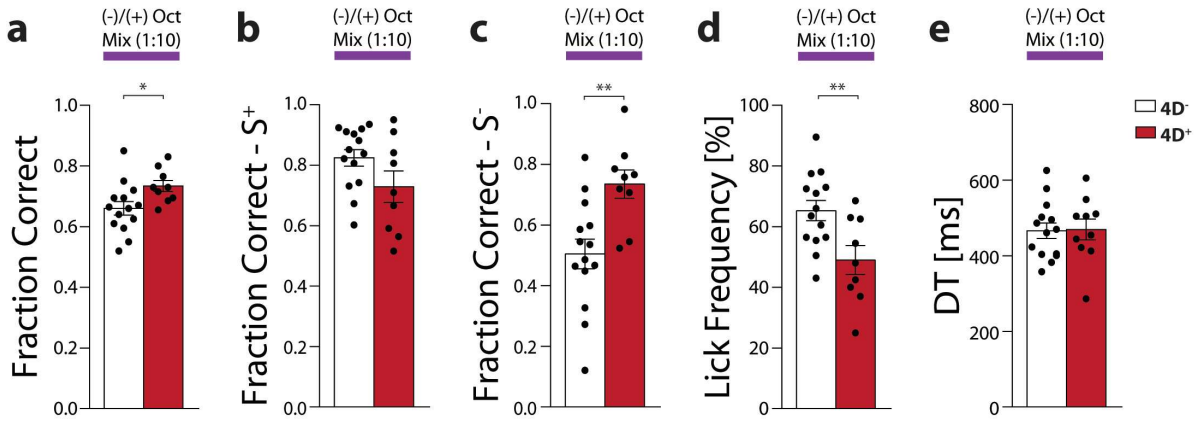

Figure 27 Results of a 200 trial probe using the diluted enantiomer mixture. **(a)** Overall performance of 4D$^+$ animals (red) compared to 4D$^-$ controls (white). **(b)** Performance for rewarded trials only. **(c)** Performance for unrewarded trials only. **(d)** Overall lick frequency for both rewarded an unrewarded trials. **(e)** Discrimination Time (DT) determined using a lowered performance threshold of 70%. Bar graphs show mean ± SEM, dots show mean for individual animals. Group sizes: 4D$^-$: n=15; 4D$^+$: n=10. Modified from[169] with permission from the publisher.

Together these results indicate, that the animals try to maximise the probability of receiving a water reward, yet the two genotypes seem to utilize two different strategies in addition to overall faster reactions: while 4D$^-$ animals increased their lick rate (i.e. resulting in a slightly increased performance for rewarded trials and a clearly reduced performance for unrewarded trials), 4D$^+$ are still capable to perform at similarly high accuracy for both trial types.

Lastly, because neurogenesis in the olfactory bulb has been linked to plasticity and odour memory, we sought to determine whether or not 4D transgenes show any behavioural differences when presented with a previously learned odour task[53–55]. Towards this end, animals in the first cohort were tasked with discriminating pure amyl acetate and ethyl butyrate after being tested on the binary enantiomer mixture (Figure 28). Both genotypes were able to immediately perform well above the performance criterion of 95% (trials to criterion: 4D$^-$: 10.00 trials ± 0.00; 4D$^+$: 10.00 trials ± 0.00; Figure 28a) and the d-prime scores were well above 1 already within the first 10 trials (Figure 28b). We found no difference between the genotypes neither in the discrimination accuracy (two-way ANOVA: $F(1, 9)=1.227$, $p=0.29$) nor the d-prime scores (two-way ANOVA: $F(1, 9)=1.168$, $p=0.31$).

As the animals were able to solve this memory task with evident ease, we challenged the second cohort to discriminate the binary mixture of amyl acetate and ethyl butyrate after having been tested on the diluted binary enantiomer mixture. While the animals did not start above the performance criterion (Figure 28a),

we found no difference in the trials required to reach the criterion ($4D^-$: 27.75 trials ± 4.08; $4D^+$: 43.23 trials ± 6.99) nor in the overall acquisition of the discrimination task (two-way ANOVA: F(1, 22)=0.34, p=0.57). Further, we found no difference in the d-prime scores (two-way ANOVA: F(1, 22)=0.11, p=0.75), all indicating, that the animals were still able to solve this more complex discrimination task even after having been trained on the highly demanding diluted enantiomer mixture for nearly one month.

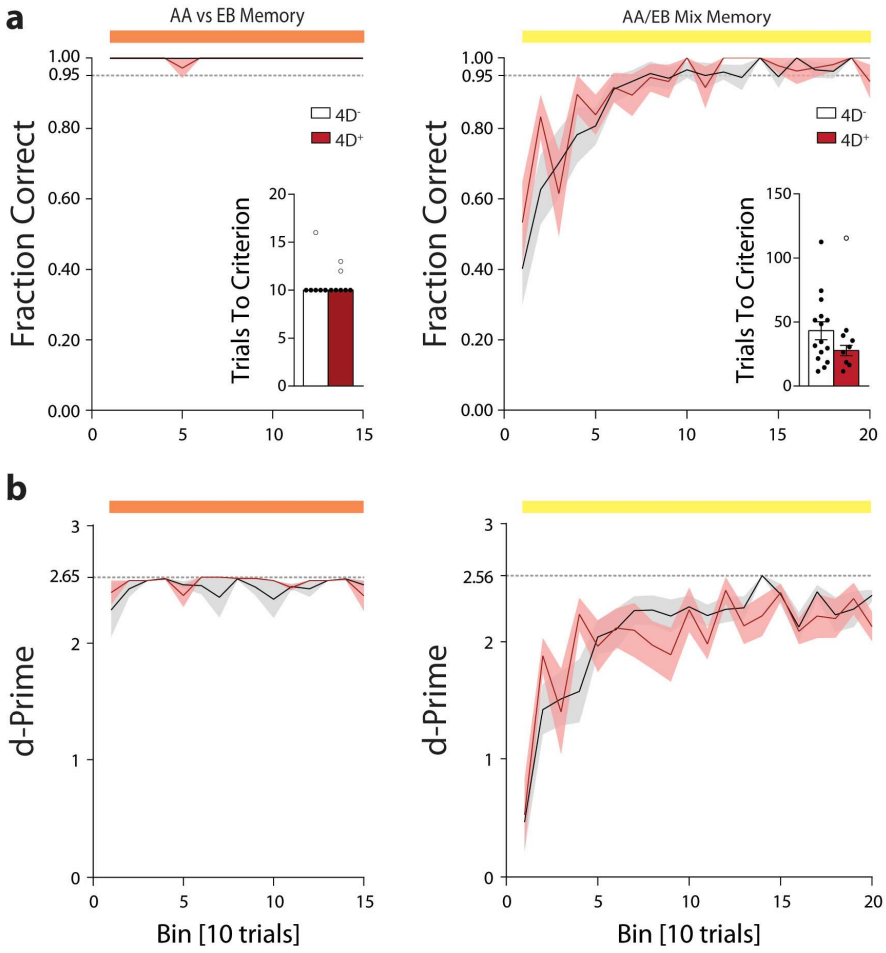

Figure 28 Effect of 4D eoverexpression on odour memory. (a) Discrimination accuracy with insert showing trials to criterion and **(b)** d-prime scores of $4D^-$ (black) and 4D+ (red) animals for the initial 150 trials and 200 trials initiated for the two memory tasks respectively. Animals of the first cohort were presented with amyl acetate or ethyl butyrate (AA vs EB Memory, orange bar) while animals from the second cohort were presented with a mixture of amyl acetate and ethyl butyrate (AA/EB Mix Memory, yellow bar). Line plots show mean ± SEM. Group sizes: AA vs EB Memory: $4D^-$: n=6; $4D^+$: n=5; AA/EB Mix Memory: $4D^-$: n=15; $4D^+$: n=9. **(a)** Dashed lines denote the threshold performance (95%). Inserts showing trials to criterion show mean ± SEM. Black dots show values for individual animals while circles denote possible outliers as identified by ROUT test. **(b)** Dashed lines denote the maximal possible d-prime score. Note that due to the smaller bin size, the maximal attainable d-prime score is 2.56.

In-depth analysis of the first cohort revealed no differences in the supra-threshold performance ($4D^-$: 1.00 ± 0.00; $4D^+$: 1.00 ± 0.00; Figure 29b) nor in the d-prime scores ($4D^-$: 2.47 ± 0.030; $4D^+$: 2.51 ± 0.013; unpaired t-test, p=0.31; Figure 29b). Similar to the previous odour pairs, we found no difference in the lick frequency ($4D^-$: 49.53% ± 1.49; $4D^+$: 50.08% ± 1.45; unpaired t-test, p=0.80; Figure 29c), the dwell rate ($4D^-$: 0.9988 ±

0.00063; 4D$^+$: 0.9995 ± 0.00029; unpaired t-test, p=0.40; Figure 29d) or the inter-trial interval (4D$^-$: 17.94s ± 0.64; 4D$^+$: 17.45s ± 0.29; unpaired t-test, p=0.54; Figure 29e).

Likewise, the second cohort showed no difference in the supra-threshold performance (4D$^-$: 1.00 ± 0.00; 4D$^+$: 1.00 ± 0.00; Figure 29f) nor in the d-prime scores (4D$^-$: 2.07 ± 0.073; 4D$^+$: 2.03 ± 0.11; unpaired t-test, p=0.75; Figure 29g). The remaining values, too, were virtually identical for the two genotypes (lick frequency: 4D$^-$: 50.76% ± 0.35; 4D$^+$: 49.94% ± 0.77; unpaired t-test, p=0.28; Figure 29g; dwell rate: 4D$^-$: 1.00 ± 0.000000; 4D$^+$: 1.00 ± 0.000014; unpaired t-test, p=0.18; Figure 29i; 4D$^-$: 14.31s ± 0.47; 4D$^+$: 14.57s ± 0.48; unpaired t-test, p=0.71; Figure 29j).

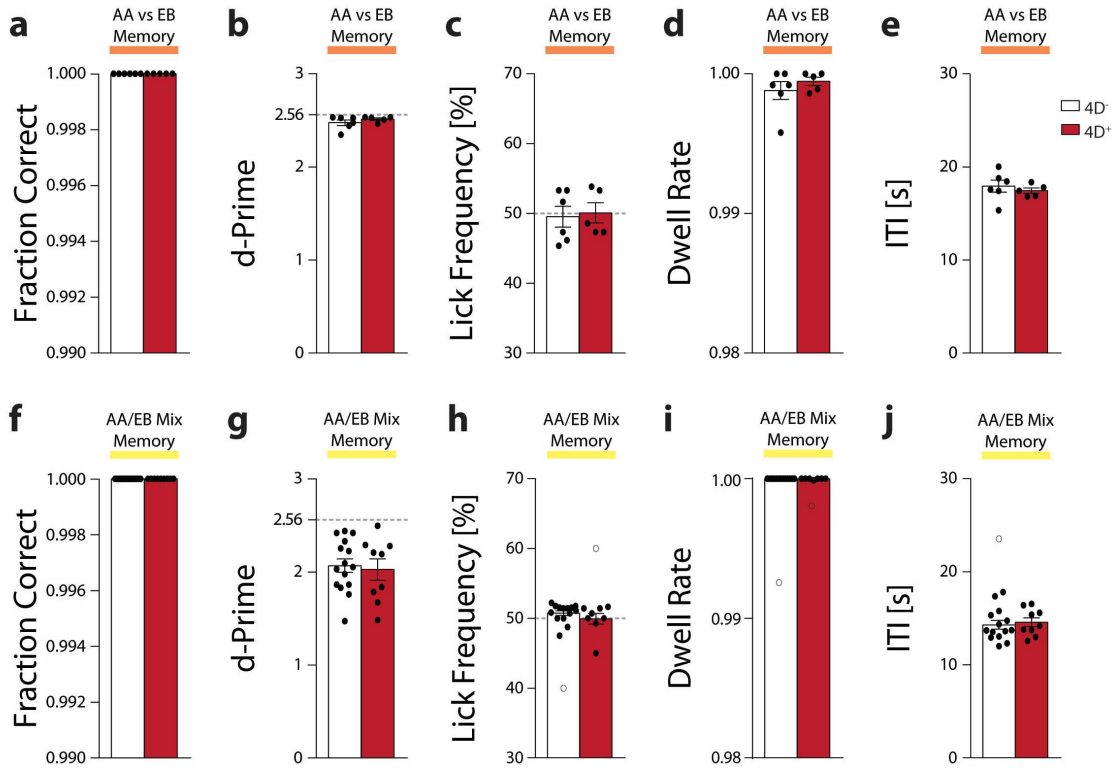

Figure 29 Detailed analysis of the two memory tasks. Average **(a)** supra-threshold performance after reaching the criterion, **(b)** d-prime across all trials **(c)** lick frequency, **(d)** dwell rate prior to the opening of the final valve **(e)** inter-trial interval for the first behavioural cohort, tasked with distinguishing amyl acetate and ethyl butyrate (AA vs EB Memory). 4D$^-$: n=6; 4D$^+$: n=5. Average **(f)** supra-threshold performance after reaching the criterion, **(g)** d-prime across all trials **(h)** lick frequency, **(i)** dwell rate prior to the opening of the final valve **(j)** inter-trial interval for the first behavioural cohort, tasked with distinguishing amyl acetate and ethyl butyrate (AA vs EB Memory). AA/EB Mix Memory: 4D$^-$: n=15; 4D$^+$: n=9. Bars show mean ± SEM. Black dots show values for individual animals while circles denote possible outliers as identified by ROUT test. **(b)/(g):** Dashed lines denote the maximal possible d-prime score. Note that due to the smaller bin size, the maximal attainable d-prime score is 2.56.

Together, both memory tests indicate, that the 4D-derived supernumerary neurons do not impact odour memory in our test paradigm.

Part 3: Influence of T-type calcium channels in olfactory bulb granule cells on odour discrimination

Assessment of the impact of low-voltage activated T-type calcium channels expressed in GCs on odour discrimination required a GC specific, simultaneous knock-down of all three subunits, as all of them are expressed throughout the olfactory bulb[139,141,188]. To achieve this in a spatially and temporally precise manner, a shRNA mediated approach was chosen, requiring the initial screening of putative shRNA sequences for all subunits. As the high sequence homology of all three genes precluded scrambled or even mismatch shRNA controls, a commercially available non-targeting sequence was used as a control sequence to account for unspecific effects due to expression of shRNAs[175].

In vitro screening of putative shRNA sequences

To efficiently screen multiple shRNA sequences, all putative knock-down sequences were subcloned into AAV expression vectors with the expression being controlled by the U6 promoter (Figure 30a). Additionally, a fluorophore was expressed under control of the CBA promoter to monitor infection of the cells. Subsequently, primary cortical and hippocampal cell cultures were infected with adeno-associated viruses (AAVs) expressing both, a shRNA sequence as well as the fluorophore, as these cells natively express all three T-type subunits (Figure 30b) [141].

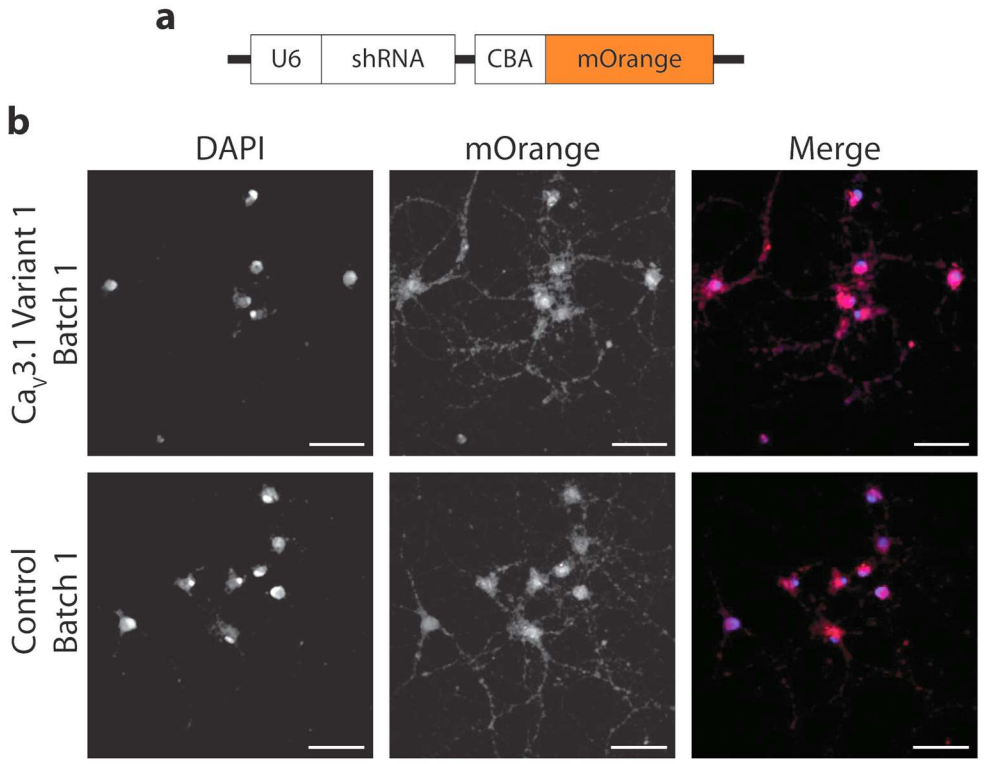

Figure 30 Schematic representation of the AAV constructs used to screen putative shRNA sequences and representative images of infected primary hippocampal cell cultures. (a) All sequences were subcloned into the same vector and expressed under control of the U6 promoter. The marker fluorophore mOrange (orange) was expressed under control of the CBA promoter. **(b)** Representative images of cells infected with AAVs expressing

shRNA targeting the $Ca_V3.1$ subunit (top) or expressing the non-targeting control sequence (bottom) showing nuclei (DAPI, blue) as well as the mOrange (red) signal. Scale: 50µm.

As an efficient shRNA sequence targeting the $Ca_V3.1$ has already been published, we chose to use this sequence and not screen additional sequences[176,189]. Nevertheless, primary cell cultures were infected with AAVs expressing this target sequence or the non-targeting control, respectively (Figure 30b). As expected, widespread fluorescence of the mOrange marker-fluorophore was observed for both viral constructs (Figure 30b). Similarly, uniform and large-scale fluorescence was detected both for AAVs expressing sequences targeting both the $Ca_V3.2$ (Figure 31) as well as the $Ca_V3.3$ (Figure 32) subunit. All viruses were expressed for 10-21 days prior to harvesting of the RNA and we failed to observe detrimental effects (i.e. morphological changes, increased cell death, changes in confluence, etc.) of this prolonged expression on the cells which is often observed in other viral delivery systems like rabies or lenti viruses[190–192].

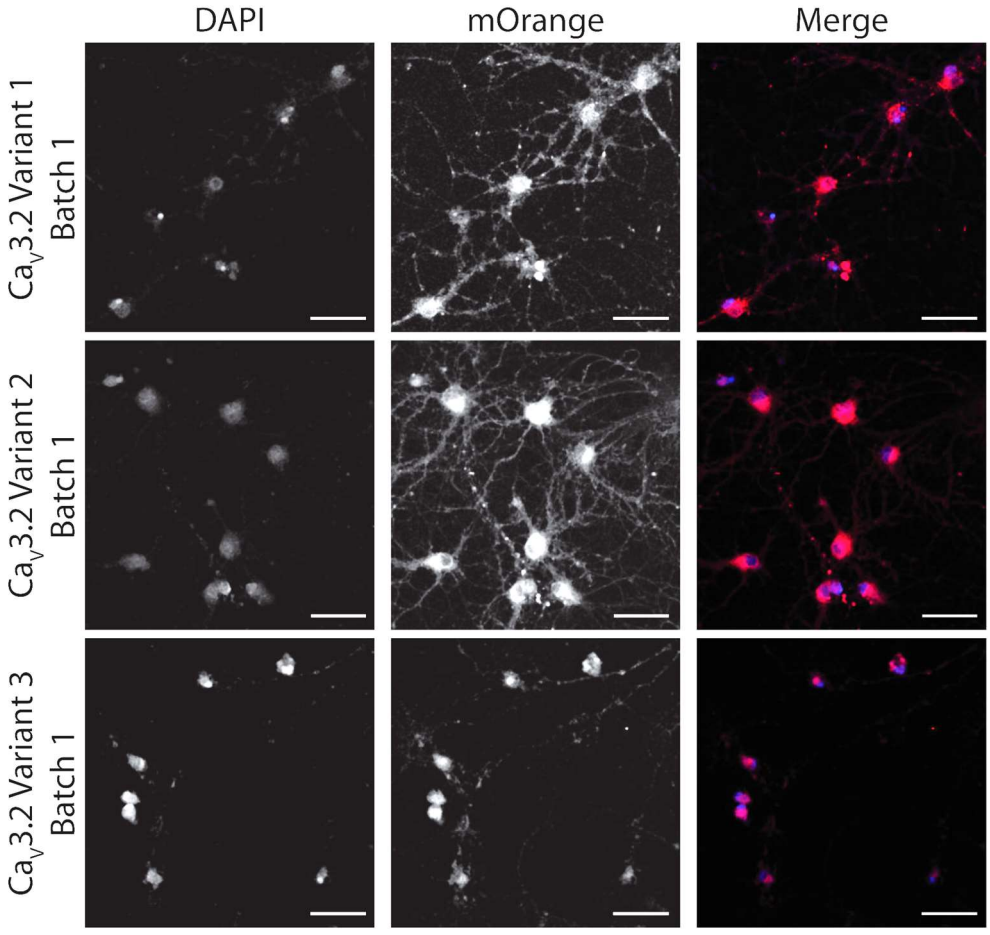

Figure 31 Representative confocal images of primary hippocampal cells infected with AAVs expressing shRNA sequences targeting $Ca_V3.2$. Images show the cell nuclei (DAPI, blue) as well as the mOrange fluorescence (red). Scale: 50µm.

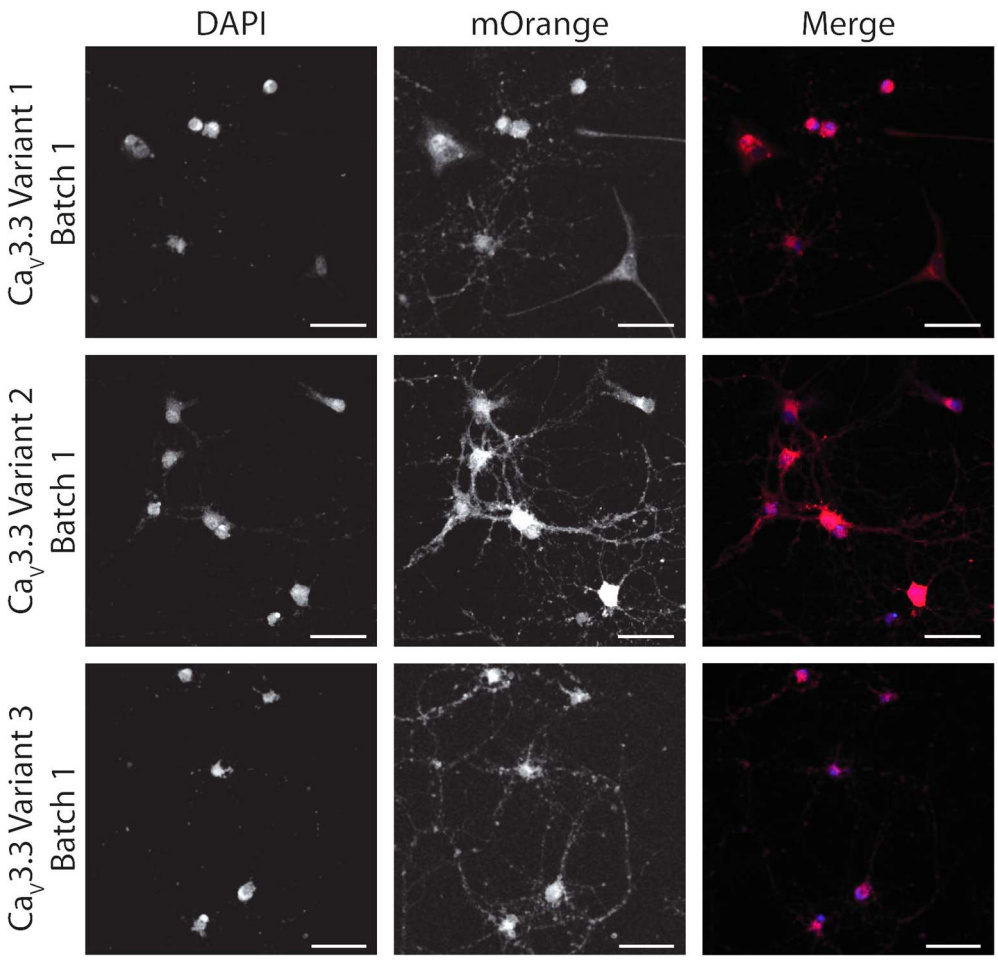

Figure 32 Representative confocal images of primary hippocampal cells infected with AAVs expressing shRNA sequences targeting $Ca_V3.3$. Images show the cell nuclei (DAPI, blue) as well as the mOrange fluorescence (red). Scale: 50µm.

Subsequent quantification of the knock-down efficiency using quantitative real-time PCR (qPCR) revealed large differences not only between different sequences but also between different viral batches containing the same coding sequences (for full data set and statistical analyses see Supplementary Table 4). For instance, the initial virus batch containing a published shRNA sequence targeting $Ca_V3.1$ only reduced the expression level of this subunit to 60% ($Ca_V3.1$ Variant 1 Batch 1; 62.00% ± 10.89) while having little effect on the remaining subunits ($Ca_V3.2$: 97.21% ± 6.59; $Ca_V3.3$: 94.35% ± 5.37; Figure 33a). Despite the reduction of $Ca_V3.1$ being significant (unpaired t-test, p=0.01), this was inconsistent with the previous publications, in which expression of the channel could no longer be detected after injection of this shRNA[176]. Repetition of the assay using a virus with a higher genomic titer and purity showed the expected nearly complete removal of the mRNA ($Ca_V3.1$ Variant 1 Batch 2; 3.2% ± 0.93) which even persisted if a dilution of this second viral batch was used ($Ca_V3.1$ Variant 1 Batch 2 1:2 dilution; 6.61% ± 1.02). Both the pure and the diluted viruses showed an appreciable effect on the remaining subunits (pure: $Ca_V3.2$: 92.52% ± 6.55; $Ca_V3.3$: 67.3% ± 21.38; dilution: $Ca_V3.2$: 88.70% ± 4.33; $Ca_V3.3$: 71.69% ± 10.42). As the aim was to knock-down all three

subunits, this potential lack in specificity would be advantageous, hence no additional shRNA sequence was tested for this particular subunit.

As production of new high-titer virus batches for all remaining sequences was not feasible, sequences for the $Ca_V3.2$ and $Ca_V3.3$ were tested with only one viral batch per sequence. Since all batches were produced simultaneously, conclusions about the relative knock-down efficiencies could still be drawn. For the sequences targeting the $Ca_V3.2$ subunit, we found that all tested variants significantly reduced the intended target to similar levels (variant 1: 31.96% ± 4.65; variant 2: 35.61% ± 3.24; variant 3: 37.08% ± 3.94; Figure 33b). Further, variant one and three significantly reduced both $Ca_V3.1$ (variant 1: 40.74% ± 6.25; variant 3: 81.63% ± 8.89) as well as $Ca_V3.3$ (variant 1: 69.02% ± 10.28; variant 3: 80.61% ± 4.58). As all three variants reduced the desired target by a similar degree, variant three was selected for the final virus, as it did not cause an upregulation of the other two subunits during any repetition of the qPCR tests (Figure 33b).

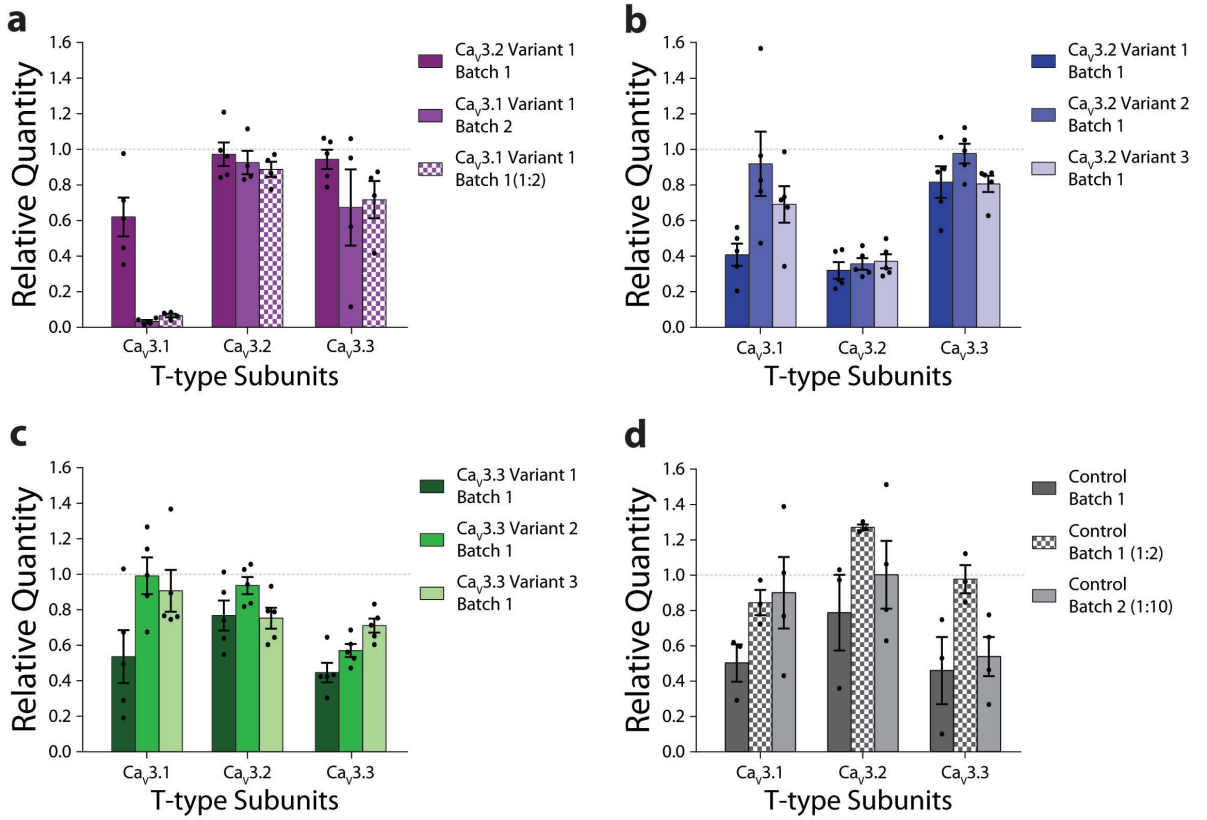

Figure 33 Knock-down efficiencies of various shRNA sequences and virus batches. Knock-down efficiencies of **(a)** $Ca_V3.1$ targeting sequences (purple), **(b)** $Ca_V3.2$ targeting sequences (blue), **(c)** $Ca_V3.3$ targeting sequences (green) and **(d)** control sequences (grey) relative to expression levels in untreated cells. Bars show mean ± SEM while black dots show values for individual qPCR runs (n=3-5). Detailed quantification results can be found in Supplementary Table 4.

Similarly, all the sequences targeting $Ca_V3.3$ caused a considerable reduction of this subunit (variant 1: 44.60% ± 5.53; variant 2: 57.01% ± 3.64; variant 3: 71.11% ± 3.97; Figure 33c), yet we found that variant one was significantly more effective than variant three (unpaired t-test, p=0.005). Moreover, variant one

also significantly reduced $Ca_V3.1$ (53.56% ± 14.91) as well as $Ca_V3.2$ (76.74% ± 8.44) while variant three only significantly affected $Ca_V3.2$ (75.24% ± 5.88). Hence, for the final virus, variant one was selected, as it had the largest effect on the intended target and $Ca_V3.1$ as well as the least number of up-regulatory effects on the remaining subunits.

Lastly, we verified the chosen commercially available control sequence. Surprisingly, we found significantly changed expression levels even when a dilution of the initial virus batch was used (pure: $Ca_V3.1$: 50.25% ± 10.56; $Ca_V3.2$: 78.75% ± 21.48; $Ca_V3.3$: 45.98% ± 18.99; dilution: $Ca_V3.1$: 84.45% ± 7.17; $Ca_V3.2$: 127.04% ± 1.65; $Ca_V3.3$: 97.71% ± 7.98; Figure 33d), prompting us to produce a second virus batch of higher purity and genomic titer ($2.45x10^{12}$ genomes per microlitre). Despite the higher initial dilution used to compensate the increased genomic titer, we still observed a significant reduction of the $Ca_V3.3$ subunit (53.88% ± 11.06). As the other two subunits were largely unaffected ($Ca_V3.1$: 90.04% ± 20.18; $Ca_V3.2$: 100.20% ± 19.20) and the remaining amount of virus from the initial batch was not sufficient for further tests or behavioural analysis, we chose not to generate and test yet another viral batch but rather to continue with this second viral batch for further analyses.

In vitro validation of pre-screened shRNA sequences

To assess the efficiency of simultaneously knocking down all three T-type subunits, we used two test scenarios. In the first case, cells were infected with an AAV carrying all three shRNA sequences as well as the fluorophore (mOrange) to visualize infected cells (Figure 34a; $6.23x10^{12}$ genomes per microlitre). To ensure high expression levels of all shRNAs, the sequence targeting $Ca_V3.2$ was expressed under control of the H1 promoter, as expression of multiple genes using the same promoter has been shown to affect expression of the individual transgenes differentially[193]. Additionally, for the two sequences expressed under control of the U6 promoter, the respective reading frames were placed in opposite direction to reduce the likelihood of recombination due to close proximity of identical sequences. In the second case, we generated high-titer viruses ($1.83x10^{11}$ to $1.07x10^{13}$ genomes per microlitre) for the three most promising sequences (each expressed from the U6 promoter and including the fluorophore) and similarly used an equi-part mixture of these viruses to infect cells.

In both approaches, we found a significant reduction of the $Ca_V3.2$ subunit compared to the control virus (Triple knock-down: 8.05% ± 2.34; unpaired t-test, p=0.003; Virus Mix: 9.36% ± 2.34; unpaired t-test, p=0.01; Figure 34b). While $Ca_V3.1$ subunit was significantly reduced by the triple knock-down virus (Triple knock-down: 1.13% ± 0.33; Virus Mix: 17.86% ± 7.03), none of the two approaches resulted in a reduced $Ca_V3.3$ expression compared to the control virus (Triple knock-down: 38.35% ± 11.46; Virus Mix: 16.27% ± 9.26).

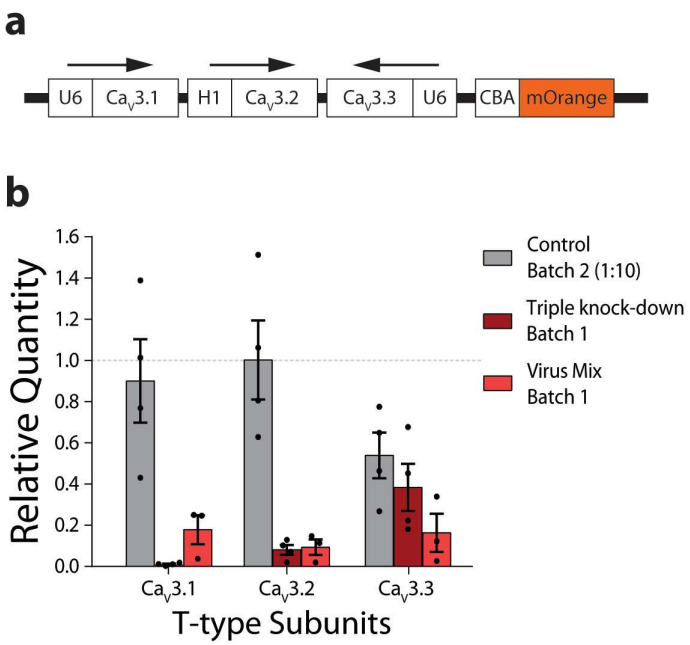

Figure 34 Validation of pre-screened shRNA sequences in vitro. **(a)** Schematic representation of the final triple knock-down virus. **(b)** Knock-down efficiencies of the control sequence (grey), the triple knock-down virus containing the three most promising sequences (dark red) and an equi-part mixture of three individual viruses (light red) relative to expression levels in untreated cells. Bars show mean ± SEM while black dots show values for individual qPCR runs (n=3-4).

Compared to the baseline, however, both approaches significantly reduced the expression of all three subunits. As the knock-down efficiencies for the $Ca_V3.1$ subunit were higher using the triple knock-down virus (unpaired t-test, p=0.036) and comparable for the remaining subunits (unpaired t-test, $Ca_V3.2$: p=0.770; $Ca_V3.3$: p=0.216), we decided to use the single AAV containing all three shRNA sequences for *in vivo* studies. Additionally, this was the only approach ensuring any infected cell would express all shRNAs, preventing potential compensatory upregulation of any non-targeted subunit as well as eliminating the need to additionally control for triple infection of the cells with all three viruses.

In vivo analysis of shRNA sequences

To determine the efficiency and precise special limitation of AAV-mediated expression of the shRNA sequences to GCs, we injected both the triple knock-down as well as well as the non-targeting control into the GCL of the OB of mice. As only the diluted non-targeting viruses showed limited changes *in vitro*, this virus was only injected in a dilution. Three weeks post-injection we found large-scale expression of the marker fluorophore mOrange for both viral constructs (Figure 35). However, injection of the undiluted triple knock-down virus lead to a massive reorganization of the OB structure, leaving only the GL undisturbed. Most notably, the MCL and the GCL were not clearly separated anymore. Further, the GCL bordered the glomerular layer directly and both the internal as well as the external plexiform layer were not visible anymore. This effect was not observed in the diluted triple knock-down virus or the non-targeting control virus. For both of these viruses the mOrange fluorescence was largely limited to the GCL and appeared to be more focussed in the centre of the GCL. Additionally, some fluorescently labelled cells were visible in the MCL, the two plexiform layers as well as the GL, consistent with the known radial migration pattern of adult-born interneurons from the centre of the OB towards the outer layers.

Together these results indicate, that the infection can successfully be limited to GCs while an overly high virus titer may adversely affect the cells.

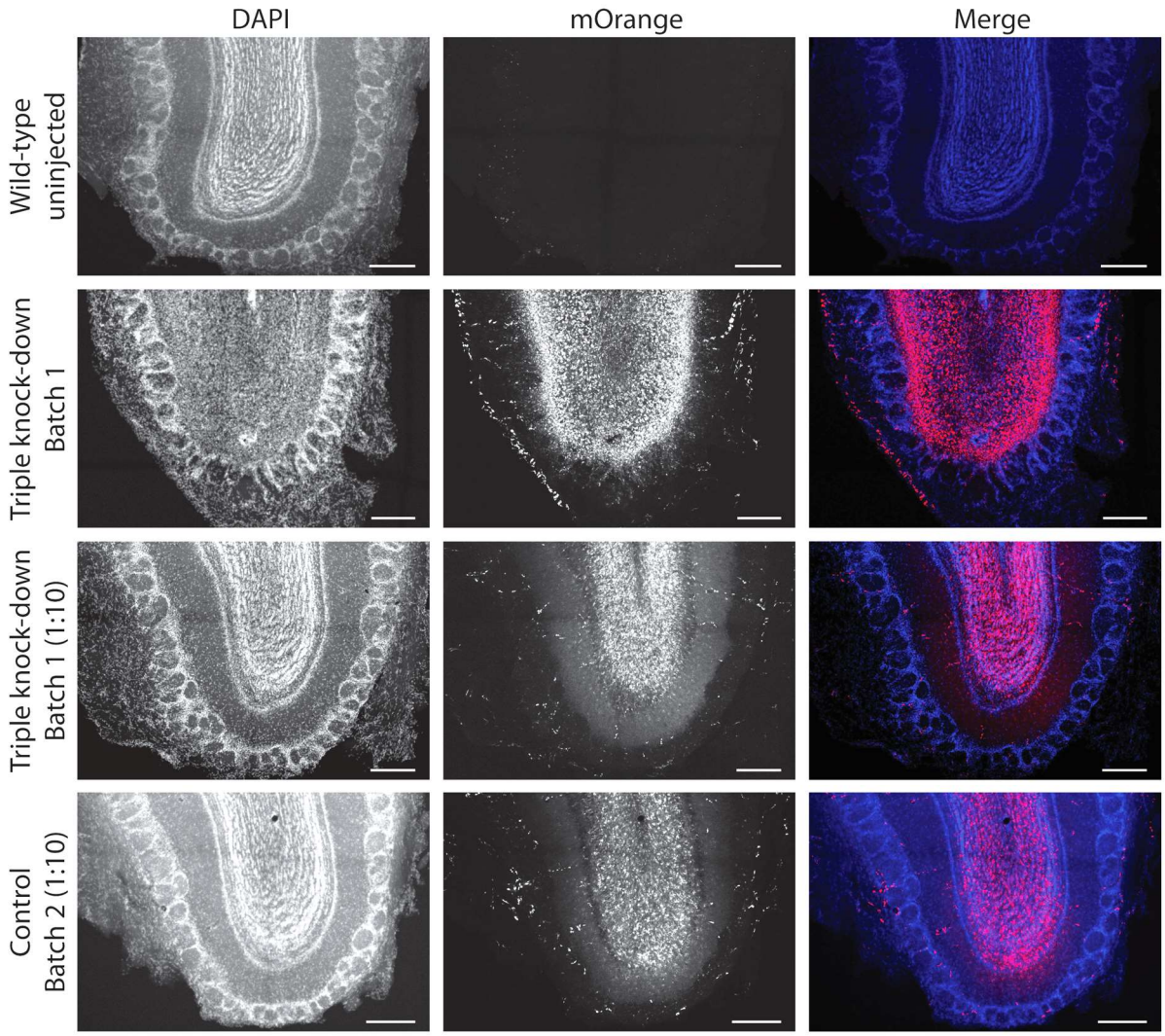

Figure 35 Representative confocal images of *in vivo* shRNA expression. Images show the cell nuclei (DAPI, blue) as well as the Orange fluorescence (red). Animals were either not injected with any virus ("Wild-type uninjected"), or with AAVs expressing either the triple knock-down construct (triple knock-down) or the non-targeting control shRNA sequence (control). Dilutions of the viruses as indicated. Scale: 200µm.

To verify the successful knock-down of the T-type calcium channels, we again used qPCR on GCLs excised from acute slices of injected animals. This excision was necessary as all subunits have been shown to be expressed in the other OB layers too, which could inflate the results due to the sensitivity of the qPCR. While, we did find a clear reduction of all three subunits relative to uninjected wild-type animals, expression of $Ca_V3.3$ remained quite high (65.01% ± 0.76; Figure 36). Conversely, expression of the other two subunits was comparably reduced well to below 50% ($Ca_V3.1$: 27.61% ± 3.79; $Ca_V3.2$: 31.89% ± 3.54; unpaired t-test, p=0.362), indicating higher knock-down efficiencies for these two subunits, similar to the *in vitro* results. Additionally, we observed quite variable $\Delta\Delta C_t$ values of the three subunits in the wild-type control animals (Figure 36 inset), something that was not observed during the initial *in vitro* screening (data not shown).

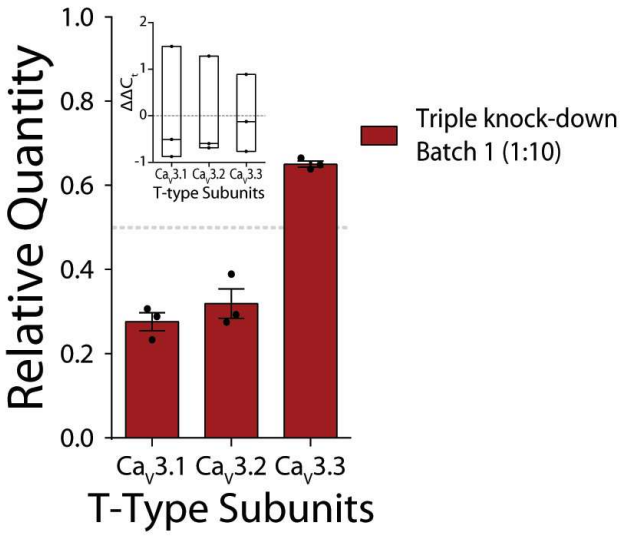

Figure 36 Validation of pre-screened shRNA sequences *in vivo*. Residual expression of T-type subunits after injection of the triple knock-down virus (dark red) compared to expression levels of uninjected wil-type animals. Inset shows the $\Delta\Delta C_t$ values for the wild-type animals used as a reference. Bars show mean ± SEM while black dots show values for individual animals (n=3). Floating bars in inset show range and mean while black dots show values for individual animals (n=3).

As the $\Delta\Delta C_t$ values represent the expression of the target gene relative to the housekeeping reference gene, this variance suggests a large variance in baseline expression of the three subunits.

Together, these results indicate that the *in vivo* knock-down was less efficient than the *in vitro* knock-down which could be due to the higher expression variability *in vivo*. Since the selected sequences were the most efficient ones in vitro and as the shRNA sequence targeting the $Ca_V3.1$ had been successfully used in at least two *in vivo* studies, we chose to use the triple knock-down virus despite the potential residual expression[176,189].

Effect of the T-type calcium channels knock-down on odour discrimination

To investigate the effect of a granule cell specific knock-down of T-type calcium channels on odour discrimination, we injected mice with the pre-screened AAVs expressing either the triple knock-down or the non-targeting control sequences. Previous studies have reported a relatively slow turnover rate of the calcium channels of approximately four to six weeks[194]. Therefore behavioural experiments were only started seven weeks post injection to reduce the contribution of residual T-type channels. Following this expression time, animals were trained on a go/no-go odour discrimination task involving a total of four different odour pairs or mixtures (Figure 37).

All mice were able to learn the discrimination task with no apparent differences between the two groups (two-way ANOVA,: Cin vs Eu: $F(1, 18)=0.79$, $p=0.64$; AA vs EB: $F(1 ,18)=2.78$, $p=0.11$; AA/EB Mix (40%/60%): $F(1, 18)=0.18$, $p=0.67$; AA/EB Mix (40%/60%): $F(1, 8)=0.40$, $p=0.54$; Figure 37a). However, several mice from both groups (control: n=5; triple knock-down: n=4) did not reach the performance criterion for the second more complex mixture of amyl acetate and ethyl butyrate (48%/52% mixture) within two weeks of training and were hence removed after this training duration and excluded from the analysis of this odour mixture. This failure to reach the established performance criterion reflects the high degree of difficulty, which is also apparent from the slower learning curves observed for this odour pair.

Similarly, both groups reached d-prime scores well above 2, indicating high accuracy for the discrimination of the individual odours (two-way ANOVA,: Cin vs Eu: F(1, 18)=0.79, p=0.64; AA vs EB: F(1 ,18)=2.78, p=0.11; AA/EB Mix (40%/60%): F(1, 18)=0.18, p=0.67; AA/EB Mix (40%/60%): F(1, 8)=0.36, p=0.57; Figure 37b). Mice that did not meet the performance criterion within two weeks also failed to reliably achieve d-prime scores above 1.5 for the second more challenging mixture.

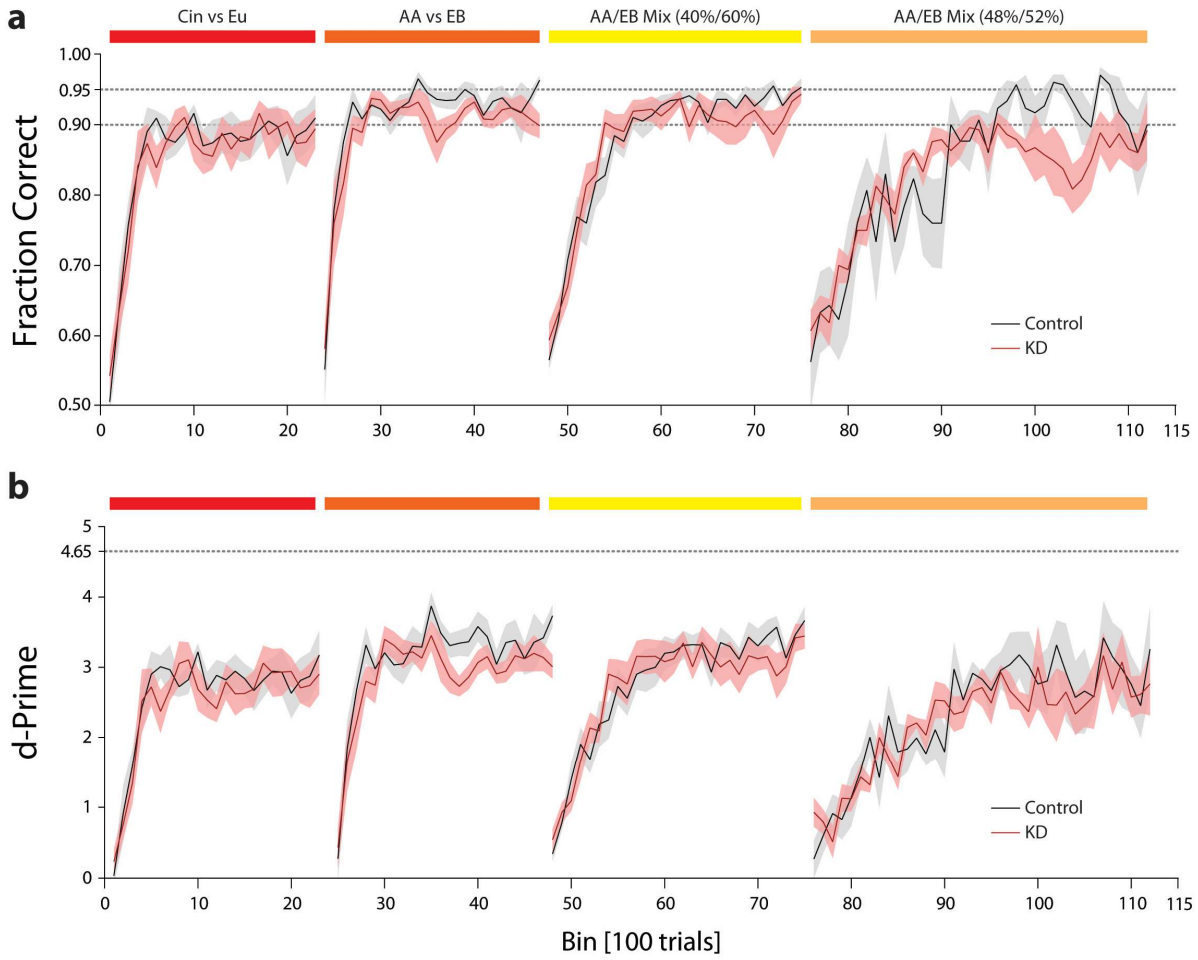

Figure 37 Effect of the knock-down of T-type calcium channel expression on odour discrimination. (a) Discrimination accuracy and **(b)** d-prime scores for animals injected with the non targeting control virus (Control; black) or the triple knock-down virus (KD; red). Animals were presented with cineole or eugenol (Cin vs Eu, red bar), amyl acetate or ethyl butyrate (AA vs EB, orange bar) and two different mixtures of amyl acetate and ethyl butyrate (AA/EB Mix (40%/60%), yellow bar: AA/EB Mix (48%/52%), gold bar). Note: animals that did not achieve the performance criterion for the AA/EB Mix (48%/52%) were excluded from the analysis. Group sizes: AA/EB Mix (48%/52%): Control: n=4; KD: n=6; remaining odours: Control: n=9; KD: n=10. Lines show mean ± SEM. Dashed lines in **(a)** show the threshold performance for the first odour pair (90%) and the subsequent pairs (95%). Dashed line in **(b)** shows the maximal possible d-prime score.

Detailed analysis of the behavioural experiments showed, that animals of both groups reached the respective performance criteria for the initial two pure odour pairs within a similar number of trials (Figure 38a; trials to criterion Cin vs Eu: Control: 302.1 trials ± 38.04; KD: 326.7 trials ± 47.50; AA vs EB: Control: 364.9 trials ± 37.63; KD: 497.0 trials ± 94.51). Additionally, we observed a significant difference in the

variability of the trials required to reach the performance threshold, but only for the discrimination of amyl acetate and ethyl butyrate (coefficient of variation: Control: 32.61%; KD: 60.13%; F(9, 9)=6.31, p=0.01).

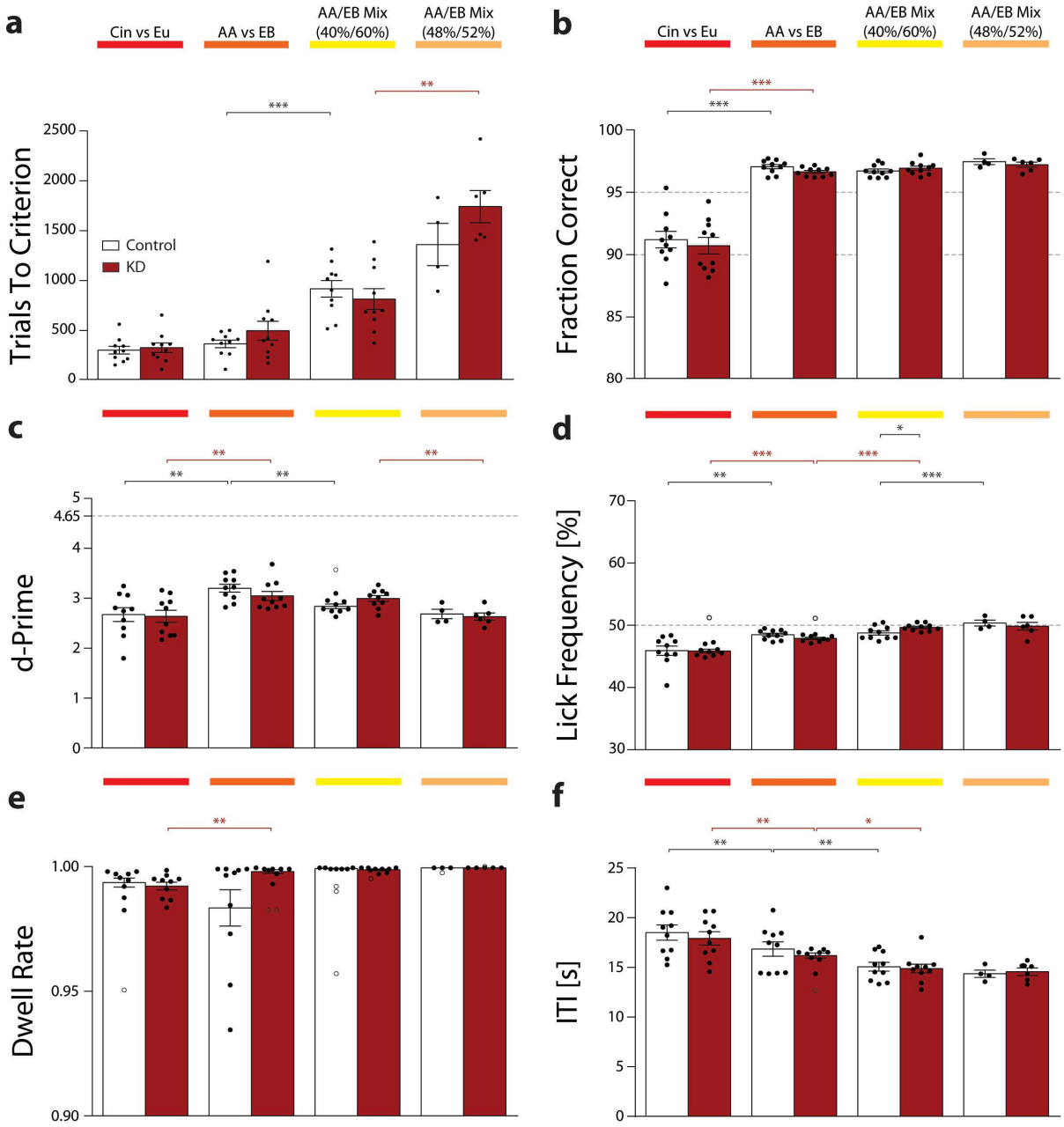

Figure 38 Detailed analysis of the behavioural effect of the knock-down of T-type calcium channel expression on discrimination of different odour pairs. **(a)** Trials to criterion (performance ≥ 90% for Cin vs Eu and ≥ 95% remaining odour tasks) for animals injected with the non-targeting AAV (Control; white) or the triple knock-down AAV (KD; red). Average **(b)** supra-threshold performance after reaching the criterion, **(c)** d-prime across all trials **(d)** lick frequency, **(e)** dwell rate prior to the opening of the final valve **(f)** inter-trial interval. For complete statistical analysis refer to Supplementary Table 5 and Supplementary Table 6. Bar graphs show mean ± SEM, dots show mean for individual animals while circles show potential outliers as identified by ROUT test. Dashed lines in **(b)** show threshold performances. Dashed line in **(c)** shows the maximal possible d-prime score. Group sizes: AA/EB Mix (48%/52%): Control: n=4; KD: n=6; remaining odours: Control: n=9; KD: n=10.

It is important to note, that a lower performance threshold was used for the initial task of discriminating cineole and eugenol. Thus the typically observed decrease in trials to criterion when transitioning from the first to the second odour pair was not seen in this experiment. For the initial binary mixture of amyl acetate and ethyl butyrate, we observed an increase in the trials to criterion compared to the pure odours which, however, was only significant for the control group (Figure 38a; trials to criterion AA/EB Mix (40%/60%): Control: 917.0 trials ± 83.12; KD: 814.0 trials ± 104.07; paired two-tailed t-test, $p<0.0001$ and $p=0.62$ respectively). Conversely, the second mixture required even more trials, reflecting the increased difficulty of this task. Yet the increase was only significant for the knock-down group (Figure 38a; trials to criterion AA/EB Mix (48%/52%): Control: 1361.0 trials ± 211.8; KD: 1741 trials ± 160.6; paired two-tailed t-test, $p<0.0001$ and $p=0.62$ respectively).

In line with the learning curves, we observed no differences in the supra-threshold performance between the two groups for any of the tested odour pairs (Figure 38b). We did find a significant increase for both groups in supra-threshold performance between the first and the second odour pair, but as a lower threshold was used for the first odour pair, this difference was to be expected (fraction correct Cin vs Eu: Control: 0.91 ± 0.007; KD: 0.91 ± 0.007; AA vs EB: Control: 0.97 ± 0.002; KD: 0.97 ± 0.001; paired two-tailed t-test, $p<0.0001$ and $p<0.0001$). Consistently with these findings, the d-prime scores were reliably ≥2.5 (Figure 38c) while the lick frequency was around 50% (Figure 38d). The dwell rate prior to opening of the final valve was close to 100% (Figure 38e) whereas the inter-trial interval gradually decrease from approximately 19s to roughly 14s over the course of the testing (Figure 38f).

Analogous to the analysis of the 4D mice (see Results Part 2), we did observe statistical differences for some of these baseline values both between different odour pairs as well as between the two groups for the same odour pair. As these differences are again fairly small (i.e. lick frequency for AA/EB Mix (40%/60%): Control: 48.76s ± 0.33; KD: 49.66s ± 0.18; unpaired two-tailed t-test, $p=0.03$ or dwell rate for the KD-group: Cin vs Eu: 0.99 ± 0.0016; AA vs EB: 1.00 ± 0.0008; paired two-tailed t-test, $p=0.01$), we consider these differences to not constitute true phenotypical differences despite being statistically significant.

Finally, we determined the discrimination time (i.e. the fastest time to elicit a behavioural response to an odour) to analyse, if the lack of T-type calcium channel expression did indeed affect the discrimination of odours (Figure 39). Interestingly we found no inter-group difference and precisely one intra-group difference, namely in the control group in the DTs required for the discrimination for pure amyl acetate and ethyl butyrate compared to the first tested mixture of the two odours (AA vs EB: 262.8ms ± 8.04; AA/EB Mix (40%/60%): 319.1ms ± 13.80; paired two-tailed t-test, $p=0.008$). For the even more complex second mixture of amyl acetate and ethyl butyrate (AA/EB Mix (48%/52%)) we observed a further increase in the DTs (Control: 370.3ms ± 18.81, paired two-tailed t-test, $p=0.134$; KD: 345.0ms ± 20.53; paired two-tailed t-test, $p=0.667$), consistent with the increased level of difficulty due to increased similarity of the odour mixtures. However, this increase was not statistically significant, potentially due to the reduced group size for this highly demanding discrimination task. One should note, that the DT for the initial odour pair (Cin vs Eu) was calculated at a lower performance threshold than the remaining odour pairs. Further, this task also

includes learning of the underlying discrimination paradigm, hence the DTs for this odour pair are not directly comparable with the values obtained for the remaining odours.

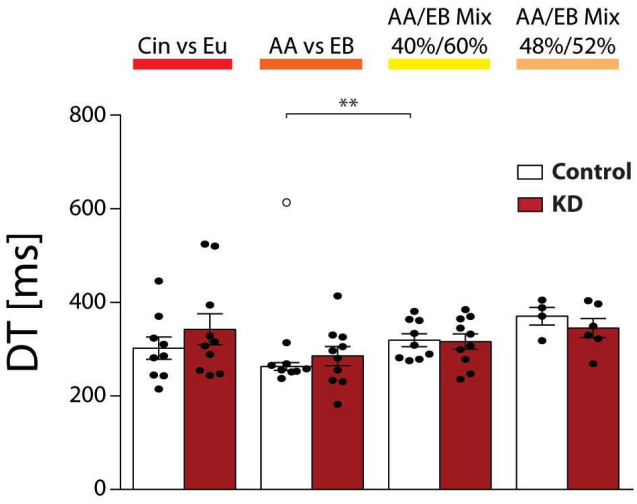

Figure 39 Analysis of the discrimination times across different odour pairs and mixtures. Discrimination times (DTs) for animals injected with the non-targeting AAV (Control; white) or the triple knock-down AAV (KD; red). Note that the DTs for Cin vs Eu were calculated at a performance of 90% while 95% was used for the remaining odours. Bar graphs show mean ± SEM, dots show mean for individual animals while circles show potential outliers as identified by ROUT test. Group sizes: AA/EB Mix (48%/52%): Control: n=4; KD: n=6; remaining odours: Control: n=9; KD: n=10.

As the DTs typically increase for more difficult odour pairs, the fact that this was not observed in the animals injected with the triple knock-down virus may suggest, that the lack of T-type calcium channels may have already impaired discrimination of simple odours.

Post-hoc verification of the knock-down of T-type calcium channel expression

To verify correct expression of the AAVs and the successful knock-down of the T-type calcium channels, animals used in the behavioural analysis were randomly chosen for post-hoc analysis using immunohistochemistry or qPCR. Similar to the initial *in vivo* testing of AAV injection into the GCL, we found strong expression of the mOrange marker fluorophore mostly within the centre of the GCL as well as some fluorescent cells in the outer layers of the OB (Figure 40). Yet, the spread of the injected AAVs as indicated by the fluorescence appeared to be smaller (approximately 50% of the GC) compared to the initial tests with no obvious differences between the triple knock-down and the non-targeting virus. Stainings for the neuronal marker-protein NeuN showed no apparent changes in overall anatomy or neuron density between the two viruses, indicating no large-scale adverse effects due to the long-term expression (> 5 months) of the viral constructs.

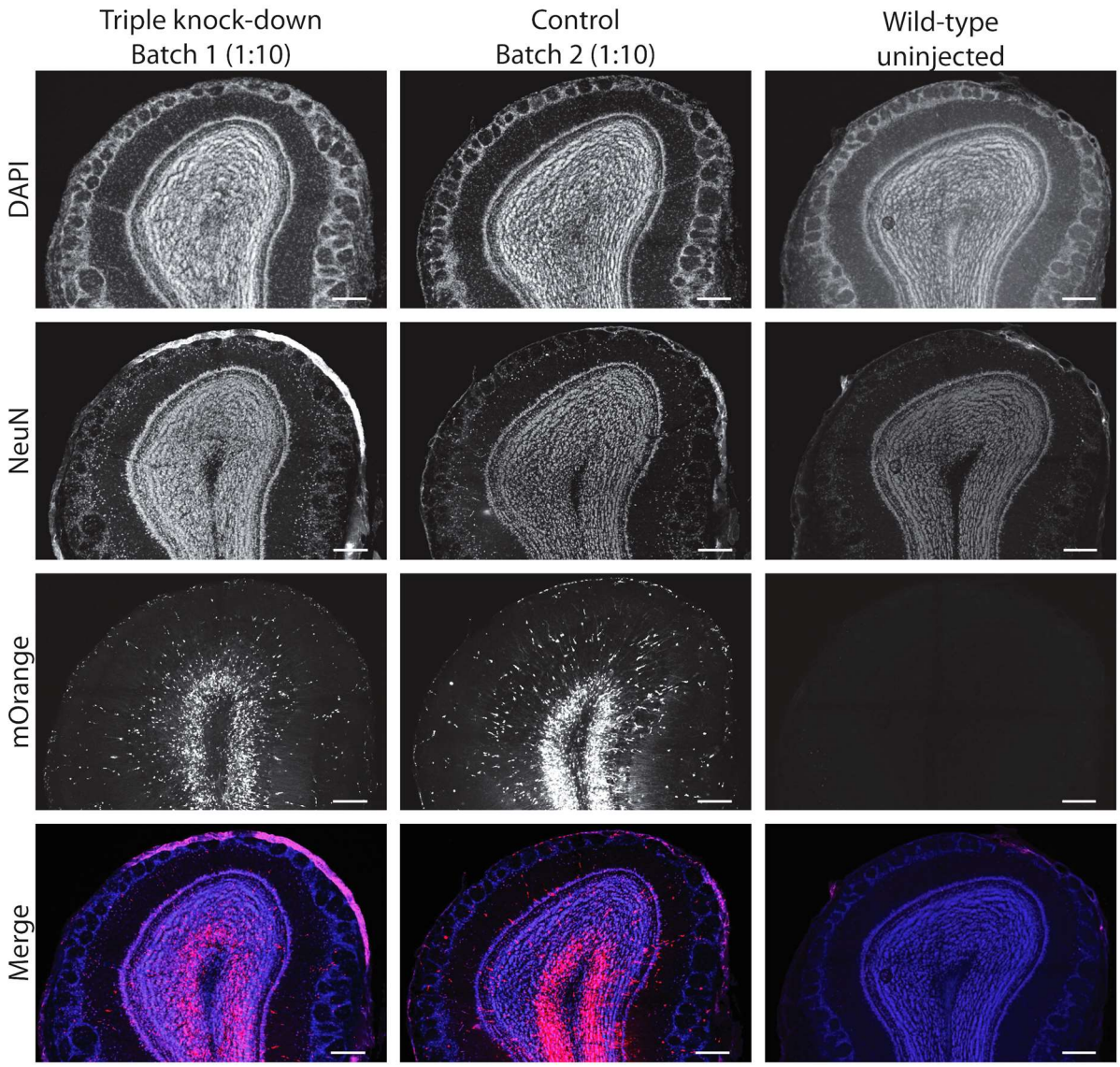

Figure 40 Representative confocal images of shRNA expression in animals used for behavioural analysis of odour discrimination. Images show the cell nuclei (DAPI, blue) as well as the nuclei of neurons (NeuN, magenta) and mOrange fluorescence (red). Animals were injected with AAVs expressing either the triple knock-down construct (triple knock-down) or the non-targeting control shRNA sequence (control), each at a dilution of 1:10. Uninjected wild-type animal is shown as a reference but was not used in the behavioural tests. Cohort size: 4 animals per treatment. Scale: 200µm.

For quantification of the residual expression levels, animals injected with the triple knock-down virus were directly compared with animals injected with the non-targeting control virus using qPCR (Figure 41a). Despite a reduction of the expression of the $Ca_V3.1$ subunit, the residual expression of all subunits was still well above 50% ($Ca_V3.1$: 0.72 ± 0.04; $Ca_V3.2$: 0.86 ± 0.09; $Ca_V3.3$: 1.10 ± 0.16). This is in stark contrast to the initial *in vivo* test, which could be due to an inefficient knock-down within the GCL, potentially due to the reduced spread of the virus as evident from the immunohistochemical analysis. Additionally, as the triple knock-down animals were not compared with unperturbed wild-type animals but with animals subjected to the non-targeting AAV, these results may also indicate, that the non-targeting AAV also reduces the

expression of the target genes which would ultimately result in a less pronounced knock-down effect. To test the latter possibility, we tested the same samples again but this time using samples obtained from uninjected wild-type animals as a reference (Figure 41b). Here we found a clear reduction of all three subunits ($Ca_V3.1$: 0.43 ± 0.13; $Ca_V3.2$: 0.26 ± 0.06; $Ca_V3.3$: 0.75 ± 0.12), indicating that the non-targeting sequence does interfere with the T-type calcium channel expression. An additional direct comparison of the animals injected with the triple knock-down virus and untreated wild-type animals was not possible due to the vast amount of RNA samples required to detect 5 different genes using qPCR. However, by extrapolating the results obtained from control sequence, the remaining expression of the $Ca_V3.1$ and $Ca_V3.2$ subunits compared to wild-type animals would have been closer to the values seen during the initial *in vivo* tests ($Ca_V3.1$: approximately 0.31; $Ca_V3.2$:approximately 0.22). However, expression of the $Ca_V3.3$ subunit would still have remained far higher than expected (approximately 1.34).

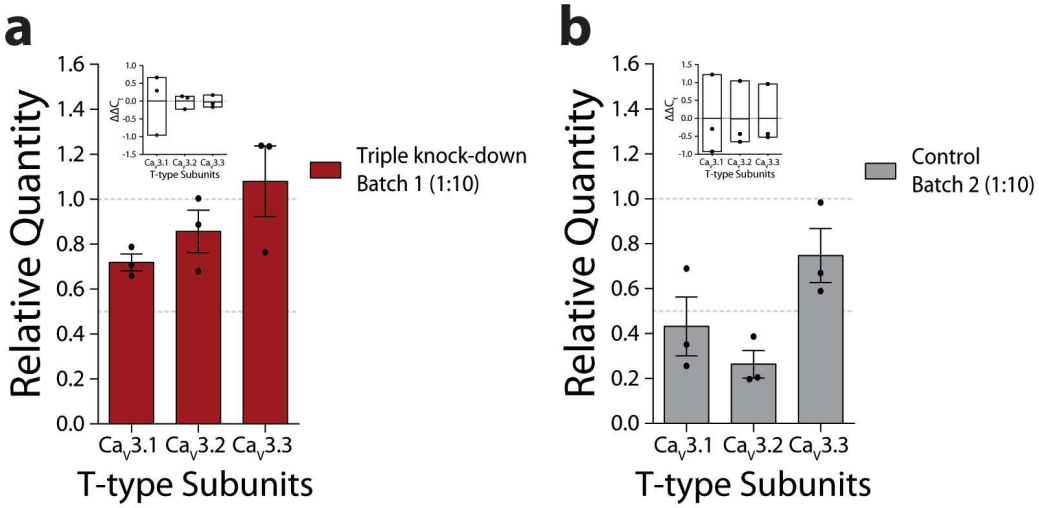

Figure 41 Post-hoc quantification of the residual T-type calcium channel expression in animals used for behavioural analysis of odour discrimination. (a) Residual T-type subunit expression in animals injected with the triple knock-down virus (dark red) relative to animals injected with AAVs expressing the non-targeting shRNA. Inset shows the $\Delta\Delta C_t$ values for the animals injected with AAVs expressing the non-targeting shRNA used as a reference. **(b)** Residual T-type subunit expression in animals injected with AAVs expressing the non-targeting shRNA relative to uninjected wild-type animals. Inset showw the $\Delta\Delta C_t$ values for the uninjected wild-type animals used as a reference. Bars show mean ± SEM while black dots show values for individual animals (n=3). Floating bars in inset show range and mean while black dots show values for individual animals (n=3).

Overall, these results indicate that the simultaneous knock-down of all three T-type calcium channels using shRNA is possible and feasible within a time frame required for prolonged behavioural analysis. Despite the observed differences in the discrimination times, a truly non-targeting control sequence needs to be established as this may have masked the full extent of T-type mediated calcium transients on the discrimination of complex odours or olfactory abilities in general.

Discussion

Part 1: Establishing an automated behaviour setup for odour discrimination

Technical validation

As the manual setups previously used for the analysis of olfaction require constant experimenter interference and are based on outdated electronics, we first established a fully automated behaviour setup for operant conditioning of group-housed mice. Towards this aim we implemented a novel dual-channel high precision olfactometer for the reliable presentation of odour stimuli (Figure 13). Here we found a uniform, stereotypical shape of the odour plume and no detectable signal for non-odorized reservoirs, indicating no cross-contamination between odour reservoirs or residual odour traces in the olfactometer. As mice have been reported to react to an odour in as little as one sniff (i.e. 50-350ms in mice), it was crucial to deliver the odour fast and preferably within this timeframe[195–197]. Hence, we measured the time of the onset of the odour as well as the time required to reach the maximal concentration. Here, the odour onset was detected within 16ms whereas the peak concentration was reached within 80ms. For the duration to reach the peak, we observed a linear increase with increased distance to the final valve. Since many organisms including mice have been reported to discriminate odour mixtures based on fluctuations of the odours within the mixture, this onset difference could represent a non-olfactory cue for the mice[198–202]. Still, the maximal difference in odour onset was less than 30ms and both the onset as well as the time to reach the peak concentration for all valves were below the duration of an average sniff (approximately 200ms) or even the inhalation period of a murine sniff cycle. Additionally, a more recent study has shown that although mice can react in as little as one sniff, the majority of mice sample for more sniffs before responding[203]. Lastly, any odour was always presented from at least two to four different odour reservoirs and the location of the reservoirs was randomly switched multiple times throughout each experiment. Thus, this olfactometer ensures that any measured reaction time is not affected by delayed odour presentation or by the presence of additional non-olfactory dues but does indeed reflect the decision making time point of the animal solely based on the presented odours.

Since high-throughput phenotyping also requires the ability to test multiple odours or different combinations of odours, we used the olfactometer to generate varying dilutions from pure odour reservoirs. Here we found, that the olfactometer can reliably produce a wide range of dilutions without affecting the timing of stimulus delivery. Coupled with the fact, that each of the 8 valves per olfactometer channel can be individually regulated, this system greatly increases flexibility compared to the previously employed manual setup and allows for arbitrary combinations of the different pure odours[153,154]. While there are olfactometers that can combine even more odours, these are often heavily customized or require long inter-trial intervals (>1min) to switch between odours and are thus not suited for unsupervised, automated training paradigms[204–206].

Behavioural validation

The lack of salient non-olfactory cues was confirmed by presenting the animals with non-odourised air for two thousand trials (Figure 14). Here, mice remained at chance level for the duration of the training without any indication of improvement. On the contrary, we observed a marked decline in the dwell rate prior to the opening of the final valve, indicating a loss in motivation to initiate a trial.

Conversely, when presented with odourised air, animals rapidly acquired the discrimination task and were able to distinguish the different odour pairs and mixtures at high accuracy (Figure 15). Further, we were able to replicate the increased time to criterion and slower learning curves for odour mixtures compared to pure odours, consistent with the increased difficulty due to overlapping OB activation[81,82,207]. The lick frequency and the inter-trial interval were stable over time and odour pairs while the dwell rate markedly declined (Figure 15), similar to the initial tests without odour cues (Figure 14). Hence the dwell rate threshold required to initiate a trial was increased for all subsequent experiments, to incentivise animals to initiate trials only when truly motivated to perform the discrimination task.

While the acquisition and discrimination of the odours is consistent with the data obtained using other established behaviour setups, these setups only allow training of a single animal at a time[61,62,81,94,154]. To verify that the setup could be used to train large (>15 animals) groups of animals simultaneously, we trained a set of 18 male wild-type mice on the previously established odour discrimination task. Despite increasing the group size over four-fold, all animals were able to acquire the task and distinguish the different odour pairs at high accuracy (Figure 16). Moreover, the learning speed appeared to be faster, as less trials were required to reach the performance threshold or high d-prime scores. However, this variability is well within the range of values reported for manual setups (i.e. approximate number of trials to reach ≥95% performance for AA vs EB: 400 to 800 trials reported by Abraham et al. in 2004; 800 to 900 trials reported by Nunes and Kuner in 2015; 400 trials reported by Nunes and Kuner in 2018) and thus does not appear to be a feature of increased group size but rather seems to reflect typical variance of behaviour testing[61,62,81]. In agreement with these studies, key behavioural parameters (supra-threshold performance, lick frequency, dwell rate or inter-trial interval) did not differ between different odour pairs and were nearly identical to the values obtained with the manual setups. It is noteworthy, that the inter-trial interval was consistently between 10s and 25s, well within the range reported by Abraham et al. in 2004 (approximately 10-30s) or Nunes et al. in 2018 (approximately 10-20s)[62,81]. This indicates that the larger group size and the resulting competition for access to the odour port did not negatively affect the ability to initiate trials. Additionally, the dwell rate prior to opening of the final valve, did not decrease over time despite similar training duration compared to the initial small cohort. This was achieved by increasing the threshold for the dwell rate, highlighting that control over the animals' behaviour even before the odour is crucial for the generation of high-quality data.

Lastly, we sought to determine the discrimination time (DT) as established by Abraham et al. in 2004, which serves as a direct measure of how fast animals can distinguish two odours[21,81]. Here we consistently found higher DTs both for pure odours and their binary mixtures (AA vs EB: 408.4ms ± 14.85; AA/EB Mix: 448.5ms

± 10.39; n=18; Figure 17; Abraham et al., 2004: AA vs EB: 240ms ± 17; AA/EB Mix: 343ms ± 21; n=6)[81]. Further we found smaller difference between the two odour pairs compared to the previous data (AA vs EB: 40.1ms; Figure 17; Abraham et al., 2004: AA vs EB: 103ms)[81]. The differences can be attributed to multiple confounding technical differences. Firstly, we employ a modified algorithm to determine the discrimination time which uses a more stringent threshold p-value for the t-test-based comparison of the sampling behaviour for rewarded and unrewarded trials (Figure 11). This threshold is not only more robust for a large variety of different sampling patterns but also removes the need for manual inspection (and possibly adjustments) of the calculations. However, it significantly increases the DTs, on average by 130ms (Figure 12a). Secondly, due to overall advances in technology, the data in the automated setup could be acquired at millisecond precision while the data obtained in the manual setups needed to be filtered at 50Hz to conserve storage space. Thus, the variance of the DTs is larger, as no filtering was performed to retain the full precision of the data. Thirdly, the IR-beams used to measure the sampling behaviour are placed at a larger distance to the lick-port compared to the manuals setups. Hence, mice insert their heads deeper into the odour port used in this setup compared to the previously used odour ports. While this greatly improves reliability of the acquired sensor data, this also increases the measured DTs by approximately 20ms (data not shown) since the mice need to retract their heads further. As the overall effect of increasing DTs with increasing stimulus complexity could still be shown (AA vs EB: 408.4ms ± 14.85; AA/EB Mix: 448.5ms ± 10.39; paired t-test, p=0.01; Figure 17) and the difference in the measured values can be directly attributed to changes in hardware, we feel the benefits of minimal experimenter involvement both in the training and the data analysis outweigh the negative aspect of not reproducing the exact values previously published. On the other hand, the analysis algorithm and the odour port design can easily be adjusted if direct comparison with the values obtained in the manual setups is essential.

Effects of varying group size on olfactory conditioning

To determine, how the group size may affect acquisition of the task or odour discrimination, we gradually reduced the group size of the large cohort by randomly removing animals (Figure 18). Here, we found a linear increase in both daily performance as well as trial numbers with reduced group size. However, the daily performance for the large cohort was still high (93%) and above the threshold of 90% or even 80% typically used for odour discrimination tasks[109,197,208,209]. Similarly, the number of daily trials for the large cohort was 80 trials lower than the amount after group reduction (385.76 trials ± 19.38 vs 305.71 trials ± 36.75), yet these values are both still higher than the 100-300 daily trials reported for the manual setups or other similar behaviour tasks[81,210–212]. As some studies found a relationship between the number of trials performed per day or conditioning session and the learning speed as well as the final performance, we re-evaluated the learning and discrimination performance based on the daily activity of the animals[213,214]. Here, we found no evidence of differential learning speeds of any of the tested odour pairs based on the daily activity (Figure 19). While we did find a significant increase in supra-threshold performance for the low activity group between discrimination of amyl acetate and ethyl butyrate and the binary mixture of the

two, the increase was negligibly small (fraction correct: AA vs EB: 0.98 ± 0.01; AA/EB Mix: 0.98 ± 0.03) and well above the performance threshold.

Typically, olfactory tests in mice are done during the night-phase as they are crepuscular (i.e. dusk and dawn active) and considered to show increased activity during the night time. Additionally, a previous study found a day-time dependency or the detection threshold of vanilla[215]. Further, others found increased activation of neurons in the OB and the PirCtx during the night phase[216,217]. We did observe an increase in trials during the night phase for the small group of animals (n=3) but for the large group (n=18), the number of trials across all animals remained fairly stable over both the day and night phase (Figure 20). However, on the level of individual animals, we did observe clear distinct activity peaks for the animals in the large group. These peaks were distributed throughout the entire day regardless of light or dark phase. Since these activity peaks remained stable during the training, this suggests that animals in larger groups each have a preferred time point for initiating trials, most likely because the single odour port leads to competition for the port. Importantly, we found no time-dependent changes in performance for odour discrimination, indicating that animals are capable to perform at high accuracy throughout the day. Further studies would be needed to determine if these activity peaks influence odour detection, since no threshold detection experiments were performed as this thesis was focussed on odour discrimination.

Advantages and limitations of automated olfactory conditioning

We trained a total of 148 mice of varying genetic background across 10 independent behaviour runs, generating 500000 to 1000000 trials per individual behavioural run. Coupled with the simultaneously acquired sensor data, this exceeds the limits of the manual behaviour setups, which lacked sensors tracking odour presentation and typically allowed for no more than 10000 trials per animal due to the taxing water deprivation and single-housing scheme[61,132]. Additionally, animals are trained with minimal experimenter presence, greatly increasing through-put while reducing the risk of unintentionally introducing a handling bias[157,218,219]. Further, as each animal carries a unique RFID chip, the training protocol can be tailored towards the needs of each individual animal. We have successfully used this option in Part 2 and Part 3 of this thesis, i.e. by adjusting the specific sequence of odour tasks. Moreover, we adjusted the amount of water dispensed per correctly identified rewarded trial for each animal individually, as maintaining the satiety state of an animal has been shown to greatly improve behaviour training[211,220,221]. Additionally, due to the large number of independently addressable odour valves, multiple odour tasks were performed in parallel using the same olfactometer, allowing animals with a high daily activity to progress with their training independently of animals with a low activity. This simultaneously reduced potential sources of variation due to the use of multiple different olfactometers.

However, the single-odour port and the group-housing setting may not be suited for aggressive mouse lines prone to fighting or burdened mouse lines which could be at a disadvantage when competing for access to the odour port. Additionally, group-housing of male and female mice would require spayed animals or a strict separation of the genders. This could be achieved by incorporating an (RFID or IR-based) access control

system at the odour port or even by using multiple access-restricted housing areas instead of a single large group-housing cage[222,223]. Furthermore, the odour port itself can easily be changed to incorporate additional sensory modalities or to perform an alternate choice task instead of a go/no-go paradigm.

Lastly, the setup can be used to generate a continuous supply of animals trained on a given behavioural paradigm that can be used for complex experiments like *in vivo* imaging or electrophysiological recordings. As these methods are inherently time consuming (i.e. multiple surgeries across at least 10-14 days for implantation of microendoscopic lenses), having a "pool" of highly trained animals could greatly improve efficiency of these experiments[224,225].

Part 2: Influence of increased neurogenesis on odour discrimination

To assess the effect of temporally and spatially defined increased neurogenesis, the novel 4D mouse line was used. In these mice, increased expression of cell cycle regulatory proteins Cdk4 and cyclin D1 results in an increase in symmetric, proliferative cell divisions of neuronal stem cells (NSC)[169]. This causes an overall increase in the number of NSCs, as shown in previous studies overexpressing the 4D complex in the developing mouse brain or other organs like the pancreas or the heart[167,168,226,227]. However, the genetic basis of the overexpression, namely the ROSA26$^{loxP(rtTA)}$-tet$^{Cdk4\text{-}cyclinD1\text{-}RFP}$ mouse line, is far more versatile, as it can be used with any Cre-driver line to create precisely restricted overexpression of the 4D complex.

In this study, the nestin^{CreERT2} diver line was chosen, limiting expression of tamoxifen-inducible Cre-recombinase to neuronal precursor cells. Through the precisely timed application of tamoxifen and doxycycline, NSC increase was restricted to the subventricular zone (SVZ) without affecting other areas of adult-neurogenesis (Figure 22 and Supplementary Figure 17). As the SVZ gives rise to different types of adult-born interneurons of the OB, the fate of these supernumerary neurons was assessed (Figure 23)[48–52]. We found a significant increase in NeuN-expressing GC as well as PGCs in the GL. This is consistent with previous studies which found that adult-born neurons from the SVZ predominantly integrate as NeuN-expressing, GABAergic interneurons in the GCL while a minority integrates as PGCs[163,183]. Overall, the ratio of cells integrating into the GL versus the GCL layer did not differ between 4D$^+$ animals and the 4D$^-$ controls or the values reported for wild-type animals[228,229]. Furthermore, electrophysiological recordings and detailed reconstructions of supernumerary GCs showed that these cells were physiologically normal and functionally integrated into the OB circuitry (Supplementary Figure 18)[65,169,184]. Since increased GC-derived inhibition of the principal OB relay cells, the MCs has been reported to improve odour discrimination, 4D$^+$ animals may outperform their littermates in odour discrimination tasks[122–125]. On the other hand, we also consistently observed a significant increase in tyrosine hydroxylase (TH) expressing cells. These dopaminergic cells act on D2 receptors found on olfactory sensory neuron (OSN) terminals and thus reduce activation MCs[67,74–78]. Thus, this increase in TH-expressing PGCs in 4D$^+$ animals could also cause them to perform worse than their littermates, as reduced MC activity has been shown to reduce the ability to discriminate odours[109].

To address these points, mice were trained on a sequence of different odour pairs and mixtures (Figure 24). We found no difference between the genotypes for learning speed or the ability to distinguish different odour pairs at high performance. Further, we found no apparent difference between the baseline parameters or the discrimination time and all of these parameters were well within the range reported by previous studies using this automated behaviour setup or manual setups (see Part 1 of the Discussion)[61,62,81]. However, we additionally presented the animals with the highly demanding task of discriminating binary mixture of two enantiomers at a 1:10 dilution. Since the enantiomers used generate highly similar glomerular activation patterns, a mixture further increases stimulus similarity while the dilution reduces the activation due to reduced binding-probability to odour receptors[207,230,231]. Thus, this task was deliberately chosen to determine the limits of the olfactory system. 4D$^+$ animals showed an

increased performance compared to their littermate controls which specifically originated from the higher response accuracy towards the unrewarded odour (Figure 27). In other words, littermate controls fail to withhold the lick response when presented with the unrewarded odour while 4D-transgenes respond to both rewarded and unrewarded odours with roughly the same accuracy. This reduced accuracy specifically for unrewarded odours can be explained as a mechanism to maximise the obtained reward: Typically, performing with high accuracy maximises the reward purely by correctly identifying each odour. However, when high accuracy is not achievable, the chances of receiving a reward can be increased by also licking for trials that cannot definitively be identified as unrewarded trials and hence still offer the opportunity of receiving a reward. This strategy switch from an approach maximising accuracy towards a "one fits all" response that reduces the overall decision-making process also resembles the cost-benefit trade-off which is well established in human decision-making processes and has been shown to result in reward sizes only minimally different from the optimized-accuracy approach[187,232].

Lastly, we did not see any effect of the supernumerary neurons on odour memory, which is in line with a previous study that also failed to detect changes in odour memory or odour discrimination[53]. However, other studies did report changes in odour memory due to changed neurogenesis[149,150,233]. As all of these studies used differing approaches to reduce the number of OB interneurons, whereas our approach aimed at increasing the number of cells, more analyses ideally using the same odour memory task are required to finally determine the effect of adult neurogenesis on olfactory memory.

Our results suggest, that the ability to discriminate highly similar odours is increased in $4D^+$ but far less pronounced than estimated based on the increase in interneurons. One explanation could be the small overall increase in interneurons compared to the pre-existing cells: While the number of adult-born GCs was increased by roughly 40% compared to controls, new-born GCs only constitute approximately 15% of the total number of GCs, meaning the actual increase was only about 5%[234]. Taking into account studies reporting that even removal of the olfactory bulb has little impact on odour discrimination, this small number of truly supernumerary cells was most likely by far too few to have a readily apparent impact on the olfactory system[230,235]. Lastly, the potential impact of TH-expressing cells warrants further investigation as recent studies have shown that PGCs are capable of completely silencing OSN input to mitral cells, resulting in a complete failure to detect the respective odour[109]. Since these cells are located in the glomerular layer, they as well as the resulting glomerular activation patterns could simultaneously be analysed using *in vivo* imaging techniques to determine if and which role these cells play in odour discrimination[81,236,237].

Part 3: Influence of T-type calcium channels in olfactory bulb granule cells on odour discrimination

Previous *in vitro* studies have shown, that the global activation of olfactory bulb (OB) granule cells (GC) after local activation is mediated by T-type calcium channels[120,130]. To investigate, if this global activation has an impact on *in vivo* odour discrimination, we used a shRNA-mediated knock-down approach for the spatially and temporally defined reduction of T-type expression in GCs.

Establishing a T-type calcium channel knock-down using shRNA

To this date, only a hand full of studies attempting shRNA-mediated knock-down of any of the three T-type subunits have been published and only a single sequence targeting $Ca_V3.1$ has been used in more than one study[176,238–241]. Further, no study has ever tried to simultaneously knock-down expression of all three subunits, hence we first needed to establish shRNA-sequences targeting $Ca_V3.2$ and $Ca_V3.3$ as well as a control sequence to account for general effects of shRNA expression. To increase screening throughput, this was done by infecting rat primary cortical and hippocampal cell cultures with AAVs expressing the sequences of interest, as these cells express all three T-type subunits. Due to the high sequence homology of the channels, all shRNA were highly similar, precluding the use of scrambled or even missmatch control sequences. Hence a commercially available non-targeting sequence was used as a control sequence, which has already been used in a similar context[175].

Subsequent quantification using real-time quantitative PCR (qPRC) revealed great variability both between the individual sequences as well as between different viral batches expressing the same shRNA sequence (Figure 33). Concerning the differences between different viral batches, we found an increased knock-down efficiency with increased viral titers and purity. This is in line with previous studies that have found a clear link between knock-down efficiency and viral titer[242,243]. However, overly high viral titers (approximately $>10^{12}$ viral genomes per microlitre) have been shown to cause toxicity and induce apoptosis[244]. Hence, virus batches of comparable titer and purity were used for the screening to ensure comparability and expression was verified using the marker fluorophore also expressed by the AAVs (Figure 30, Figure 31 and Figure 32). Overall, we found no evidence of cytotoxicity and reduced expression of the subunits targeted by the respective shRNA sequences. However, we also observed considerable variation of the expression of the not-targeted subunits, consistent with compensatory upregulation of the targeted subunit[245]. Therefore we decided to use a single AAV to express the most promising sequences, as this is the only way to ensure that any infected cell would express shRNAs targeting all subunits, preventing compensatory upregulation that could mask the overall physiological effect. This approach was supported by the finding that the triple knock-down virus showed higher knock-down efficiencies for $Ca_V3.1$ as well as $Ca_V3.2$ compared to a virus mixture of three individual viruses (Figure 34). The residual high expression of the $Ca_V3.3$ subunit could be caused by the use of the same promoter already used for the $Ca_V3.1$ which could cause promoter competition[246,247]. However, previous studies have successfully used up to 10 instances of the same promoter within a single AAV without any negative effects[248].

In vivo verification of the viruses showed massive anatomical changes and reorganization in the olfactory bulbs of animals injected with the pure triple-knock down virus. This was not seen in animals injected with either the diluted triple-knock down virus or the diluted non-targeting control virus, consistent with the toxic effects of overly high viral titers observed by others[244]. The knock-down efficiency was again assessed using qPCR, showing a clear reduction of all subunits (Figure 36). However, the residual expression was still considerably higher (up to 30%) compared to the *in vitro* results. This could be a technical issue, as only one housekeeping gene was used as a reference during the *in vitro* screening while two were used for the *in vivo* validation, potentially leading to less accurate results[249,250]. However, re-analysis using the same reference used in the cell-culture data only had a minor effect on the residual expression levels (data not shown). On the other hand, the cell-culture experiments were performed in cells obtained from rats while the *in vivo* analysis was performed in mice. Despite the fact, that both animals show significant sequence homology for the three T-types subunits and that shRNA sequences were specifically designed to target mRNA of both species, they may still be differentially effective *in vivo*. Lastly, infection of a cell-culture with an AAV results in massive, large-scale infection while injection into tissue often fails to capture all cells. Despite infecting 50-75% if the neurons in the granule cell layer, the remaining non-infected cells may greatly affect the observed knock-down efficiency. Since these sequences still were the most efficient sequences of the screening and as previous studies using the very same sequence targeting $Ca_V3.1$ did result in an altered phenotype, we chose to continue the behavioural analysis with these sequences and use the high-throughput capability of the setup to determine, if further improvements to the sequences would be feasible.

Effect of the T-type calcium channel knock-down on odour discrimination

For the behavioural assessment, we trained mice on a sequence of odour pairs and mixtures (Figure 37). All mice were able to acquire the discrimination task and discriminate the odours at high accuracy with no apparent differences between the knock-down and the control group. Interestingly, the typical increase in trials to reach criterion for the binary mixture of amyl acetate and ethyl butyrate compared to the pure odours was only present in the control group and not the knock-down group. Conversely, only the knock-down group showed an increase in trials to performance for an even more similar mixture (AA/EB Mix (48%/52%)). However due to the failure of many animals to reach the performance criterion within two weeks, the groups were considerably reduced for the more complex mixture. For the remaining baseline parameters we again observed the usual variations as discussed previously, but no evident difference between the two groups.

As a block of T-type mediated calcium transients has been shown to reduce the inhibition onto mitral cells by nearly half, a lack of these transients *in vivo* should considerably increase the discrimination time for complex odour stimuli, similar to the effect found in mice lacking NMDAR-subunits reported by Abraham et al. in 2010[120,132]. Yet, we observed no change in the discrimination time between pure odours and their binary mixture for the knock-down group whereas the control group showed a clear increase (Figure 39).

This result could indicate, that the lack of the global activation of granule cells already affects discrimination of pure odours. As the reduction of mitral cell inhibition was less pronounced in NMDAR-knockout mice compared to reduction when blocking T-type calcium channels, this may explain why this affected discrimination of pure odours was not seen in NMDAR-knockout animals[120,132]. Additionally, post-hoc verification of the knock-down efficiency revealed, that a far smaller percentage of the GCL was infected by the AAVs and that the ostensibly non-targeting control sequence did have a considerable effect of the expression of all T-type subunits (Figure 41). As the viral titers of both viruses were comparable (approximately 10^8 viral genomes per microlitre), it is unlikely that the effect of the control sequences is due to titer-based toxicity. Additionally, the knock-down efficiency is determined in relation to the expression of two housekeeping genes, hence it is unlikely that the reduction is due to unspecific off-target effects of the control sequence that only affect the T-type calcium channels but not either of the references. Yet, additional tests determining the expression levels of other synaptic proteins or ion channels could show if truly only T-type channels are affected or if the control sequences also impaired expression of other genes. Lastly, the prolonged high expression of the marker fluorophore may have negatively impacted the infected cells as derivatives of the dsRed fluorophore have a tendency of aggregating and triggering cytotoxic effects[251]. This may cause infected cells to reduce expression of any non-essential genes resulting in their decrease while maintaining high expression of housekeeping genes. Thus use of a different fluorophore and a weaker promoter than the CAG-promoter used in this study may be beneficial to the overall health of the infected cells.

Taken together, these results report the first attempt simultaneous shRNA-mediated knock-down of all three T-type subunits. Despite the residual expression *in vivo*, this approach can serve as the basis for further studies and improvements to the knock-down efficiency, i.e. by incorporating more shRNA-sequences. The subtle behavioural effects indicate the definitive need to revisit the olfactometric testing once an improved shRNA toolkit is available. Considering the small net-reduction of the T-type expression in this present study, the behavioural results may greatly underestimate the influence of T-type calcium channels on odour learning and discrimination.

Acknowledgements

I'd like to thank my supervisor, Prof. Dr. Thomas Kuner, for the opportunity to work in his lab. Over the past years, I have learned invaluable lessons on time-management, communication skills, personnel management and best practices of basic research, which I hopefully will not soon forget.

I am extremely thankful to Dr. Christoph Körber for the continued scientific guidance, general lab advice, helpful discussions and support regarding virtually all aspects of this thesis.

I am very grateful to Prof. Dr. Stefan Frings and Prof. Dr. Christoph Schuster for being part of my Thesis Advisory Committee, the discussions and many points of constructive feedback both during and outside of the TAC meetings.

Further I'd like to thank Dr. Rolf Sprengel for the scientific discussions, his input in the tracer project and the generous access to lab equipment.

I am grateful to all members of the DFG priority programme 1392 for the scientific discussions and funding.

I would also like to thank my collaborators, Prof. Dr. Andreas Schaefer for sharing the concept of the behaviour setup and feedback on improving data acquisition and analysis, Dr. Christoph Körber for sharing his Task5 knock-out mice and including me in his ephys projects and Prof. Dr. Federico Calegari as well as Dr. Sara Bragado Alonso for sharing the 4D-transgenic mice and establishing their biomolecular features.

I am grateful for the technical support from the workshops of the Max Planck Institute for Medical Research and the University of Heidelberg during construction of the behaviour setup; most importantly from Niklas Neef and Martin Lukat (MPI mechanical workshop), Jürgen Tritthardt and Walter Rödel (MPI electronic workshop) and Gero Hofmann (mechanical workshop) as well as Edgar Bäuerle (electronics workshop).

I would like to thank my fellow students, especially Patric, both Daniels, Frank, Firat, Hannah and my office (in)-mate Ivo, for their help and making science seem fun despite the madness.

I'd like to thank the staff of the Kuner and Sprengel Labs for their help over the years, especially

Ursel Lindenberger for her invaluable administrative work;

Michaela Kaiser for cloning the plasmids and advice on all things molecular biology;

Marion Schmitt for generating primary cell cultures and help with histology;

Gerald Bendner for his advice on molecular biology, his incredibly detailed protocols and sharing the labelmaker;

Annette Herold for generating high-titer AAVs, help with histology and cell-culture work;

Claudia Kocksch for generating AAVs and cell-culture work;

I am extremely grateful to my friends and family for their continued support throughout this seemingly never-ending thesis.

And last but not least, Raspel, Anja & Niedi: thank you guys. For absolutely everything

Abbreviations

%	Percent
°C	Degrees centigrade
µg	Microgram
µl	Microlitre
µm	Micrometre
3D	Three dimensional
4D	Cdk4/cyclin D1
AAV	Adeno-associated virus
ACSF	artificial cerebro-spinal fluid
AI	Analogue input
AMPA	α-amino-3-hydroxy-5-methyl-4-isoxazolepropionic acid
AMPAR	AMPA receptor
ANOVA	Analysis of variance
AO	Analogue output
AOB	Accessory olfactory bulb
AOE	Accessory olfactory epithelium
ASCII	American standard code for information interchange
BNC	Bayonet Neill-Concelman
BrdU	Bromodeoxyuridine
BSA	Bovine serum albumin
CAD	Computer-aided design
CAG	CMV early enhancer/chicken beta actin
CalB	Calbindin
CalR	Calretinin
cDNA	Coding deoxyribonucleic acid
cm	Centimetre
C_m	membrane capacitance
C_t	Cycle threshold
CV	Coefficient of variation
DAPI	4',6-diamidino-2-phenylindole
DAQ	Data acquisition
DCX	Doublecortin
DMEM	Dulbecco's modified eagle medium
DMSO	Dimethyl sulfoxide
DNA	Deoxyribonucleic acid
DT	Discrimination time
E	Embryonic day
EDTA	Ethylenediaminetetraacetic acid
EGFP	Enhanced green-fluorescent protein
EPL	External plexiform layer

ETC	External tufted cell
FAM-dye	Fluorescein amidite dye
FCS	Fetal calf serum
FPLC	Fast protein liquid chromatography
FV	Final valve
g	Gram
GABA	Gamma-aminobutyric acid
GC	Granule cell
GCL	Granule cell layer
GFP	Green-fluorescent protein
GL	Glomerular layer
HEK cell	Human embryonic kidney cell
HEPES	4-(2-hydroxyethyl)-1-piperazineethanesulfonic acid
Hz	Hertz
I/O	Input/Output
IPL	Internal plexiform layer
IR	Infrared
ITI	Inter-trial interval
ITR	inverted-tandem-repeats
kg	Kilogram
LED	Light-emitting diode
loxP	locus of X(cross)-over in P1
MC	Mitral cell
MCL	Mitral cell layer
mg	Milligram
mGFP	Membrane-bound green-fluorescent protein
min	Minute
mM	Millimolar
mm	Millimetre
MOB	Main olfactory bulb
MOE	Main olfactory epithelium
mOrange	Monomeric Orange (fluorescent protein; derivative of DsRed)
ms	Millisecond
mV	Millivolt
MΩ	Megaohm
NA	Numerical aperture
NC	Normally closed
NeuN	neuronal nuclei
NGS	Normal goat serum
NI	National Instruments
nl	Nanolitre
NMDA	N-methyl-D-aspartate
NMDAR	NMDA receptor

NO	Normally open
OB	Olfactory bulb
OE	Olfactory epithelium
OSN	Olfactory sensory neuron
pA	Picoampere
PA sequence	poly-A sequence
PBS	Phosphate buffered solution
PCI	Peripheral component interconnect
PCR	Polymerase chain reaction
PEI	Polyethilenimine
PirCtx	Piriform cortex
PFA	Para-formaldehyde
PGC	Periglomerular cell
PLA	Polylactic acid
PVC	Polyvinyl chloride
qPCR	Quantitative real-time PCR
RFID	Radio-frequency identification
RFP	Red-fluorescent protein
R_{in}	input resistance
RNA	Ribonucleic acid
rtTA	reverse tetracycline-controlled transactivator
s	Second
SAC	Short axon cell
sccm	Standard cubic centimeters per minute
SEM	Standard error of the mean
shRNA	Short hairpin ribonucleic acid
slpm	Standard litre per minute
TC	Tufted cell
TH	Tyrosine hyroxylase
TRP channel	Transient receptor potential channel
U	Enzyme unit
UNF	Unified fine thread
V	Volt
VDC	Volt direct current
V_{hold}	holding potential
VNO	Vomeronasal organ
V_{Rest}	resting membrane potential
WPRE	woodchuck post-transcriptional regulatory element
wt	Wild-type
z	standard normal cumulative distribution function
τ_m	membrane constant

References

1. Bargmann, C. I., Hartwieg, E. & Horvitz, H. R. Odorant-selective genes and neurons mediate olfaction in C. elegans. *Cell* **74,** 515–527 (1993).
2. Thesen, A., Steen, J. B. & Døving, K. B. Behaviour of dogs during olfactory tracking. *J. Exp. Biol.* **180,** 247–51 (1993).
3. Bitterman, M. E., Menzel, R., Fietz, A. & Schäfer, S. Classical conditioning of proboscis extension in honeybees (Apis mellifera). *J. Comp. Psychol.* **97,** 107–119 (1983).
4. Porter, J. *et al.* Mechanisms of scent-tracking in humans. *Nat. Neurosci.* **10,** 27–29 (2007).
5. Mystery, U. The Human Sense of Smell: Are We Better Than We Think? *PLoS Biol.* **2,** 572–575 (2004).
6. Weiss, T. *et al.* Perceptual convergence of multi-component mixtures in olfaction implies an olfactory white. *Proc. Natl. Acad. Sci. U. S. A.* **109,** 19959–64 (2012).
7. Buck, L. & Axel, R. A novel multigene family may encode odorant receptors: a molecular basis for odor recognition. *Cell* **65,** 175–87 (1991).
8. Young, J. M. The sense of smell: genomics of vertebrate odorant receptors. *Hum. Mol. Genet.* **11,** 1153–1160 (2002).
9. Zhang, X. & Firestein, S. The olfactory receptor gene superfamily of the mouse. *Nat. Neurosci.* **5,** 124–133 (2002).
10. Ache, B. W. & Young, J. M. Olfaction: Diverse species, conserved principles. *Neuron* **48,** 417–430 (2005).
11. Lledo, P., Gheusi, G. & Vincent, J. Information processing in the mammalian olfactory system. *Physiol. Rev.* **85,** 281–317 (2005).
12. Luo, M. Encoding Pheromonal Signals in the Accessory Olfactory Bulb of Behaving Mice. *Science (80-.).* **299,** 1196–1201 (2003).
13. Bear, D. M., Lassance, J.-M., Hoekstra, H. E. & Datta, S. R. The Evolving Neural and Genetic Architecture of Vertebrate Olfaction. *Curr. Biol.* **26,** R1039–R1049 (2016).
14. Mombaerts, P. Genes and ligands for odorant, vomeronasal and taste receptors. *Nat. Rev. Neurosci.* **5,** 263–278 (2004).
15. Duchamp-Viret, P., Duchamp, A. & Chaput, M. A. Peripheral Odor Coding in the Rat and Frog: Quality and Intensity Specification. *J. Neurosci.* **20,** 2383–2390 (2000).
16. Malnic, B., Hirono, J., Sato, T. & Buck, L. B. Combinatorial receptor codes for odors. *Cell* **96,** 713–23 (1999).
17. Kaupp, U. B. Olfactory signalling in vertebrates and insects: differences and commonalities. *Nat. Rev. Neurosci.* **11,** 188–200 (2010).
18. Munger, S. D., Leinders-Zufall, T. & Zufall, F. Subsystem Organization of the Mammalian Sense of Smell. *Annu. Rev. Physiol.* **71,** 115–140 (2008).
19. Duchamp-Viret, P., Chaput, M. A. & Duchamp, A. Odor response properties of rat olfactory receptor neurons. *Science (80-.).* **284,** 2171–2179 (1999).
20. Shepherd, G. M. *The Synaptic Organization of the Brain*. *The Synaptic Organization of the Brain* (2004). at <http://www.lavoisier.fr/notice/fr603507.html>
21. Kuner, T. & Schaefer, A. T. Molecules, cells and networks involved in processing olfactory stimuli in the mouse olfactory bulb. *e-Neuroforum* **2,** 61–67 (2011).
22. Pinching, A. J. & Powell, T. P. S. the Neuron Types of the Glomerular Layer of the Olfactory Bulb. *J. Cell Sci* **9,** 305–345 (1971).
23. Zhu, P. X. *et al.* The neuropil of the periglomerular region of the olfactory bulb. *Neuron* **24,** 379–409 (2001).
24. Kasowski, H. J., Kim, H. & Greer, C. A. Compartmental organization of the olfactory bulb glomerulus. *J. Comp. Neurol.* **407,** 261–274 (1999).
25. Shipley, M. T. & Ennis, M. Functional organization of olfactory system. *J. Neurobiol.* **30,** 123–76 (1996).
26. Cavarretta, F., Marasco, A., Hines, M. L., Shepherd, G. M. & Migliore, M. Glomerular and Mitral-Granule Cell Microcircuits Coordinate Temporal and Spatial Information Processing in the Olfactory Bulb. *Front. Comput. Neurosci.* **10,** 1–19 (2016).
27. Aungst, J. L. *et al.* Centre–surround inhibition among olfactory bulb glomeruli. *Nature* **426,** 623–629 (2003).
28. McQuiston, A. R. & Katz, L. C. Electrophysiology of interneurons in the glomerular layer of the rat olfactory bulb. *J. Neurophysiol.* **86,** 1899–907 (2001).
29. Kiyokage, E. *et al.* Molecular Identity of Periglomerular and Short Axon Cells. *J. Neurosci.* **30,** 1185–1196 (2010).
30. Nagayama, S., Homma, R. & Imamura, F. Neuronal organization of olfactory bulb circuits. *Front. Neural Circuits* **8,** 1–19 (2014).

31. Orona, E., Rainer, E. C. & Scott, J. W. Dendritic and axonal organization of mitral and tufted cells in the rat olfactory bulb. *J. Comp. Neurol.* **226,** 346–356 (1984).
32. Salin, P.-A., Lledo, P.-M., Vincent, J.-D. & Charpak, S. Dendritic Glutamate Autoreceptors Modulate Signal Processing in Rat Mitral Cells. *J. Neurophysiol.* **85,** 1275–1282 (2017).
33. Rall, W., Shepherd, G. M., Reese, T. S. & Brightman, M. W. Dendrodendritic synaptic pathway for inhibition in the olfactory bulb. *Exp. Neurol.* **14,** 44–56 (1966).
34. Haberly, L. B. & Price, J. L. The axonal projection patterns of the mitral and tufted cells of the olfactory bulb in the rat. *Brain Res.* **129,** 152–7 (1977).
35. Nagayama, S. Differential Axonal Projection of Mitral and Tufted Cells in the Mouse Main Olfactory System. *Front. Neural Circuits* **4,** 1–8 (2010).
36. Igarashi, K. M. *et al.* Parallel mitral and tufted cell pathways route distinct odor information to different targets in the olfactory cortex. *J. Neurosci.* **32,** 7970–85 (2012).
37. Macrides, F. & Schneider, S. P. Laminar organization of mitral and tufted cells in the main olfactory bulb of the adult hamster. *J. Comp. Neurol.* **208,** 419–430 (1982).
38. Tatti, R. *et al.* A population of glomerular glutamatergic neurons controls sensory information transfer in the mouse olfactory bulb. *Nat. Commun.* **5,** 1–16 (2014).
39. Liu, W. ???L & Shipley, M. T. Intrabulbar associational system in the rat olfactory bulb comprises cholecystokinin???containing tufted cells that synapse onto the dendrites of GABAergic granule cells. *J. Comp. Neurol.* **346,** 541–558 (1994).
40. Wachowiak, M. & Shipley, M. T. Coding and synaptic processing of sensory information in the glomerular layer of the olfactory bulb. *Semin. Cell Dev. Biol.* **17,** 411–23 (2006).
41. Banerjee, A. *et al.* An Interglomerular Circuit Gates Glomerular Output and Implements Gain Control in the Mouse Olfactory Bulb. *Neuron* **87,** 193–207 (2015).
42. Mori, K. Membrane and synaptic properties of identified neurons in the olfactory bulb. *Prog. Neurobiol.* **29,** 275–320 (1987).
43. Schoppa, N. E. & Urban, N. N. Dendritic processing within olfactory bulb circuits. *Trends Neurosci.* **26,** 501–506 (2003).
44. Shepherd, G. M. Synaptic organization of the mammalian olfactory bulb. *Physiol. Rev.* **52,** 864–917 (2017).
45. Parrish-Aungst, S., Shipley, M. T., Erdelyi, F., Szabo, G. & Puche, A. C. Quantitative analysis of neuronal diversity in the mouse olfactory bulb. *J. Comp. Neurol.* **501,** 825–36 (2007).
46. Didier, a *et al.* A dendrodendritic reciprocal synapse provides a recurrent excitatory connection in the olfactory bulb. *Proc. Natl. Acad. Sci. U. S. A.* **98,** 6441–6 (2001).
47. Isaacson, J. S. Mechanisms governing dendritic gamma-aminobutyric acid (GABA) release in the rat olfactory bulb. *Proc. Natl. Acad. Sci. U. S. A.* **98,** 337–42 (2001).
48. Kelsch, W., Mosley, C. P., Lin, C. W. & Lois, C. Distinct mammalian precursors are committed to generate neurons with defined dendritic projection patterns. *PLoS Biol.* **5,** 2501–2512 (2007).
49. Merkle, F. T. *et al.* Adult neural stem cells in distinct microdomains generate previously unknown interneuron types. *Nat. Neurosci.* **17,** 207–14 (2014).
50. Merkle, F. T., Mirzadeh, Z. & Alvarez-Buylla, A. Mosaic organization of neural stem cells in the adult brain. *Science* **317,** 381–4 (2007).
51. Li, W. L. *et al.* Adult-born neurons facilitate olfactory bulb pattern separation during task engagement. *Elife* **7,** 1–26 (2018).
52. Lemasson, M. Neonatal and Adult Neurogenesis Provide Two Distinct Populations of Newborn Neurons to the Mouse Olfactory Bulb. *J. Neurosci.* **25,** 6816–6825 (2005).
53. Breton-Provencher, V., Lemasson, M., Peralta, M. R. & Saghatelyan, A. Interneurons Produced in Adulthood Are Required for the Normal Functioning of the Olfactory Bulb Network and for the Execution of Selected Olfactory Behaviors. *J. Neurosci.* **29,** 15245–15257 (2009).
54. Cecchi, G. A., Petreanu, L. T., Alvarez-Buylla, A. & Magnasco, M. O. Unsupervised learning and adaptation in a model of adult neurogenesis. *J. Comput. Neurosci.* **11,** 175–182 (2001).
55. Alonso, M. *et al.* Olfactory discrimination learning increases the survival of adult-born neurons in the olfactory bulb. *J. Neurosci.* **26,** 10508–13 (2006).
56. Takahashi, H., Yoshihara, S. & Tsuboi, A. The Functional Role of Olfactory Bulb Granule Cell Subtypes Derived From Embryonic and Postnatal Neurogenesis. *Front. Mol. Neurosci.* **11,** 1–11 (2018).
57. Woolf, T., Shepherd, G. & Greer, C. Local information processing in dendritic trees: subsets of spines in granule cells of the mammalian olfactory bulb. *J. Neurosci.* **11,** 1837–1854 (2018).
58. Woolf, T. B., Shepherd, G. M. & Greer, C. A. Serial reconstructions of granule cell spines in the mammalian olfactory bulb. *Synapse* **7,** 181–192 (1991).

59. Egger, V. & Urban, N. N. Dynamic connectivity in the mitral cell-granule cell microcircuit. *Semin. Cell Dev. Biol.* **17,** 424–32 (2006).
60. Bywalez, W. G. *et al.* Local postsynaptic voltage-gated sodium channel activation in dendritic spines of olfactory bulb granule cells. *Neuron* **85,** 590–601 (2015).
61. Nunes, D. & Kuner, T. Disinhibition of olfactory bulb granule cells accelerates odour discrimination in mice. *Nat. Commun.* **6,** 8950 (2015).
62. Nunes, D. & Kuner, T. Axonal sodium channel NaV1.2 drives granule cell dendritic GABA release and rapid odor discrimination. *PLOS Biol.* **16,** e2003816 (2018).
63. Scott, J. W., Wellis, D. P., Riggott, M. J. & Buonviso, N. Functional organization of the main olfactory bulb. *Microsc. Res. Tech.* **24,** 142–56 (1993).
64. Isaacson, J. S. & Strowbridge, B. W. Olfactory reciprocal synapses: dendritic signaling in the CNS. *Neuron* **20,** 749–61 (1998).
65. Schoppa, N. E. & Westbrook, G. L. Regulation of synaptic timing in the olfactory bulb by an A-type potassium current. *Nat. Neurosci.* **2,** 1106–13 (1999).
66. Margrie, T. W., Sakmann, B. & Urban, N. N. Action potential propagation in mitral cell lateral dendrites is decremental and controls recurrent and lateral inhibition in the mammalian olfactory bulb. *Proc. Natl. Acad. Sci. U. S. A.* **98,** 319–24 (2001).
67. Murphy, G. J., Darcy, D. P. & Isaacson, J. S. Intraglomerular inhibition: signaling mechanisms of an olfactory microcircuit. *Nat. Neurosci.* **8,** 354–64 (2005).
68. Gall, C. M., Hendry, S. H. C., Seroogy, K. B., Jones, E. G. & Haycock, J. W. Evidence for coexistence of GABA and dopamine in neurons of the rat olfactory bulb. *J. Comp. Neurol.* **266,** 307–318 (1987).
69. Kosaka, T., Hataguchi, Y., Hama, K., Nagatsu, I. & Jang-Yen, W. Coexistence of immunoreactivities for glutamate decarboxylase and tyrosine hydroxylase in some neurons in the periglomerular region of the rat main olfactory bulb: possible coexistence of gamma-aminobutyric acid (GABA) and dopamine. *Brain Res.* **343,** 166–171 (1985).
70. Kosaka, K. & Kosaka, T. Synaptic organization of the glomerulus in the main olfactory bulb : Compartments of the glomerulus and heterogeneity of the periglomerular cells. *Anat. Sci. Int.* 80–90 (2005).
71. Whitman, M. C. & Greer, C. A. Adult-generated neurons exhibit diverse developmental fates. *Dev. Neurobiol.* **67,** 1079–93 (2007).
72. De Marchis, S. *et al.* Generation of Distinct Types of Periglomerular Olfactory Bulb Interneurons during Development and in Adult Mice: Implication for Intrinsic Properties of the Subventricular Zone Progenitor Population. *J. Neurosci.* **27,** 657–664 (2007).
73. Kosaka, K. & Kosaka, T. Chemical properties of type 1 and type 2 periglomerular cells in the mouse olfactory bulb are different from those in the rat olfactory bulb. *Brain Res.* **1167,** 42–55 (2007).
74. Ennis, M. *et al.* Dopamine D2 Receptor–Mediated Presynaptic Inhibition of Olfactory Nerve Terminals. *J. Neurophysiol.* **86,** 2986–2997 (2017).
75. Berkowicz, D. a & Trombley, P. Q. Dopaminergic modulation at the olfactory nerve synapse. *Brain Res.* **855,** 90–9 (2000).
76. Pignatelli, A., Kobayashi, K., Okano, H. & Belluzzi, O. Functional properties of dopaminergic neurones in the mouse olfactory bulb. *J. Physiol.* **564,** 501–514 (2005).
77. Shao, Z., Puche, A. C., Kiyokage, E., Szabo, G. & Shipley, M. T. Two GABAergic Intraglomerular Circuits Differentially Regulate Tonic and Phasic Presynaptic Inhibition of Olfactory Nerve Terminals. *J. Neurophysiol.* **101,** 1988–2001 (2009).
78. Gabellec, M.-M., Panzanelli, P., Sassoè-Pognetto, M. & Lledo, P.-M. Synapse-specific localization of vesicular glutamate transporters in the rat olfactory bulb. *Eur. J. Neurosci.* **25,** 1373–83 (2007).
79. Hayar, A., Shipley, M. T. & Ennis, M. Olfactory bulb external tufted cells are synchronized by multiple intraglomerular mechanisms. *J. Neurosci.* **25,** 8197–208 (2005).
80. Shao, Z., Puche, A. C., Liu, S. & Shipley, M. T. Intraglomerular inhibition shapes the strength and temporal structure of glomerular output. *J. Neurophysiol.* **108,** 782–793 (2012).
81. Abraham, N. M. *et al.* Maintaining accuracy at the expense of speed: stimulus similarity defines odor discrimination time in mice. *Neuron* **44,** 865–76 (2004).
82. Spors, H. & Grinvald, A. Spatio-temporal dynamics of odor representations in the mammalian olfactory bulb. *Neuron* **34,** 301–15 (2002).
83. Rubin, B. D. & Katz, L. C. Optical imaging of odorant representations in the mammalian olfactory bulb. *Neuron* **23,** 499–511 (1999).
84. Meister, M. & Bonhoeffer, T. Tuning and topography in an odor map on the rat olfactory bulb. *J. Neurosci.* **21,** 1351–60 (2001).

85. Wachowiak, M. & Cohen, L. B. Representation of odorants by receptor neuron input to the mouse olfactory bulb. *Neuron* **32,** 723–35 (2001).
86. Belluscio, L. & Katz, L. C. Symmetry, stereotypy, and topography of odorant representations in mouse olfactory bulbs. *J. Neurosci.* **21,** 2113–22 (2001).
87. Uchida, N., Takahashi, Y. K., Tanifuji, M. & Mori, K. Odor maps in the mammalian olfactory bulb. *Nat. Neurosci.* **3,** 1035–1043 (2000).
88. Bozza, T., McGann, J. P., Mombaerts, P. & Wachowiak, M. In vivo imaging of neuronal activity by targeted expression of a genetically encoded probe in the mouse. *Neuron* **42,** 9–21 (2004).
89. Mori, K., Takahashi, Y. K., Igarashi, K. M. & Yamaguchi, M. Maps of odorant molecular features in the Mammalian olfactory bulb. *Physiol. Rev.* **86,** 409–33 (2006).
90. Vincis, R., Gschwend, O., Bhaukaurally, K., Beroud, J. & Carleton, A. Dense representation of natural odorants in the mouse olfactory bulb. *Nat. Neurosci.* **15,** 537–539 (2012).
91. Schaefer, A. T. & Margrie, T. W. Spatiotemporal representations in the olfactory system. *Trends Neurosci.* **30,** 92–100 (2007).
92. Carey, R. M. & Wachowiak, M. Effect of sniffing on the temporal structure of mitral/tufted cell output from the olfactory bulb. *J. Neurosci.* **31,** 10615–26 (2011).
93. Khan, R. M. & Sobel, N. Neural processing at the speed of smell. *Neuron* **44,** 744–7 (2004).
94. Uchida, N., Kepecs, A. & Mainen, Z. F. Seeing at a glance, smelling in a whiff: rapid forms of perceptual decision making. *Nat. Rev. Neurosci.* **7,** 485–91 (2006).
95. Lledo, P. M., Merkle, F. T. & Alvarez-Buylla, A. Origin and function of olfactory bulb interneuron diversity. *Trends Neurosci.* **31,** 392–400 (2008).
96. Shipley, M. T. & Ennis, M. Functional organization of olfactory system. *J. Neurobiol.* **30,** 123–76 (1996).
97. Murphy, G. J. Sensory Neuron Signaling to the Brain: Properties of Transmitter Release from Olfactory Nerve Terminals. *J. Neurosci.* **24,** 3023–3030 (2004).
98. Cheetham, C. E. J., Park, U. & Belluscio, L. Rapid and continuous activity-dependent plasticity of olfactory sensory input. *Nat. Commun.* **7,** 1–11 (2016).
99. Urban, N. N. & Sakmann, B. Reciprocal intraglomerular excitation and intra- and interglomerular lateral inhibition between mouse olfactory bulb mitral cells. *J. Physiol.* **542,** 355–367 (2002).
100. Christie, J. M. & Westbrook, G. L. Lateral excitation within the olfactory bulb. *J. Neurosci.* **26,** 2269–77 (2006).
101. Pimentel, D. O. & Margrie, T. W. Glutamatergic transmission and plasticity between olfactory bulb mitral cells. *J. Physiol.* **586,** 2107–19 (2008).
102. Aroniadou-Anderjaska, V., Ennis, M. & Shipley, M. T. Dendrodendritic Recurrent Excitation in Mitral Cells of the Rat Olfactory Bulb. *J. Neurophysiol.* **82,** 489–494 (2017).
103. Halabisky, B., Friedman, D., Radojicic, M. & Strowbridge, B. W. Calcium influx through NMDA receptors directly evokes GABA release in olfactory bulb granule cells. *J. Neurosci.* **20,** 5124–34 (2000).
104. Carlson, G. C., Shipley, M. T. & Keller, A. Long-Lasting Depolarizations in Mitral Cells of the Rat Olfactory Bulb. *J. Neurosci.* **20,** 2011–2021 (2018).
105. Panzanelli, P., López-Bendito, G., Luján, R. & Sassoé-Pognetto, M. Localization and developmental expression of GABA B receptors in the rat olfactory bulb. *J. Neurocytol.* **33,** 87–99 (2004).
106. Pirez, N. & Wachowiak, M. In Vivo Modulation of Sensory Input to the Olfactory Bulb by Tonic and Activity-Dependent Presynaptic Inhibition of Receptor Neurons. *J. Neurosci.* **28,** 6360–6371 (2008).
107. McGann, J. P. *et al.* Odorant representations are modulated by intra- but not interglomerular presynaptic inhibition of olfactory sensory neurons. *Neuron* **48,** 1039–1053 (2005).
108. Fukunaga, I., Berning, M., Kollo, M., Schmaltz, A. & Schaefer, A. T. Two Distinct Channels of Olfactory Bulb Output. *Neuron* **75,** 320–329 (2012).
109. Roland, B. *et al.* Massive normalization of olfactory bulb output in mice with a 'monoclonal nose'. *Elife* **5,** 1–25 (2016).
110. Smith, T. C. & Jahr, C. E. Self-inhibition of olfactory bulb neurons. *Nat. Neurosci.* **5,** 760–766 (2002).
111. Puopolo, M. & Belluzzi, O. Inhibitory Synapses Among Interneurons in the Glomerular Layer of Rat and Frog Olfactory Bulbs. *J. Neurophysiol.* **80,** 344–349 (2017).
112. Laurie, D. J., Seeburg, P. H. & Wisden, W. The distribution of 13 GABAA receptor subunit mRNAs in the rat brain. II. Olfactory bulb and cerebellum. *J. Neurosci.* **12,** 1063–76 (1992).
113. Gire, D. H. *et al.* Mitral cells in the olfactory bulb are mainly excited through a multistep signaling path. *J. Neurosci.* **32,** 2964–75 (2012).
114. Hayar, A., Karnup, S., Ennis, M. & Shipley, M. T. External tufted cells: a major excitatory element that coordinates glomerular activity. *J. Neurosci.* **24,** 6676–85 (2004).
115. De Saint Jan, D., Hirnet, D., Westbrook, G. L. & Charpak, S. External Tufted Cells Drive the Output of

Olfactory Bulb Glomeruli. *J. Neurosci.* **29,** 2043–2052 (2009).
116. Aroniadou-Anderjaska, V., Ennis, M. & Shipley, M. . Glomerular synaptic responses to olfactory nerve input in rat olfactory bulb slices. *Neuroscience* **79,** 425–434 (1997).
117. Cleland, T. A., Johnson, B. A., Leon, M. & Linster, C. Relational representation in the olfactory system. *Proc. Natl. Acad. Sci.* **104,** 1953–1958 (2007).
118. Lowe, G. Electrical signaling in the olfactory bulb. *Curr. Opin. Neurobiol.* **13,** 476–481 (2003).
119. Jahr, B. Y. C. E. & Nicoll, R. A. An intracellular analysis of dendrodendritic inhibition in the turtle in vitro olfactory bulb. 213–234 (1982).
120. Egger, V., Svoboda, K. & Mainen, Z. F. Dendrodendritic synaptic signals in olfactory bulb granule cells: local spine boost and global low-threshold spike. *J. Neurosci.* **25,** 3521–30 (2005).
121. Chen, W. R., Xiong, W. & Shepherd, G. M. Analysis of relations between NMDA receptors and GABA release at olfactory bulb reciprocal synapses. *Neuron* **25,** 625–33 (2000).
122. Yokoi, M., Mori, K. & Nakanishi, S. Refinement of odor molecule tuning by dendrodendritic synaptic inhibition in the olfactory bulb. *Proc. Natl. Acad. Sci. U. S. A.* **92,** 3371–5 (1995).
123. Katoh, K., Koshimoto, H., Tani, A. & Mori, K. Coding of odor molecules by mitral/tufted cells in rabbit olfactory bulb. II. Aromatic compounds. *J. Neurophysiol.* **70,** 2161–2175 (1993).
124. Mori, K. & Shepherd, G. M. Emerging principles of molecular signal processing by mitral/tufted cells in the olfactory bulb. *Seminars in Cell and Developmental Biology* **5,** 65–74 (1994).
125. Economo, M. N., Hansen, K. R. & Wachowiak, M. Control of Mitral/Tufted Cell Output by Selective Inhibition among Olfactory Bulb Glomeruli. *Neuron* **91,** 397–411 (2016).
126. Luo, M. & Katz, L. C. Response correlation maps of neurons in the mammalian olfactory bulb. *Neuron* **32,** 1165–1179 (2001).
127. Mori, K., Kogure, S. & Takagi, S. F. Alternating responses of olfactory bulb neurons to repetitive lateral olfactory tract stimulation. *Brain Res.* **133,** 150–155 (1977).
128. Cang, J. & Isaacson, J. S. In vivo whole-cell recording of odor-evoked synaptic transmission in the rat olfactory bulb. *J. Neurosci.* **23,** 4108–16 (2003).
129. Margrie, T. W. & Schaefer, A. T. Theta oscillation coupled spike latencies yield computational vigour in a mammalian sensory system. *J. Physiol.* **546,** 363–74 (2003).
130. Egger, V., Svoboda, K. & Mainen, Z. F. Mechanisms of lateral inhibition in the olfactory bulb: efficiency and modulation of spike-evoked calcium influx into granule cells. *J. Neurosci.* **23,** 7551–8 (2003).
131. Pinato, G. & Midtgaard, J. Regulation of granule cell excitability by a low-threshold calcium spike in turtle olfactory bulb. *J. Neurophysiol.* **90,** 3341–3351 (2003).
132. Abraham, N. M. *et al.* Synaptic inhibition in the olfactory bulb accelerates odor discrimination in mice. *Neuron* **65,** 399–411 (2010).
133. Shimshek, D. R. *et al.* Enhanced odor discrimination and impaired olfactory memory by spatially controlled switch of AMPA receptors. *PLoS Biol.* **3,** e354 (2005).
134. Gschwend, O., Beroud, J., Vincis, R., Rodriguez, I. & Carleton, A. Dense encoding of natural odorants by ensembles of sparsely activated neurons in the olfactory bulb. *Sci. Rep.* **6,** 36514 (2016).
135. Labarrera, C., London, M. & Angelo, K. Tonic inhibition sets the state of excitability in olfactory bulb granule cells. *J. Physiol.* **591,** 1841–1850 (2013).
136. Perez-Reyes, E. Molecular physiology of low-voltage-activated t-type calcium channels. *Physiol. Rev.* **83,** 117–61 (2003).
137. Cazade, M., Bidaud, I., Lory, P. & Chemin, J. Activity-dependent regulation of T-type calcium channels by submembrane calcium ions. *Elife* **6,** (2017).
138. Talavera, K. & Nilius, B. Biophysics and structure – function relationship of T-type Ca 2 + channels. **40,** 97–114 (2006).
139. Yunker, a. M. R. *et al.* Immunological characterization of T-type voltage-dependent calcium channel Cav3.1 (alpha1G) and Cav3.3 (alpha1I) isoforms reveal differences in their localization, expression, and neural development. *Neuroscience* **117,** 321–335 (2003).
140. Perez-Reyes, E. Molecular characterization of T-type calcium channels. *Cell Calcium* **40,** 89–96 (2006).
141. Talley, E. M. *et al.* Differential distribution of three members of a gene family encoding low voltage-activated (T-type) calcium channels. *J. Neurosci.* **19,** 1895–911 (1999).
142. Whitman, M. C. & Greer, C. a. Synaptic integration of adult-generated olfactory bulb granule cells: basal axodendritic centrifugal input precedes apical dendrodendritic local circuits. *J. Neurosci.* **27,** 9951–61 (2007).
143. Coskun, V. & Luskin, M. B. Intrinsic and extrinsic regulation of the proliferation and differentiation of cells in the rodent rostral migratory stream. *J. Neurosci. Res.* **69,** 795–802 (2002).
144. Carleton, A., Petreanu, L. T., Lansford, R., Alvarez-Buylla, A. & Lledo, P.-M. Becoming a new neuron in the

adult olfactory bulb. *Nat. Neurosci.* **6,** 507–518 (2003).
145. Lledo, P. M. & Valley, M. Adult olfactory bulb neurogenesis. *Cold Spring Harb. Perspect. Biol.* **8,** (2016).
146. Altman, J. Autoradiographic and histological studies of postnatal neurogenesis. *J. Comp. Neurol.* **137,** 433–457 (1969).
147. Gheusi, G. & Chaumont, F. De. Cellular and Behavioral Effects of Cranial Irradiation of the Subventricular Zone in Adult Mice. **4,** 1–11 (2009).
148. Bath, K. G. *et al.* Variant Brain-Derived Neurotrophic Factor (Val66Met) Alters Adult Olfactory Bulb Neurogenesis and Spontaneous Olfactory Discrimination. *J. Neurosci.* **28,** 2383–2393 (2008).
149. Kim, W. R. *et al.* Impaired Migration in the Rostral Migratory Stream But Spared Olfactory Function after the Elimination of Programmed Cell Death in Bax Knock-Out Mice. *J. Neurosci.* **27,** 14392–14403 (2007).
150. Gheusi, G. *et al.* Importance of newly generated neurons in the adult olfactory bulb for odor discrimination. *Proc. Natl. Acad. Sci. U. S. A.* **97,** 1823–8 (2000).
151. Larsen, C. M. & Grattan, D. R. Prolactin-induced mitogenesis in the subventricular zone of the maternal brain during early pregnancy is essential for normal postpartum behavioral responses in the mother. *Endocrinology* **151,** 3805–3814 (2010).
152. Larimer, P., Spatazza, J., Stryker, M. P., Alvarez-Buylla, A. & Hasenstaub, A. R. Development and long-term integration of MGE-lineage cortical interneurons in the heterochronic environment. *J. Neurophysiol.* **118,** 131–139 (2017).
153. Bodyak, N. & Slotnick, B. Performance of Mice in an Automated Olfactometer : Odor Detection , Discrimination and Odor Memory. *Chem. Senses* 637–645 (1999).
154. Slotnick, B. & Restrepo, D. Olfactometry with mice. *Curr. Protoc. Neurosci.* **Chapter 8,** Unit 8.20 (2005).
155. Van Loo, P. L. P., Van De Weerd, H. A., Van Zutphen, L. F. M. & Baumans, V. Preference for social contact versus environmental enrichment in male laboratory mice. *Lab. Anim.* **38,** 178–188 (2004).
156. Van Loo, P. L. P., Van Zutphen, L. F. M. & Baumans, V. Male management: Coping with aggression problems in male laboratory mice. *Lab. Anim.* **37,** 300–313 (2003).
157. Lewejohann, L. *et al.* Environmental bias? Effects of housing conditions, laboratory environment and experimenter on behavioral tests. *Genes, Brain Behav.* **5,** 64–72 (2006).
158. Maor, I., Elyada, Y. & Mizrahi, A. The Educage: an automated platform for studying auditory perceptual learning in mice. *bioRxiv* (2018). at <http://biorxiv.org/content/early/2018/03/04/273342.abstract>
159. Murphy, T. H. *et al.* High-throughput automated home-cage mesoscopic functional imaging of mouse cortex. *Nat. Commun.* **7,** 11611 (2016).
160. Shimshek, D. R. *et al.* Forebrain-specific glutamate receptor B deletion impairs spatial memory but not hippocampal field long-term potentiation. *J. Neurosci. Off. J. Soc. Neurosci.* **26,** 8428–8440 (2006).
161. Gschwend, O. *et al.* Neuronal pattern separation in the olfactory bulb improves odor discrimination learning. *Nat. Neurosci.* **18,** 1474–82 (2015).
162. Sakamoto, M. *et al.* Continuous Postnatal Neurogenesis Contributes to Formation of the Olfactory Bulb Neural Circuits and Flexible Olfactory Associative Learning. *J. Neurosci.* **34,** 5788–5799 (2014).
163. Imayoshi, I. *et al.* Roles of continuous neurogenesis in the structural and functional integrity of the adult forebrain. *Nat. Neurosci.* **11,** 1153–1161 (2008).
164. Mouret, A. *et al.* Learning and survival of newly generated neurons: when time matters. *J. Neurosci.* **28,** 11511–6 (2008).
165. Wang, W. *et al.* Inducible Activation of ERK5 MAP Kinase Enhances Adult Neurogenesis in the Olfactory Bulb and Improves Olfactory Function. *J. Neurosci.* **35,** 7833–7849 (2015).
166. Uchida, N. & Mainen, Z. F. Speed and accuracy of olfactory discrimination in the rat. *Nat. Neurosci.* **6,** 1224–9 (2003).
167. Artegiani, B., Lindemann, D. & Calegari, F. Overexpression of cdk4 and cyclinD1 triggers greater expansion of neural stem cells in the adult mouse brain. *J. Exp. Med.* **208,** 937–48 (2011).
168. Nonaka-Kinoshita, M. *et al.* Regulation of cerebral cortex size and folding by expansion of basal progenitors. *EMBO J.* **32,** 1817–28 (2013).
169. Bragado Alonso, S. *et al.* An increase in neural stem cells and olfactory bulb adult neurogenesis improves discrimination of highly similar odorants. *EMBO J.* **38,** e98791 (2019).
170. Miyoshi, G. *et al.* Genetic Fate Mapping Reveals That the Caudal Ganglionic Eminence Produces a Large and Diverse Population of Superficial Cortical Interneurons. *J. Neurosci.* **30,** 1582–1594 (2010).
171. Klugmann, M. *et al.* AAV-mediated hippocampal expression of short and long Homer 1 proteins differentially affect cognition and seizure activity in adult rats. *Mol. Cell. Neurosci.* **28,** 347–60 (2005).
172. Xia, X. G. *et al.* An enhanced U6 promoter for synthesis of short hairpin RNA. *Nucleic Acids Res.* **31,** e100 (2003).
173. Yuan, J. *et al.* Mammalian Pol III promoter H1 can transcribe shRNA inducing RNAi in chicken cells. *Mol.*

Biol. Rep. **33,** 33–41 (2006).
174. Jun-ichi, M. *et al.* Expression vector system based on the chicken β-actin promoter directs efficient production of interleukin-5. *Gene* **79,** 269–277 (1989).
175. Staquicini, F. I. *et al.* A subset of host B lymphocytes controls melanoma metastasis through a melanoma cell adhesion molecule/MUC18-dependent interaction: Evidence from mice and humans. *Cancer Res.* **68,** 8419–8428 (2008).
176. Park, Y.-G. *et al.* CaV3.1 is a tremor rhythm pacemaker in the inferior olive. *Proc. Natl. Acad. Sci.* **107,** 10731–10736 (2010).
177. Bolaños, F., LeDue, J. M. & Murphy, T. H. Cost effective raspberry pi-based radio frequency identification tagging of mice suitable for automated in vivo imaging. *J. Neurosci. Methods* **276,** 79–83 (2017).
178. Dresbach, T. *et al.* Functional regions of the presynaptic cytomatrix protein Bassoon: Significance for synaptic targeting and cytomatrix anchoring. *Mol. Cell. Neurosci.* **23,** 279–291 (2003).
179. Schindelin, J. *et al.* Fiji: an open-source platform for biological-image analysis. *Nat. Methods* **9,** 676–82 (2012).
180. Dondzillo, A. *et al.* Targeted three-dimensional immunohistochemistry reveals localization of presynaptic proteins Bassoon and Piccolo in the rat calyx of Held before and after the onset of hearing. *J. Comp. Neurol.* **518,** 1008–29 (2010).
181. Abraham, N. M., Guerin, D., Bhaukaurally, K. & Carleton, A. Similar odor discrimination behavior in head-restrained and freely moving mice. *PLoS One* **7,** e51789 (2012).
182. Brown, R. & Motulsky, H. Detecting outliers when fitting data with nonlinear regression - a new method based on robust nonlinear regression and the false discovery rate. *BMC Bioinformatics* **7,** 1–20 (2006).
183. Bagley, J., LaRocca, G., Jimenez, D. A. & Urban, N. N. Adult neurogenesis and specific replacement of interneuron subtypes in the mouse main olfactory bulb. *BMC Neurosci.* **8,** 1–13 (2007).
184. Burton, S. D. & Urban, N. N. Rapid Feedforward Inhibition and Asynchronous Excitation Regulate Granule Cell Activity in the Mammalian Main Olfactory Bulb. *J. Neurosci.* **35,** 14103–14122 (2015).
185. Zacksenhouse, M., Bogacz, R. & Holmes, P. Robust versus optimal strategies for two-alternative forced choice tasks. *J. Math. Psychol.* **54,** 230–246 (2010).
186. Ratcliff, R. A theory of memory retrieval. *Psychol. Rev.* **85,** 59–108 (1978).
187. Holmes, P. & Cohen, J. D. Optimality and some of its discontents: Successes and shortcomings of existing models for binary decisions. *Top. Cogn. Sci.* **6,** 258–278 (2014).
188. Lee, J. H. *et al.* Cloning and expression of a novel member of the low voltage-activated T-type calcium channel family. *J. Neurosci.* **19,** 1912–21 (1999).
189. Seol, M. & Kuner, T. Ionotropic glutamate receptor GluA4 and T-type calcium channel Cav3.1 subunits control key aspects of synaptic transmission at the mouse L5B-POm giant synapse. *Eur. J. Neurosci.* **42,** 3033–3044 (2015).
190. Callaway, E. M. & Luo, L. Monosynaptic Circuit Tracing with Glycoprotein-Deleted Rabies Viruses. *J. Neurosci.* **35,** 8979–85 (2015).
191. Wickersham, I. R., Finke, S., Conzelmann, K. K. & Callaway, E. M. Retrograde neuronal tracing with a deletion-mutant rabies virus. *Nat. Methods* **4,** 47–49 (2007).
192. Pan, D. *et al.* Biodistribution and toxicity studies of VSVG-pseudotyped lentiviral vector after intravenous administration in mice with the observation of in vivo transduction of bone marrow. *Mol. Ther.* **6,** 19–29 (2002).
193. Choi, O. R. B. & Engel, J. D. Developmental regulation of β-globin gene switching. *Cell* **55,** 17–26 (1988).
194. B'SYS GmbH Laboratories. *Assay Catalogue*. (2009).
195. Uchida, N. & Mainen, Z. F. Speed and accuracy of olfactory discrimination in the rat. *Nat. Neurosci.* **6,** 1224–1229 (2003).
196. Shusterman, R., Smear, M. C., Koulakov, A. A. & Rinberg, D. Precise olfactory responses tile the sniff cycle. *Nat. Neurosci.* **14,** 1039–1044 (2011).
197. Jordan, R., Kollo, M. & Schaefer, A. T. Sniffing Fast: Paradoxical Effects on Odor Concentration Discrimination at the Levels of Olfactory Bulb Output and Behavior. *Eneuro* **5,** ENEURO.0148-18.2018 (2018).
198. Nagel, K. I., Hong, E. J. & Wilson, R. I. Synaptic and circuit mechanisms promoting broadband transmission of olfactory stimulus dynamics. *Nat. Neurosci.* (2014). doi:10.1038/nn.3895
199. Szyszka, P., Stierle, J. S., Biergans, S. & Galizia, C. G. The speed of smell: odor-object segregation within milliseconds. *PLoS One* **7,** e36096 (2012).
200. Sehdev, A., Mohammed, Y. G., Triphan, T. & Szyszka, P. Olfactory Object Recognition Based on Fine-Scale Stimulus Timing in Drosophila. *iScience* **13,** 113–124 (2019).
201. Aldworth, Z. N. & Stopfer, M. A. Trade-off between information format and capacity in the olfactory

system. *J. Neurosci.* **35,** 1521–9 (2015).
202. Parabucki, A. *et al.* Odor Concentration Change Coding in the Olfactory Bulb. *Eneuro* **6,** ENEURO.0396-18.2019 (2019).
203. Jordan, R., Fukunaga, I., Kollo, M. & Schaefer, A. T. Active Sampling State Dynamically Enhances Olfactory Bulb Odor Representation. *Neuron* **98,** 1214–1228.e5 (2018).
204. Soucy, E. R., Albeanu, D. F., Fantana, A. L., Murthy, V. N. & Meister, M. Precision and diversity in an odor map on the olfactory bulb. *Nat. Neurosci.* **12,** 210–20 (2009).
205. Lundström, J. N., Gordon, A. R., Alden, E. C., Boesveldt, S. & Albrecht, J. Methods for building an inexpensive computer-controlled olfactometer for temporally-precise experiments. *Int. J. Psychophysiol.* **78,** 179–89 (2010).
206. Davison, I. G. & Katz, L. C. Sparse and Selective Odor Coding by Mitral/Tufted Neurons in the Main Olfactory Bulb. *J. Neurosci.* **27,** 2091–2101 (2007).
207. Abraham, N. M. *et al.* Similarity and strength of glomerular odor representations define neural metric of sniff-invariant discrimination time. *bioRxiv* 356279 (2018). doi:10.1101/356279
208. Laska, M. Olfactory discrimination learning in an outbred and an inbred strain of mice. *Chem. Senses* **40,** 489–496 (2015).
209. Kelliher, K. R., Ziesmann, J., Munger, S. D., Reed, R. R. & Zufall, F. Importance of the CNGA4 channel gene for odor discrimination and adaptation in behaving mice. *Proc. Natl. Acad. Sci.* **100,** 4299–4304 (2003).
210. Scott, B. B., Brody, C. D. & Tank, D. W. Cellular Resolution Functional Imaging in Behaving Rats Using Voluntary Head Restraint. *Neuron* **80,** 371–384 (2013).
211. Guo, Z. V. *et al.* Procedures for behavioral experiments in head-fixed mice. *PLoS One* **9,** (2014).
212. Zinyuk, L. E., Datiche, F. & Cattarelli, M. Cell activity in the anterior piriform cortex during an olfactory learning in the rat. *Behav. Brain Res.* **124,** 29–32 (2001).
213. Kishimoto, Y. *et al.* Task-specific enhancement of hippocampus-dependent learning in mice deficient in monoacylglycerol lipase, the major hydrolyzing enzyme of the endocannabinoid 2-arachidonoylglycerol. *Front. Behav. Neurosci.* **9,** 1–14 (2015).
214. Kehoe, E. J. & Gormezano, I. Effects of trials per session on conditioning of the rabbit's nictitating membrane response. *Bull. Psychon. Soc.* **4,** 434–436 (1974).
215. Granados-Fuentes, D. *et al.* Daily rhythms in olfactory discrimination depend on clock genes but not the suprachiasmatic nucleus. *J. Biol. Rhythms* **26,** 552–60 (2011).
216. Granados-Fuentes, D., Tseng, A. & Herzog, E. D. A Circadian Clock in the Olfactory Bulb Controls Olfactory Responsivity. *J. Neurosci.* **26,** 12219–12225 (2006).
217. Funk, D. & Amir, S. Circadian modulation of Fos responses to odor of the red fox, a rodent predator, in the rat olfactory system. *Brain Res.* **866,** 262–267 (2000).
218. Mandillo, S. *et al.* Reliability, robustness, and reproducibility in mouse behavioral phenotyping: a cross-laboratory study. *Physiol. Genomics* **34,** 243–255 (2008).
219. Sorge, R. E. *et al.* Olfactory exposure to males, including men, causes stress and related analgesia in rodents. *Nat. Methods* **11,** 629–632 (2014).
220. Zariwala, H. A., Kepecs, A., Uchida, N., Hirokawa, J. & Mainen, Z. F. The limits of deliberation in a perceptual decision task. *Neuron* **78,** 339–351 (2013).
221. Berditchevskaia, A., Cazé, R. D. & Schultz, S. R. Performance in a GO/NOGO perceptual task reflects a balance between impulsive and instrumental components of behaviour. *Sci. Rep.* **6,** 1–15 (2016).
222. Winter, Y. & Schaefers, A. T. U. A sorting system with automated gates permits individual operant experiments with mice from a social home cage. *J. Neurosci. Methods* **196,** 276–280 (2011).
223. Rivalan, M., Munawar, H., Fuchs, A. & Winter, Y. An automated, experimenter-free method for the standardised, operant cognitive testing of rats. *PLoS One* **12,** 1–19 (2017).
224. Resendez, S. L. *et al.* Visualization of cortical, subcortical and deep brain neural circuit dynamics during naturalistic mammalian behavior with head-mounted microscopes and chronically implanted lenses. *Nat. Protoc.* **11,** 566–597 (2016).
225. Gulati, S., Cao, V. Y. & Otte, S. Multi-layer Cortical Ca^{2+} Imaging in Freely Moving Mice with Prism Probes and Miniaturized Fluorescence Microscopy. *J. Vis. Exp.* 1–9 (2017). doi:10.3791/55579
226. Azzarelli, R. *et al.* Multi-site Neurogenin3 Phosphorylation Controls Pancreatic Endocrine Differentiation. *Dev. Cell* **41,** 274–286.e5 (2017).
227. Mohamed, T. M. A. *et al.* Regulation of Cell Cycle to Stimulate Adult Cardiomyocyte Proliferation and Cardiac Regeneration. *Cell* **173,** 104–116.e12 (2018).
228. Whitman, M. C. & Greer, C. A. Adult neurogenesis and the olfactory system. *Prog. Neurobiol.* **89,** 162–175 (2009).
229. Lledo, P. M. & Saghatelyan, A. Integrating new neurons into the adult olfactory bulb: Joining the network,

life-death decisions, and the effects of sensory experience. *Trends Neurosci.* **28,** 248–254 (2005).
230. McBride, K. & Slotnick, B. Discrimination between the Enantiomers of Carvone and of Terpinen-4-ol Odorants in Normal Rats and Those with Lesions of the Olfactory Bulbs. *J. Neurosci.* **26,** 9892–9901 (2006).
231. Linster, C. *et al.* Odorant Enantiomers. *Eur. J. Neurosci.* **21,** 9837–9843 (2001).
232. Balci, F. *et al.* Acquisition of decision making criteria: reward rate ultimately beats accuracy. *Atten. Percept. Psychophys.* **73,** 640–57 (2011).
233. Rossi, B., Maton, G. & Collin, T. Calcium-permeable presynaptic AMPA receptors in cerebellar molecular layer interneurones. *J. Physiol.* **586,** 5129–45 (2008).
234. Ninkovic, J., Mori, T. & Gotz, M. Distinct Modes of Neuron Addition in Adult Mouse Neurogenesis. *J. Neurosci.* **27,** 10906–10911 (2007).
235. Lu, X. C. M. & Slotnick, B. M. Olfaction in rats with extensive lesions of the olfactory bulbs: Implications for odor coding. *Neuroscience* **84,** 849–866 (1998).
236. Rothermel, M., Brunert, D., Zabawa, C., Díaz-Quesada, M. & Wachowiak, M. Transgene expression in target-defined neuron populations mediated by retrograde infection with adeno-associated viral vectors. *J. Neurosci.* **33,** 15195–206 (2013).
237. Spors, H., Wachowiak, M., Cohen, L. B. & Friedrich, R. W. Temporal dynamics and latency patterns of receptor neuron input to the olfactory bulb. *J. Neurosci.* **26,** 1247–59 (2006).
238. Seol, M. & Kuner, T. Ionotropic glutamate receptor GluA4 and T-type calcium channel Ca v 3.1 subunits control key aspects of synaptic transmission at the mouse L5B-POm giant synapse. *Eur. J. Neurosci.* **42,** 3033–3044 (2015).
239. Li, X., Peng, C., Wang, X. & Wen, X. One-cell model for inhibiting Cav3.3 mRNA expression by RNA interference. *Biotechnol. Biotechnol. Equip.* **31,** 349–355 (2017).
240. Gackière, F. *et al.* CaV3.2 T-type calcium channels are involved in calcium-dependent secretion of neuroendocrine prostate cancer cells. *J. Biol. Chem.* **283,** 10162–10173 (2008).
241. Bourinet, E. *et al.* Silencing of the Cav3.2 T-type calcium channel gene in sensory neurons demonstrates its major role in nociception. *EMBO J.* **24,** 315–324 (2005).
242. Koornneef, A. *et al.* Apolipoprotein B knockdown by AAV-delivered shRNA lowers plasma cholesterol in mice. *Mol. Ther.* **19,** 731–740 (2011).
243. de Solis, C. A. *et al.* Viral delivery of shRNA to amygdala neurons leads to neurotoxicity and deficits in Pavlovian fear conditioning. *Neurobiol. Learn. Mem.* **124,** 34–47 (2015).
244. Ehlert, E. M., Eggers, R., Niclou, S. P. & Verhaagen, J. Cellular toxicity following application of adeno-associated viral vector-mediated RNA interference in the nervous system. *BMC Neurosci.* **11,** (2010).
245. Rosati, B. & McKinnon, D. Regulation of Ion Channel Expression. *Circ. Res.* **94,** 874–883 (2004).
246. Conte, C., Dastugue, B. & Vaury, C. Promoter competition as a mechanism of transcriptional interference mediated by retrotransposons. *EMBO J.* **21,** 3908–3916 (2002).
247. Hirschman, J. E., Durbin, K. J. & Winston, F. Genetic evidence for promoter competition in Saccharomyces cerevisiae. *Mol. Cell. Biol.* **8,** 4608–15 (1988).
248. Fink, S. *et al.* A simple approach for multi-targeted shRNA-mediated inducible knockdowns using Sleeping Beauty vectors. *PLoS One* **13,** 1–13 (2018).
249. Guénin, S. *et al.* Normalization of qRT-PCR data: the necessity of adopting a systematic, experimental conditions-specific, validation of references. *J. Exp. Bot.* **60,** 487–93 (2009).
250. Kozera, B. & Rapacz, M. Reference genes in real-time PCR. *J. Appl. Genet.* **54,** 391–406 (2013).
251. Zhou, J., Lin, J., Zhou, C., Deng, X. & Xia, B. Cytotoxicity of red fluorescent protein DsRed is associated with the suppression of Bcl-xL translation. *FEBS Lett.* **585,** 821–827 (2011).

Appendix

List of supplementary figures

Supplementary Figure 1 Assembly of the setup frame (part 1). 101
Supplementary Figure 2 Assembly of the setup frame (part 2). 102
Supplementary Figure 3 Assembly of the setup frame (part 3). 103
Supplementary Figure 4 Construction of the housing cage. 104
Supplementary Figure 5 Assembly of the bedding stopper placed underneath the housing cage. 104
Supplementary Figure 6 Assembly of the lid of the housing cage. 105
Supplementary Figure 7 Assembly of the tunnel placed on the housing cage lid. 105
Supplementary Figure 8 Mounting of the tunnel to the housing cage lid. 106
Supplementary Figure 9 Assembly of the olfactometer. 106
Supplementary Figure 10 Overview of the inputs to the olfactometer. 107
Supplementary Figure 11 Assembly of the lick spout and the 3D printed odour port. 108
Supplementary Figure 12 Overview of the water delivery system and the custom 3D printed holder. 108
Supplementary Figure 13 Assembly of the caps for the odour reservoirs. 109
Supplementary Figure 14 Placement of the air filters on the back of the pneumatics back plane. 109
Supplementary Figure 15 Placement of the parts on the front of the pneumatics back plane. 110
Supplementary Figure 16 Schematic representation of the pneumatics connections of the setup. 111
Supplementary Figure 17 Effect of the 4D transgene on the subventricular zone (SVZ) and the rostral migratory stream (RMS). 112
Supplementary Figure 18 Electrophysiological properties of 4D-derived granule cells in the olfactory bulb. 114

Assembly of the automated behaviour setup

Please refer to the detailed parts lists in the methods section (see Automated behaviour setup) of the main part of this thesis as well as the 3D CAD plans of the setup which can be found in the accompanying online repository (https://github.com/AutomatedOlfactoryBehaviour/Beast).

Assembly of the setup frame

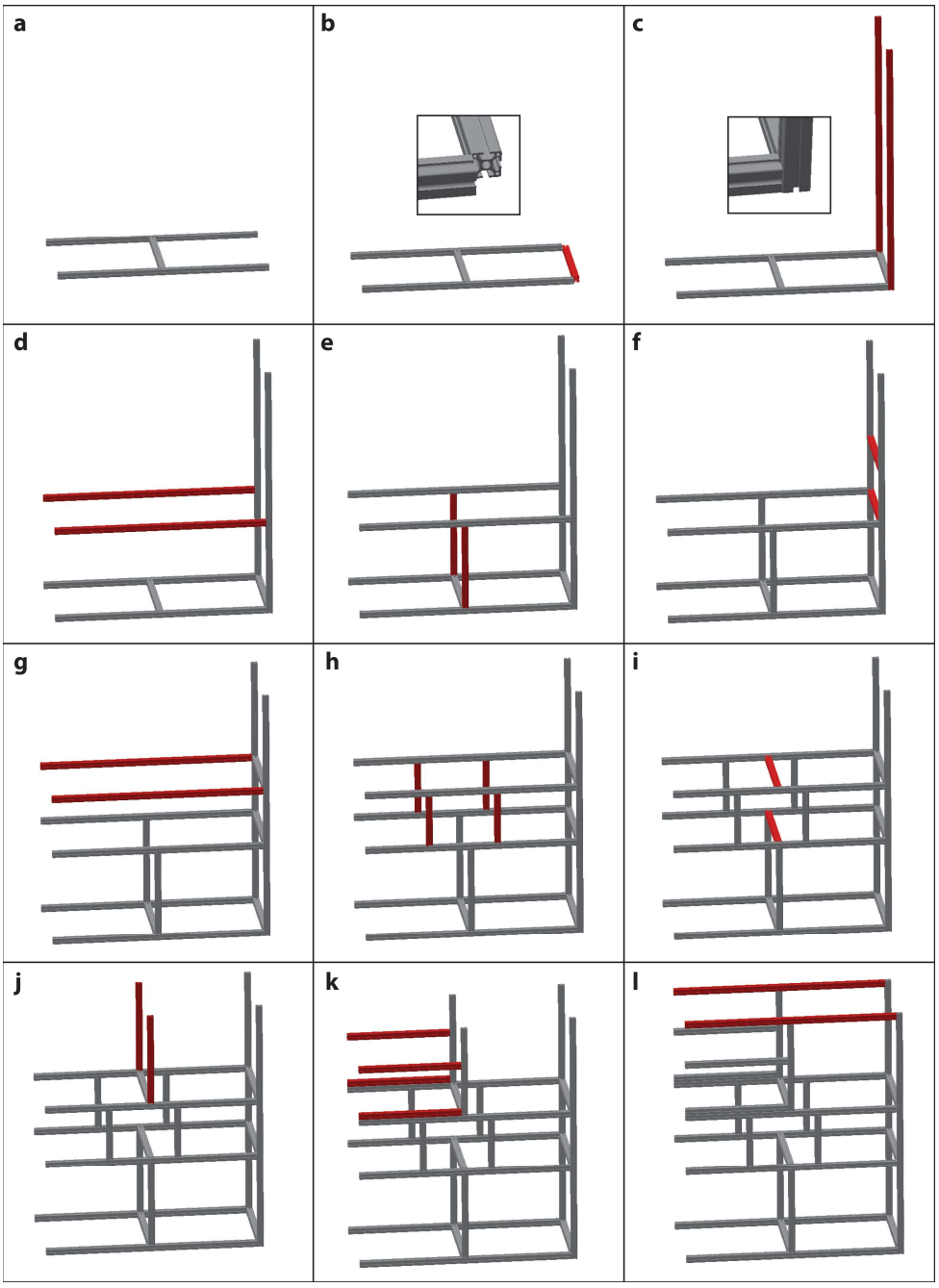

Supplementary Figure 1 Assembly of the setup frame (part 1). (a) Assemble two 1360mm and a 620mm aluminium profile in the form of the letter "H". **(b)** Add another 620mm profile on one end of the H leaving a gap at the corner. **(c)** Add two vertical beams (1627mm) into the free corner. **(d)** Add two 1360mm profiles horizontally spaced 550mm from the bottom profiles. **(e)** Add two vertical 550mm beams. **(f)** Add two 620mm beams with one spaced 550mm from the bottom and the second 880mm from the bottom. **(g)** Add two 1360mm profiles horizontally spaced 880mm from the bottom. **(h)** Add four vertical beams (330mm) between the horizontal beams. The rightmost two should be spaced roughly 490mm from the vertical beams to accommodate the NIM-Bin power supply. **(i)** Add two 620mm beams. **(j)** Add two vertical beams (587mm) spaced roughly 660mm from the right-hand vertical beam. **(k)** Add four horizontal beams (660mm). The bottom ones should sit flush on top of the vertical beams and will hold the rollers for the housing cage. The top ones should be placed roughly 278mm higher and will serve as the anchor point for the housing cage lid. **(l)** Add two 1360mm horizontal beams at the top of the setup.

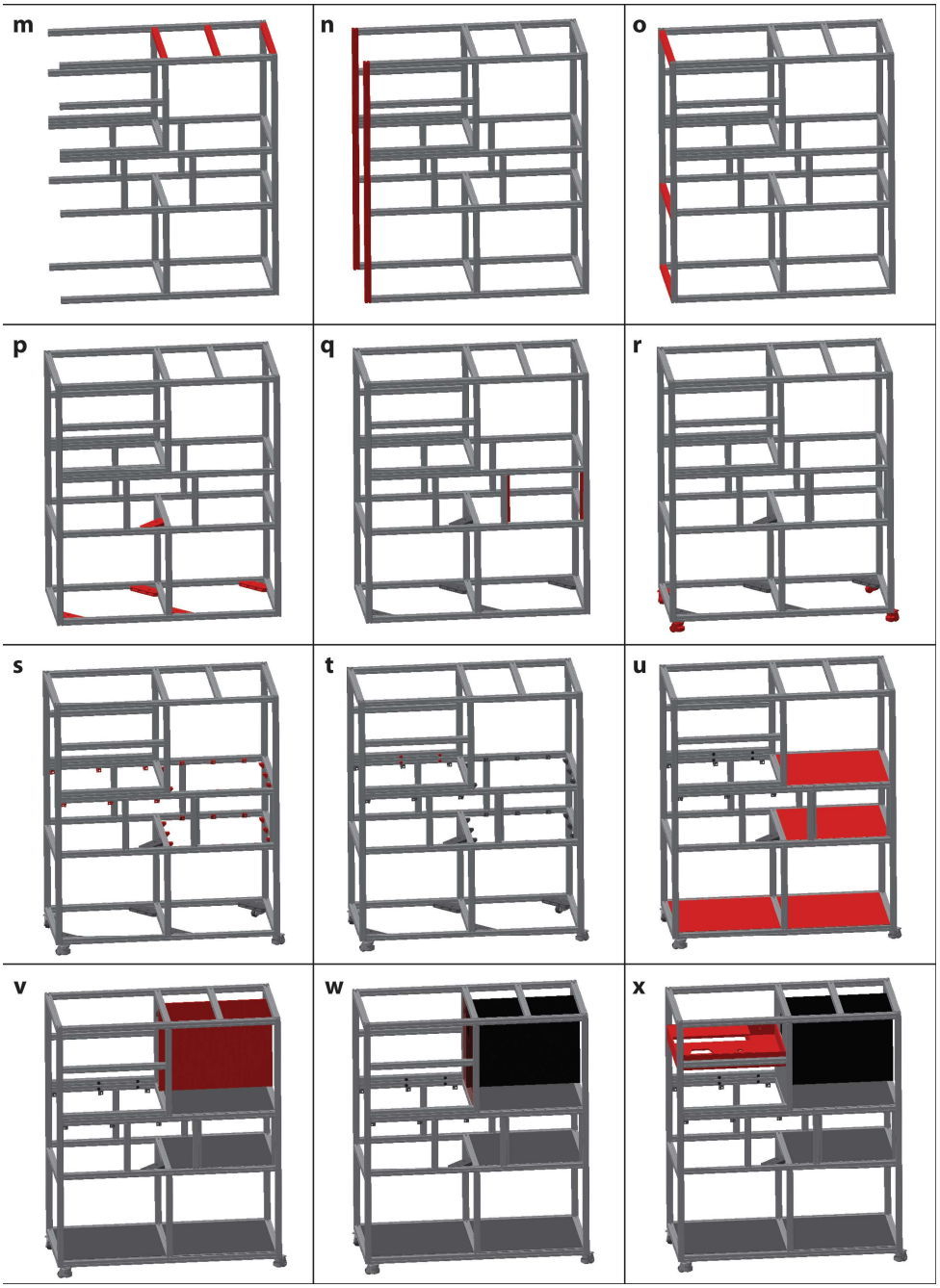

Supplementary Figure 2 Assembly of the setup frame (part 2). (m) Add three 620mm profiles at the top of the setup. The leftmost one should be the same position as the vertical beams installed in **(j)**. **(n)** Add two vertical 1627mm beams at the left side of the setup. **(o)** Add three 620mm beams at the left side of the setup. **(p)** Add the corner pieces to stabilize the bottom and middle compartments of the frame. **(q)** Add the attachments for 19'' profiles in the right-hand middle compartment. These will be used to secure the NIM-Bin power supply in place. **(r)** Add the wheels to the bottom of the setup. **(s)** Add mounting blocks to support the PVC plates in the middle and top compartment. **(t)** Add the slot rollers for the housing cage and the bedding stopper. Make sure to use the appropriate M8 T-nuts to fasten the slot rollers into the profile. **(u)** Add the PVC plates for the three compartments and secure them in place using the mounting blocks. **(v)** Add the pneumatics backplane to the right-hand top compartment. **(w)** Add the backplane for the mouse housing cage. **(x)** Add the lid of the housing cage.

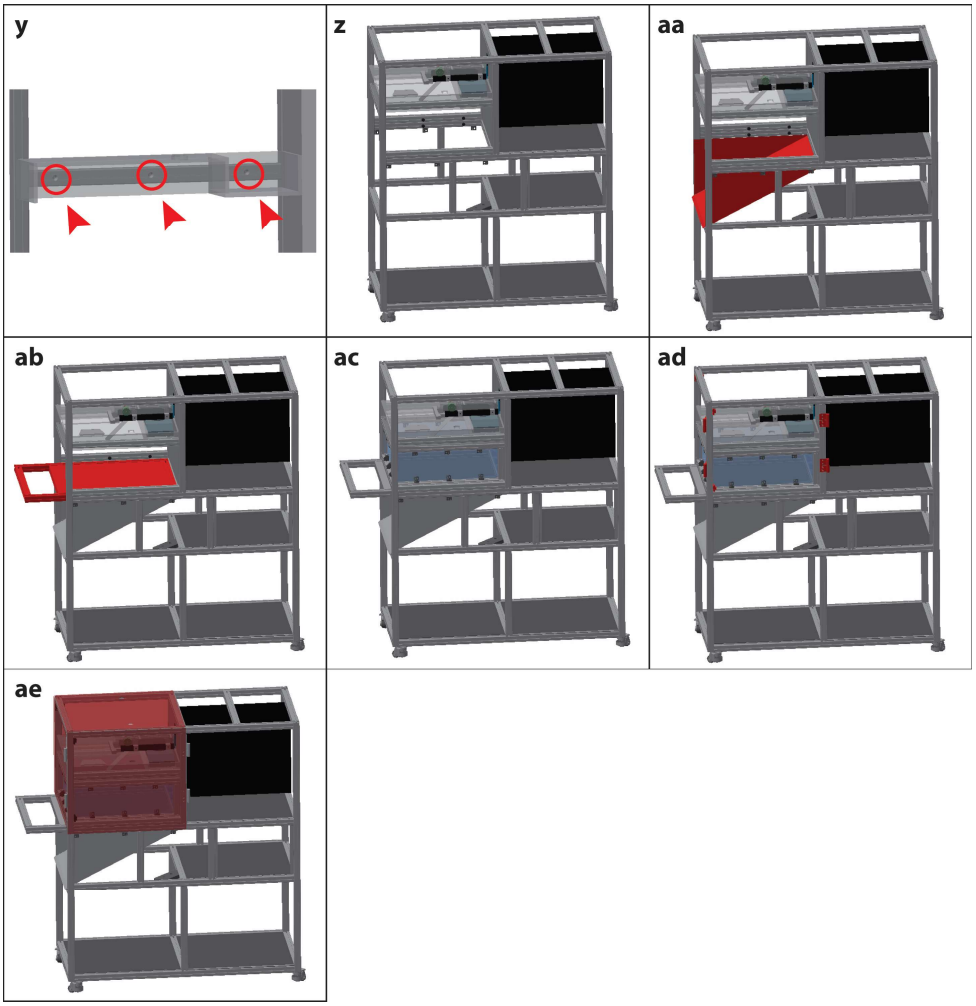

Supplementary Figure 3 Assembly of the setup frame (part 3). (y) Ensure that the T-nuts are placed at the correct location before inserting the housing cage lid into the setup frame. **(z)** Add the tunnel to the housing cage lid. **(aa)** Add the metal bedding shute. **(ab)** Insert the bedding stopper. **(ac)** Insert the housing cage. (ad) Add the aluminium hinges and magnetic locks for the setup covers. **(ae)** Add the cover plates to enclose the setup.

Construction of the housing cage

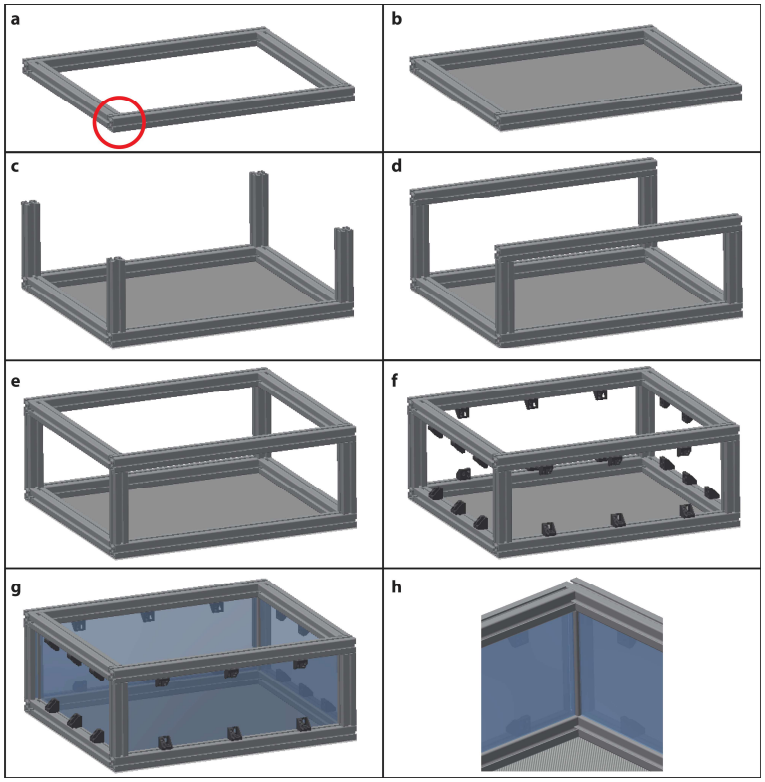

Supplementary Figure 4 Construction of the housing cage. **(a)** Use two short (529.8mm) and two long (700mm) profiles to assemble the base of the housing cage leaving the lateral grove of the long slots free. **(b)** Fix the sheet of perforated stainless steel to the bottom side of the base. **(c)** Add the vertical profiles (200mm). **(d)** Add the long (700mm) profiles. **(e)** Add the two short (529.8mm) profiles. **(f)** Fix the mounting blocks to the profiles. **(g)**. Fix the macrolon plates using the mounting blocks. **(h)** Make sure the macrolon plates are flush against the metal profiles.

Construction of the bedding stopper

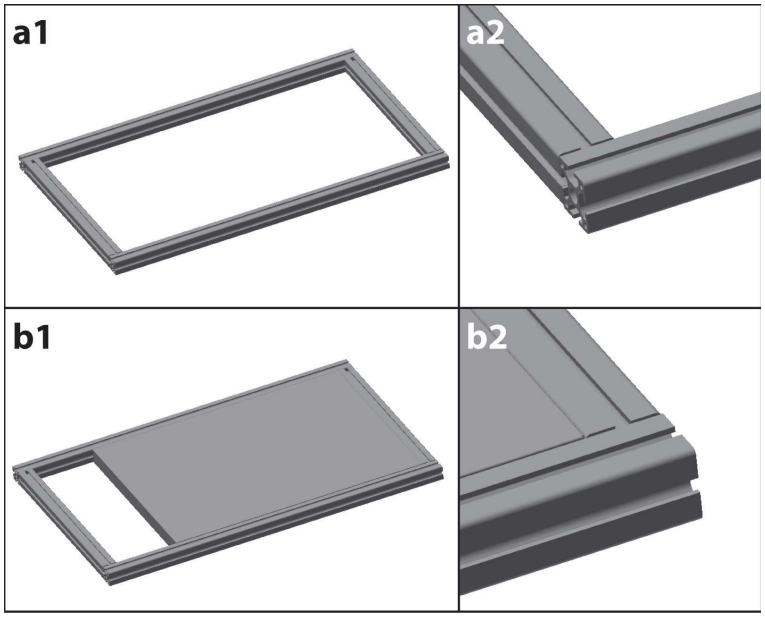

Supplementary Figure 5 Assembly of the bedding stopper placed underneath the housing cage. (a1) Use two short (529.8mm) and two long (950mm) profiles to assemble the frame of the bedding stopper **(a2)** leaving the lateral groves of the long profiles free. **(b1)** Insert the folded sheet of stainless steel into the frame **(b2)** making sure that the top sides of the profiles and the surface of the sheet form a flat, even surface.

Construction of the housing cage lid

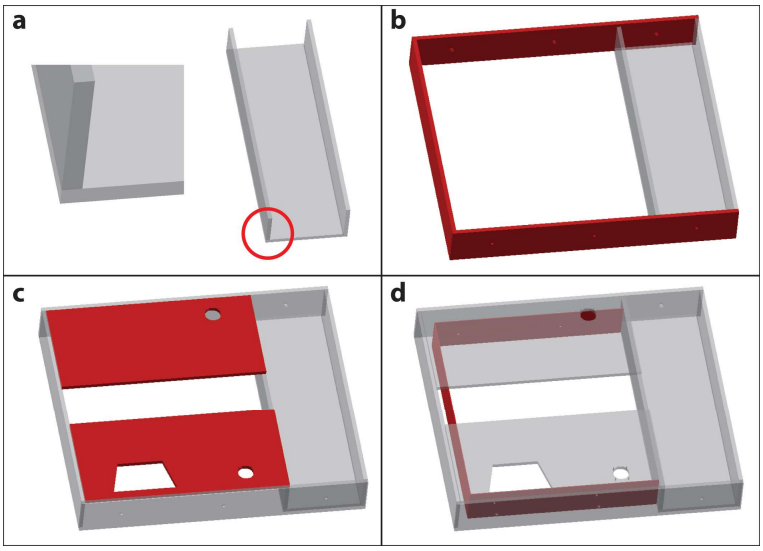

Supplementary Figure 6 Assembly of the lid of the housing cage. (a) Fix the two side panels of the scale compartment to the floor plate, placing them on top of the floor plate. **(b)** Fix the front panel (600mm) and the two side panels (700mm) to the scale compartment. **(c)** Fix the top panels to the lid. **(d)** Fix the three inlet plates to the inside of the cage lid.

Construction of the tunnel leading towards the odour port

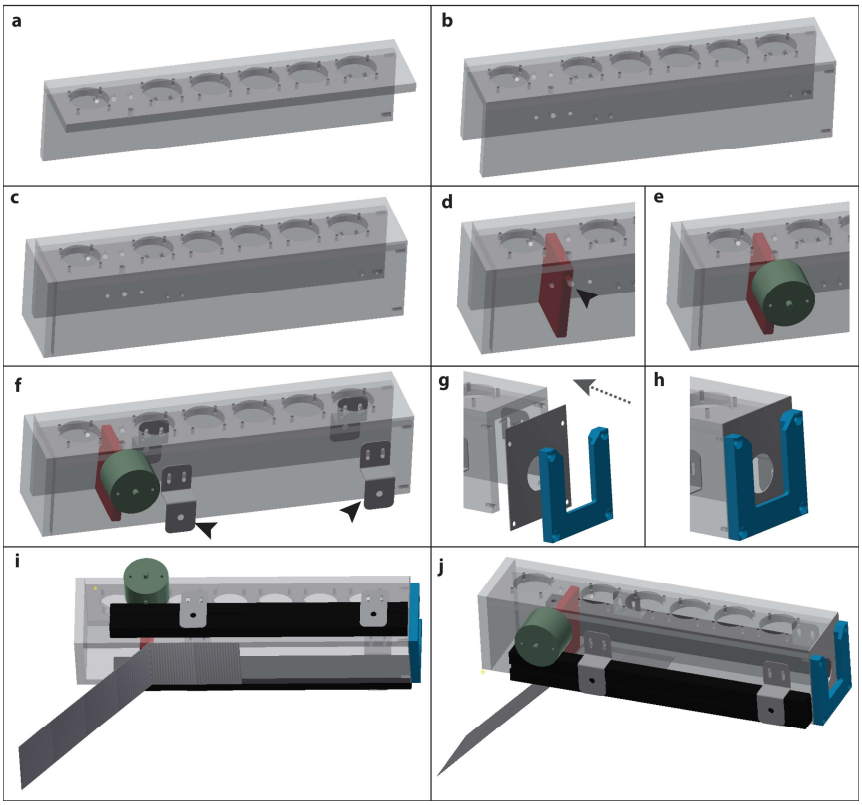

Supplementary Figure 7 Assembly of the tunnel placed on the housing cage lid. (a) Fix the lid with the fan holes to the lateral tunnel panel **(b)** and add the second lateral panel. **(c)** Add the front tunnel panel. **(d)** Insert the door (red) at the position of the central of the three motor holes (highlighted by the arrow). **(e)** Fix the motor in place. **(f)** Add the IR beam holders (arrows). **(g)**. Add the tunnel back cover (dark grey) and the sliding mechanism for the odour port (blue) and **(h)** fix them to the tunnel. **(i)**. Add the IR curtains and fix the sheet of perforated stainless steel to the bottom side of the tunnel. **(j)** Finished tunnel ready for placement on the housing cage lid.

Placement of the tunnel on the housing cage lid

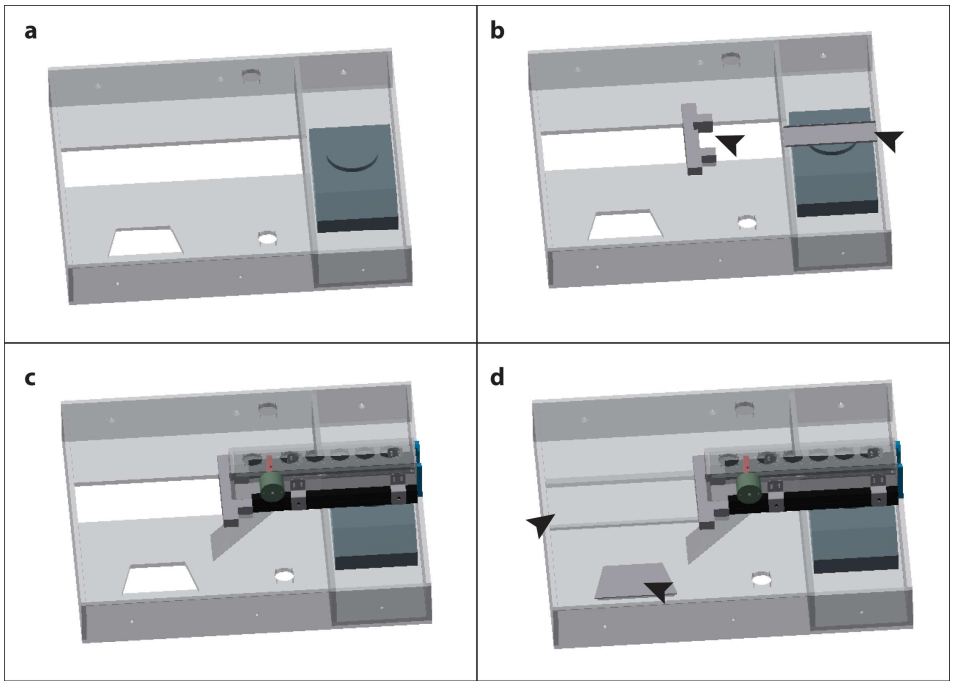

Supplementary Figure 8 Mounting of the tunnel to the housing cage lid. (a) Place the scale into the scale compartment. **(b)** Add the 3D-printed tunnel holder and the floor plate of the tunnel. **(c)** Place the tunnel into the holder. **(d)** Add the lid for the food hopper (arrow) and the maintenance cover (arrow).

Construction of the olfactometer

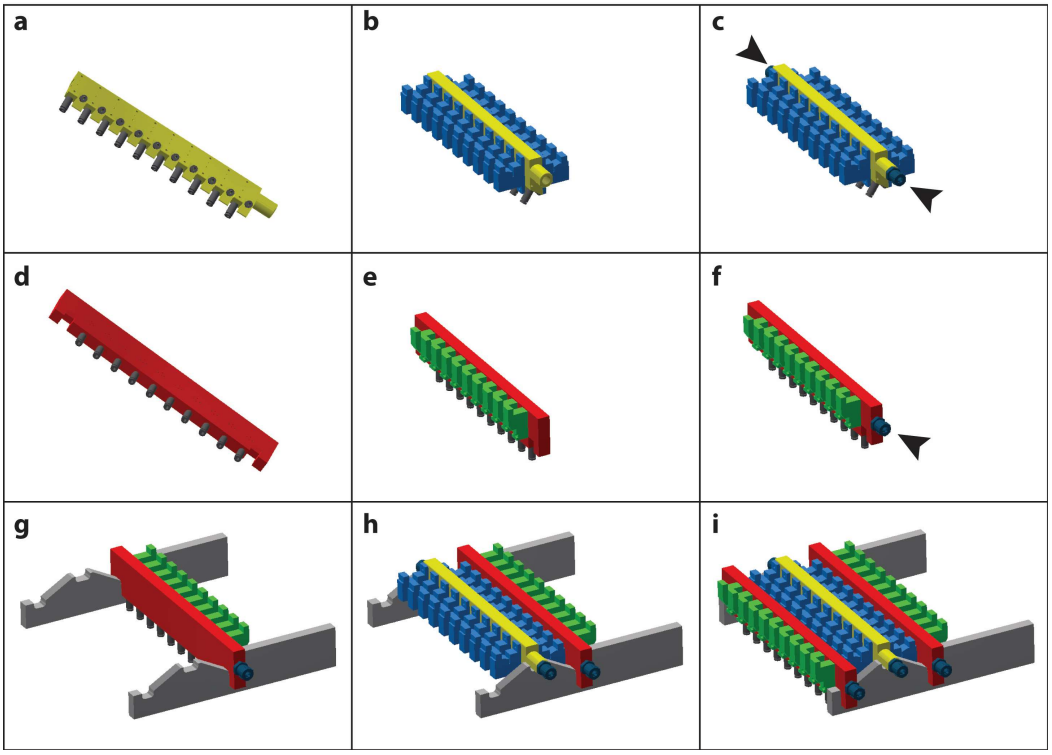

Supplementary Figure 9 Assembly of the olfactometer. (a) Screw the odour tubing fittings (SMC, #KQ2S23-M5N) into the threaded holes at the tapered bottom edges of the central manifold (yellow). **(b)** Fix the 2/2-Odour

Valves (Asco #SCS067A028) to the central manifold with the connector pins facing upwards. **(c)** Fix the tube connectors (Festo, #CK-1/8-PK-4) to the air inlet and outlet at the front and back of the central manifold (arrows). **(d)** Screw the odour tubing fittings (SMC, #KQ2S23-M5N) into the threaded holes along the bottom edges of the outer olfactometer channels (red). **(e)** Fix the 3/2-Micro Odour Valves (Asco # 18801088) to the outer olfactometer channels with the connector pins facing upwards. **(f)** Fix the tube connectors (Festo, #CK-1/8-PK-4) to the air inlet at the front of the outer olfactometer channels (arrow). **(g)** Place the right-hand side outer olfactometer channel into the olfactometer holders with the tube connector facing to the front and the valve connector pins facing upwards. **(h)** Place the central manifold into the olfactometer holder with the elongated side facing the front and the valve connector pins facing upwards. **(i)** Place the left-hand side outer olfactometer channel into the olfactometer holders with the tube connector facing to the front and the valve connector pins facing upwards.

Detailed overview of the input connections into the olfactometer

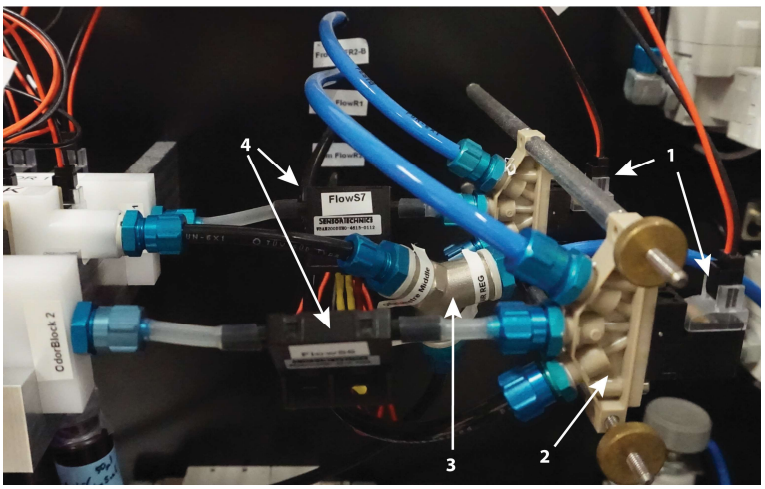

Supplementary Figure 10 Overview of the inputs to the olfactometer. Air is diverted by prepulse valves **(1)** fixed to the valve mounting blocks **(2)**. The central manifold receives clean air directly via the Y-connector **(3)** while the outer channels are measured using flow sensors **(4)**.

Assembly of the odour port

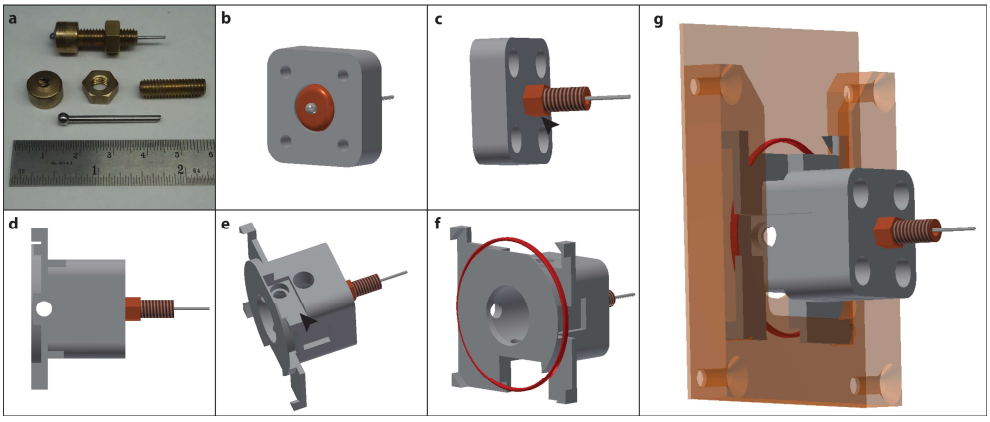

Supplementary Figure 11 Assembly of the lick spout and the 3D printed odour port. (a) Assemble the lick spout by inserting a 14G-feeding tube into a threaded copper pipe. Secure the feeding tube using a copper cap. **(b)** Insert the lick spout into the odour port back plate and **(c)** fix it in place using a copper nut (arrow). **(d)** Attach the back plate to the odour port. **(e)** Insert the IR beams into the corresponding cavities on the odour port. **(f)** Place the RFID reader antenna (red) into the grove of the odour port. **(g)** Fix the odour port to the tunnel by sliding it into the sliding holder at the back of the odour port tunnel.

Detailed overview of the water delivery system

Supplementary Figure 12 Overview of the water delivery system and the custom 3D printed holder. The 3D printed holder **(1)** is used to fix the Micro Annular Gear Pump **(2)** to the frame of the setup. The tubing is connected to a filter and fluid adapter via a pipe fitting **(3)**. The water is delivered to the lick spout through a dosing nozzle **(4)**.

Preparation of the odour reservoir caps

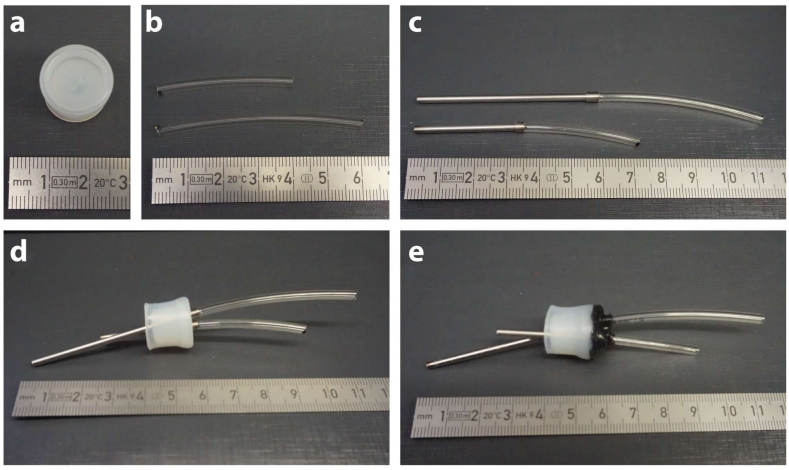

Supplementary Figure 13 Assembly of the caps for the odour reservoirs. (a) Drill two holes (diameter 3mm) into a silicone bottle cap. **(b)** Cut odour reservoir tubing to 4cm and 6cm respectively. **(c)** Fix the short tubing to the short steel pipe and the long tubing to the long pipe. **(d)** Thread the steel pipes through the holes in the silicone bottle cap. **(e)** Seal everything in place using silicone glue.

Detailed overview of the placement of the air filters

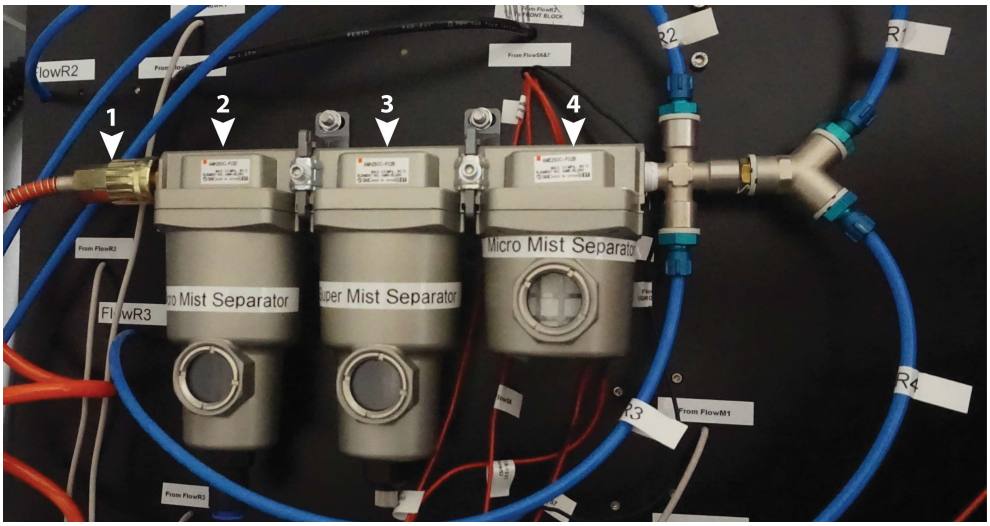

Supplementary Figure 14 Placement of the air filters on the back of the pneumatics back plane.. The input of the pressurized air **(1)** is connected to the Micro Mist Separator **(2)**, which is connected to the Micro Mist Separator **(3)** and the Supermicro Mist Separator **(4)**.

Detailed overview of the pneumatics back plane

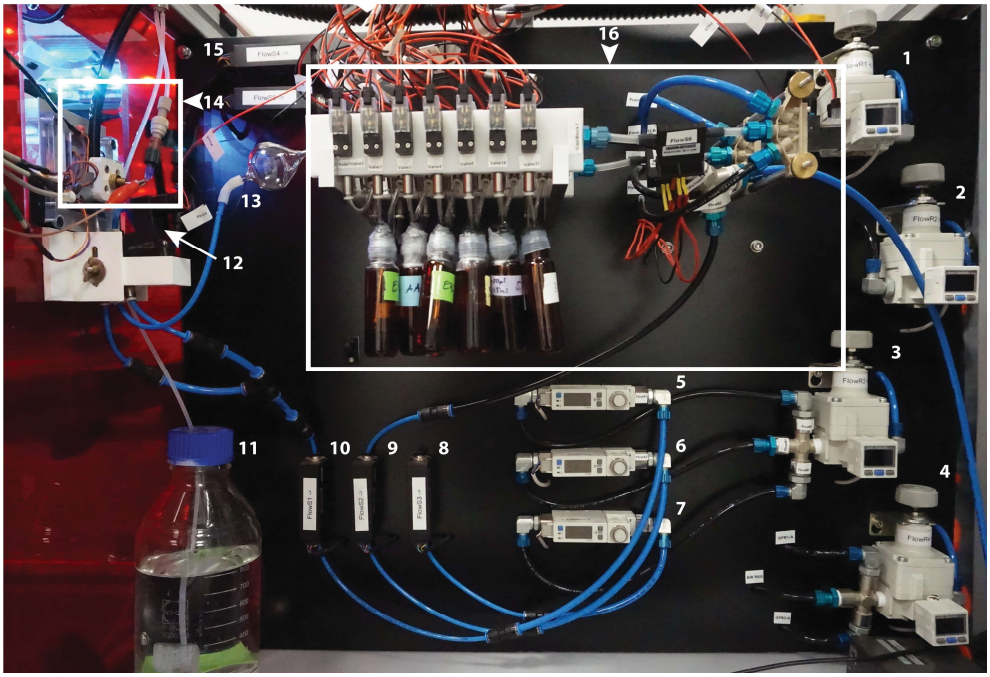

Supplementary Figure 15 Placement of the parts on the front of the pneumatics back plane. The filtered air is first passed through the pressure reducers **(1-4)** as well as the flowmeters **(5-7)** and flow sensors **(8-10)**. The water is delivered from the water reservoir **(11)** while the final valve **(12)** receives the odourised air from the glass air mixing bowl **(13)**.The water delivery system is attached to the odour port **(14)**. Exhaust air is passed through an exhaust flow sensor **(15)** while clean air is odourised through the olfactometer **(16)**.

Connection of the pneumatics tubing

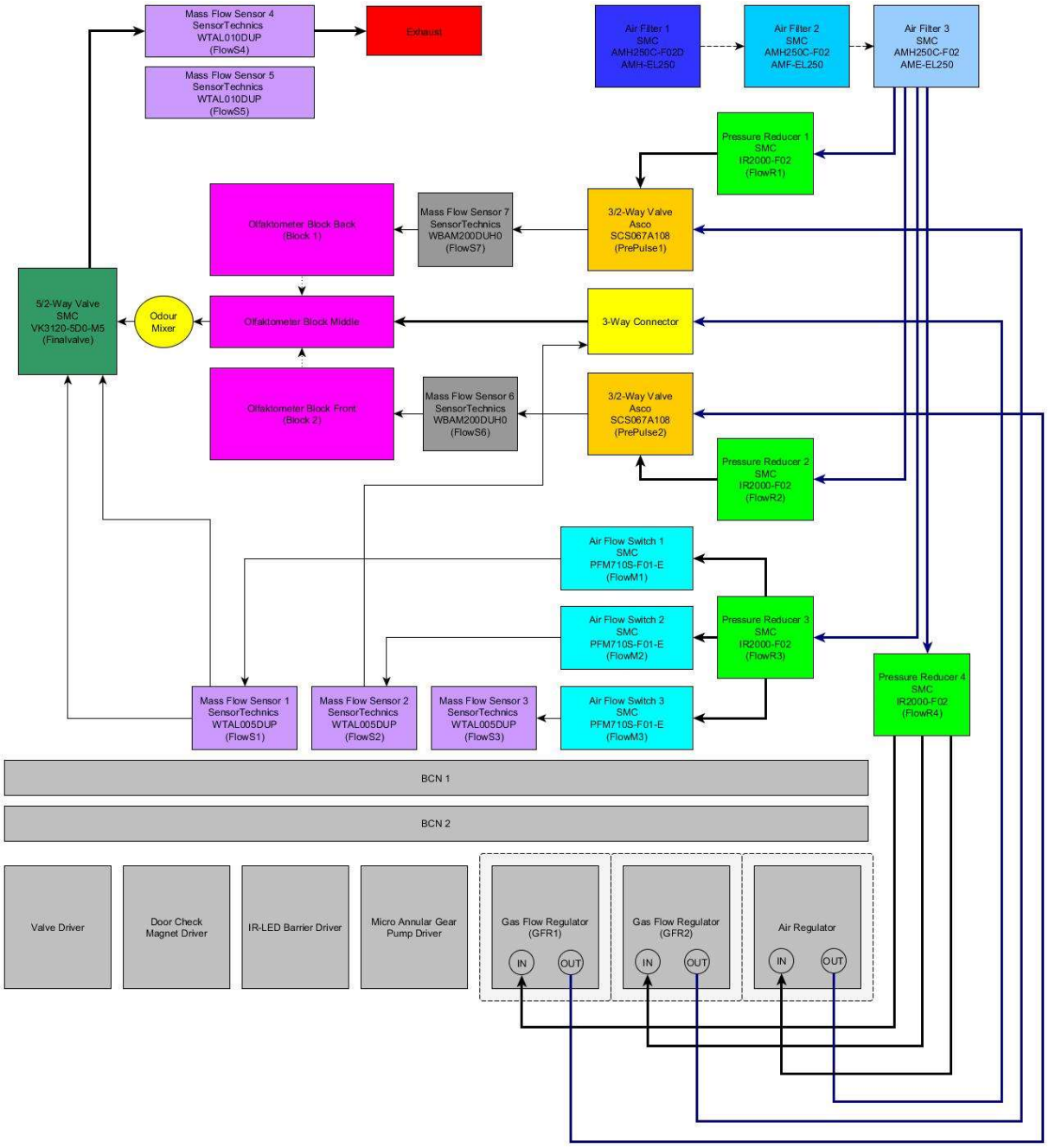

Supplementary Figure 16 Schematic representation of the pneumatics connections of the setup. Dashed lines denote direct physical connections, thick lines denote large diameter tubing (Festo, #PUN-6x1-SW and Festo, #PUN-6x1-BL) while thin lines denote small diameter tubing (Festo, #PUN-4x0,75-BL). Dotted lines between the olfactometer parts denote indirect connections through the odour reservoirs.

Detailed analysis of 4D transgenes

To analyse the effects of the transgene overexpression in more detail, we used the same induction method but additionally administered BrdU on the last day of the doxycycline administration, 12 hours prior to sacrificing the animals to label all proliferating cells (Supplementary Figure 17a). Immunostainings and subsequent quantification of BrdU-labelled cells in the SVZ revealed a substantial increase ($4D^-$: 46.9% ± 2.3; $4D^+$: 76.1% ± 5.4; unpaired t-test, $p<0.01$) of cells positive for the neuronal transcription factor Mash1, a marker used to identify intermediate progenitor cells (Supplementary Figure 17b). Further, the number of putative immature neurons or neuronal progenitor cells (as identified via doublecortin-immunoreactivity) increased nearly two-fold ($4D^-$: 35.8% ± 3.2; $4D^+$: 69.5% ± 6.4; unpaired t-test, $p<0.01$).

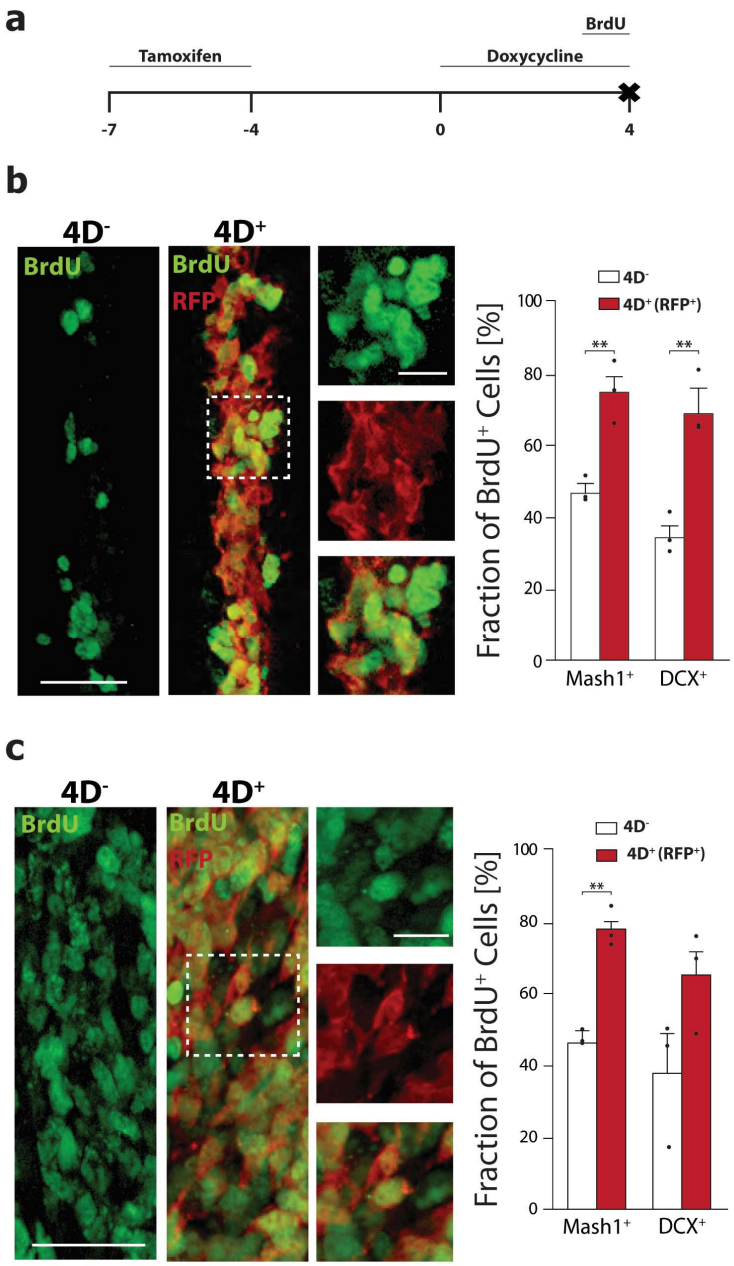

Supplementary Figure 17 Effect of the 4D transgene on the subventricular zone (SVZ) and the rostral migratory stream (RMS). **(a)** Schematic of the induction of the 4D transgene. **(b)** Representative images of the SVZ. Quantification of the BrdU-labelled cells shows a significant increase in Mash1-positive ($4D^-$: 46.9% ± 2.3; $4D^+$: 76.1% ± 5.4; unpaired t-test, $p<0.01$) as well as doublecortin (DCX) positive cells ($4D^-$: 35.8% ± 3.2; $4D^+$: 69.5% ± 6.4; unpaired t-test, $p<0.01$). $n_{Mice} = 3$, $n_{Cells} > 423$ per quantification. **(c)** Representative images of the RMS. Quantification of the BrdU-labelled cells shows a significant increase in Mash1-positive ($4D^-$: 47.9% ± 2.0; $4D^+$: 78.5% ± 2.1; unpaired t-test, $p<0.01$) cells. DCX-positive cells increased 1.6-fold ($4D^-$: 39.0% ± 10.5; $4D^+$: 65.4% ± 8.8; unpaired t-test, $p=0.13$). Scale: 50µm and 20µm (inset). $N_{Mice} = 3$, $n_{Cells} > 1100$ per quantification. **(b)/(c)**: Bar graphs show mean ± SEM, dots show mean for individual animals. Modified from[169] with permission from the publisher.

Similarly, quantification of BrdU-labelled cells in the RMS showed a significant increase of intermediate progenitor cells as identified by Mash1-immunoreactivity (Supplementary Figure 17c; $4D^-$: 47.9% ± 2.0; $4D^+$:

78.5% ± 2.1; unpaired t-test, p<0.01). While the number of doublecortin-immunoreactive cells also increased by over 50% (1.6-fold increase), this change was quite variable and hence was determine to no be statistically significant ($4D^-$: 39.0% ± 10.5; $4D^+$: 65.4% ± 8.8; unpaired t-test, p=0.13).

These results are consistent with the previously established effect of 4D overexpression on the cell cycle, ultimately resulting in an increase in cell proliferation.

Electrophysiological properties of supernumerary olfactory bulb granule cells

To determine whether or not the 4D-derived granule cells were functional and properly integrated into the olfactory bulb circuitry, whole-cell recordings from superficial granule cells were performed. As these measurements required age-matched granule cells as a control, the triple transgenic mouse line was further crossed with a mouse line expressing GFP in a Cre-dependent manner (see Materials and methods for details) which results in labelling of all Cre-ER^{T2} –expressing neuronal stem cells with GFP upon tamoxifen administration.

Both 4D-induced cells as well as the age-matched controls showed repetitive firing patterns upon injection of different current pulses (Supplementary Figure 18a, top). We found no difference between the spike frequency ($4D^-$: 12.5 spikes per 0.5s ± 0.9; $4D^+$: 13.7 spikes per 0.5s ± 2.8; unpaired t-test, p=0.71; Supplementary Figure 18a and c), nor individual features of those action potentials (spike amplitude $4D^-$: 66.7mV ± 3.5; $4D^+$: 72.3mV ± 4.8; unpaired t-test, p=0.35; spike width: $4D^-$: 1.7ms ± 0.1; $4D^+$: 1.4ms ± 0.1; unpaired t-test, p=0.12; AHP amplitude: $4D^-$: 38.1mV ± 3.9; $4D^+$: 43.1mV ± 2.3; unpaired t-test, p=0.33; Supplementary Figure 18c). Excitability was also similar between the groups, as evident from the similar threshold voltage necessary to elicit a spike (V_{th}; $4D^-$: -39.50mV± 4.85; $4D^+$: 32.20mV ± 3.32; unpaired t-test, p=0.25; Supplementary Figure 18c) and the comparable rheobase values ($4D^-$: 22.92pA± 1.90; $4D^+$: 19.00pA ± 3.49; unpaired t-test, p=0.27; Supplementary Figure 18c)

Further we found a delayed spike initiation for lower current pulses compared to higher current pulses (lag to spike; $4D^-$: 78.5ms ± 12.2; $4D^+$: 79.5ms ± 12.3; unpaired t-test, p=0.95; Supplementary Figure 18a, bottom), characteristic for OB granule cells[65].

Additionally, cells from both genotypes received spontaneous synaptic input of similar strength ($4D^-$: 2.6mV ± 0.5; $4D^+$: 2.7mV ± 0.7; unpaired t-test, p=0.87; Supplementary Figure 18b and c) and frequency ($4D^-$: 2.9Hz ± 0.8; $4D^+$: 3.6Hz ± 0.8; unpaired t-test, p=0.52; Supplementary Figure 18b and c), indicating proper functional integration into the OB circuitry of 4D-derived cells. Passive membrane properties, like the resting membrane voltage (V_{Rest}; $4D^-$: -66.0mV ± 3.4; $4D^+$: -60.7mV ± 4.2; unpaired t-test, p=0.33; Supplementary Figure 18c), the input resistance (R_{in}; $4D^-$: 892.7MΩ ± 86.6; $4D^+$: 956.8MΩ ± 103.7; unpaired t-test, p=0.64; Supplementary Figure 18c) or the membrane capacitance (C_m; $4D^-$: 18.66pF± 1.99; $4D^+$: 17.80pF ± 1.38; unpaired t-test, p=0.25; Supplementary Figure 18c), also showed no difference between the two genotypes.

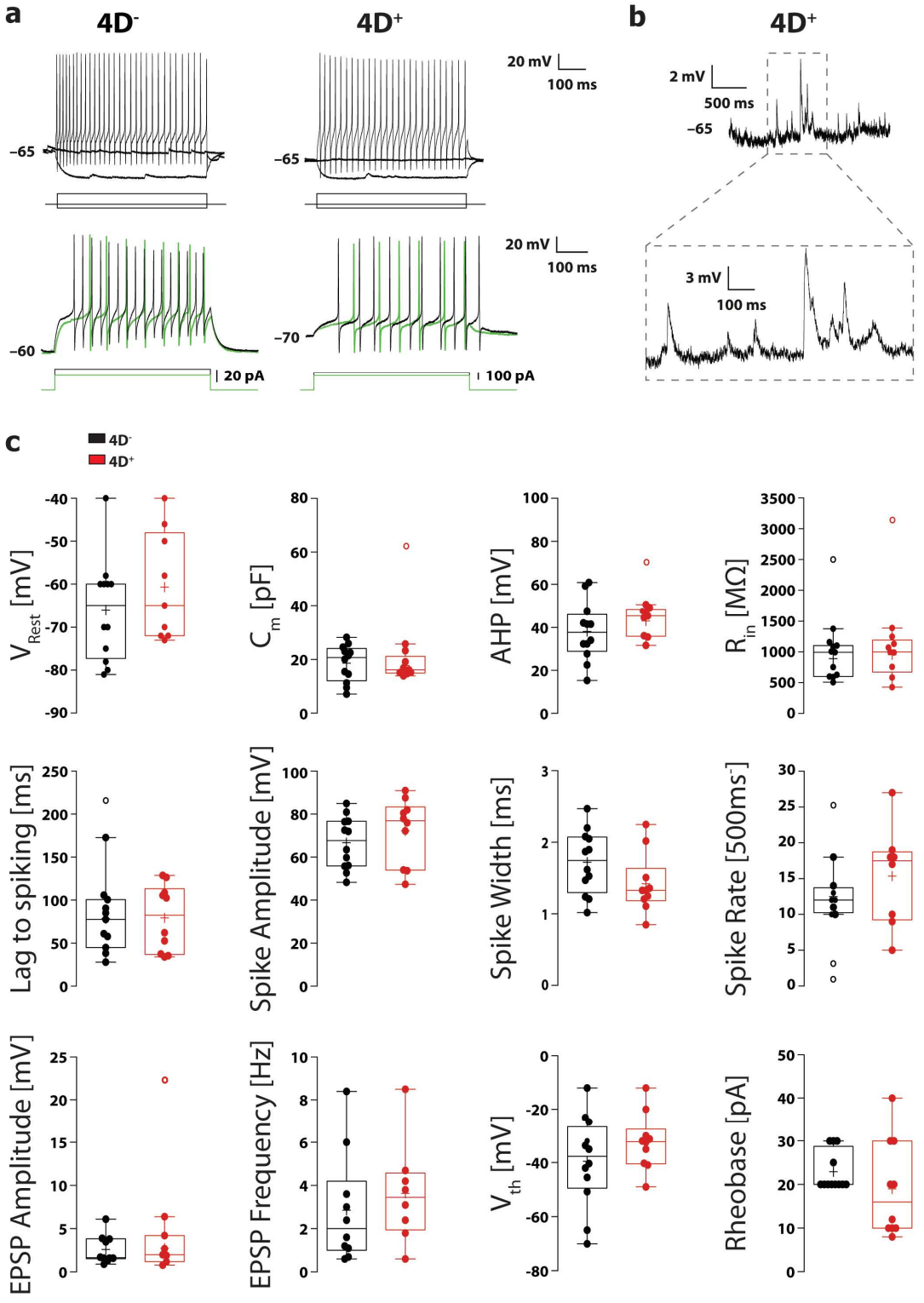

Supplementary Figure 18 Electrophysiological properties of 4D-derived granule cells in the olfactory bulb. (a) Exemplary current clamp recordings showing spiking in response to current steps. Note the increased lag in spike initiation at lower currents (green) compared to higher currents (black). **(b)** Exemplary recording showing spontaneous synaptic potentials in a 4D+ animal. **(c)** Different electrophysiological properties of patched granule cells from $4D^-$ (black) and $4D^+$ (red) animal show no differences between the genotypes. Whiskers show 1.5 interquartile range, line denotes median while cross denotes mean. Dots show individual cells while circles show outlier's as identified by Tukey's test. $4D^-$ $n_{Neurons} = 12$; $4D^+$ $n_{Neurons} = 10$; $n_{Mice} > 5$. Modified from[169] with permission from the publisher.

Supplementary Methods: Electrophysiological recordings

Mice were anesthetised using isoflurane (Abbvie, #Forane), decapitated and the dissected brains transferred to chilled standard artificial cerebro-spinal fluid (ACSF; 125mM NaCl, 2.5mM KCl, 25mM $NaHCO_3$, 2mM $CaCl_2$, 1mM $MgCl_2$, 1.25mM NaH_2PO_4, 25mM glucose in H_20, pH 7.4; aerated with carbogen). Coronal sections of 300µm thickness were incubated in protective ACSF (92mM N-methyl-D-glucamine, 2.5mM KCl, 1.25mM NaH_2PO_4, 30mM $NaHCO_3$, 20mM HEPES, 25mM glucose, 2mM thiourea, 5 Na-Ascorbate, 3 Na-Pyruvate, 0.5mM $CaCl_2$ x $4H_2O$, 10mM $MgSO_4$ x $7H_2O$ in H_20, pH 7.4; aerated with carbogen) at 34°C for 10-15min and subsequently incubated for 60min at room-temperature in standard ACSF. For recordings, slices were transferred to a recording chamber, superfused with standard ACSF, visualized using an Axio Imager 2 (Zeiss) and recordings performed using an Axopatch 200B amplifier (Molecular Devices) and a Digidata 1440A digitizer (Molecular Devices) controlled using pClamp 10 software (Molecular Devices). Capillaries from borosilicate glass (Sutter Instruments, #BF150-86-10) were pulled on a horizontal puller (Sutter Instruments, #P-1000) with a tip resistance of 5-10MΩ and filled with a solution of 125mM K-gluconate, 5mM NaCl, 2mM Na_2-ATP, 2mM $MgCl_2$, 10mM EGTA, 10mM HEPES, 10mM biocytin in H_20, pH 7.4. This solution was further supplemented with 0.2mM Alexa 488 hydrazine (Invitrogen, #A10436) or Alexa 594 hydrazine (Invitrogen, #A10438) to enable morphological reconstructions of the recorded cells. Recordings were made from superficial granule cells identified through GFP/RFP fluorescence ($4D^-$: GFP^+/RFP^-; $4D^+$: GFP^+/RFP^+). Cells were kept at a holding potential (V_{hold}) of around -60mV and the recordings were excluded if at least one of the following criteria was fulfilled: no RFP or GFP signal (depending on genotype), seal resistance <4GΩ or >18 GΩ, no attachment of the soma to the pipette or series resistance >40MΩ (± 20%) throughout the recording. Series resistance, whole-cell capacitance and the junction potential were not corrected for.

Analysis of electrophysiological recordings

Data was recorded and analysed using pClamp 10 software (Molecular Devices). Membrane properties were determined through a series of hyperpolarizing and depolarizing current steps (10pA steps) with a duration of 500ms each. The resting membrane potential (V_{Rest}) was determined at the current of 0A while the input resistance (R_{in}) was calculated from the response to a hyperpolarizing current step of 50pA for the duration of 500ms. The membrane capacitance (C_m) was determined using the membrane constant (τ_m) according to the following formula:

$$C_m = \frac{\tau_m}{R_{in}}$$

The membrane constant was obtained by fitting a single exponential curve to the voltage response to a hyperpolarizing current step of 50pA for the duration of 500ms. Detailed analysis of action potentials was performed on the first spike at rheobase, with rheobase being defined as the amplitude of the first

depolarizing step to elicit a firing response. The voltage threshold (V_{th}) for the initiation of an action potential was defined as the voltage at the inflection point of the action potential. The spike width was measured at half-maximal spike amplitude. The spike amplitude was defined as the distance between the voltage threshold and the peak of the spike while the after-hyperpolarization amplitude was defined as the distance between the voltage threshold and the lowest voltage during repolarization after the spike. The lag to spike was measured as the distance between the start of the current step and the voltage threshold for the first spike at a holding potential of -80mV. The spike frequency was determined by counting the number of spikes during the 500ms of a 30pA current step.

For the analysis of spontaneous events, a 20s recording in the "*Gap-free"* mode was performed without any stimulation and subsequently analysed using the built in *"Clampfit template search"* function of pClamp 10.

Detailed analysis of the effect of the 4D transgene on odour discrimination

Supplementary Table 1 Data (mean ± SEM) and statistical analysis underlying plots shown in Figure 25

Parameter	Odour Pair	4D-	4D+	Inter-group comparison
Trials To Criterion	Cin vs Eu	513.3 ± 101.2	783.7 ± 256.3	0.3770
	AA vs EB	257.3 ± 54.7	231.5 ± 26.36	0.0976
	AA/EB Mix	427 ± 41.04	463.7 ± 61.16	0.6109
	(-) vs (+)-Oct	243.2 ± 74.87	219.4 ± 38.47	0.9796
	(-)/(+) Oct Mix	322.6 ± 46.13	373.3 ± 58.22	0.1463
Fraction Correct	Cin vs Eu	0.98 ± 0.004	0.97 ± 0.005	0.1781
	AA vs EB	0.98 ± 0.002	0.98 ± 0.002	0.2786
	AA/EB Mix	0.98 ± 0.002	0.97 ± 0.002	**0.0260**
	(-) vs (+)-Oct	0.99 ± 0.001	0.98 ± 0.002	0.1327
	(-)/(+) Oct Mix	0.98 ± 0.001	0.98 ± 0.002	0.475
d-prime	Cin vs Eu	2.98 ± 0.25	2.75 ± 0.24	0.5276
	AA vs EB	3.64 ± 0.11	3.44 ± 0.11	0.2364
	AA/EB Mix	3.09 ± 0.09	2.85 ± 0.13	0.1051
	(-) vs (+)-Oct	3.92 ± 0.08	3.75 ± 0.11	0.2221
	(-)/(+) Oct Mix	3.32 ± 0.16	3.16 ± 0.17	0.4975
Lick Frequency [%]	Cin vs Eu	51.28 ± 1.86	49.47 ± 0.82	0.4291
	AA vs EB	49.91 ± 0.23	48.74 ± 0.30	**0.0035**
	AA/EB Mix	51.69 ± 0.46	51.33 ± 0.71	0.6572
	(-) vs (+)-Oct	49.24 ± 0.23	49.40 ± 0.35	0.7130
	(-)/(+) Oct Mix	49.99 ± 0.31	49.66 ± 0.39	0.5113
Dwell rate	Cin vs Eu	0.9993 ± 0.0002	0.9996 ± 0.0002	0.3786
	AA vs EB	0.9998 ± 0.00007	0.9994 ± 0.0001	**0.0096**
	AA/EB Mix	0.9999 ± 0.00005	0.9997 ± 0.0001	0.1384
	(-) vs (+)-Oct	0.9997 ± 0.00008	0.9997 ± 0.0001	0.9202
	(-)/(+) Oct Mix	0.9997 ± 0.00010	0.9998 ± 0.00006	0.3424
ITI [s]	Cin vs Eu	19.93 ± 1.40	20.66 ± 0.78	0.6758
	AA vs EB	15.52 ± 0.42	17.27 ± 0.72	**0.0404**
	AA/EB Mix	15.94 ± 0.49	17.43 ± 0.72	0.0858
	(-) vs (+)-Oct	14.46 ± 0.46	15.71 ± 0.42	0.0587
	(-)/(+) Oct Mix	14.91 ± 0.61	16.02 ± 0.78	0.2662

Inter-genotype comparisons were performed using unpaired, two-tailed t-tests. Values showing significant differences at a significance level of 0.05 are highlighted in bold.

Supplementary Table 2 Results of the inter-group comparisons of the data shown in Figure 25

Parameter	Odour Pair 1	Odour Pair 2	4D-	4D+
Trials to Criterion	Cin vs Eu	AA vs EB	**0,0413**	0,0928
	AA vs EB	AA/EB Mix	**< 0,0001**	**0,0008**
	AA/EB Mix	(-) vs (+)-Oct	**< 0,0001**	**0,0002**
	(-) vs (+)-Oct	(-)/(+) Oct Mix	0,0529	**0,0120**
Fraction Correct	Cin vs Eu	AA vs EB	0,2083	**0,0482**
	AA vs EB	AA/EB Mix	**0,0045**	**0,0004**
	AA/EB Mix	(-) vs (+)-Oct	**< 0,0001**	**0,0003**

	(-) vs (+)-Oct	(-)/(+) Oct Mix	**0,0194**	0,1095
d-prime	Cin vs Eu	AA vs EB	0,0736	0,0924
	AA vs EB	AA/EB Mix	**0,0003**	**0,0009**
	AA/EB Mix	(-) vs (+)-Oct	**< 0,0001**	**< 0,0001**
	(-) vs (+)-Oct	(-)/(+) Oct Mix	**0,0053**	**0,01**
Lick Frequency [%]	Cin vs Eu	AA vs EB	0,3444	0,5274
	AA vs EB	AA/EB Mix	**0,0002**	**0,0016**
	AA/EB Mix	(-) vs (+)-Oct	**< 0,0001**	**0,0240**
	(-) vs (+)-Oct	(-)/(+) Oct Mix	**0,0337**	0,2124
Dwell rate	Cin vs Eu	AA vs EB	0,2856	0,2420
	AA vs EB	AA/EB Mix	0,5416	0,1105
	AA/EB Mix	(-) vs (+)-Oct	0,4346	>0,9999
	(-) vs (+)-Oct	(-)/(+) Oct Mix	0,8409	0,2377
ITI [s]	Cin vs Eu	AA vs EB	0,9973	0,2153
	AA vs EB	AA/EB Mix	0,7146	0,7765
	AA/EB Mix	(-) vs (+)-Oct	**0,0016**	**0,0087**
	(-) vs (+)-Oct	(-)/(+) Oct Mix	0,8577	0,1718

Intra-genotype comparisons were performed using paired, two-tailed t-tests. Values showing significant differences at a significance level of 0.05 are highlighted in bold.

Supplementary Table 3 Data (mean ± SEM) and statistical analysis underlying plots shown in Figure 28 as well as Figure 29.

Parameter	Odour Pair	4D-	4D+	Inter-group comparison
Trials To Criterion	AA vs EB Memory	10.00 ± 0.00	10.00 ± 0.00	(groups identical)
	AA/EB Mix Memory	27.75 ± 4.08	43.23 ± 6.99	0.1404
Fraction Correct	AA vs EB Memory	1.00 ± 0.00	1.00 ± 0.00	(groups identical)
	AA/EB Mix Memory	1.00 ± 0.00	1.00 ± 0.00	(groups identical)
d-prime	AA vs EB Memory	2.47 ± 0.030	2.51 ± 0.013	0.3086
	AA/EB Mix Memory	2.07 ± 0.073	2.027 ± 0.114	0.7490
Lick Frequency [%]	AA vs EB Memory	49.53 ± 1.49	50.08 ± 1.45	0.8000
	AA/EB Mix Memory	50.76 ± 0.35	49.94 ± 0.77	0.2812
Dwell rate	AA vs EB Memory	0.9988 ± 0.00063	0.9995 ± 0.00029	0.4047
	AA/EB Mix Memory	1.0000 ± 0.000000	1.0000 ± 0.000014	0.1769
ITI [s]	AA vs EB Memory	17.94 ± 0.64	17.45 ± 0.29	0.5363
	AA/EB Mix Memory	14.31 ± 0.47	14.57 ± 0.48	0.7059

Inter-genotype comparisons were performed using unpaired, two-tailed t-tests.

Detailed analysis T-type calcium channel knock-downs

Supplementary Table 4 Relative quantity of T-type subunits after expression of shRNA sequences and virus result of comparison against baseline expression levels.

	$Ca_V3.1$				$Ca_V3.2$				$Ca_V3.3$			
	Mean	**SEM**	**n**	**p-Value**	**Mean**	**SEM**	**n**	**p-Value**	**Mean**	**SEM**	**n**	**p-Value**
Control Batch 1	0,50	0,11	3	**0,001**	0,79	0,21	3	0,22	0,46	0,19	3	**0,01**
Control Batch 1 (1:2)	0,84	0,07	3	**0,03**	1,27	0,02	3	**< 0,0001**	0,98	0,08	3	0,71
Control Batch 2 (1:10)	0,90	0,20	4	0,59	1,00	0,19	4	0,99	0,54	0,11	4	**0,002**
$Ca_V3.1$ Variant 1 Batch 1	0,62	0,11	5	**0,01**	0,97	0,07	5	0,68	0,94	0,05	5	0,32
$Ca_V3.1$ Variant 1 Batch 2	0,03	0,01	4	**< 0,0001**	0,93	0,07	4	0,23	0,67	0,21	4	0,13
$Ca_V3.1$ Variant 1 Batch 2 (1:2)	0,07	0,01	4	**< 0,0001**	0,89	0,04	4	**0,02**	0,72	0,10	4	**0,02**
$Ca_V3.2$ Variant 1 Batch 1	0,41	0,06	5	**< 0,0001**	0,32	0,05	5	**< 0,0001**	0,82	0,09	5	**0,07**
$Ca_V3.2$ Variant 2 Batch 1	0,92	0,18	5	0,66	0,36	0,03	5	**< 0,0001**	0,98	0,06	5	0,68
$Ca_V3.2$ Variant 3 Batch 1	0,69	0,10	5	**0,02**	0,37	0,04	5	**< 0,0001**	0,81	0,05	5	**0,003**
$Ca_V3.3$ Variant 1 Batch 1	0,54	0,15	5	**0,01**	0,77	0,08	5	**0,02**	0,45	0,06	5	**< 0,0001**
$Ca_V3.3$ Variant 1 Batch 1	0,99	0,10	5	0,94	0,94	0,05	5	0,22	0,57	0,04	5	**< 0,0001**
$Ca_V3.3$ Variant 3 Batch 1	0,91	0,12	5	0,45	0,75	0,06	5	**0,003**	0,71	0,04	5	**< 0,0001**
Triple knock-down	0,01	0,00	4	**<0,0001**	0,08	0,02	4	**< 0,0001**	0,38	0,11	4	**0,0005**
Virus Mix	0,18	0,07	3	**< 0,0001**	0,09	0,04	3	**< 0,0001**	0,16	0,09	3	**< 0,0001**

Comparisons were performed using unpaired, two-tailed t-tests. Values showing significant differences at a significance level of 0.05 are highlighted in bold.

Supplementary Table 5 Data (mean ± SEM) and statistical analysis underlying Figure 38

Parameter	Odour Pair	Control	Triple knock-down	Inter-group comparison
Trials To Criterion	Cin vs Eu	302.1 ± 38.04	326.7 ± 47.5	0.69
	AA vs EB	364.9 ± 37.63	497.0 ± 94.51	0.21
	AA/EB Mix (40%/60%)	917.0 ± 83.12	841.0 ± 104.7	0.45
	AA/EB Mix (48%/52%)	1361.0 ± 211.8	1741.0 ± 160.6	0.18
Fraction Correct	Cin vs Eu	0.91 ± 0.007	0.91 ± 0.007	0.61
	AA vs EB	0.97 ± 0.002	0.97 ± 0.001	0.06
	AA/EB Mix (40%/60%)	0.97 ± 0.001	0.97 ± 0.001	0.32
	AA/EB Mix (48%/52%)	0.97 ± 0.002	0.97 ± 0.002	0.46
d-prime	Cin vs Eu	2.67 ± 0.14	2.64 ± 0.12	0.85
	AA vs EB	3.20 ± 0.08	3.04 ± 0.09	0.22
	AA/EB Mix (40%/60%)	2.84 ± 0.05	3.00 ± 0.06	0.05
	AA/EB Mix (48%/52%)	2.68 ± 0.10	2.63 ± 0.07	0.66
Lick Frequency [%]	Cin vs Eu	45.92 ± 0.75	45.87 ± 0.28	0.95
	AA vs EB	48.48 ± 0.24	47.88 ± 0.17	0.66
	AA/EB Mix (40%/60%)	48.76 ± 0.33	49.66 ± 0.18	**0.03**
	AA/EB Mix (48%/52%)	50.35 ± 0.47	49.84 ± 0.62	0.57
Dwell rate	Cin vs Eu	0.99 ± 0.0018	0.99 ± 0.0016	0.56
	AA vs EB	0.98 ± 0.0072	1.00 ± 0.0008	0.10
	AA/EB Mix (40%/60%)	1.00 ± 0.0001	1.00 ± 0.0003	0.19

	AA/EB Mix (48%/52%)	1.00 ± 0.0000	1.00 ± 0.0000	(groups identical)
ITI [s]	Cin vs Eu	18.50 ± 0.77	17.92 ± 0.67	0.58
	AA vs EB	16.84 ± 0.72	16.19 ± 0.26	0.42
	AA/EB Mix (40%/60%)	15.06 ± 0.45	14.88 ± 0.44	0.78
	AA/EB Mix (48%/52%)	14.36 ± 0.37	14.56 ± 0.37	0.72

Inter-genotype comparisons were performed using unpaired, two-tailed t-tests. Values showing significant differences at a significance level of 0.05 are highlighted in bold.

Supplementary Table 6 Results of the inter-group comparisons of the data shown in Figure 38

Parameter	Odour Pair 1	Odour Pair 2	Control	Triple knock-down
Trials to Criterion	Cin vs Eu	AA vs EB	0.22	0.13
	AA vs EB	AA/EB Mix (40%/60%)	**< 0.0001**	0.06
	AA/EB Mix (40%/60%)	AA/EB Mix (48%/52%)	0.16	**0.006**
Fraction Correct	Cin vs Eu	AA vs EB	**< 0.0001**	**< 0.0001**
	AA vs EB	AA/EB Mix (40%/60%)	0.09	0.18
	AA/EB Mix (40%/60%)	AA/EB Mix (48%/52%)	0.39	0.51
d-prime	Cin vs Eu	AA vs EB	**0.002**	**0.007**
	AA vs EB	AA/EB Mix (40%/60%)	**0.005**	0.60
	AA/EB Mix (40%/60%)	AA/EB Mix (48%/52%)	0.14	**0.004**
Lick Frequency [%]	Cin vs Eu	AA vs EB	**0.008**	**< 0.0001**
	AA vs EB	AA/EB Mix (40%/60%)	0.54	**< 0.0001**
	AA/EB Mix (40%/60%)	AA/EB Mix (48%/52%)	**0.0009**	0.93
Dwell rate	Cin vs Eu	AA vs EB	0.28	**0.01**
	AA vs EB	AA/EB Mix (40%/60%)	0.19	0.28
	AA/EB Mix (40%/60%)	AA/EB Mix (48%/52%)	0.111*	0.18
ITI [s]	Cin vs Eu	AA vs EB	**0.0006**	**0.002**
	AA vs EB	AA/EB Mix (40%/60%)	**0.002**	**0.02**
	AA/EB Mix (40%/60%)	AA/EB Mix (48%/52%)	0.41	0.43

Intra-genotype comparisons were performed using paired, two-tailed t-tests. Values showing significant differences at a significance level of 0.05 are highlighted in bold.

*Due to removal of potential outliers, an unpaired two-tailed t-test was used.